# Investigating the effect of chronic activation of AMP-activated protein kinase in vivo

**Alice Pollard**

CASE Studentship Award

A thesis submitted to Imperial College London for the degree of Doctor of Philosophy

September 2017

Cellular Stress Group

Medical Research Council

London Institute of Medical Sciences

Imperial College London

# Declaration

I declare that the work presented in this thesis is my own, and that where information has been derived from the published or unpublished work of others it has been acknowledged in the text and in the list of references. This work has not been submitted to any other university or institute of tertiary education in any form.

**Alice Pollard**

The copyright of this thesis rests with the author and is made available under a Creative Commons Attribution Non-Commercial No Derivatives license. Researchers are free to copy, distribute or transmit the thesis on the condition that they attribute it, that they do not use it for commercial purposes and that they do not alter, transform or build upon it. For any reuse or redistribution, researchers must make clear to others the license terms of this work.

# Abstract

The prevalence of obesity and associated diseases has increased significantly in the last decade, and is now a major public health concern. It is a significant risk factor for many diseases, including cardiovascular disease (CVD) and type 2 diabetes. Characterised by excess lipid accumulation in the white adipose tissue, which drives many associated pathologies, obesity is caused by chronic, whole-organism energy imbalance; when caloric intake exceeds energy expenditure. Whilst lifestyle changes remain the most effective treatment for obesity and the associated metabolic syndrome, incidence continues to rise, particularly amongst children, placing significant strain on healthcare systems, as well as financial burden.

AMP-activated protein kinase (AMPK) is widely regarded as a master regulator of energy homeostasis, acting as a cellular 'fuel gauge' to maintain intracellular ATP concentrations under conditions of metabolic stress. AMPK is known to promote catabolic pathways, including lipolysis, fatty acid oxidation and glycolysis, whilst inhibiting anabolic pathways in response to energy deprivation. AMPK is a strong therapeutic candidate for the treatment of obesity and the metabolic syndrome, with several studies providing evidence for the amelioration of type 2 diabetes *in vivo.*

In collaboration with AstraZeneca, a novel transgenic mouse model was generated, expressing a gain-of-function mutation in the regulatory γ-subunit of AMPK; D316A, resulting in a constitutively active AMPK complex expressed globally. Initial observations revealed a polycystic kidney-like disease with a possible mouse strain effect, as well as cardiac glycogen accumulation, with no associated conductance defect. The subsequent characterisation of this mouse model revealed a novel role for AMPK activation in the protection from diet-induced obesity, conferred by a significant increase in exercise-independent energy expenditure, driven by UCP1-independent thermogenesis in the subcutaneous white adipose tissue (WATsc). It was found that, on a chow diet, the WATsc resembled classical brown adipose tissue which, when exposed to a high-fat diet, was subjected to transcriptional re-programming leading to the expression of many muscle-related genes associated with calcium/creatine futile cycling. This work highlights a role for AMPK in the protection from obesity, through the alteration of cell fate.

# Acknowledgements

I would sincerely like to thank my supervisors, Professor David Carling and Dr. Angela Woods, for their help, support and enthusiasm for this work over the course of this PhD project. I am grateful for the opportunity to work with such accomplished and passionate scientists, who have been so open and willing to share their knowledge and experience to make this work possible. I would like to thank Angela for her assistance in the laboratory, and for her dedication to helping not just myself but to everyone working in our group. It has been a pleasure to work in such an open and honest environment, facilitating many thought-provoking scientific discussions. I would very much like to thank AstraZeneca, the BBSRC and Imperial College London for their generous funding that has supported both this work and my development as a scientist.

In addition, I would like to thank those at AstraZeneca, particularly my supervisor, Jon Read, for the support of this work, Maryam Clausen and Aurelie Bornot for their assistance with RNA sequencing, and Daniel Sutton for his assistance and technical expertise with immunohistochemistry.

I would like to thank Phillip Muckett for his help, guidance and technical expertise with all animal studies. Without it, the work presented here could not have been achieved.

In addition, I would like to thank the members of the animal physiology team for their help with *in* vivo studies. I would like to thank Dr. Luis Martins for his technical assistance with several key studies and for his expertise surrounding several aspects of this work. I would like to thank Laura Wilson for her work on the heart and kidney, for embracing this aspect of the project and taking it on as her own.

Over the course of my PhD I have received invaluable support and friendship from every member of the Cell Stress Group, for which I am especially grateful. It has been an amazing experience to work in such a fun and supportive environment, with many laughs and engaging discussions over coffee. I would like to thank my family, my friends, my colleagues and my partner for their unwavering support over the years. Though no longer with us, I would like to thank my grandfather for passing on to me his passion for science, I am sure we would have had many enjoyable discussions.

# Contents

Declaration ..... 2
Abstract ..... 3
Acknowledgements ..... 4
Table of figures ..... 9
List of Abbreviations, Terms and Acronyms ..... 13
1 CHAPTER 1: INTRODUCTION ..... 18
1.1 Pathogenesis of Obesity and the Metabolic Syndrome ..... 20
1.1.1 Food Intake ..... 25
1.1.2 Energy Expenditure ..... 35
1.2 Current Treatments and Therapeutic Strategies ..... 43
1.2.1 Current Treatments ..... 43
1.3 AMP-Activated Protein Kinase: A Master Regulator of Energy Homeostasis 45
1.3.1 A Highly Conserved Metabolic Regulator ..... 45
1.3.2 Structure and Regulation of AMPK ..... 47
1.3.3 Downstream Targets of AMPK ..... 52
1.4 Studying AMPK Activation *in vivo* ..... 58
1.4.1 Activators and Inhibitors ..... 58
1.4.2 Mouse Models of AMPK Signalling ..... 62
1.4.3 The Activating Mutant: An Novel Tool to Study Gain of Function *in vivo* 68
1.5 Project Aims ..... 69
2 CHAPTER 2: MATERIALS AND METHODS ..... 71
2.1 Materials ..... 71
2.1.1 General Reagents ..... 71
2.1.2 Buffers ..... 72
2.1.3 Antibodies ..... 72
2.1.4 Primers ..... 74
2.2 Animal Studies ..... 76
2.2.1 Declaration ..... 76
2.2.2 Animal Models ..... 76
2.2.3 Diet Administration ..... 77
2.2.4 Blood sampling ..... 77
2.2.5 Glucose Tolerance ..... 77

2.2.6 Comprehensive Laboratory Animal Monitoring System (CLAMS) ..... 78
2.2.7 Feeding studies (BioDAQ) ..... 78
2.2.8 Ultrasound and Echocardiogram ..... 78
2.2.9 ECGenie (Electrocardiogram) ..... 78
2.2.10 Tamoxifen Administration for the Induction of D316A-Tg Expression 79
2.2.11 Genotyping ..... 79
2.3 General Methods ..... 80
2.3.1 Dissection and tissue preservation ..... 80
2.3.2 Homogenisation of whole tissue ..... 80
2.3.3 RNA extraction ..... 80
2.3.4 cDNA synthesis ..... 81
2.3.5 Quantitative polymerase chain reaction (qPCR) ..... 81
2.3.6 Gel electrophoresis and Western blotting ..... 82
2.3.7 Immunohistochemistry ..... 82
2.3.8 Glycogen Assay ..... 83
2.3.9 Enzyme Linked ImmunoSorbent Assay (ELISA) ..... 84
2.3.10 Triglyceride Assay ..... 85
2.3.11 Immunoprecipitation (for Western blotting) ..... 86
2.4 RNA sequencing ..... 86
2.4.1 RNA Extraction and Quality Assessment ..... 86
2.4.2 RNA Sequencing Analysis Pipeline ..... 86
2.4.3 Manual annotation with Online Gene/Pathway Analysis ..... 87
2.4.4 Ingenuity Pathway Analysis ..... 87
2.5 Mitochondrial respiration in subcutaneous white adipocytes ..... 87
2.5.1 White adipocyte isolation (whole cell suspension) ..... 87
2.5.2 Mitochondrial respiration (OROBOROS O2K) ..... 88
2.6 Statistical analyses ..... 89
3 CHAPTER 3: METABOLIC CONSEQUENCES OF GLOBAL AMPK ACTIVATION ..... 91
3.1 Mouse Model Characterisation ..... 91
3.1.1 Genotyping Strategy ..... 91
3.1.2 Confirmation of AMPKγ1-D316A Transgenic Protein Expression *in vivo* 92
3.2 Metabolic Phenotyping of the D316A-Tg Mouse Model ..... 94
3.2.1 Bodyweight and total body composition on a chow diet ..... 94

3.2.2 Food intake (chow) ..... 95
3.2.3 Glucose Homeostasis (chow) ..... 96
3.2.4 Tissue weight (chow) ..... 99
3.2.5 Bodyweight and total body composition (HFD) ..... 100
3.2.6 Food intake (HFD) ..... 104
3.2.7 Glucose handling and hormonal signalling (HFD) ..... 106
3.2.8 Energy Expenditure (EE) ..... 113
3.2.9 Brown Adipose Tissue-Mediated Thermogenesis ..... 116
3.3 Characterisation of D316A-Tg subcutaneous white adipose tissue ..... 120
3.3.1 Tissue weight and morphology ..... 121
3.3.2 RNA sequencing ..... 126
3.3.3 Principal Component Analysis ..... 126
3.3.4 WATsc RNA sequencing ..... 129
3.3.5 Confirmation of DEG expression by qPCR ..... 132
3.3.6 Characterisation of D316A-Tg WATsc on a chow diet ..... 134
3.3.7 Lineage determination in D316A-Tg WATsc ..... 140
3.3.8 Mitochondrial activity (O2K) ..... 145
3.4 Tamoxifen Inducible Model ..... 147
3.5 Discussion ..... 154
3.5.1 Protection from Diet Induced Obesity ..... 154
3.5.2 Food intake ..... 157
3.5.3 Energy expenditure and thermogenesis in the D316A-Tg mouse model 158
3.5.4 ‘Browning’ of the WATsc ..... 160
3.5.5 Future work: Metabolic consequences of AMPK activation ..... 170
4 CHAPTER 4: CHARACTERISATION OF THE CARDIORENAL PHYSIOLOGY OF D316A-TG MICE ..... 175
4.1 Introduction ..... 175
4.2 Observation of kidneys from D316A-Tg mice revealed a cystic phenotype 180
4.2.1 Monitoring of the D316A-Tg kidney phenotype in vivo ..... 182
4.2.2 Characterisation of D316A-Tg kidney morphology ..... 184
4.2.3 Kidney development and glycogen accumulation ..... 186
4.2.4 Increased Proliferation is a Hallmark of the D316A-Tg Kidney Phenotype 191
4.2.5 Polycystic kidney disease gene expression ..... 194

4.2.6 129S2/SvHsd D316A-Tg kidney characterisation ..... 195
4.3 Cardiac phenotyping of the D316A mouse ..... 199
4.3.1 D316A-Tg$^{129Sv}$ cardiac hypertrophy and glycogen storage ..... 206
4.4 Discussion ..... 210
5 SUMMARY AND PERSPECTIVES ..... 221
5.1.1 Summary of findings ..... 221
5.1.2 AMPK as a therapeutic target ..... 226
5.1.3 Closing remarks ..... 227
6 APPENDICES ..... 246
6.1 RNA Sequencing Extended Data ..... 246
6.2 Extended Metabolic Data ..... 304

Table of figures

Figure 1.1 Location of brown adipose (BAT) and white adipose tissue (WAT) depots in mouse and human. ..... 21
Figure 1.2 Distinct morphology of brown adipose, beige adipose and subcutaneous white adipose tissue depots. ..... 23
Figure 1.3 Possible crosstalk between insulin, leptin and adiponectin signalling. ..... 28
Figure 1.4 The role of adipose inflammation and lipolysis in hepatic steatosis. ..... 33
Figure 1.5 Induction of Ucp1 gene expression by cold exposure in BAT. ..... 39
Figure 1.6 Origins of skeletal muscle, brown, white and beige adipose. ..... 42
Figure 1.7 Overview of the roles of AMPK in vivo. ..... 46
Figure 1.8 AMPK subunit structure and complex formation. ..... 48
Figure 1.9 Regulation of AMPK activity by upstream kinases and nucleotides. ..... 50
Figure 1.10 Regularly identified downstream targets of AMPK. ..... 52
Figure 1.11 Molecular mechanism of glycogen accumulation promoted by AMPK activation. ..... 55
Figure 1.12 Summary of direct AMPK activation in vivo using activators and mouse models. ..... 66
Figure 1.13 Generation of the WT-Tg and D316A-Tg mouse model. ..... 68
Figure 3.1 Detection of D316A-Tg FLAG-tagged protein expression in isolated tissues. ..... 92
Figure 3.2 Detection of endogenous AMPKγ1 (AMPK-endog.) and FLAG-tagged WT-Tg and D316A-Tg protein. ..... 93
Figure 3.3 Bodyweight and total body composition on a chow diet. ..... 94
Figure 3.4 Daily food intake on a chow diet. ..... 95
Figure 3.5 Glucose homeostasis in the D316A-Tg mouse model on a chow diet. ..... 97
Figure 3.6 Terminal tissue weights of chow-fed WT-Tg and D316A-Tg mice. ..... 99
Figure 3.7 Protection from HFD-induced obesity exhibited by D316A-Tg mice. ..... 100
Figure 3.8 Total body composition of D316A-Tg mice on a HFD. ..... 101
Figure 3.9 Terminal tissue weights from HFD-fed male WT-Tg and D316A-Tg mice. ..... 102
Figure 3.10 Protection from HFD-induced hepatic steatosis. ..... 103
Figure 3.11 Daily food intake and feeding behaviour of D316A-Tg mice on a HFD. ..... 105

Figure 3.12 Circulating factors in chow-fed and HFD-fed WT-Tg and D316A-Tg mice. ..... 107
Figure 3.13 Glucose tolerance and fatty acid metabolism in WT-Tg and D316A—Tg mice. ..... 109
Figure 3.14 Glycogen accumulation in D316A-Tg skeletal muscle. ..... 111
Figure 3.15 Oxygen consumption ($VO_2$) is increased in D316A-Tg HFD-fed mice. 113
Figure 3.16 Respiratory exchange ratio (RER) of 6-week HFD-fed (14-week old) WT-Tg and D316A-Tg mice. ..... 114
Figure 3.17 Assessment of spontaneous locomotor activity..... 115
Figure 3.18 Average rectal (core) and subcutaneous temperature of WT-Tg and D316A-Tg 12-week HFD-fed (20-week old) male mice. ..... 116
Figure 3.19 Thermogenic response to the β3-adrenoreceptor agonist CL316, 243117
Figure 3.20 UCP1 expression in response to β3-adrenoceptor stimulation. ..... 118
Figure 3.21 Mitochondrial content and UCP1 expression in chow- and HFD-fed mice. ..... 119
Figure 3.22 Subcutaneous white adipose tissue (WATsc) mass is reduced in D316A-Tg HFD-fed mice. ..... 121
Figure 3.23 WATsc morphology from WT-Tg and D316A-Tg 4-week HFD-fed (12-week old) male mice. ..... 123
Figure 3.24 Assessment of mitochondrial biogenesis in HFD-fed D316A-Tg mice. 124
Figure 3.25 Expression of UCP1 in WATsc from 4-week HFD-fed WT-Tg and D316A-Tg male mice. ..... 125
Figure 3.26 Principal component analysis..... 127
Figure 3.27 Differentially expressed genes in sequenced tissues..... 128
Figure 3.28 Volcano plot: WATsc..... 129
Figure 3.29 IPA Network analysis of differentially expressed genes in D316A-Tg WATsc. ..... 130
Figure 3.30 Characterisation of muscle gene expression in D316A-Tg WATsc. .... 131
Figure 3.31 Differentially expressed gene confirmation by qPCR ..... 132
Figure 3.32 Creatine kinase protein expression in chow and HFD-fed mice ..... 133
Figure 3.33 ‘BAT-like’ morphology of D316A-Tg WATsc on a chow diet..... 134
Figure 3.34 Mitochondrial biogenesis in chow-fed D316A-Tg mice..... 135
Figure 3.35 Mitochondrial content in WATsc of chow- and HFD-fed D316A-Tg mice ..... 137

Figure 3.36 BAT-associated gene expression in D316A-Tg WATsc ..... 139
Figure 3.37 Evidence for a BAT-muscle transition in D316A-Tg WATsc..... 140
Figure 3.38 Overlap of gene expression between D316A-Tg WATsc and EHMT1 KO BAT. ..... 142
Figure 3.39 Evidence for the endothelial origin of D316A-Tg WATsc. ..... 144
Figure 3.40 Mitochondrial respiration and response to palmitate in D316A-Tg WATsc ..... 146
Figure 3.41 Detection of tamoxifen-induced D316A-Tg-FLAG expression. ..... 147
Figure 3.42 Bodyweight curve of HFD-fed $WT^{TMX}$ and D316A-$Tg^{TMX}$ male mice. .. 148
Figure 3.43 Total body composition of $WT^{TMX}$ and D316A-$Tg^{TMX}$ HFD-fed mice. .. 149
Figure 3.44 Protection from HFD-associated hyperinsulinaemia and hepatic steatosis in D316A-$Tg^{TMX}$ mice. ..... 150
Figure 3.45 Resistance to lipid accumulation in D316A-$Tg^{TMX}$ BAT and WATsc. ... 151
Figure 3.46 Vascularisation of D316A-$Tg^{TMX}$ WATsc ..... 151
Figure 3.47 Mitochondrial biogenesis in D316A-$Tg^{TMX}$ WATsc. ..... 152
Figure 3.48 Creatine kinase-SERCA futile cycling ..... 163
Figure 3.49 Hypothesis: AMPK promotes $Myf5^{+}$ cell development in WATsc, facilitating Ckmt2/SERCA futile cycling. ..... 166
Figure 3.50 Location and proportion of $Myf5^{+}$ BAT and WAT depots in wild type mice, adapted from Sanchez-Gurmaches and Guertin, 2014. ..... 169
Figure 4.1 Schematic outlining renal development, outlining murine kidney development..... 176
Figure 4.2 Schematic of cyst development in cystic kidney disease, adapted from Wallace et al., 2011..... 178
Figure 4.3 AMPK D316A-Tg, 129sv/C57BL/6J, chow-fed animals display a cystic kidney phenotype on a chow diet ..... 181
Figure 4.4 Monitoring of the D316A-Tg cystic kidney phenotype in vivo ..... 183
Figure 4.5 AMPKγ1-D316A-Tg mice develop cystic kidneys from 3 weeks of age 184
Figure 4.6 AMPKγ1-D316A-Tg Mice on a mixed background develop chronic kidney disease with associated renal failure (preliminary) at 33 weeks of age. ..... 185
Figure 4.7 Non-Tg and D316A-Tg kidney development ..... 188
Figure 4.8 Nephrogenic zone of neonatal (P1) Non-Tg and D316A-Tg kidneys. ... 189
Figure 4.9 D316A-Tg kidney development and glycogen deposition. ..... 190
Figure 4.10 Proliferation in the D316A-Tg developing kidney ..... 192

Figure 4.11 Sustained, irregular proliferation in the D316A-Tg kidney ..... 193
Figure 4.12 Expression of key genes associated with a cystic kidney phenotype are unaltered in D316A-Tg kidneys at 7 weeks of age. ..... 194
Figure 4.13 D316A-Tg Mice on a 129Sv background display a severe cystic kidney phenotype on a chow diet. ..... 196
Figure 4.14 PAS staining of Non-Tg and D316A-Tg 129Sv mice at 30 weeks of age. ..... 197
Figure 4.15 AMPK D316A-Tg chow-fed animals display increased heart weight on a chow diet. ..... 200
Figure 4.16 AMPK D316A-Tg chow-fed animals do not exhibit any ECG abnormalities associated with Wolff-Parkinson-White Syndrome..... 202
Figure 4.17 AMPK D316A-Tg chow-fed animals display cardiac glycogen accumulation. ..... 204
Figure 4.18 D316A-Tg chow- and HFD-fed mice display enhanced cardiac glycogen synthase phosphorylation. ..... 205
Figure 4.19 D316A-Tg Mice on a 129Sv background display cardiac hypertrophy and glycogen accumulation, with indication of severe cardiac defects..... 206
Figure 4.20 PAS staining of Non-Tg and D316A-Tg$^{129Sv}$ hearts. ..... 208
Figure 4.21 D316A-Tg Mice on a 129Sv background display cardiac hypertrophy and glycogen accumulation, with indication of severe cardiac defects..... 209
Figure 4.22 Potential mechanisms for the development of polycystic kidney diseases. ..... 217
Figure 6.1 Neuropeptide expression in chow-fed mice..... 304
Figure 6.2 Normalised tissue wet weight..... 305
Figure 6.3 BAT/muscle gene expression in D316A-Tg$^{TMX}$ WATsc ..... 306
Figure 6.4 Lipolysis in tamoxifen-treated gonadal WAT ..... 307
Figure 6.5 Individual cohort bodyweight curves (HFD)..... 308

# List of Abbreviations, Terms and Acronyms

Acta1 Skeletal muscle α-actin

A/D Analogue digital converter

ACC Acetyl-CoA carboxylase

ADP Adenosine 5’-diphosphate

AF Atrial fibrillation

AgRP Agouti-related peptide

AICAR 5-amino-4-imidazolecarboxamide riboside

AMP Adenosine 5’-monophosphate

AMPK AMP-activated protein kinase

ANCOVA Analysis of covariance

ANOVA Analysis of variance

ARC Arcuate nucleus of the hypothalamus

ATP Adenosine 5’-triphosphate

AUC Area under the curve

BAT Brown adipose tissue

BCA Bicinchoninic acid

BMI Body mass index

BSA Bovine serum albumin

BW Body weight

CA Constitutively active

CaMKKβ Ca2+/calmodulin-dependent protein kinase kinase-β

CART Cocaine- and amphetamine-regulated transcript

Casr Calcium sensing receptor

CBS Cystathionine β–synthase

Cebpα CCAAT/Enhancer Binding Protein Alpha

Cebpβ CCAAT/Enhancer Binding Protein Beta

Ckm Creatine kinase, muscle

Ckmt2 Creatine kinase, muscle, mitochondrial

CPT1 Carnitine palmitoyltransferase 1

CREB cAMP response element-binding protein

Csq Calsequestrin

DIO Diet-induced obesity

DN Dominant negative
dNTPs Deoxynucleotide triphosphates
ECG Electrocardiogram
EDTA Ethylenediaminetetraacetic acid
EE Energy expenditure
EF Ejection fraction
EHMT1 Euchromatic Histone Lysine Methyltransferase 1
ELISA Enzyme-linked immunosorbent assay
eMRI echo magnetic resonance imaging
Eno3 Enolase 3
ER Endoplasmic reticulum
ES cells Embryonic stem cells
FBS Fetal bovine serum
FC Fold-change
FoxO Forkhead box subfamily O
FS Fractional shortening
G6P Glucose-6-phosphate
GAP GTPase-Activating Proteins
GBD Glycogen-binding domain
gDNA Genomic DNA
GLUT4 Glucose transporter 4
GP Glycogen phosphorylase
GS Glycogen synthase
GSD Glycogen storage disorder
GTP Guanosine triphosphate
GTT Glucose tolerance test
HBSS Hank’s Balanced Salt Solution
HCM Hypertrophic cardiomyopathy
H&E Haematoxylin and eosin
HEPES Hydroxyethyl piperazineethanesulfonic acid
HFD High fat diet
HMG-CoA 3-hydroxy-3-methylglutaryl-CoA
HW Heart weight
IGF-1 Insulin-like growth factor 1

IL6 Interleukin 6
I.P. Intraperitoneal
IP Immunoprecipitation
IP3 Inositol-1,4,5-trisphosphate
IRS Insulin receptor substrate
IVCs Individually ventilated cages
KI Knock-in
KO Knock-out
LEPR Leptin receptor
LKB1 Liver kinase B1
loxP Locus of crossover [x] in P1
LV Left ventricle
LVH Left ventricular hypertrophy
MEF2 Myocyte enhancer factor-2
mRNA Messenger ribonucleic acid
mTORC1 Mammalian TOR complex 1
Myh7 β-myosin heavy chain
MyoD Myogenic differentiation factor
MyoG Myogenin
N-terminus Amino-terminus
NADH Nicotinamide adenine dinucleotide
NADPH Reduced form of NADP+
NADP+ Nicotinamide adenine dinucleotide phosphate
Neb Nebulin
NPY Neuropeptide Y
Nrf1 Nuclear respiratory factor 1
ob/ob Obese/obese, leptin deficient
PAS Periodic Acid-Schiff
PBS Phosphate-buffered saline
PCA Principle components analysis
PCR Polymerase chain reaction
PEPCK Phosphoenolpyruvate carboxykinase
PGC-1α Peroxisome proliferator-activated receptor γ co-activator 1α
PI(3)K Phosphatidylinositol-3-OH kinase

Pln Phospholamban
POMC Proopiomelanocortin
PP1 Type 1 protein phosphatase
PP2A Protein phosphatase-2A
PPARγ Peroxisome proliferator-activated receptor γ
Prdm16 PR domain containing 16
qRT-PCR Quantitative, real-time reverse-transcriptase PCR
RA Right atrium
RNA Ribonucleic acid
RN Rendement Napole
ROS Reactive oxygen species
RT Room temperature
RV Right ventricular
Ryr1 Ryanodine receptor 1
Ryr2 Ryanodine receptor 2
Ryr3 Ryanodine receptor 3
RXR Retinoid X receptor
SDS Sodium dodecyl sulphate
SEM Standard error of the mean
shRNA Short hairpin ribonucleic acid
SERCA2 Sarco/endoplasmic reticulum Ca2+ ATPase
SGLT-1 Sodium-dependent glucose transporter
Slc2a4 Solute carrier family 2 (facilitated glucose transporter)
Snf1 Sucrose non-fermenting
STAT3 Signal transducer and activator of transcription 3
STRAD STE-20 related adaptor protein
TBC1D4 TBC1 domain family member 4
TBST Tris-Buffered Saline with Tween-20
TG Transgenic
Tm Melting temperature
TMX Tamoxifen
TNFα Tumour necrosis factor-α
Tnnc1 Troponin C1, slow, skeletal and cardiac
Tnnc2 Troponin C2, fast, skeletal type

TnnI1 Troponin 1, slow skeletal type

TORC2 Transducer of regulated CREB activity 2

TSC2 Tuberous sclerosis protein 2

Ttn Titin

UCP1 Uncoupling protein 1

UNAG urine N-acetyl-β-D-glucosaminidase

UCRT Urine creatinine

VMH Ventromedial nucleus of the hypothalamus

WAT White adipose tissue

WATg Gonadal white adipose tissue

WATsc Subcutaneous/inguinal white adipose tissue

WHO World Health Organisation

WPW Wolff-Parkinson White

WT Wild-type

WT-Tg Transgenic wild-type (AMPK-WT-$\gamma1^{flox/STOP/flox}$)

# 1 CHAPTER 1: INTRODUCTION

Obesity, defined as excessive or abnormal adiposity, is a leading cause of death worldwide. Previously regarded as a disease of the Western world, obesity and associated health conditions collectively referred to as the metabolic syndrome, now affects 200-300 million adults worldwide, with 1.4 billion adults categorised as 'overweight' in 2008. By 2030, it is predicted that 74% of men and 64% of women will be obese, in the United Kingdom alone (Collaboration, 2016). However, this disease is now known to affect developing and semi-developed nations worldwide, including a significant increase in incidence in Africa and South-East Asia, predicted to match those of developed countries in the near future, perhaps even exceeding them as awareness and availability of treatment increases in socio-economically advanced nations (Bhurosy and Jeewon, 2014).

The World Health Organisation (WHO) defines obesity based on the measurement of Body Mass Index (BMI), calculated as weight (kg) divided by height squared ($m^2$). The current threshold for a diagnosis of overweight is a BMI of between 25 and 30, with obesity defined as a BMI above 30. However, within this diagnosis exists three 'classes' of obesity; Class I (moderately obese) defined by a BMI of 30-35, Class II (severely obese) from 35-40 and Class III (very severely/morbidly obese) identified by a BMI greater than 40 (Fruhbeck et al., 2013, Hebebrand, 2008). Whilst this provides a reasonable estimation of overweight/obese, it does not account for lean muscle mass, and is therefore accompanied by a measurement of waist to hip ratio and fat mass assessed by dual-energy X-ray absorptiometry (DEXA) body scanning to calculate fat and lean mass percentage, in addition to bone density.

Identification of overweight/obese individuals is, however, intrinsically difficult, given that weight gain is not often seen as a medical condition by patients until other symptoms come to the forefront. Indeed, in recent years, the promotion of obesity-acceptance in the overweight population (Robinson and Christiansen, 2014), a sedentary lifestyle and the explosion of a high-calorie 'food culture' in Western society has detracted from the severity of these conditions, often caused by 'invisible', visceral adiposity affecting internal organs including, but not limited to, non-alcoholic fatty liver disease (NAFLD), diabetes and cardiovascular disease. These, amongst others, contribute to the metabolic syndrome.

The increase in prevalence of obesity, particularly amongst children and adolescents, can be attributed almost entirely to the availability of high-fat, high-sugar diets, in conjunction with a reduction in physical activity, promoted by a rise in sedentary activities such as television, video games and, more recently, social media. It has also been shown that parental influence can directly affect the predisposition to and development of childhood and adolescent obesity, stemming from a reluctance to accept one's own bodyweight and lifestyle concerns, coupled with resistance to, or a lack of knowledge of factors influencing weight gain (Savage et al., 2007). In addition, limited household income in lower socio-economic classes and developing countries has promoted the growth of cheap, 'fast-food' establishments promoting consumption of fried foods, sugary beverages and sodium, whilst providing convenience, discouraging home cooking and resulting in a reduction in the consumption of fresh, nutrient rich foods (Bhurosy and Jeewon, 2014).

Whilst the environmental and lifestyle factors influencing the onset of obesity are clear, a significant proportion of the world's population is not overweight or obese. Although some of these individuals may fall into higher socio-economic categories, this has not been shown to be preventative as a stand-alone measurement of risk, suggesting that underlying, non-environmental factors also play a role in the development of this disease (Bhurosy and Jeewon, 2014). Those participating in an active lifestyle with a healthy diet consisting of fresh fruit, vegetables, wholegrains and sufficient protein intake are protected from obesity in almost all cases, with a significant reduction in the incidence of CVD, type 2 diabetes and NAFLD (reviewed in (Fock and Khoo, 2013)). However, though lifestyle and dietary choices play a significant role in the prevention of obesity, the implementation of such changes are inherently difficult, with success relying on acceptance, commitment and reversal of existing pathology. In addition, underlying conditions can impair the amelioration of obesity, particularly those inhibiting regular movement, such as multiple sclerosis (MS), stroke, physical disabilities and pulmonary disorders, which in turn contributes to the deterioration of patients suffering from such conditions.

For a modest proportion of the obese population, defects in certain regulatory networks governing food intake, lipid handling and storage and basal metabolic rate can predispose patients to early-onset obesity, though these are often reversed by lifestyle adaptation if managed by a healthcare professional. To what extent the

development of obesity is propagated by acquired behavioural traits that subsequently alter these biological networks is subject to debate, though a plethora of studies have connected the consumption of high-calorie foods to alterations in food-seeking behaviour and dysregulation of appetite (Lerma-Cabrera et al., 2016, Beck, 2000, Savastano and Covasa, 2005). Furthermore, it is estimated that obesity exhibits heritability ranging from 30-70%, with mutations identified in specific regions of the brain relating to food seeking behaviour, satiety and energy expenditure, predisposing individuals to weight gain. However, these factors can often be overcome by strict diet and administration of appetite suppressants, and are more associated with risk than with inability to lose weight (Ahima, 2008, Cambridge et al., 2013, Halford, 2001).

In the following section, the pathogenesis of obesity and associated metabolic syndrome are discussed, with reflections on the acquisition and subsequent promotion of 'bad habits' that are potential drivers of the obesity epidemic society faces today.

## 1.1 Pathogenesis of Obesity and the Metabolic Syndrome

The pathogenesis of obesity is multifactorial, with both genetic and environmental components that create a complex network of cause-and-effect relationships which are often difficult to disentangle. The progression to obesity from a diagnosis of 'overweight' has been studied at length in both clinics and in laboratory models of disease, to begin to understand how external factors can influence a seemingly simple concept of energy imbalance, cured in its entirety in the majority of cases by re-balancing the scale.

These alarming statistics highlight the need for further understanding of the relationship between 'will-power', food intake, adiposity and the development of chronic obesity. Therefore, many studies have focussed on the amelioration of aspects of the metabolic syndrome, whilst implementing lifestyle changes, to improve the prognosis of obese patients.

The metabolic syndrome is defined as a cluster of metabolic abnormalities, originally recognised as significant risk factors for cardiovascular disease, include abdominal obesity, increased blood pressure, impaired fasting glucose, high circulating cholesterol and triglyceride concentrations (Expert Panel on Detection and Treatment of High Blood Cholesterol in, 2001). Though it was previously thought that insulin resistance preceded the onset of other tissue abnormalities (Reaven, 1988), it is now

known to be secondary to the onset of obesity, and the expansion of the adipose tissue (reviewed in (Laclaustra et al., 2007).

Excessive food intake results in the conversion of dietary lipid to triglycerides, subsequently stored in adipose tissue depots in several discreet anatomical locations, outlined in Fig 1.1. Both brown and white adipose tissues are capable of storing lipids in the form of triacylglycerol, though have unique primary functions.

The brown adipose, found in abundance in small mammals such as rodents, is an evolutionarily adaptation necessary to sustain life below thermoneutrality (Foster and Frydman, 1979). Brown adipose tissue is rich in mitochondria, with small, multilocular

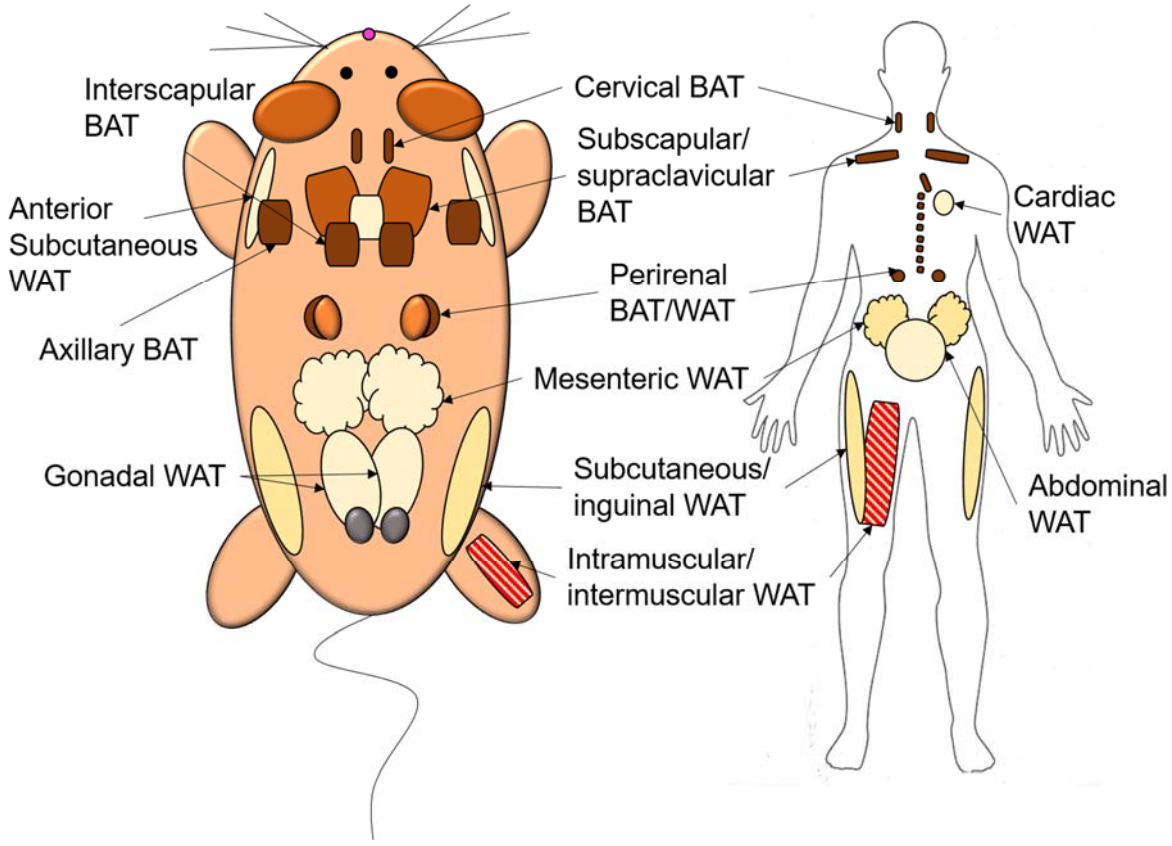



***Figure 1.1 Location of brown adipose (BAT) and white adipose tissue (WAT) depots in mouse and human.***

*Discreet depot locations found in mouse and human. Common nomenclature; iBAT interscapular BAT; asWAT anterior scapular WAT; aBAT axillary BAT; gWAT/WATg gonadal WAT; cBAT cervical BAT; sBAT subscapular/supraclavicular (human) BAT; pWAT/pBAT perirenal WAT/BAT; mWAT mesenteric WAT; scWAT/iWAT subcutaneous/inguinal WAT, imWAT inter/intramuscular WAT; cWAT cardiac WAT; aWAT abdominal WAT (human). Data obtained from de Jong et al., (de Jong et al., 2015)*

lipid droplets facilitating the rapid release of free fatty acids required for the activation of the uncoupling protein UCP1 (Nedergaard et al., 1999, Nicholls, 2001). The role of BAT in energy expenditure and obesity will be discussed at length later in this work. In contrast, the white adipose is a specialised lipid-storage facility, with the majority of mature WAT consisting of large, unilocular adipocytes containing abundant triacylglycerol stores. The cytoplasm, mitochondria, other organelles and nuclear components are compressed to the cell membrane. The defining features of these cell types are outlined in Fig 1.2.

The expansion of the white adipose tissue is a hallmark of obesity, and is often associated with, or indeed the cause of, many additional pathologies that contribute to the metabolic syndrome. Once thought to be a metabolically inactive storage unit, it is now recognised as the body's largest endocrine organ, responsible for the production of adipose-secreted hormones, or adipokines, as well as inflammatory signals, and has been shown to regulate and coordinate systemic energy homeostasis.

Each white adipose depot is unique in texture and morphology, and are separated into two general categories, visceral and subcutaneous. It has now been shown that these groups may have different developmental origins, with significant impact on their contribution to the role of the adipose as a whole (Chau et al., 2014). Visceral adipose

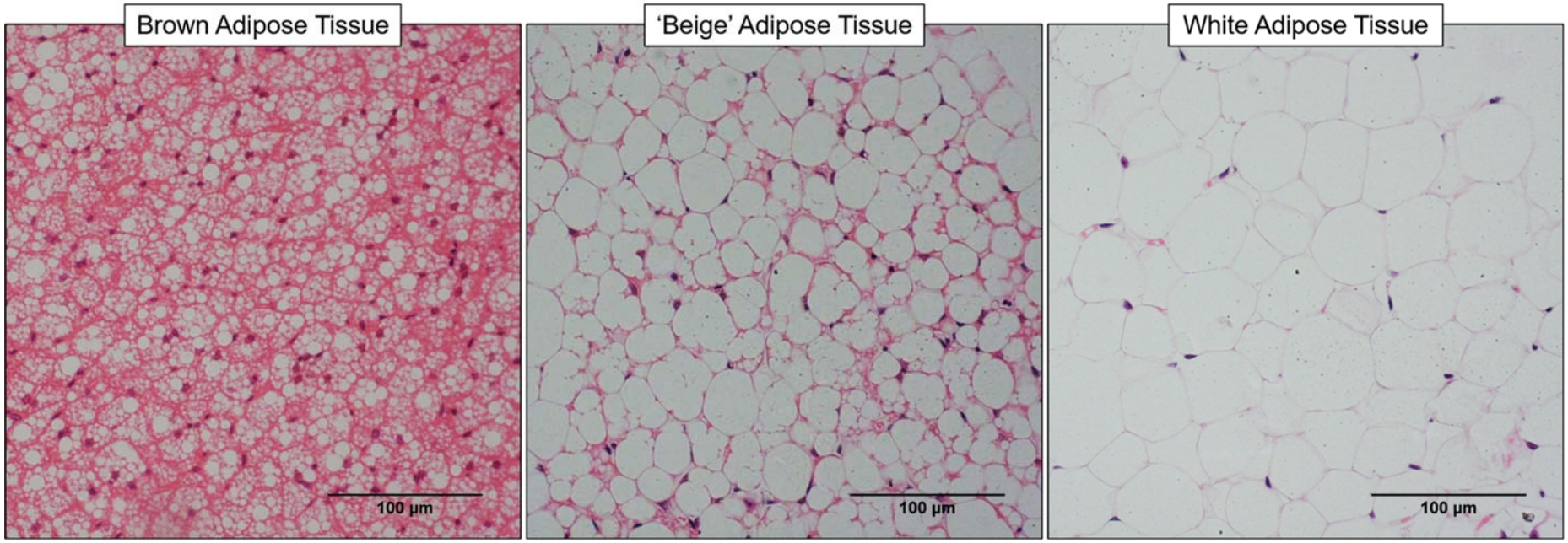



***Figure 1.2 Distinct morphology of brown adipose, beige adipose and subcutaneous white adipose tissue depots.***

***A)*** *Classical brown adipose tissue, characterised by small hexagonal multilocular adipocytes, abundant cytoplasm and dense cellularity.*

***B)*** *Spontaneous Beige or brite adipocytes situated in the subcutaneous adipose tissue depot of a wild-type mouse without cold exposure. Small, multilocular adipocytes are interspersed with classical mature white adipocytes.*

***C)*** *Classical, mature subcutaneous white adipose, characterised by large, unilocular adipocytes and low cytoplasmic content.*

*Original images, wild-type (non-Tg) male mice at thermo-normality. Sections stained with haematoxylin and eosin (H+E). Scale bar 100µm, 20x magnification. Morphology characteristic of depots as reviewed in (Keipert and Jastroch, 2014).*

tissue (VAT), can be divided into omental, mesenteric, retroperitoneal, gonadal and pericardial depots, and are generally associated with other internal organs, perhaps owing to their mesothelial cell origin (Chau et al., 2014). In contrast, the subcutaneous adipose does not express the same mesothelial markers; Wilms' tumour gene Wt1, mesothelin (Msln) or uroplakin (Upk3b) (Chau et al., 2014). Subcutaneous depots are located beneath the skin, predominantly associated with the gluteal muscle and quadriceps (gluteofemoral adipose tissue) and the abdominal area. Important for the prognosis of obesity, the expansion of the visceral adipose tissue, but not subcutaneous, is highly correlated with the development of cardiovascular disease and type 2 diabetes, highlighting further, more subtle differences between these two classes of adipose (Wajchenberg et al., 2002, Wajchenberg, 2000). Indeed, the separate origins of these depots are reflected in many other features, namely their morphology.

Subcutaneous white adipose is naturally heterogeneous, with both mature, unilocular adipocytes and smaller, multilocular adipocytes sporadically integrated between these mature cells (Cousin et al., 1992). These cells are now known to be inducible, particularly upon cold exposure, and are referred to as 'brite' or 'beige' (Fig 1.2) (Shabalina et al., 2013). It is thought that the high rate of turnover and lower lipolytic rates contribute to the observed protection from obesity-associated inflammation and mitochondrial dysfunction in this depot (Fisher et al., 2002b). In contrast, the visceral adipose is comprised almost entirely of large, unilocular adipocytes and is well associated with many important visceral organs, in both proximity and through the circulation.

The expansion of the visceral white adipose tissue in response to caloric excess has been identified as a significant risk factor for many aspects of the metabolic syndrome (Faust et al., 1978, Wajchenberg, 2000). Whilst the mechanisms underlying each pathology associated with obesity are complex, the development of this disease rests on energy imbalance, driven primarily by an increase in food intake, in conjunction with insufficient activity. The following sections summarise both axes, with reflection on therapeutic intervention.

### 1.1.1 Food Intake

Given that weight gain occurs when ingested calories exceed energy output, it is not surprising that the most commonly identified driver of the acquisition of excess bodyweight is the ingestion of surplus calories. As described previously, the primary cause of excessive caloric intake is the consumption of high-fat, high-sugar foods and beverages in large portions, eaten in excess given the added convenience and failure to elicit a satiety response. Indeed, it has been identified that these foods, labelled as highly-palatable, have addictive properties, with similar stimulation of reward processing-neuronal populations to the actions of recreational drugs (Lerma-Cabrera et al., 2016, Ziauddeen et al., 2012). In the 1940's the ventromedial hypothalamic nucleus (VMN) was identified as a satiety centre, and the lateral hypothalamus (LH) as a feeding centre (Hetherington and Ranson, 1940) (1983). These areas of the hypothalamus are now well characterised, particularly the arcuate (ARC), paraventricular (PVN), dorsomedial (DMN) and suprachaismatic nuclei, for their contribution to energy intake and expenditure (Beck, 2000). Within the arcuate nucleus (ARC), several populations of neuroendocrine neurons control a wide range of biological functions. Responsible for the regulation of feeding are the Npy/Agrp and Pomc/CART neurons, secreting neuropeptide Y/agouti-related peptide and proopiomelanocortin/cocaine-and-amphetamine-regulated transcript respectively (Beck, 2000, Varela and Horvath, 2012). The release of Npy/Agrp peptides acts to stimulate appetite after food deprivation, whilst POMC release inhibits feeding. Both populations of neurons are sensitive to hormonal signals such as insulin, ghrelin and leptin, to allow control of feeding behaviour in response to energy stores and environmental cues (Varela and Horvath, 2012).

Whilst the body of evidence for the role of neuronal signalling in food intake grows, the application of this knowledge for the development of therapeutics is limited. Many agents, such as $CB_1$ (cannabinoid-1) receptor antagonist rimonabant, though exhibiting high efficacy in terms of bodyweight reduction (Van Gaal et al., 2005), have been withdrawn based on safety concerns, including severe psychiatric disorders such as anxiety, depression and suicidal tendencies (Vickers et al., 2011). Though aspects of food intake, particularly in obese patients, are pre-determined, most are a combination of exposure to palatable foods in abundance, leading to positive reinforcement from 'pleasure-centres' in the brain, coupled with significant energy

imbalance due to lack of energy expenditure. Many of these reward-seeking behaviours can be attributed to circulating factors involved in the regulation of food intake based on nutrient availability, often mediated by the primary site of energy storage: the adipose.

The study of the crosstalk between the digestive system, the brain and the primary energy storage facility; the adipose, has revealed a number of factors that mediate feeding behaviour in response to available nutrient stores, which have subsequently been correlated with the progression of obesity in rodent models and in patients. Perhaps the most well documented of these is leptin, a predominantly adipose derived hormone first identified by Zhang *et al.,* in 1994, along with its gene; OB (obese) (Zhang et al., 1994). Capable of crossing the blood-brain barrier, leptin acts through its receptor, LEPR or OBR, which is highly expressed in the hypothalamus, where it is now known to inhibit food intake and to regulate bodyweight and energy homeostasis (Halaas et al., 1995). The discovery of leptin as an adipose-secreted hormone, however, altered the perception of adipose tissue as a secretory organ, capable of regulating whole organism energy homeostasis.

In rodent models of obesity, leptin binds to its receptor in the hypothalamus and suppresses the expression of orexigenic peptides, such as Npy and Agrp, and increases the expression of anorexigenic peptides, including corticotrophin-releasing hormone, to reduce food intake, through JAK-STAT3 signalling (Ahima, 2008) (Fig 1.3). However, certain factors can influence the production of leptin, such as food intake, adiposity, gender and age. Elevated circulating leptin levels are found in obese patients, and are associated with the development of leptin resistance (Considine et al., 1996, Scarpace et al., 2005). Some controversy exists surrounding the mechanism governing this resistance, with several studies showing a reduction in leptin receptor expression in the hypothalamus of DIO rats, with the authors suggesting a reduction in leptin signalling is responsible, contributing to the development of obesity (Levin et al., 2004). However, no difference in the expression of the leptin receptor mRNA has been found between lean and obese human patients, and may be a consequence of increased bodyweight and food intake, as opposed to a driving factor (Considine et al., 1996).

Perhaps the most elegant demonstration of the effects of leptin on food intake can be observed in the Ob/Ob mouse model, which is entirely leptin-deficient. Animals develop obesity from as early as 3 weeks of age, driven by extreme and persistent hyperphagia, which can be reversed by administration of leptin. However, it is unlikely that the administration of leptin alone is sufficient to combat obesity, particularly in cases of endogenous leptin resistance, with the most effective treatments hypothesised to be a combination of diet, exercise and the potential use of anti-obesity agents (Klok et al., 2007).

Shortly after the discovery of leptin, several groups reported the existence of another adipose-secreted factor, adiponectin, with aliases including AdipoQ and apm1 (Hu et al., 1996, Maeda et al., 1996). An overview of adiponectin signalling summarises the role of this fat-derived hormone as playing a critical role in the protection from insulin resistance, diabetes, CVD and obesity, through its actions in peripheral tissues and the CNS (Achari and Jain, 2017). Indeed, a decrease in adiponectin signalling has been demonstrated in both humans and rodent models of obesity, with particular consequences for insulin signalling and the development of type 2 diabetes.

Adiponectin receptors AdipoR1 and AdipoR2 are ubiquitously expressed, with R1 predominantly expressed in skeletal muscle and R2 in the liver (Yamauchi et al., 2003, Mao et al., 2006). It is the structure of circulating adiponectin that confers specificity to these receptors, with the former possessing high affinity for globular adiponectin and the latter for the full length protein. Hexameric and high-molecular weight (HMW) adiponectin have been shown to interact with a third protein; T-cadherin, though other forms are not recognised by this cell-surface receptor (Achari and Jain, 2017, Denzel et al., 2010). To initiate a signalling cascade, adiponectin binds to AdipoR at the cell surface, recruiting the adaptor protein APPL1. It is through APPL1 that adiponectin exerts its effects in mammals, facilitating crosstalk between adiponectin signalling and other signalling pathways, notably insulin receptor substrates IRS 1 and 2 which in turn trigger PI3K-Akt insulin signalling pathways, the p38MAPK pathway and PPARα signalling, promoting glucose uptake and fatty acid oxidation (reviewed in (Achari and Jain, 2017)) (Fig 1.3).

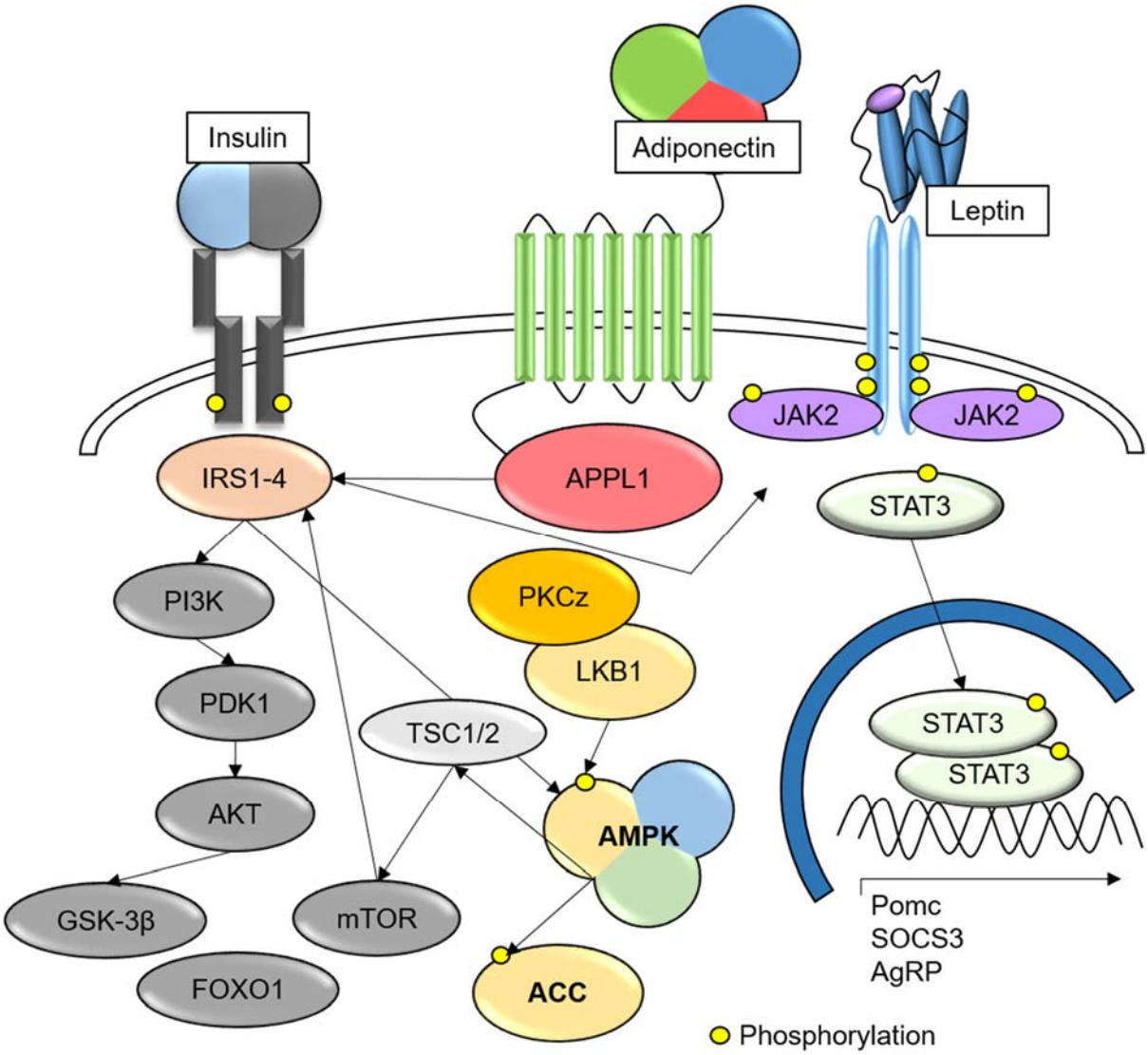



***Figure 1.3 Possible crosstalk between insulin, leptin and adiponectin signalling.***

*Insulin binding to its receptor triggers phosphorylation of the intracellular domain, facilitating IRS binding and activation, leading to activation of downstream pathways (PI3K, AMPK). Binding of leptin causes dimerization of the leptin receptor, activating JAK2-mediated STAT3 phosphorylation. STAT3 translocates to the nucleus where it promotes the expression of several neuropeptides (Pomc, AgRP) (reviewed in (Ahima, 2008)). Adiponectin binds to the extracellular domain of the AdipR1 receptor, recruiting the adapter protein APPL1, activating a signalling cascade resulting in the phosphorylation of LKB1 and subsequent AMPK activity (Achari and Jain, 2017). It is possible that this pathway then reduces mTOR activity, thus enhancing IRS signalling. AgRP, agouti-related peptide; Akt, protein kinase B;* FOXO*, forkhead transcription factor O; GSK3, glycogen synthase kinase 3; JAK, janus kinase; LKB, serine/threonine kinase 11; mTOR, mammalian target of rapamycin; PI3K, phosphatidylinositol 3 kinase; H2-domain-containing cytoplasmic tyrosine phosphatase; SOCS, suppressor of cytokine signalling; STAT, signal transducer and activator of transcription; TSC, tuberous sclerosis. Adapted from (Dridi and Taouis, 2009)*

Indeed, the activation of IRS1/2 by adiponectin-APPL1 signalling is the primary route

for insulin sensitisation by adiponectin in insulin responsive tissues (Berg et al., 2001).

Adiponectin signalling has also been shown to initiate a cascade through APPL1-PKCz that leads to LKB1 dephosphorylation at $Ser^{307}$, which facilitates AMP-activated protein kinase (AMPK) activation via phosphorylation of $Thr^{172}$ (Deepa et al., 2011). Activation of AMPK by this pathway has been shown to promote FAO, vasodilation (through phosphorylation of eNOS) and enhanced glucose uptake in skeletal muscle (Cheng et al., 2007).

Insulin signalling is well-known for its promotion of glucose uptake in peripheral tissues, predominantly skeletal muscle, liver and adipose (Wilcox, 2005). The production of circulating insulin can be attributed entirely to the pancreatic β-cell, the predominant cell type of micro-organs known as Islets of Langerhans, hereafter referred to as pancreatic islets, found exclusively in the pancreas (reviewed in (Rutter et al., 2015)). The β-cell shares the islet with several other endocrine cell types, namely the α-cell, responsible for the secretion of glucagon, and the somatostatin-secreting δ-cell which, in rodents, surround a β-cell core (Rahier et al., 1983, Orci and Unger, 1975). In contrast, human islets display a less rigid cellular arrangement, which may allow for more diverse cell-cell interactions leading to alterations in the control of insulin signalling. Indeed, it has been shown that the sympathetic and parasympathetic innervation of rodent islets is distinct from human, with the latter favouring the innervation of surrounding blood vessel smooth muscle, which may regulate hormone secretion through local blood flow, rather than through direct modulation of hormone production as seen in rodent islets (Rodriguez-Diaz et al., 2011).

The β-cell is highly sensitive to glucose, with other stimuli such as glucagon-like peptide-1 (GLP-1) capable of enhancing insulin release only at predetermined glucose levels (typically above 6mM) (Rutter et al., 2015). Insulin is synthesised within β-cells as the pro-hormone proinsulin, and is later converted to mature insulin by prohormone convertases PC1 and PC2 and stored in secretory granules. In response to changes in blood glucose concentrations, an initial release of pre-formed insulin granules from β-cells (between 5-10000 per cell) (Fava et al., 2012) into circulation is mediated by glucokinase-dependent ATP production, from the phosphorylation of glucose to G6P. Subsequent membrane depolarisation by the closure of $K^+$-ATP channels causes activation of voltage-dependent calcium channels, which in turn activates secretory

granule-associated small *N*-ethylmaleimide-sensitive factor receptor (SNARE) proteins, allowing fusion of the granule with the plasma membrane (Sudhof and Rothman, 2009, Jahn and Fasshauer, 2012). In addition, the resulting increase in intracellular calcium concentration, as calcium is released from intracellular organelles, such as the endoplasmic reticulum, may also promote insulin secretion in this manner (Gustafsson et al., 2005). This pathway may also be activated in a glucose-independent manner, by factors including amino acids and peptide hormones such as leptin and adiponectin. Circulating insulin is then able to bind to insulin receptors through the extracellular α-subunit, which enables ATP to bind to the intracellular β-subunit (Fig 1.3). Insulin receptor substrates; IRS1-4, are then responsible for the subsequent downstream effects of insulin signalling in their respective tissues, with IRS1 and 2 expressed in most tissues, with selectivity for IRS1 in skeletal muscle and IRS2 in the liver. IRS3 is expressed predominantly in the adipose, beta-cells and the liver, and IRS4 found in the thymus, kidney and brain (Burks and White, 2001, White, 2006).

Deficiency in insulin production and/or systemic insulin resistance results in clinical diabetes, affecting approximately 8% of the human population. Diabetic patients, both type 1 and type 2 present with persistent hyperglycaemia as a result of β-cell dysfunction, leading to systemic insulin deficiency and insulin resistance respectively. Type 1 diabetes, an autoimmune disease presenting in childhood, is characterised by β-cell stress, dysfunction, inflammation, leading to insufficient insulin production and systemic insulin deficiency (Eizirik et al., 2009). Studies have shown that β-cell dysfunction precedes the inflammatory response associated with clinical manifestation of type 1 diabetes, with several mutations identified that contribute to reduced β-cell function and destruction (reviewed in (Ashcroft and Rorsman, 2012)).

In contrast, type 2 diabetes is influenced heavily by lifestyle factors, leading to excessive production of insulin from pancreatic beta-cells in response to excess energy consumption. These factors are positively correlated with body mass index (BMI), waist circumference and waist to hip ratio, indicators of increased adiposity in humans (Wilcox, 2005). Obese patients display significant β-cell apoptosis as a result of exposure to high glucose and free fatty acid concentrations, which contributes to the loss of β-cell mass and therefore impairment of insulin secretion (Russo et al., 2014).

In addition to increased insulin production, triglyceride accumulation in peripheral tissues has been shown to promote insulin resistance through a decrease in IRS1-PI3K signalling, a consequence of IKK-beta mediated inflammation (Perseghin et al., 2003). The combined effect of β-cell dysfunction and peripheral insulin resistance promotes the persistent hyperglycaemic state in obese, diabetic patients. Current strategies to target insulin resistance have employed compounds, such as the indirect AMPK activator metformin, currently prescribed to over 120 million people worldwide. The actions of metformin are discussed in section 1.4.1.

In summary, leptin, adiponectin and insulin, alongside several other circulating factors, are responsible for the crosstalk between peripheral tissues and the CNS, and play a significant role in energy homeostasis in response to nutrient availability (Fig 1.3). It is not surprising, therefore, that dysregulation of these factors is widely associated with the onset of obesity and are implicated in manifestations of the metabolic syndrome.

However, it is only in a minority of cases that the dysregulation of these factors is a causative factor in the development of obesity. Several cases of leptin deficiency have been reported in humans, with a strong hereditary component that results in the manifestation of symptoms within families. These individuals were found to possess mutations in the leptin gene resulting a premature stop codon leading to the absence of functional circulating leptin (Montague et al., 1997, Paz-Filho et al., 2010). All patients presented with childhood-onset morbid obesity, low serum leptin and a BMI greater than 50 in adulthood. Strikingly, all symptoms were reversed upon treatment with leptin, suggesting that leptin deficiency alone was responsible for the development of obesity in these patients. However, few obese patients are categorised as leptin-deficient, rather leptin resistant, driven by the expansion of adipose tissue in response to caloric excess. This supports the hypothesis that, in most cases, being overweight is a precursor to the development of leptin resistance through the expansion of white adipose, which, in turn, is exacerbated by a decrease in satiety, usually mediated by leptin itself. Indeed, it has been shown that chronic leptin treatment increases food consumption and weight gain in diet-induced obese rats (Scarpace et al., 2005). Therefore, the treatment of obesity with leptin is limited to those patients not already categorised as leptin-resistant, who harbour mutations in the leptin gene. These patients make up a very small fraction of the total obese population, suggesting that most patients would not benefit from this treatment, nor

can defective leptin signalling alone be the driving factor behind the development of obesity in these cases.

In addition to promoting insulin and leptin resistance, expansion of visceral adipose depots in response to caloric excess is, at least in part, responsible for the accumulation of triglycerides in the liver, a condition known as hepatic steatosis.

Under normal conditions, in the fed state, glucose is taken up by the liver and converted to glycogen, or into fatty acids. These free fatty acids are then esterified to generate triacylglycerol and stored in small lipid droplets in hepatocytes. In response to fasting, these substrates are released and taken up in the periphery in response to metabolic demand. The liver is also responsible for the oxidation of non-esterified fatty acids (NEFAs) released by adipose tissue in conjunction with glycerol, which is used in the synthesis of glucose, known as gluconeogenesis (Rui, 2014) . Fatty acid β-oxidation of NEFAs in hepatocyte mitochondria leads to the production of ketone bodies, a process known as ketogenesis. These ketone bodies are subsequently used by the muscle and other peripheral tissues during exercise and starvation (Rui, 2014, Laffel, 1999). However, the excessive accumulation of FFAs as TAG within hepatocytes, known as hepatic steatosis, is responsible for the disruption of many signalling pathways that promote insulin resistance and the development of type 2 diabetes (Alkhouri et al., 2009, Zambo et al., 2013). Obesity-associated hepatic steatosis is driven, in part, by excess deposition of lipids in visceral adipose depots, in response to caloric excess (Fig 1.4).

Under normal conditions, the adipose tissue is well equipped to adapt and expand to accommodate lipid under these conditions, providing that these stores are then called upon to facilitate energy expenditure, through hydrolysis of triacylglycerol to free fatty acids and glycerol, a process known as lipolysis (reviewed in (Duncan et al., 2007)). The rate of lipolysis is determined by the activity of lipases such as hormone-sensitive lipase (HSL) and adipose triglyceride lipase (ATGL). These lipases are responsive to external cues such as hormones and catecholamines such as glucagon (Perea et al., 1995, Albalat et al., 2005) and norepinephrine respectively, promoting free fatty acid release to meet metabolic demand.

However, in the event of chronic overfeeding, hypertrophic adipose tissue expansion leads to an increase in adipocyte-associated inflammatory genes such as Mcp-1 and

Tnf-α, which drive immune cell infiltration (Weisberg et al., 2003). These pro-inflammatory stimuli lead to increased adipocyte lipolysis, promoting the release of free fatty acids (FFAs) into the blood and subsequent accumulation of triglycerides in hepatocytes. Inflamed adipose tissue also secretes the ubiquitous, pro-inflammatory

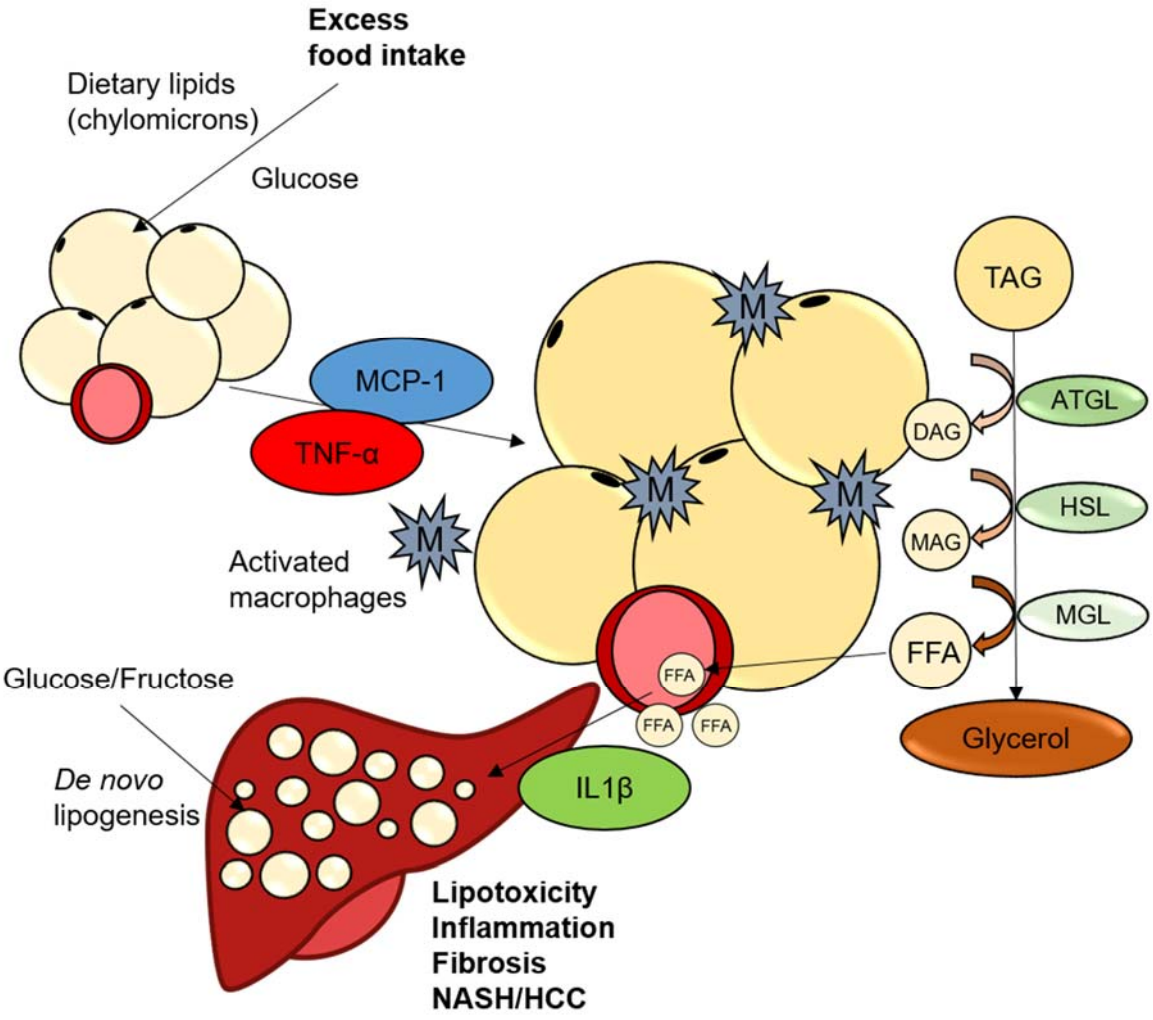



***Figure 1.4 The role of adipose inflammation and lipolysis in hepatic steatosis.***

*Schematic outlining the effects of HFD-feeding on liver triglyceride accumulation. Excessive caloric intake leads to adipocyte expansion, immune cell infiltration and inflammatory-cytokine stimulated lipolysis. Desnutrin/ATGL, a triacylglycerol (TAG) lipase, hydrolyses TAG to diacylglycerol (DAG) and free fatty acids (FFA). Hormone sensitive lipase (HSL) converts DAG to monoacylglycerol (MAG) and FFA. Monoacylglycerol lipase (MGL) completes the hydrolysis of MAG to FFA and glycerol. FFA released into the blood stream are taken up and stored by the liver, where several lipid species contribute to the progression of hepatic steatosis. Excess carbohydrate intake contributes to this development through the stimulation of de novo lipogenesis from sugars, particularly fructose (Mota et al., 2016, Oakhill et al., 2012).*

cytokine IL1β, which has been shown to connect visceral adipose inflammation to hepatic insulin resistance and steatosis through local crosstalk via hepatic portal blood (Nov et al., 2013). Hepatic steatosis, or non-alcoholic fatty liver disease (NAFLD) is further exacerbated by the inherent toxicity of some ingested lipid species, particularly those unsaturated fatty acids which contain one or more conjugated double bonds, known as trans fatty acids, or TFAs. TFAs are particularly associated with a Western diet, found in many popular foods including cakes, cookies and pastries. However, these lipids have been shown to confer hepatotoxicity, through the promotion of inflammatory pathways, leading to activation of resident fibroblasts and generation of reactive oxygen species (ROS) (Zambo et al., 2013). These events, known as non-alcoholic steatohepatitis or NASH, promote hepatocyte apoptosis and fibrosis of the liver, which has been shown to be a precursor to hepatocellular carcinoma. The accumulation of triglycerides in the liver is also known to promote peripheral insulin resistance, resulting in type 2 diabetes (reviewed in (Wilcox, 2005)).

Other clinical manifestations of the metabolic syndrome are often secondary to systemic inflammation as a result of peripheral lipid accumulation, with elevated adipose-secreted inflammatory cytokines including interleukin 6 (IL6) and TNF-α, and circulating NEFAs. In response to high-fat, high-sugar feeding, it has been shown that the ability of blood vessels to relax (vasorelaxation) is significantly impaired, an observation subsequently associated with nitric oxide deficiency, in conjunction with ROS generation in the vascular endothelium (Roberts et al., 2005). The loss of vascular elasticity, in conjunction with lipid laden macrophages, known as foam cells, and the deposition of lipid as ‘fatty streaks’ in the endothelium promotes the development of atherosclerosis, a chronic inflammatory condition then perpetuated by the resulting hypertension (Redinger, 2007).

It is clear that excessive food intake and subsequent adipose tissue expansion is the principle driving force for the development of the metabolic syndrome. However, if calorie intake is balanced with energy expenditure, adipose expansion is limited, with glucose and FFAs redirected to sites of active metabolism, particularly the muscle and brown adipose. The following section will address the concept of energy expenditure in mammals, and the potential for therapeutic intervention.

### 1.1.2 Energy Expenditure

Obesity is widely accepted as a disease of both excessive food intake and low physical activity. Indeed, the first law of thermodynamics supports equal responsibility on both sides, as bodyweight maintenance must be a direct consequence of equal energy intake and expenditure. If energy intake is too great, weight will increase. Conversely, if energy expenditure is greater than energy consumption, energy stores must be recruited, resulting in a decrease in bodyweight (Hill et al., 2012). It would appear therefore that the treatment of obesity would be to simply alter this balance, utilising excessive energy stores to facilitate an increase in energy expenditure in the form of exercise, whilst decreasing food intake.

Exercise requires the mobilisation of stored energy, predominantly in the form of glycogen, stored in the liver and skeletal muscle, and lipid in the form of either albumin-bound long-chain fatty acids, or from triacylglycerol stored in the intra-muscular adipose depots. In addition, fatty acids can be mobilised from visceral and subcutaneous adipose stores, facilitated by lipolysis, though this process is often reserved until exercise has ceased. The lipolysis of triglycerides from intramyocellular triglyceride stores is facilitated by three key lipases; adipose triglyceride lipase, hormone sensitive lipase and monoglyceride lipase (Jeppesen and Kiens, 2012). Fatty acids are taken up by the skeletal muscle cells in response to contraction, mediated by the transporter FAT/CD36, relocated to the plasma membrane (Holloway et al., 2008, Jeppesen et al., 2011) and activated by reaction with long-chain acyl-CoA synthetase (ACSL1), the first step in the oxidation, elongation and desaturation of fatty acids, located on the outer mitochondrial membrane (Coleman et al., 2000). The high mitochondrial content of the skeletal muscle then facilitates ATP generation from both glycolysis and fatty acid oxidation at a rate approximately 5- to 10-fold higher than at rest (Jeppesen and Kiens, 2012). In addition to acute lipolysis and metabolism of fatty acids, exercise also exerts longer-term ‘fat-burning’ effects, including enhanced mitochondrial biogenesis through increased peroxisome proliferator-activated receptor γ co-activator 1α (PGC1α) expression (Winder et al., 2000, Lantier et al., 2014). This role has been attributed to the master regulator of energy homeostasis, AMP-activated protein kinase, and will be discussed in detail later in this work.

The desire to exercise, or lack thereof, is now considered to be a significant driving force in the obesity epidemic, as opposed to a ‘low’ basal metabolism previously

thought to be causative (Flatt, 2011). Therefore, though it is theoretically possible to lose weight without increasing physical activity, few have achieved this, suggesting maintenance of energy balance in a low-energy environment is not a viable therapeutic strategy for the treatment of obesity. Instead, studies have focussed on the promotion of energy expenditure independent of physical activity, with significant emphasis on the second method of energy dissipation in mammals; thermogenesis.

The expenditure of excess energy as heat has been acknowledged for a significant period of time, particularly in the brown adipose of rodents, as a highly conserve mechanism of temperature regulation in response to cold environments (Kurahashi and Kuroshima, 1978, Foster and Frydman, 1979, Block, 1994). However, significant differences in the evolution of humans and rodents reflects the necessity for energy conservation versus expenditure, with humans requiring an energy storage surplus to survive long periods of caloric restriction, as opposed to rodents, prioritising obligatory thermogenesis in order to maintain body temperature both at rest and at temperatures below thermoneutrality (Rosenbaum and Leibel, 2010). Though the existence of BAT has now been confirmed in adult humans, it was long-thought to be present only at birth, to maintain core body temperature in the earliest stages of life outside of the uterus. Even so, the contribution of BAT to total energy expenditure in humans is minimal unless subjected to cold exposure (<19$^{o}$C) (Virtanen et al., 2009, Borga et al., 2014). Nevertheless, much effort has been directed to understand the mechanisms governing BAT activation and its contribution to energy expenditure, with a view to harnessing such an ability for application in humans. However, in many mammals and birds, where BAT is lacking, non-shivering thermogenesis is mediated by the skeletal muscle. Indeed, many studies have identified a skeletal muscle origin for BAT, with specialised cells, derived from skeletal muscle progenitor cells, first identified in fish and birds, that have the characteristics of a muscle cell; mitochondria, endoplasmic reticulum and sacro/endoplasmic reticulum $Ca^{2+}$-ATPase (SERCA), working together to produce heat (Block, 1994). In fish, these cells were identified as ‘heater cells’, derived from the eye muscle, responsible for warming the brain and eyes of several ocean species. In these cells, it was noted that contractile filaments were virtually non-existent, the cytosol instead packed with mitochondria and highly-associated smooth membranes known as the endoplasmic reticulum (ER), facilitating heat production in

a similar fashion to muscle; through the ATP-dependent cycling of calcium at the ER (Rowland et al., 2015).

Brown adipose tissue, a specialised thermogenic organ, has been identified as a relatively recent adaptation of mammals, particularly rodents, to life on land, allowing the habitation of regions with colder climates (Enerback et al., 1997) (reviewed in (Rowland et al., 2015)). Brown adipose tissue, or BAT, located in rodents in the anterior- and sub-scapular regions, is a mitochondria-rich, highly vascularised metabolically active adipose depot, specialising in the production of heat in response to sympathetic nerve activity, which is provoked by cold exposure.

BAT morphology is distinct from other adipose depots, with plentiful cytoplasm rich in mitochondria, poised for fatty acid oxidation. Mitochondria, descendants of an α-protobacteria that formed a symbiotic relationship with a host cell, are key regulators of cellular homeostasis, responsible for ATP production from products of glycolysis and the tricarboxylic acid cycle, including NADH and succinate, a process termed oxidative phosphorylation (OXPHOS). Mitochondria are membrane-bound organelles, comprised of an outer membrane (OMM) and a highly folded inner membrane, forming cristae. Embedded in the inner mitochondrial membrane (IMM) are several key enzyme complexes which act as electron acceptors, collectively known as the electron transport chain (ETC). To produce ATP, the electron acceptors NADH dehydrogenase (Complex I) and succinate dehydrogenase (Complex II) receive electrons from NADH and succinate respectively, producing NAD+ and fumarate. Electrons are then donated to coenzyme Q, forming ubiquinol and reactive oxygen species (ROS). From coenzyme Q, electron transfer to Complex IV (COX) is catalysed by cytochrome $bc_1$ complex (Complex III), reducing oxygen to form water. Energy from the transfer of electrons is used to pump protons into the intermembrane space (IMS), forming an electrochemical gradient. The energy stored in this gradient is then used by a fifth member of the ETC, ATP synthase (Complex V) to produce ATP from ADP and inorganic phosphate ($P_i$) (reviewed in (Rich and Marechal, 2010)).

In addition to classical mitochondrial respiratory chain proteins, BAT mitochondria are identified by the expression of the uncoupling protein UCP1. To date, approximately 50 regulators of brown adipocyte development have been identified, though these have, in general, been associated with four major transcriptional regulators that govern

BAT development; peroxisome proliferator activated receptor γ (PPARγ), peroxisome proliferator activated receptor γ –co-activator 1α (PGC1α), PR-domain containing 16 (PRDM16) and CCAAT/enhancer binding protein β (C/EBPβ) (reviewed by (Inagaki et al., 2016)).

PRDM16 is absolutely required for brown adipose tissue determination development (Cohen et al., 2014, Seale et al., 2008, Seale et al., 2011), and forms a transcriptional complex with PPARγ and C/EBPβ, known DNA-binding transcription factors. In addition, the PRDM16 complex, containing the enzymatic component euchromatic histone methyltransferase 1 (EHMT1) is crucial for the repression of myogenesis, the default lineage of BAT precursors (Ohno et al., 2013).

The importance of this repression has been shown by two independent studies, targeting the PRDM16/EHMT1 complex, resulting in the ectopic expression of myogenic genes, including myogenin, a key transcriptional regulator of myogenesis (Ohno et al., 2013, Seale et al., 2008). This complex is required for both the initiation of brown adipogenesis from a $Myf5^{+}$ precursor, shared by *bona fide* skeletal muscle, and the continued repression of this lineage in vivo (Ohno et al., 2013). The deletion of PRDM16 alone, however, is not sufficient to induce this ‘switch’ *in vivo*, possibly due to a compensatory role played by PRDM3, also known to bind to both EHMT1 and

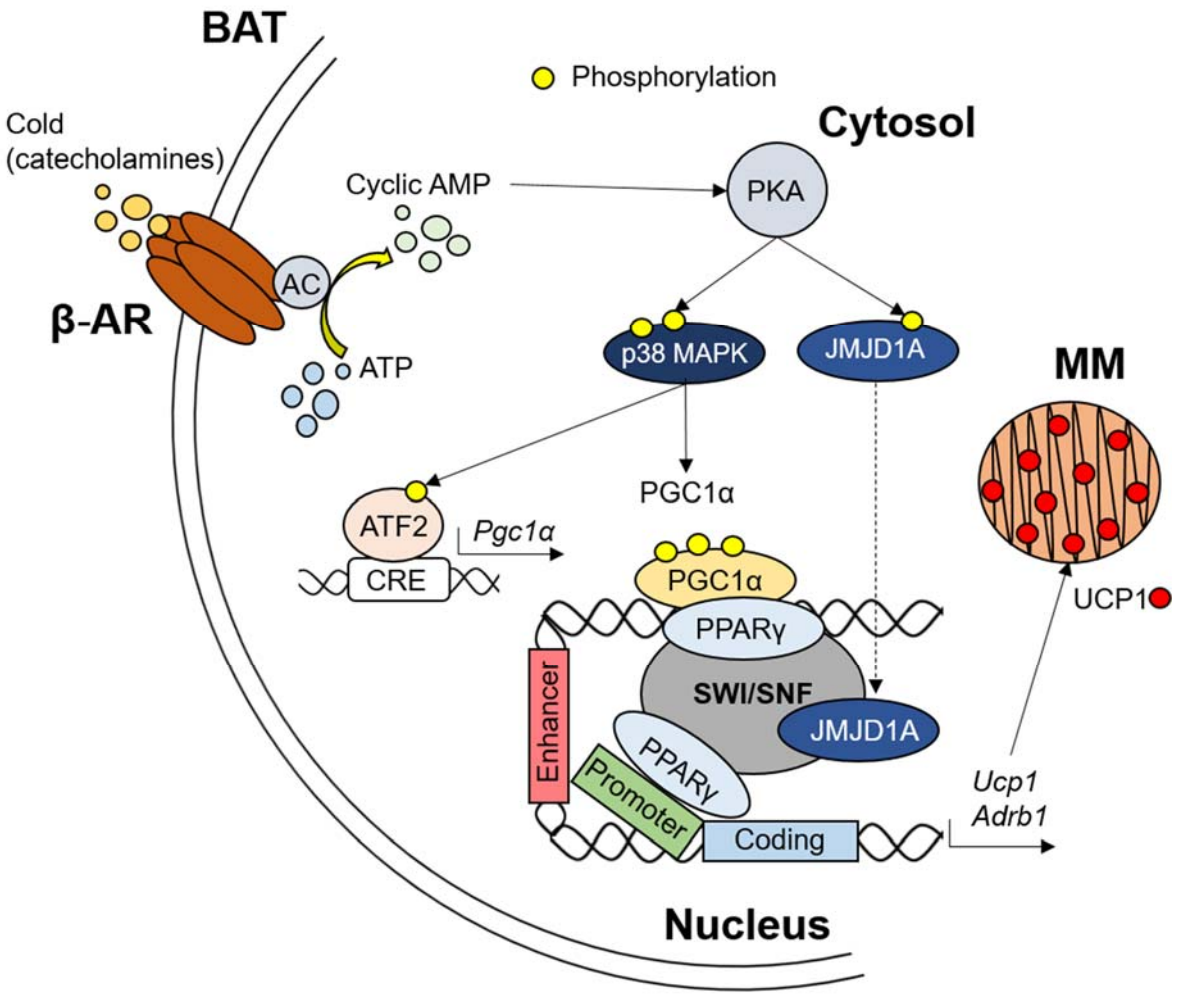



***Figure 1.5 Induction of Ucp1 gene expression by cold exposure in BAT.***

*Exposure to a cold environment triggers the release of catecholamines from sympathetic nerve terminals within the brown adipose tissue (BAT) which bind to β-adrenergic receptors expressed on brown adipocytes. This binding activates adenylate cyclase (AC), increasing intracellular cyclic AMP (cAMP), subsequently activating protein kinase A (PKA). Active PKA phosphorylates the epigenetic modifier Jumonji-domain containing 1A (JMJD1A) and p38 mitogen-activated protein kinase (p38 MAPK). Phosphorylated p38 MAPK induces the expression of peroxisome proliferator-activated receptor γ (PPARγ) co-activator 1α (PGC1α) through phosphorylation of the transcription factor ATF2, causing it to bind to cAMP-response element (CRE) in the promoter of the Pgc1α gene. Phosphorylated PGC1α, a co-activator of PPARγ, forms a complex with PPARγ and phosphorylated JMJD1A and the Switch/Sucrose Non-Fermentable (SWI/SNF) chromatin remodeller, bringing the Ucp1 promoter sequence into close proximity of its enhancer, promoting Ucp1 gene expression, as well as other thermogenic genes including the β-adrenergic receptor itself (Adrb1/β-AR). UCP1 protein is subsequently expressed on the mitochondrial membrane in close proximity to the mitochondrial respiratory chain (mtRC) (MM). Adapted from Inagaki et al., 2016.*

C/EBPβ (Pinheiro et al., 2012). Many additional factors have been identified that drive

the development of BAT in association with these complexes. Once committed, BAT function is determined by additional transcriptional complexes to drive both mitochondrial biogenesis and maintenance, and the expression of UCP1.

The expression of UCP1, contrary to prior popular belief, is generally dependent on cold stimulation, in response to β-adrenergic stimuli relaying through β-adrenergic receptors expressed by brown adipocytes. Stimulation of this pathway leads to an increase in intracellular cAMP and subsequent activation of protein kinase A (PKA). PKA then activates the transcription factors cAMP-responsive element-binding (CREB) and ATF2, as well as phosphorylating the epigenetic modifier Jumonji domain containing 1A (JMJD1A) and p38 mitogen activated protein kinase (MAPK) (Cao et al., 2004) (Fig 1.5).

PGC1α is then phosphorylated by p38 MAPK, and together with ATF2, are responsible for the formation of a transcriptional complex with the SWI/SNF chromatin modifier and PPARγ. It is this complex that brings UCP1 into close proximity with its enhancer sequence, resulting in its transcription (Inagaki et al., 2016). UCP1 protein is then transported to the mitochondrial membrane where it is activated through a conformational change initiated by free fatty acids released from intracellular triglyceride stores, characteristic of a true adipocyte (Divakaruni et al., 2012). UCP1 acts to uncouple the mitochondrial respiratory chain from ATP synthesis, instead increasing inner mitochondrial membrane conductance for hydrogen ions, dissipating the mitochondrial $H^+$ gradient and converting substrate energy into heat (Fedorenko et al., 2012). It is through this mechanism that BAT is able to maintain the core body temperature in response to cold exposure (Fig 1.5).

The role of BAT in adaptive thermogenesis has been of great interest to those looking to harness energy expenditure to treat metabolic diseases such as obesity. Though the activation of classical BAT in humans is both dangerous if uncontrolled, given the increase in core body temperature and associated side effects (Harper et al., 2008), the identification of a subpopulation of adipocytes within white adipose, termed ‘brite’ or ‘beige’ was met with numerous subsequent studies highlighting the inducible nature of these cells. Beige adipocytes resemble BAT in both morphology and uncoupling potential, displaying multilocular lipid droplets and inducible UCP1 expression.

The origin of these ‘beige’ cells was, until recently, heavily debated, with some studies suggesting either trans- or de-differentiation of mature white adipocytes in response to stimuli (Himms-Hagen et al., 2000), whilst others described a unique population of adipose-resident stem cells capable of differentiation into specialised BAT-like cells on command (Wu et al., 2012). Through several elegant lineage-tracing studies (Berry and Rodeheffer, 2013), it is now accepted that these cells, whilst sharing a common progenitor cell with classical white adipocytes ($Pdgfr\alpha^{+}$; $Sca1^{+}$; $Myh11^{+}$; $Myf5^{-}$), are fundamentally distinct once differentiated (Fig 1.6).

Both white and beige precursors of this lineage are resident in the vasculature of mature WATsc depots and respond to various stimuli; either for the development and expansion of white adipose, or the development of beige adipocytes, in response to cold exposure, exercise and circulating hormones (Inagaki et al., 2016). Like classical BAT, UCP1 expression is induced upon β-adrenergic receptor stimulation, as well as by several circulating factors such as the hormone fibroblast growth factor 21 (FGF21), produced by the liver and brown adipose, and natriuretic peptides released by the heart in response to pressure, also known to stimulate lipolysis (Harms and Seale, 2013). It is this inducible potential that has made the ‘beiging’ of the white adipose tissue an exciting and attractive therapeutic avenue for the treatment of obesity and the metabolic syndrome.

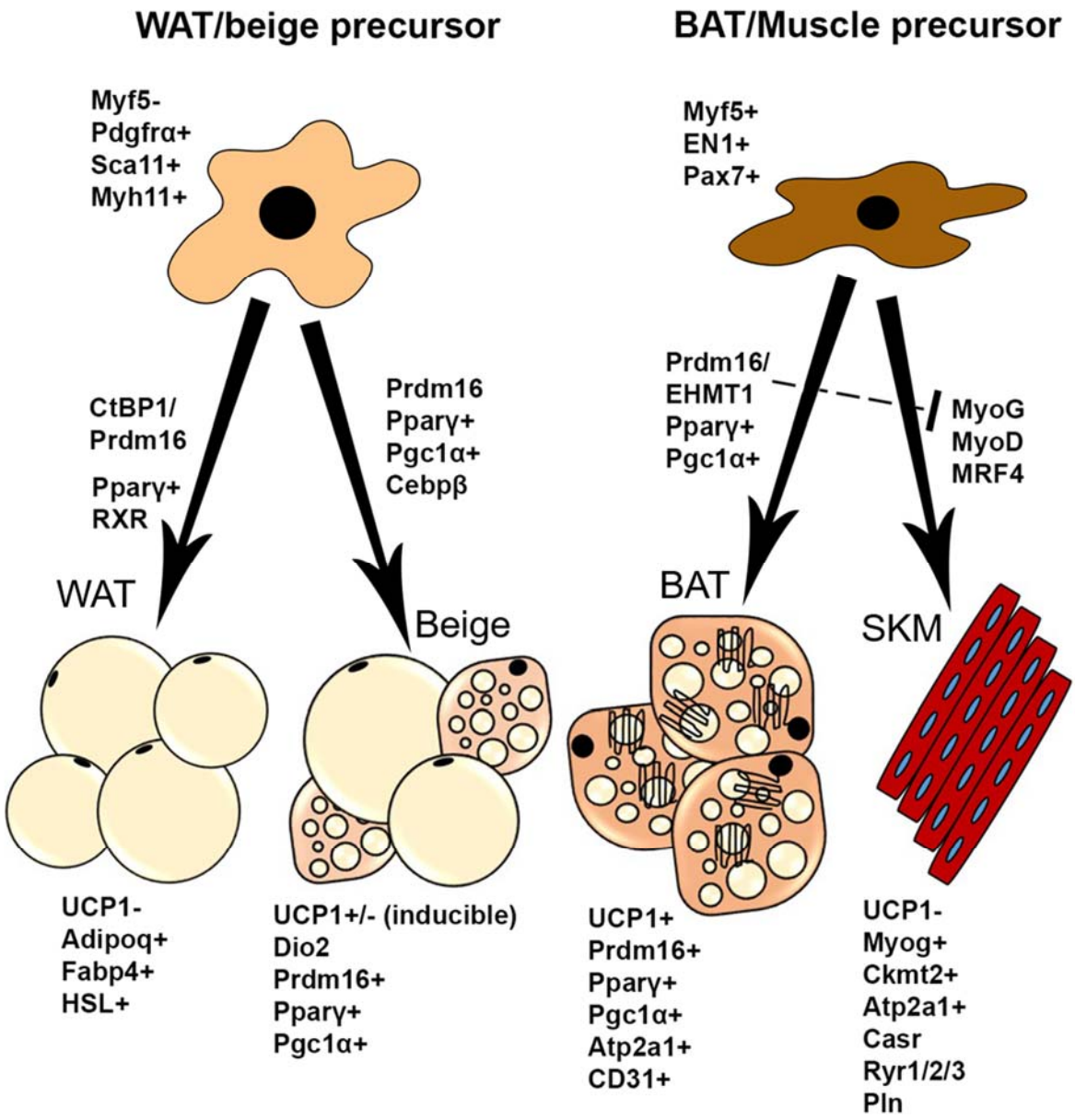



***Figure 1.6 Origins of skeletal muscle, brown, white and beige adipose.***

*Classical white adipocytes arise from a Pdgfrα+ precursor. Differentiation is controlled by Prdm16/CtBP1, repressing the WAT lineage. Dissociation of this complex recruits Pparγ to its regulator complex, driving WAT gene expression. Beige adipocytes arise from the same Pdgfrα+ precursor and are induced to differentiate by external stimuli (cold exposure, exercise, hormones). Differentiation is promoted by Prdm16/Pgc1α/Pparγ complex formation leading to the transcription of UCP1, conferring thermogenic activity (reviewed by (Inagaki et al., 2016)). Classical brown adipose tissue shares a precursor with skeletal muscle; Myf5$^{+}$, Entrail 1$^{+}$ (EN1), Pax7$^{+}$. Early complexes of Prdm16/EHMT1 inhibit myogenesis through the repression of myogenin, driving the BAT lineage assisted by Pparγ and its co-activator Pgc1α. Deletion of either Prdm16 or EHMT1 results in a BAT-muscle 'switch'. (Kajimura, 2015, Seale et al., 2008, Ohno et al., 2013).*

## 1.2 Current Treatments and Therapeutic Strategies

The pathology of obesity and the metabolic syndrome are well studied in both humans and in rodent models. Therapeutic targets have been identified, as well as a deeper understanding gained of the underlying mechanisms governing behaviour that, ultimately, drives the progression of these diseases. The manipulation of laboratory diets to reflect the nature of the modern diet was first documented, in modern research form, by Mickelsen *et al.,* in 1955, with the use of diet enriched with vegetable-derived frying oil (60 Crisco® (Proctor & Gamble, Cincinnati, OH, USA), with 85% total calories from fat (Mickelsen et al., 1955). Rats fed this diet showed dramatic increases in bodyweight and adiposity, thus providing a highly reproducible, relevant and flexible model for diet-induced obesity in rodents.

In subsequent years, customised high-fat and high-sugar diets were developed for research purposes, some using basic oils and lard to supplement a chow base, and others exploring more creative avenues, such as the use of chocolate, peanut butter, cookies, salami and other palatable supermarket foods to boost fat and sugar content (Sclafani and Springer, 1976). The diversity in these so-called 'Western diets' has provided researchers with insight into the effects of nutrients on animal behaviour and subsequent development of metabolic disease, particularly diabetes and obesity.

However, these studies have also highlighted the inherent complexity between diet, behaviour and the development of physical symptoms of disease, with each model requiring in-depth phenotyping, coupled with strict environmental control, to determine true cause and effect relationships pertaining to disease progression. In an effort to reduce variability, several manufacturers have developed highly reproducible, customisable laboratory diets, which are now widely used to study effects on behaviour, adiposity and metabolic disease.

The following section identifies the current therapeutic strategies to target obesity and the associated metabolic syndrome, identified through the use of both genetic and diet-induced obesity models, with successful translation to humans.

### 1.2.1 Current Treatments

Diet and exercise remain the safest and most effective treatments for most patients suffering from obesity and associated metabolic disorders. However, in many cases this strategy falls short based on extenuating circumstances, or through lack of

commitment which has now been shown to require more than just ‘will-power’. Nevertheless, an ideal anti-obesity agent would ultimately facilitate the implementation of such strategies, through an immediate improvement in the more restrictive aspects of the metabolic syndrome, such as hypertension, insulin resistance and cardiovascular disease.

For the vast majority of the obese population, surgical intervention is not a possibility, being reserved for those with a BMI >40, due to high costs and associated risk factors (Fock and Khoo, 2013, Manning et al., 2014). Therefore, the demand for effective pharmacological agents is high. Several therapeutic avenues have been explored, including the reduction of food intake, alteration of metabolism and the induction of thermogenesis. Currently, only five drugs are approved by the Food and Drug Administration (FDA) and of those only 3 approved by the European Medicines Agency (EMA) for the treatment of obesity, despite considerable efforts from researchers in academia and the pharmaceutical industry.

The first of these, Orlistat (Roche), a pancreatic lipase inhibitor, was introduced in 1990, and was until 2012 the only FDA-approved anti-obesity agent. Early studies showed that, in addition to a reduction in bodyweight through reduced fat absorption (approximately -30%) and the instance of the metabolic syndrome, rats fed a HFD combined with Orlistat had a reduced preference for high fat foods, adding to its efficacy (Ackroff and Sclafani, 1996). However, side effects include steatorrhea and in some cases nephrotoxicity and pancreatitis, make the relatively mild weight loss achieved with its use negligible. It is currently used for the treatment of mild obesity and the metabolic syndrome (Daneschvar et al., 2016).

The glucagon-like peptide-1 (GLP-1) receptor agonist Liraglutide (Novo Nordisk), with 97% sequence homology with endogenous GLP-, is the only approved injectable anti-obesity treatment on the market. Its therapeutic benefits are largely attributed to an increase in pancreatic beta cell proliferation, increased insulin sensitivity and a decrease in hepatic glucose output, and is particularly effective for the treatment of type 2 diabetes (Mehta et al., 2017). However, side effects include increased heart rate, nausea and vomiting, and an increased risk for pancreatitis.

Of the other three approved treatments, Lorcaserin, Phentermine and Naltrexone, all target the release of serotonin and dopamine for the control of appetite, proven to

reduce food cravings, though have been associated with several adverse effects including depression, anxiety and in some cases suicidal tendencies (Daneschvar et al., 2016). Many other anti-obesity agents have been withdrawn, primarily due to reported adverse effects, highlighting the need for more targeted treatments (Manning et al., 2014). Recent efforts have been made to develop small molecule activators with high target specificity, reducing potential off-target effects. Of particular interest is the control of energy homeostasis, to capitalise on the conserved regulation of anabolism and catabolism, to tip the scales in favour of energy expenditure without suppression of nutrient intake. At the centre of this balance lies a highly-conserved metabolic regulator, AMP-activated protein kinase, that provides a potential therapeutic target for the treatment of obesity and the metabolic syndrome.

## 1.3 AMP-Activated Protein Kinase: A Master Regulator of Energy Homeostasis

### 1.3.1 A Highly Conserved Metabolic Regulator

It is a requirement of all living things to acquire energy from external sources in the form of adenosine 5'-triphosphate (ATP) to facilitate cellular processes. Energy is derived from the hydrolysis of the phosphoanhydride bonds of ATP to produce ADP and AMP, generating an ATP:ADP ratio which is maintained in a 'fully-charged' battery-like state, where ATP:ADP concentrations are approximately 10:1 (Hardie et al., 2003). Following metabolic work (anabolic processes), ATP concentrations fall as a result of increased hydrolysis, which results in a concurrent increase in cellular ADP/AMP concentrations. It is vital, therefore, that the cell possesses the ability to sense this low-energy state and restore ATP levels, through catabolism of metabolic substrates via glycolysis and fatty acid oxidation. Given that all anabolic processes are almost perfectly balanced by catabolism, the system requires a regulatory sensing mechanism capable of responding to low-energy status by reducing anabolism (ATP-consuming pathways) and promoting catabolism (ATP-producing pathways). It is now known that at highly conserved protein kinase cascade is responsible for maintaining

this energy balance, mediated by an enzyme known as AMP-activated protein kinase, or AMPK.

AMPK is widely regarded as a master regulator of energy homeostasis, and is conserved from plants, yeast and nematodes to mammals and indeed, humans. AMPK acts as a cellular 'fuel gauge', capable of sensing alterations in ATP:ADP:AMP ratios. It is regulated by upstream kinases and allosteric activation by nucleotide binding directly to the regulatory γ-subunit (Carling et al., 1989) (reviewed in (Carling et al., 2012)). In broad terms, AMPK is responsible for orchestrating the generation

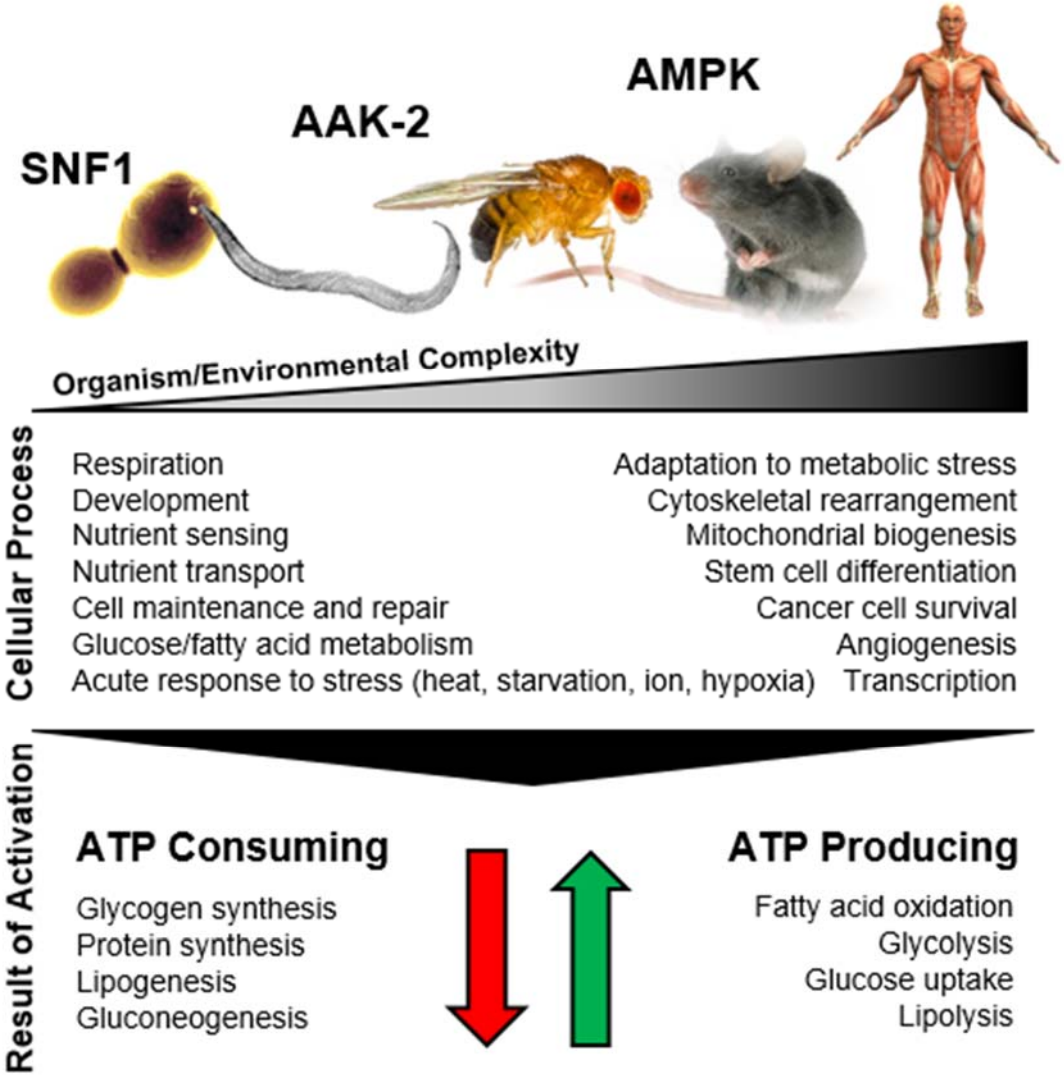



***Figure 1.7 Overview of the roles of AMPK in vivo.***

AMPK is a highly conserved metabolic regulator, responsible for the promotion of ATP-producing (catabolic) pathways and inhibition of ATP-consuming (anabolic) processes. AMPK has been associated with many key cellular processes present in all living organisms, as well as the promotion of adaptations to metabolic stress.

and conservation of ATP, acting through multiple pathways to promote catabolism and inhibit anabolism during times of energy shortage. AMPK is activated by a number of physiological and pathological stimuli, including, but not limited to, exercise, starvation, hypoxia, ischemia and hormonal signalling.

In simple organisms, the role of AMPK is primarily to allow growth only in the presence of sufficient energy, and to restrict growth in favour of survival when energy is scarce. In yeast, for example, the AMPK homologue SNF1 kinase is responsible for the switch from glucose to non-glucose carbon metabolism in a low-glucose environment (Woods et al., 1994). As organism complexity increased however, so did the network of AMPK-regulated pathways, with multiple tissues requiring local and systemic regulation of energy homeostasis. Whilst the basic cellular processes (Fig 1.7, left) are maintained, AMPK has since been implicated in the control of more complex and long-term regulatory pathways, such as mitochondrial biogenesis (Canto and Auwerx, 2009), angiogenesis (Nagata et al., 2003) and, recent literature suggests, stem cell differentiation (Ito and Suda, 2014). However, many of these pathways are subject to validation in specific models of AMPK activation.

### 1.3.2 Structure and Regulation of AMPK

AMPK complexes are heterotrimeric, comprised of three subunits; α, β and γ. In mammalian systems, the catalytic α subunit exists as two isoforms, α1 and α2, the β regulatory subunit as β1 and β2, and the second, γ-regulatory subunit as γ1, γ2 and γ3 (Woods et al., 1996, Stapleton et al., 1996). All subunits are capable of forming a complex, leading to 12 possible AMPK complexes, with varying degrees of tissue specificity (Thornton et al., 1998, Lang et al., 2000). The α subunits confer catalytic activity, containing a kinase domain (KD) and a typical kinase C-lobe. Phosphorylation of AMPK by upstream kinases $Ca^{2+}$/calmodulin-dependent protein kinase (CaMKKβ) and liver kinase B1 (LKB1/STK11) on threonine 172 of the α subunit stimulates AMPK activity more than 100-fold (Woods et al., 2003, Woods et al., 2005).

The binding of AMP and ADP to the γ-subunit promotes phosphorylation of $Thr^{172}$, as well as protecting this site from rapid dephosphorylation by various protein phosphatases. In addition, the kinase is allosterically activated by AMP binding to the γ-subunit. The γ-subunit is comprised of four CBS sequence repeats, with a nucleotide binding pocket located on each. In mammals, Sites 1 and 3 are able to bind ATP, ADP

and AMP, thus presenting as key regulatory sites for enzymatic activity (Xiao et al., 2011).

Site 2 has been found to interact with an aspartic acid residue (224) of the β-subunit, but is not occupied by nucleotides, suggesting that it is not directly involved in the activation of the complex (Oakhill et al., 2012). Site 4 has been designated as an AMP-bound, non-exchangeable site, which cannot be replaced by ATP *in vitro*, and is thought to reflect the status of this site *in vivo* (Xiao et al., 2011). Previously, aspartic acid residues were identified within all three of these occupied sites in the γ1 subunit.

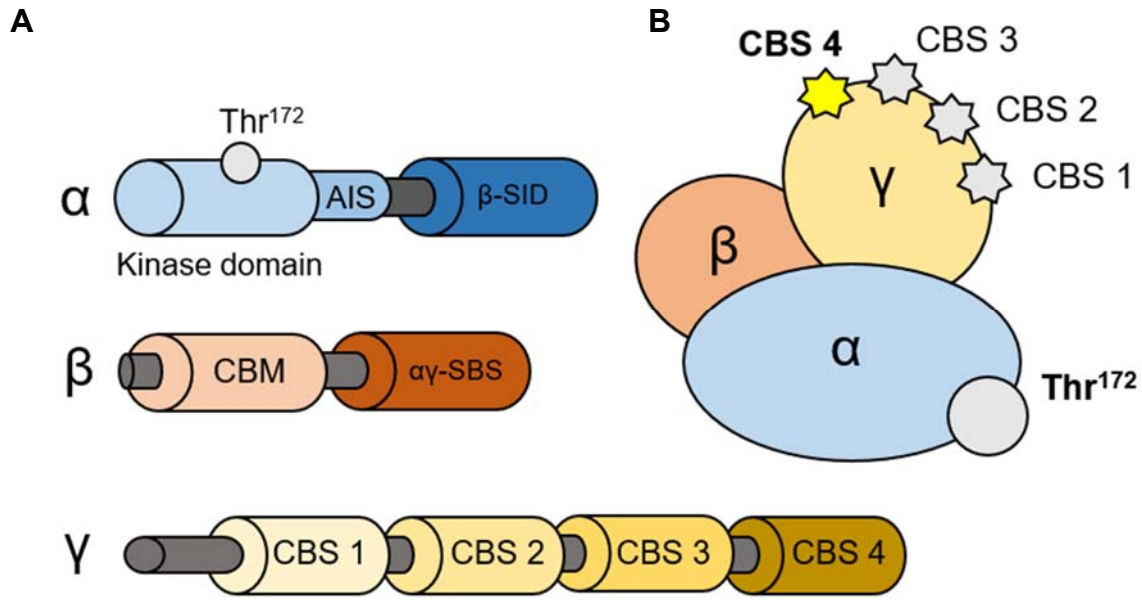



***Figure 1.8 AMPK subunit structure and complex formation.***

***A)*** *Structure of α1, β1 and γ1 subunits of AMPK, encoded by distinct genes. The α-subunit kinase domain activation loop contains a threonine residue (172), phosphorylated by upstream kinases and rapidly dephosphorylated by protein phosphatases. Binding of AMP to the regulatory γ-subunit protects Thr$^{172}$ from dephosphorylation and conferring allosteric activation. Adapted from (Oakhill et al., 2012)*

***B)*** *Tertiary structure of the inactive AMPK complex, with ATP bound at CBS sites 1, 2 and 3, and non-exchangeable AMP bound at CBS site 4. Threonine 172 is dephosphorylated by protein phosphatases to maintain inactivation.*

*Abbreviations; AIS, autoinhibitory sequence; β-SID, β-subunit interaction domain; CMB, carbohydrate binding module; αγ-SBS, α and γ-subunit binding sequence; CBS,*

The mutation of one of these residues, D316, in the non-exchangeable AMP binding site 4, lead to increased protection from dephosphorylation by protein phosphatase

2C (PP2C) and subsequent increase in basal activity of the complex (Woods et al., 2017). It is this mutation that will form the basis of this work, with the generation of the D316A-Tg mouse model.

The β- subunit interacts with both the α- and γ-subunits and contains a C-terminal domain (CTD), forming the structural core of the AMPK complex, and a carbohydrate-binding module (CBM), usually occurring in enzymes responsible for the metabolism of starch and glycogen (Steinberg and Kemp, 2009). In all mammalian heterotrimeric complexes, the CBM of the β subunit interacts with the N-lobe of the KD of the α subunit, forming a 'pocket' where many activators, such as 991 and A662, bind (Xiao et al., 2013).The structure of AMPK allows activity to be conferred both by upstream kinase phosphorylation and through AMP/ADP binding, which, in turn, protects $Thr^{172}$ from dephosphorylation (Xiao et al., 2011). In addition, binding of AMP, but not ADP, to the γ-subunit facilitates phosphorylation at this site, and itself instigates a 10-fold allosteric activation of the complex (Carling et al., 1989) (Fig 1.8).

The activation of AMPK by upstream kinases has been of particular interest in the context of disease, as one of the two primary AMPK-kinases, liver kinase B (LKB1), is a *bona fide* tumour suppressor, with mutations leading to the development of the autosomal-dominant, inherited Peutz-Jeghers Syndrome, associated with the development of intestinal cancer (Boardman et al., 1998, Hemminki et al., 1998). The deletion of LKB1 has been implicated in a number of other, sporadic cancers, such as skin, cervical and lung cancers (Wingo et al., 2009). LKB1 forms a complex with two other proteins; Ste-20-related adaptor protein-α (STRAD) and mouse protein 25-α (MO25α) to facilitate AMPK activation. It has been hypothesised that the loss of AMPK activation through LKB1-deletion in Peutz-Jeghers syndrome may drive the development of tumours, though this is still to be confirmed (Hardie, 2013, Hawley et al., 2003).

The second upstream kinase of AMPK is calcium/calmodulin-dependent protein kinase (CaMKKβ), which itself is activated by alterations in intracellular calcium. The

CaMKK family of protein kinases are closely related to yeast kinases Elm1, Pak1 and Tos3, all known to activate the AMPK homolog SNF1 (Hong et al., 2003).

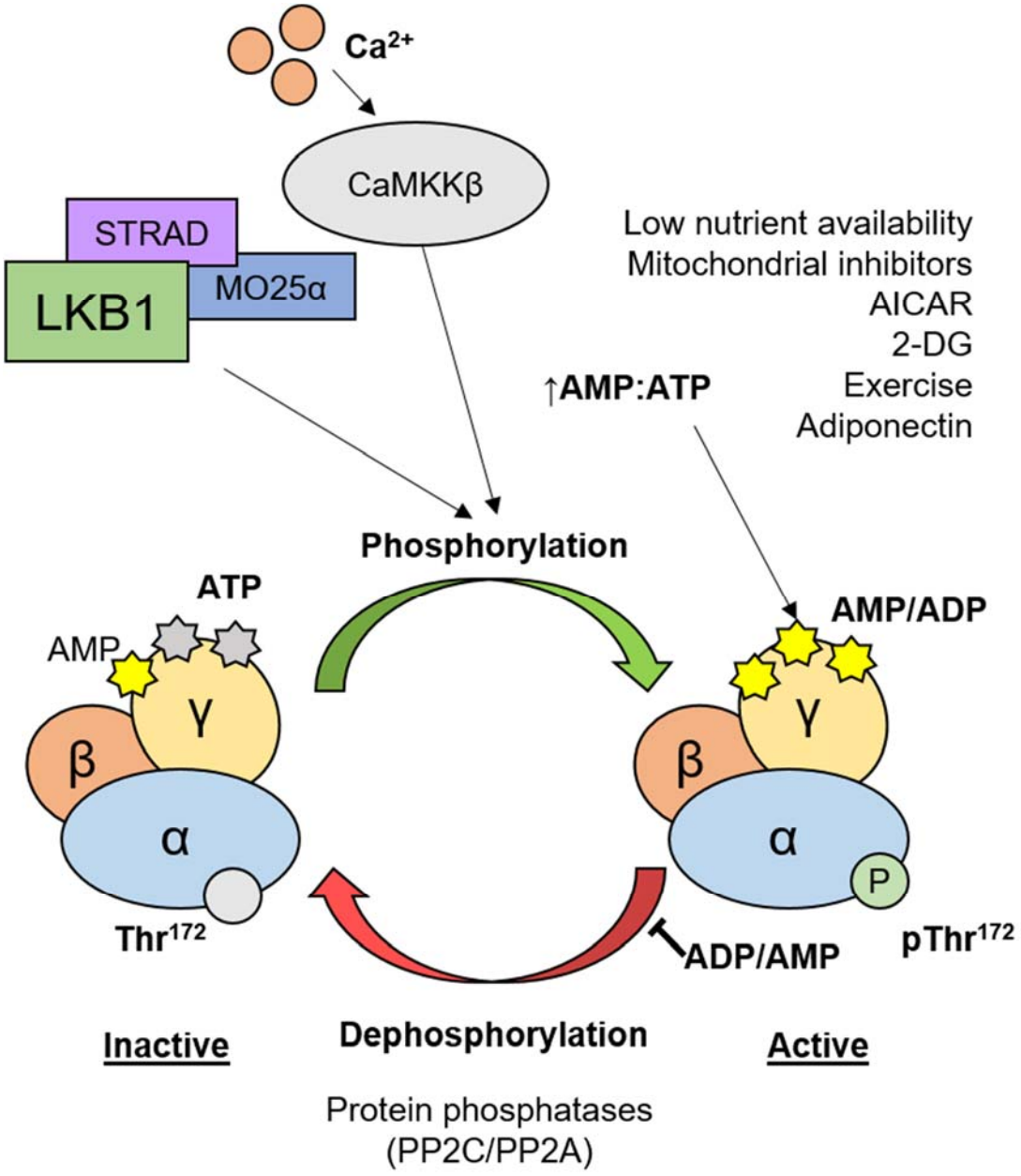



***Figure 1.9 Regulation of AMPK activity by upstream kinases and nucleotides.***

*AMPK is held in the inactive state when the ATP: AMP ratio is high, with ATP bound to the regulatory γ-subunit and AMPKα$^{Thr172}$ is dephosphorylated. In response to cellular stress signals, the AMP: ATP ratio increases, and AMP and ADP bind to the γ-subunit. Threonine 172 is phosphorylated by activated upstream kinases; LKB1(in complex with STRAD/MO25α) and CaMKKβ ($Ca^{2+}$), conferring protection from dephosphorylation by protein phosphatases. The binding of ADP/AMP also protects from dephosphorylation (Xiao et al., 2011). Adapted from (Viollet et al., 2010).*

Given that many conditions that are known to activate AMPK are also associated with the release of intracellular $Ca^{2+}$, such as muscle contraction and mitochondrial uncoupling, it has been hypothesised that the CaMKKβ-AMPK pathway is responsible for mediating calcium signalling pathways (Woods et al., 2005, Oliveira et al., Hawley et al., 1995, Jensen et al., 2007). However, unpublished work from our laboratory has suggested that several downstream pathways associated with CaMKKβ are not mediated by AMPK signalling, highlighting the importance of delineating targets of AMPK from those of its upstream kinases (*Penfold, L, unpublished)*. The regulation of AMPK by nucleotides and upstream kinases is outlined in Fig 1.9.

### 1.3.3 Downstream Targets of AMPK

The first identified downstream target of AMPK, acetyl-CoA carboxylase (ACC1), shares a conserved AMPK 'target sequence', which has subsequently been identified in a number of other proteins now known to be direct targets of AMPK (Sim and Hardie, 1988, Hardie et al., 2003, Marin et al., 2015). As a serine-threonine kinase, AMPK is responsible for the phosphorylation of these downstream targets, with both stimulatory and inhibitory consequences. Figure 1.10 outlines well-known targets and suggested of AMPK and the consequence of phosphorylation *in vitro/in vivo.* Many of these targets are well-validated, and form the basis for the known roles of AMPK *in vivo*, particularly the inhibition of fatty acid synthesis through phosphorylation of ACC. Indeed, it is believed that AMPK is the kinase responsible for the phosphorylation of ACC *in vivo*, providing key inhibition of FAS when nutrient availability is low. In

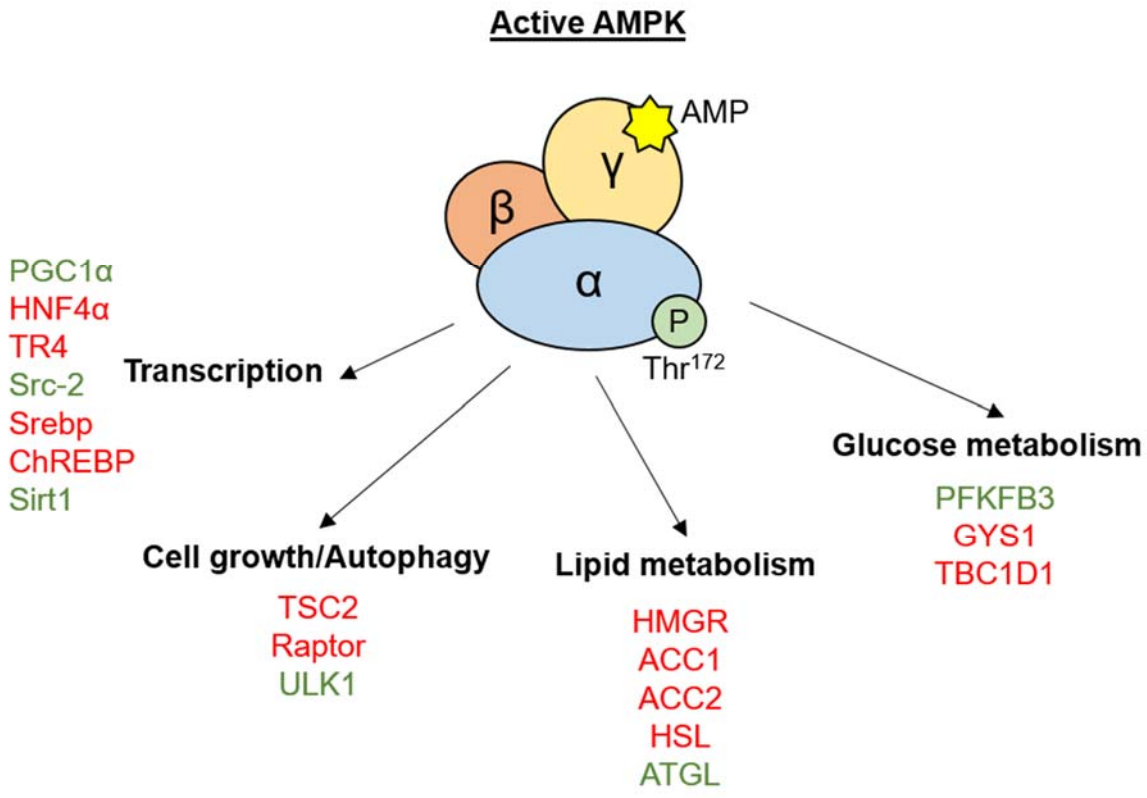



***Figure 1.10 Regularly identified downstream targets of AMPK.***

*AMPK has been implicated in many cellular processes, including glucose and lipid metabolism, cell growth, autophagy and transcription. Several targets of AMPK have been identified in each of these processes, though whether they are direct targets is subject to debate. Those shown to be inhibited by AMPK activity are highlighted in red, with those activated shown in green. Adapted from (Mihaylova and Shaw, 2011)*

addition, AMPK is also responsible for the phosphorylation of HMG-CoA reductase, thus providing a break on the sterol synthesis for which this enzyme is responsible (Carling et al., 1987).

It is through the inhibition of this *de novo* lipogenesis that AMPK activation is thought to prevent hepatic steatosis from high-fructose feeding (Woods et al., 2017), as well as studies reporting the facilitation of fatty acid oxidation in hepatocytes (Fullerton et al., 2013, Velasco et al., 1997, Tateya et al., 2013) and skeletal muscle (Minokoshi et al., 2002). Some controversy remains as to whether AMPK directly promotes FAO through ACC in some tissues, as studies using double knock-in mouse models of ACC1/2 lacking functional AMPK phosphorylation sites have shown FAO to be AMPK-pACC independent, at least in the heart (Zordoky et al., 2014). AMPK is also thought to influence lipid metabolism through the inhibition of sterol regulatory element binding protein 1 (SREBP1), a key lipogenic transcription factor responsible for the activation of fatty acid and triglyceride synthesis. (Li et al., 2011, Jung et al., 2011, Dessalle et al., 2012). It is thought that the efficacy of Liraglutide (GLP-1 analogue) can be at least in part attributed to the activation of AMPK, though this study requires further validation *in vivo* (Wang and Yang, 2015).

Aside from ACC, SREBP and HMGR, AMPK activation is also known to promote glucose transport in contracting skeletal muscle, through the phosphorylation and inhibition of the Rab-GTPase-activating protein (Rab-GAP) TBC1D1, which subsequently leads to the activation of Rab-GTP, facilitating the translocation of the glucose transporter GLUT4 to the plasma membrane (Sakamoto and Holman, 2008).

Canonical insulin signalling through the IRS-PI3K- and mTORC2-Akt pathways are also known to promote glucose uptake in this manner, with Akt responsible for the phosphorylation of both TBC1D1 and a second substrate, AS160/TBC1D4 promoting the binding of the scaffold-protein 14-3-3, reducing the activity of Rab-GAP (Sakamoto and Holman, 2008).

AMPK has also been shown to play a significant role in another prominent arm of insulin signalling; within the β-cell itself. AMPK is known to modulate β-cell gene expression in response to glucose stimulation, and its activity is inhibited by glucose *in vitro (da Silva Xavier et al., 2003).* Several studies have explored the role of AMPK in both the promotion and inhibition of glucose stimulated insulin secretion (GSIS) in

pancreatic β-cell lines (Jiang et al., 2014). Whilst stimulation of insulin secretion by acute AMPK activation is subject to debate, it is widely accepted that chronic activation of AMPK in β-cell line and islets inhibits insulin secretion (Fu et al., 2013). Expression of a constitutively active AMPK complex (CA-AMPK) in MIN6 cells has been shown to block glucose-induced mitochondrial ATP concentrations that are required for the subsequent release of insulin. Administration of AMPK activators *in vivo* have been reported to improve glucose homeostasis (Cokorinos et al., 2017, Kjobsted et al., 2015, Fisher et al., 2002a), and decrease obesity-induced insulin resistance. However, further investigation is required into the effects of AMPK activation on β-cell function, as improvements such as these may be both as a result of peripheral glucose uptake through insulin-independent pathways, and through direct action on the β-cell itself.

The promotion of GLUT4 expression in skeletal and cardiac muscle is thought to facilitate the excessive glycogen storage associated with chronic AMPK activation *in vivo*, even in the presence of phosphorylated glycogen synthase (GYS1/GS), another target of AMPK (Fig 1.11). AMPK has been shown to directly phosphorylate GS on an inhibitory site, serine 8, thus reducing its activity (Hunter et al., 2011). However, it is known that chronic activation of AMPK leads to glycogen accumulation in both skeletal (Milan et al., 2000, Barnes et al., 2004) and cardiac muscle (Murphy et al., 2005, Barre et al., 2007), which has been attributed to an increase in intracellular glucose-6-phosphate as a result of increased glucose transport. G6P is a potent allosteric

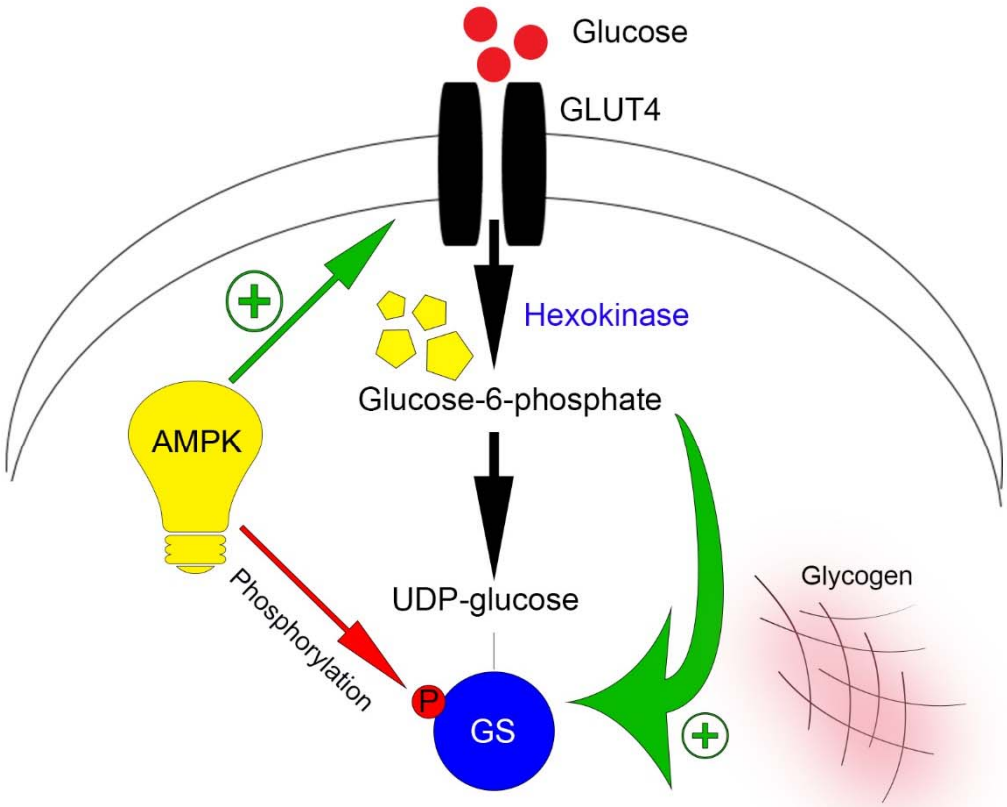



***Figure 1.11 Molecular mechanism of glycogen accumulation promoted by AMPK activation.***

*AMPK activation promotes the translocation of the glucose transporter GLUT4 to the plasma membrane, through the phosphorylation and inhibition of TBC1D1 (Sakamoto and Holman, 2008). AMPK activation leads to the phosphorylation and inhibition of glycogen synthase. Increased glucose transport results in an increase in intracellular G6P, allosterically activating GS and overriding the inhibition by AMPK. AMPK activation leads to glycogen accumulation in skeletal muscle and cardiomyocytes (adapted from (Hunter et al., 2011, Inagaki et al., 2016)).*

activator of GS, capable of overriding the inhibition laid down by AMPK, resulting in glycogen synthesis (Hunter et al., 2011).

AMPK acts as a checkpoint for cellular growth, responsible for the inhibition of proliferation and expansion in conditions of cellular stress. This action is facilitated by the phosphorylation and subsequent inhibition of the tumour suppressor TSC2 (Inoki et al., 2003), a key component of the mammalian target of rapamycin complex 1 (mTORC1) pathway. AMPK is known to directly phosphorylate TSC2 on serine 1387, in addition to the regulatory associated protein of mTOR (Raptor), resulting in the inability of mTORC1 to phosphorylate its substrates and promote cell growth and proliferation (Mihaylova and Shaw, 2011, Gwinn et al., 2008).

AMPK also plays a role in the regulation of another pathway downstream of mTOR; autophagy. Autophagy is defined as the process by which cells break down organelles and cytosolic components to promote survival when faced with nutrient deprivation. It is also a key process in the removal of defective mitochondria, known as mitophagy, facilitating replacement with functional, efficient organelles. Autophagy is a highly conserved cellular process, with the core components first identified in budding yeast (Atg1) (Mihaylova and Shaw, 2011). Later, cloning of mammalian homologs ULK1 and ULK2 led to the identification of AMPK as a conserved regulator of ULK1 activity, and therefore a key regulator of autophagy and mitochondrial maintenance (Egan et al., 2011, Lee et al., 2010). Indeed, mice lacking functional AMPK or ULK1 suffer from severe mitophagy and autophagy defects, with the authors demonstrating that phosphorylation of ULK1 by AMPK is absolutely required for autophagy and cell survival during nutrient deprivation (Egan et al., 2011).

AMPK has been shown to regulate both mitophagy and mitochondrial biogenesis, through direct and indirect mechanisms converging on the activation of PGC1α (Wan et al., 2014, Canto and Auwerx, 2009). PGC1α, known to co-activate many nuclear receptors and transcription factors is a key player in the regulation of mitochondrial biogenesis, particularly in tissues with high rates of oxidative metabolism, such as skeletal muscle and brown adipose (Jager et al., 2007, Canto and Auwerx, 2009). AMPK has been shown to phosphorylate PGC1α directly, at threonine-177 and serine-538 (Jager et al., 2007), required for the induction of the PGC1α promotor and

subsequent target gene expression, encompassing key mitochondrial enzymes, the glucose transporter GLUT4 and cytochrome c (Winder et al., 2000).

The regulation of mitochondrial biogenesis by AMPK has also been attributed to the modulation of the NAD+-dependent deacetylase SIRT1, a member of the sirtuin family. A mammalian homolog of the yeast Sir2 protein, the SIRT1 enzyme is responsible for the deacetylation of substrates, including transcription factors and coregulators including PPARγ (Picard et al., 2004), p53 (Vaziri et al., 2001, Lee et al., 2012) and FOXO (Brunet et al., 2004), involved in the regulation of metabolism, as well as PGC1α (Rodgers et al., 2005). In skeletal muscle and brown adipose tissue, treatment with SIRT1 agonists leads to the deacetylation of PGC1α, resulting in mitochondrial biogenesis and enhanced oxidative metabolism, a pathway that has been linked to AMPK through an increase in intracellular NAD+ levels. Oxidised nicotinamide adenine dinucleotide (NAD+) along with another pyridine nucleotide NADP+, are electron-carrying coenzymes that play vital roles in energy transduction, and have been identified as key elements in a number of regulatory pathways (Pollak et al., 2007). AMPK has been shown to increase cellular NAD+: NADH (reduced) levels through mitochondrial β-oxidation, which subsequently acts as a messenger to activate SIRT1, resulting in PGC1α activation and target gene expression. Thus, AMPK activation promotes mitochondrial biogenesis both by directly phosphorylating PGC1α, and through NAD+-SIRT1 mediated deacetylation. It is possible that this dual control plays a significant role in the regulation of mitochondrial metabolism and adaption to metabolic stress (Canto and Auwerx, 2009).

Many other roles of AMPK have been identified, predominantly through the use of commercially available agents known to result in activation. However, several caveats have been identified with this approach, and it is often difficult to determine direct targets of AMPK by these methods. The development of AMPK knock-out mouse models has provided useful tools with which to study these potential targets, particularly the isolation of mouse embryonic fibroblasts (MEFs) and primary cells that can then be interrogated using the same activators to identify AMPK-dependent and –independent effects. Indeed, many *bona fide* AMPK targets have been confirmed *in vivo* with the identification of naturally occurring mutations leading to constitutive activation (Aschenbach et al., 2002, Zou et al., 2005, Folmes et al., 2007, Costford et al., 2007, Barre et al., 2007). The study of these mutations has shed light on the

potential positive and negative consequences of chronic AMPK activation, with considerations for potential therapeutics targeting AMPK complexes.

## 1.4 Studying AMPK Activation *in vivo*

### 1.4.1 Activators and Inhibitors

Since the identification of kinase activity associated with ACC and HMGR, AMPK, has been directly and indirectly implicated in numerous cellular processes, but also in several pathologies. Indeed, many conditions are associated with a decrease in AMPK activity, in particular in the progression of obesity, though it is not clear as to whether this decrease is a cause or a consequence. The following sections will explore the most commonly referenced methods for the activation of AMPK *in vivo* using natural and synthetic compounds, with reflections on specificity and applications in translational medicine.

***INDIRECT ACTIVATORS***

It is well known that exercise exerts beneficial effects in terms of weight loss, insulin sensitivity and the amelioration of type 2 diabetes, and it is thought that these effects are, in part, mediated by AMPK activation in skeletal muscle (Fisher et al., 2002a). Several studies have recapitulated these effects *in vivo* with the use of the 5-aminoimidazole-4-carboxamide ribonucleoside (AICAR), to treat mouse models of obesity such as the genetically obese (GO) ob/ob mouse, or in models of diet-induced obesity, as discussed previously.

AICAR is rapidly taken up into cells and converted into ZMP, an AMP-mimetic, thus stimulating AMPK activity through the alteration of the ATP: ZMP ratio. Treatment of DIO/GO mice with AICAR has been shown to reduce plasma triglyceride and free fatty acid (FFA) concentrations and reverse glucose intolerance (Narkar et al., 2008). It has also been shown that AICAR is capable of promoting glucose uptake, as well as oxidative metabolism and angiogenesis-related gene expression *in vivo* and that, by inhibiting AMPK in C2C12 myotubes, the insulin sensitising effects of AICAR are reduced (Smith et al., 2005). In hepatocytes, AICAR has been shown to reduce gluconeogenic gene expression, including phosphoenolpyruvate carboxykinase (PEPCK) and glucose-6-phosphatase (G6Pase), achieved, at least in part, through the regulation of transducer of CREB activity 2 (TORC2) (Lochhead et al., 2000, Koo et al., 2005).

Though AICAR has provided a plethora of studies linking AMPK activation to the protection from DIO and type 2 diabetes, results from the infusion of AICAR into diabetic patients suggest that its effects are largely confined to the liver, resulting in a reduction in hepatic glucose output and subsequent reduction in blood glucose levels (Boon et al., 2008). Activation of AMPK by AICAR in the skeletal muscles of these patients was not detected. Aside from the liver, AICAR has also been shown to decrease adipose tissue inflammation and insulin resistance in DIO mice, thought to be as a partial result of the modulation of SIRT1 in macrophages. Indeed, myeloid SIRT1 knock out mice (MSKO) were resistant to the anti-inflammatory effects of AICAR, though its ability to reduce blood glucose and improve insulin sensitivity were largely intact. It was discussed that the ability of AMPK to ameliorate type-2 diabetes was, at least in part, due to a reduction in adipose tissue inflammation, though the observed glucose lowering effects were not completely abolished by the removal of this pathway, highlighting the significance of AMPK activation in the liver and skeletal muscle (Yang et al., 2012, Schug et al., 2010).

AICAR remains a useful tool for the interrogation of the AMPK signalling pathway. However, as a non-specific direct activator, it has been recognised that other pathways, also activated by changes in intracellular nucleotide ratios, contribute to the beneficial effects of AICAR treatment in cells and *in vivo,* particularly those involving enzymes also activated by AMP. Several studies have identified some of these 'off-target' effects, including the induction of programmed necrosis in prostate cancer cells through the production of reactive oxygen species (ROS). This mechanism was then identified as AMPK-independent, as the use of ROS scavengers, but not AMPKα shRNA was able to ameliorate AICAR-induced ROS generation and subsequent cytotoxicity (Guo et al., 2016). In a separate study, AICAR was found to have AMPK-independent effects on tumour growth and proliferation through the direct inhibition of the cell cycle, by degradation of the G2M phosphatase cdc25c, an effect not recapitulated by the direct AMPK activator A769662. Interestingly, similar inhibition of tumour growth, this time through the direct inhibition of mTOR, was seen with the use of another indirect AMPK activator metformin (Liu et al., 2014).

Metformin, a biguanide derivative, is one of the most widely used oral anti-diabetic agents prescribed today. It has proven efficacy in the lowering of blood glucose and insulin sensitisation independent of insulin secretion, thought to be largely attributable

to the activation of AMPK in the liver. However, various studies have shown that AMPK activation by metformin is secondary to its effects on mitochondria through the direct inhibition of complex I of the mitochondrial respiratory chain (Owen et al., 2000). Furthermore, the inhibition of mTORC1 by metformin was found to be AMPK-independent, instead relying on the action of Rag-GTPases (Kalender et al., 2010). Whilst it is clear that some beneficial effects of metformin are indeed orchestrated by the activation of AMPK, there are additional effects mediated by AMPK-independent effects that, in the past, may have been attributed to AMPK.

The development of small molecule, AMPK-specific, activators have, and continue to, delineate the effects of AICAR and metformin, alongside other notable activators, such as the grape-skin derivative resveratrol, curcumin, berberine and quercetin, all known to activate AMPK in an indirect manner, through inhibition of mitochondrial ATPase/ATP synthase and complex I, leading to an increase in intracellular ATP: AMP (Kim et al., 2016).

### *DIRECT ACTIVATORS*

The identification of a small molecule AMPK activator A-769662, hereafter referred to as A662, was developed in 2006 by Abbott Laboratories. Animals treated with A662 showed an increase in fat oxidation, a decrease in bodyweight and improvements in plasma glucose and triglyceride levels (Scott et al., 2014, Cool et al., 2006). The resolution of the crystal structure of AMPK complexed with A662 revealed a drug binding site between the β-CBM and the α-kinase domain (Xiao et al., 2013), a molecular mechanism distinct from previously identified AMPK activators primarily targeting AMPK through alterations in nucleotide concentrations. This allosteric binding of A662 inhibited the dephosphorylation of $Thr^{172}$, conferring activity. Because of this unique binding, A662 exhibited high specificity towards AMPK, unlike AICAR, and has since provided an invaluable tool in the study of AMPK in cells and *in vitro*. Previously it was shown that the activation of AMPK by A662 was possible without phosphorylation on $Thr^{172}$, rather that phosphorylation on serine 108 of the β-subunit was sufficient to confer maximal activation of the complex (Scott et al., 2014). However, a recent study published by our laboratory has disputed this, demonstrating that in the absence of upstream kinases, AMPK activity mediated by small molecule activation is almost undetectable, and that instead, the binding of these compounds

confers an active-like conformation of the activation loop. These findings suggest that phosphorylation of $Thr^{172}$ is absolutely required for the activation of AMPK in cells and, most likely, *in vivo* (Willows et al., 2017b).

A similar small activator, 991, produced by Merck, was found to bind in the same α-β pocked as A662, though was found to be 5-10 fold more potent in both allosteric activation and protection from dephosphorylation (Xiao et al., 2013). Since the discovery of A662, other 'direct' activators have been developed, with varying degrees of activation reported (Zadra et al., 2014). All of these compounds share a very similar core structure to A662, suggesting that this is the primary structure conferring binding in the α-β pocket, with extensions and truncations conferring varying degrees of solubility and potency in *in vitro* drug screens (Kim et al., 2016). Whilst these compounds are invaluable tools for the interrogation of AMPK *in vitro,* the use of these compounds *in vivo* has since been challenging, primarily due to their low solubility and bioavailability. Current efforts are being made to improve the biochemical profile of small molecule activators so that they can be used to study AMPK activation *in vivo.*

Recently, two independent groups have demonstrated the use of small molecule AMPK activators *in vivo*; PF-739 and MK-8722. PF-739, developed by Pfizer, is a pan-AMPK activator demonstrating anti-diabetic glucose lowering effects in rodents and non-human primates, mediated by skeletal muscle AMPK activation (Cokorinos et al., 2017). Interestingly, another compound examined in the same study, this time exhibiting β1 specificity, did not activate AMPK in skeletal muscle, instead exerting its effects in the liver, and could not recapitulate the anti-diabetic effects exhibited by PF-739 (Cokorinos et al., 2017).

In a similar fashion, the Merck compound MK-8722 activated AMPK in the skeletal muscle, resulting in insulin-independent lowering of blood glucose, mediated by AMPK-driven glucose uptake. Again, this effect was maintained across species, though this study also reported mild cardiac hypertrophy and glycogen accumulation, though without any observable pathology (Myers et al., 2017). These studies are extremely encouraging, particularly for those looking to AMPK as a therapeutic target for diabetes, though none to date have exhibited a lowering of bodyweight or protection from DIO. It is possible, however, that this may be due to the tissue into which these compounds are taken up, with most exerting their effects on the liver and

skeletal muscle. Nevertheless, in the absence of potent, tissue penetrative compounds, the study of AMPK activation *in vivo* requires the use of transgenic mouse models, several of which have been extensively characterised, and are outlined in the following section. There have also been many knock-out models which have also helped to shed light on the role of AMPK in various tissues (Viollet et al., 2003, Jorgensen et al., 2005, Steinberg et al.) but these will not be commented on as the aim of this study is to investigate the consequences of activation of AMPK

### 1.4.2 Mouse Models of AMPK Signalling

The identification of several naturally occurring mutations in the AMPK γ-subunit have revealed many features of the activation of this kinase *in vivo*, with significant implications for drug discovery. The following section will review the current understanding of these mutations, reflections on isoform specificity and their importance for the future of AMPK as a therapeutic target.

***AMPKγ2 Mutants, Wolff Parkinson-White Syndrome and Cardiac Glycogen Storage.***

In 2001, a gene was identified as being responsible for the development of familial Wolff Parkinson-White syndrome (WPW), a heart condition presenting with tachycardia, cardiac hypertrophy and ventricular pre-excitation. This gene was identified as PRKAG2, the γ2 regulatory subunit of AMPK. In this particular study conducted on two families with a history of WPW, the mutation was identified as a substitution of glutamine for arginine at residue 302 (Gollob et al., 2001). In a subsequent study, three further mutations were identified in AMPKγ2; Arg302Gln, Thr400Asn and Asn488Ile, all shown to be causative of WPW, conferring alterations in AMPK activity (Arad et al., 2002). Further evaluation of the hearts of these patients revealed a distinctive ventricular hypertrophy, myocyte enlargement and large cytosolic vacuoles containing glycogen, similar to those seen in adult-onset Pompe disease (Arad et al., 2002). However, both stimulatory and inhibitory mutations in γ2 have since been identified, raising questions over the molecular mechanisms by which mutations in AMPKγ2 cause WPW. In a subsequent study, one of six mutations identified did not present with cardiac hypertrophy, though exhibited electrophysiological abnormalities, a mutation of arginine to glycine at residue 531 (R531G) (Davies et al., 2006). These studies highlight that the role of AMPKγ2 in the

development of WPW is not necessarily driven by enhanced basal activity, rather through alterations in the ability to respond to environmental cues, and also to engage with target proteins and molecules, such as glycogen. Indeed, until recently it was thought that glycogen accumulation was a driver of the conductance defects seen in WPW, though later studies have since identified these defects in the absence of glycogen, and vice versa (Arad et al., 2002).

To investigate the effects of these mutations in more detail, transgenic animal models have since been developed, harbouring these mutations or over-expressing AMPKγ2 globally. In particular, the N488I and R531G mutations have been intensively studied, and are believed to confer constitutive activation to the harbouring AMPKγ2 complex. However, they differ with respect to AMP sensitivity, with the former retaining AMP sensitivity, the latter lacking the ability to bind AMP. In line with previous studies (Kim et al., 2014), over-expression of both of these mutations in transgenic mouse models drove dramatic cardiac glycogen accumulation, but in contrast to the R531G mutant, physiological expression (not overexpression) of the AMPKγ2$^{NI}$ mutation did not. Strikingly, the R531G mutant also exhibited renal glycogen accumulation and cyst development. This was attributed by the authors to an increase in pFOXO3a leading to apoptosis, inflammation and cyst development, resulting in kidney injury and impairment of renal function (Yang et al., 2016b). Both of these models, however, developed WPW, suggesting that glycogen accumulation is not causative of WPW, but rather a feature of AMPK activation or over-expression (Yang et al., 2016b).

The observation that AMPK activation leads to glycogen accumulation is supported by another naturally occurring mutation, identified prior to the discovery of causative PRKAG2 mutations in WPW, the RN$^{-}$ mutation in the skeletal muscle of Hampshire pigs.

### *Skeletal Muscle Glycogen Accumulation; Mutations in AMPKγ3*

Whilst AMPK is a ubiquitously expressed kinase, there are several tissue specificities associated with subunit isoforms, particularly with respect to γ2 and γ3. Whilst γ2 is expressed in several tissues, including the heart and kidney, the γ3 isoform is exclusively expressed in the skeletal muscle (Thornton et al., 1998). A naturally occurring mutation in AMPKγ3 in Hampshire pigs, known formerly as the rendement Napole (RN$^{-}$) mutation, was identified as the cause of excessive (>70%) glycogen

accumulation, originally selected for based on the beneficial effects on meat content, but was found to be associated with poor processing yield once cooked, with a low water-holding capacity (Estrade et al., 1993a, Estrade et al., 1993b). This mutation was subsequently identified as nonconservative substitution of arginine to glutamine at residue 200, denoted R200Q and located in CBS1 of AMPKγ3 (Milan et al., 2000). The expression of the mouse equivalent of this mutation, R225Q, revealed that this missense mutation is sufficient to drive glycogen accumulation in skeletal muscle, and is associated with higher basal AMPK activity and lack AMP dependence (Barnes et al., 2004).

Interestingly, these mice also exhibited an increase in fatty acid oxidation when challenged with a high-fat diet, associated with an increase in mitochondrial content, PGC1α and respiratory chain complexes, with no observable change in fibre type (Garcia-Roves et al., 2008, Barnes et al., 2004). No significant pathology was associated with skeletal muscle glycogen accumulation in mice or in pigs, though mice expressing the R225Q mutation were significantly more resistant to exercise-related fatigue and were protected from diet-induced insulin resistance (Garcia-Roves et al., 2008). Finally, humans bearing the R225W mutation, analogous to the R225Q mutation in pigs, displayed an approximate 90% increase in skeletal muscle glycogen, as well as a 30% decrease in intramuscular triglyceride (Costford et al., 2007). Together, these studies suggest that AMPKγ3 plays an important regulatory role in skeletal muscle, particularly in the re-synthesis of glycogen, with no differences found in the rate of depletion (Costford et al., 2007).

Though these findings bear significance with respect to the role of AMPK in skeletal and aforementioned cardiac function, the expression of the γ2 and γ3-containing complexes is restricted in comparison to the ubiquitously expressed γ1 isoform. Therefore, the understanding of the consequences of the activation of AMPKγ1 *in vivo* is imperative. To date, two mutations have been explored in the γ1 subunit; the H151R and R70Q mutations.

***Skeletal and Cardiac Muscle-Specific AMPKγ1 Mutations***

The R200 residue in the first CBS domain of γ3, associated with the $RN^-$ mutation is preserved in all mammalian γ-isoforms. The mutation of the equivalent residue, R70 to a glutamine (R70Q), reported in 2001, caused a significant increase in both acute

and chronic AMPK activation, with 5-9 fold and 2-3-fold activation respectively. The R70Q mutation was shown to increase phosphorylation on $Thr^{172}$ and conferred AMP-independence (Hamilton et al., 2001). Subsequent expression of this mutation in neonatal rat cardiomyocytes lead to marked glycogen accumulation, glycogen synthase phosphorylation and an increase in palmitate oxidation (Folmes et al., 2007). Though considerable work has been conducted using this mutation *in vitro*, no studies to date have expressed this mutation chronically *in vivo.* In contrast, the second γ1 mutation, H151R, has been implicated in whole body energy homeostasis and insulin

Originally identified in yeast at histidine 151, the H151R mutation (murine homolog H150R) presented with strong, AMP-independent activation of AMPKγ1 complexes, both *in vitro* and *in vivo* (Schonke et al., 2015, Minokoshi et al., 2004). When expressed under the skeletal-specific myosin light chain (MLC1) inducible cre driver, skeletal muscle glycogen was increased more than 10-fold, with cardiac glycogen equivalent to controls. Interestingly, food intake and $VO_2/VCO_2$ was increased in male, but not female, transgenic mice, with enhanced reliance on carbohydrates and a reduction in locomotor activity in both sexes (Schonke et al., 2015). None of these parameters, however, conferred any alterations in bodyweight, though white adipose tissue mass was reduced in female mice. These observations were coupled with an increase in expression of the uncoupling protein UCP1 in perigonadal WAT and BAT, as well as whole body glucose oxidation and an increase in insulin sensitivity, indicating that skeletal muscle overexpression of $AMPK\gamma1^{H151R}$ is sufficient to ameliorate many features of DIO and the metabolic syndrome, without an adverse cardiac phenotype. These studies are somewhat recapitulated by the recent use of novel small molecule activators *in vivo*, discussed previously, though with no obvious effects on whole body oxygen consumption (Myers et al., 2017, Cokorinos et al., 2017).

The only documented expression of constitutively active AMPK globally to date is that of Yavari *et al.,* in 2016, using the R302Q murine equivalent R299Q, introduced into the murine PRKAG2 gene. These heterozygous and homozygous knock-in mice expressed 2-3-fold constitutively active AMPKγ2 confirmed in white adipocytes, liver and skeletal muscle. Interestingly, no cardiomyopathy was observed in these animals,

but instead exhibited age-related bodyweight gain and adiposity, in conjunction with

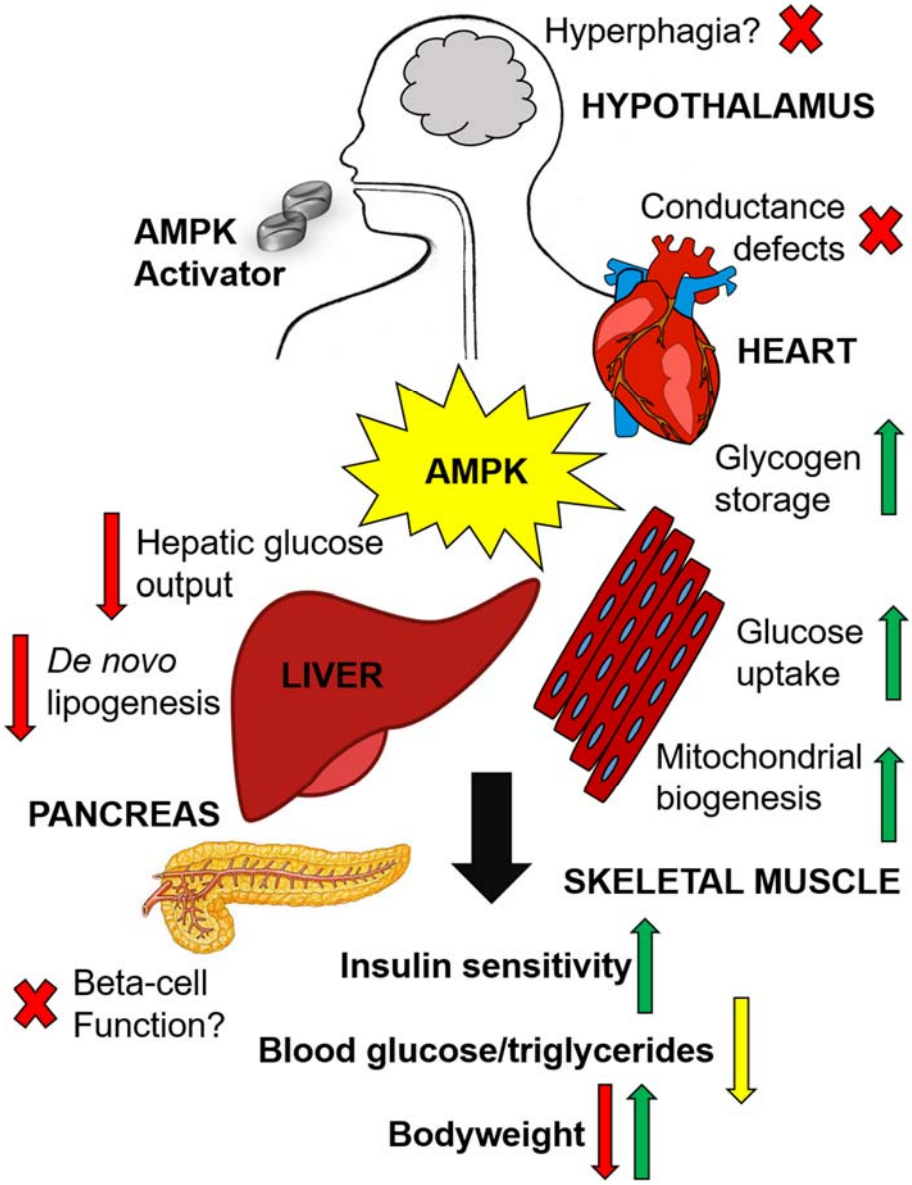



***Figure 1.12 Summary of direct AMPK activation in vivo using activators and mouse models.***

*Documented effects of tissue-specific CA- and knock-in mouse models, and small molecule AMPK activators in vivo. AMPK activation has been shown to result in a reduction in hepatic glucose output and de novo lipogenesis (Woods et al., 2017), increased glucose uptake, glycogen storage and mitochondrial biogenesis in skeletal muscle(Rosso and Lucioni, 2006, Cokorinos et al., 2017), cardiac glycogen accumulation (Myers et al., 2017, Cokorinos et al., 2017, Yavari et al., 2016), hyperphagia and decreased beta-cell function (reported by one study, (Yavari et al., 2016). Studies report increased insulin sensitivity, reduced blood glucose and triglyceride concentrations with mixed, isoform-specific bodyweight effects. No conductance defects reported with small molecule activators despite glycogen accumulation.*

hyperleptinemia, consistent with obesity. it was determined that this obesity was driven by hyperphagia, with no significant difference in locomotor activity (Yavari et al., 2016).

This was then attributed to the expression of mutant $\gamma2^{R299Q}$ in the arcuate nucleus, with a concurrent increase in the phosphorylation of ACC, confirming AMPK activity. This activity was associated with increased expression of Agrp, promoting food intake in response to enhanced ghrelin signalling, but not circulating ghrelin levels. In addition, AMPK activation led to a suppression of islet insulin release, a phenotype recapitulated by the corresponding R302Q mutation in humans. Indeed, humans carrying this mutation were found to have an increase in adiposity and suspected liver triglyceride accumulation, as well as higher fasting glucose levels (Yavari et al., 2016). This study suggests that AMPKγ2 may play a key role in the regulation of food intake and that activation of this isoform with small molecule activators may induce a phenotype opposite to that which is desired; the amelioration of obesity and the metabolic syndrome. However, other studies expressing mutations of AMPKγ2 (N488I and R531G) globally did not observe any associated hyperphagia or pancreatic dysfunction (Yang et al., 2016b), though noted kidney injury in the RG mutant. It is therefore of particular interest to understand the divergent roles of AMPK isoform mutations in the brain, and indeed in a whole organism, thus informing the development of more specific therapeutics.

In summary, several mutations in AMPK have been identified, both synthetic and naturally occurring, the use of which has elucidated roles of AMPK in several different tissues (Fig 1.12). It is clear that AMPK plays a key role in the regulation of glucose uptake and glycogen storage, particularly in the heart and skeletal muscle, with subsequent glucose lowering effects that can be recapitulated by small molecule activators. Though improvements in whole body insulin sensitivity and reduction in adiposity have been reported through AMPK activation in skeletal muscle, as yet no study has used a transgenic mouse model expressing constitutively active AMPKγ1 globally, thus mimicking a hypothetical potent, tissue penetrative compound. Therefore, this work is focussed on the characterisation of a previously identified

mutation in AMPKγ1, conferring constitutive activation and protection from dephosphorylation; D316A.

### 1.4.3 The Activating Mutant: An Novel Tool to Study Gain of Function *in vivo*

Recently published by Woods *et al.,* mutation of an aspartic acid residue 316 to an alanine (317 in human) in AMPKγ1 in CBS site 4 abolishes the non-exchangeable binding of AMP, protecting the complex from dephosphorylation by protein phosphatase 2C and conferring 2-3-fold constitutive activity (Woods et al., 2017).

To achieve global, constitutive activation of AMPKγ1, ROSA26 targeting vectors were designed, containing a flox/STOP/flox sequence enabling Cre mediated excision and recombination, preceded by a CMV early-enhancer/chicken β-actin (CAG) promoter. Inserted into this construct was either γ1WT or γ1D316A cDNA with a 3' FLAG

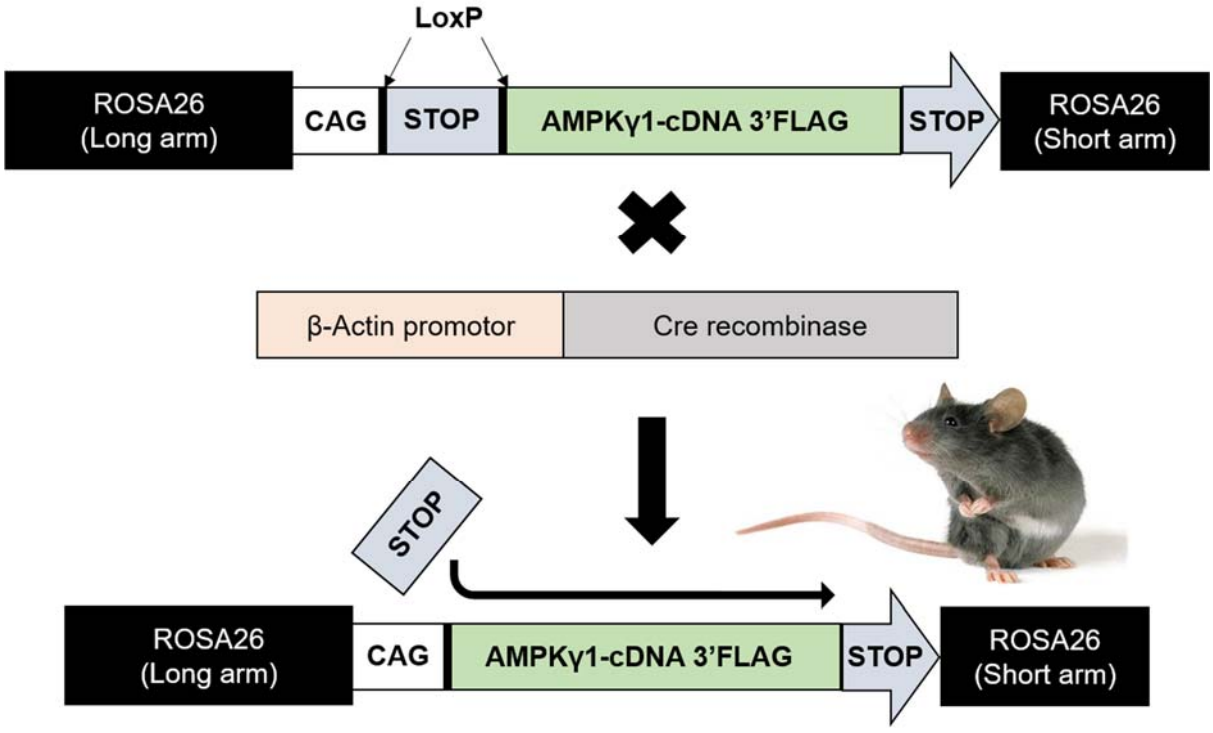



***Figure 1.13 Generation of the WT-Tg and D316A-Tg mouse model.***

*Mice harbouring either WT- or D316A-AMPKγ1, preceded by a STOP cassette flanked by LoxP sites, were crossed with mice expressing Cre recombinase under the ubiquitously expressed β-actin promoter. Cre-mediated excision of the STOP cassette and subsequent recombination facilitated the expression of WT-Tg and D316A-Tg in tissues expressing β-actin. The strong CMV early enhancer/chicken β-actin promoter should drive AMPKγ1 overexpression to compete with endogenous γ1 for binding with α- and β- subunits.*

sequence to allow detection in subsequent experiments. The CAG promoter sequence resulted in the overexpression of either WT or D316A γ1, with complex formation limited by the endogenous expression of α- and β-subunits. By pairing γ1 flox/STOP/flox animals with mice expressing cre recombinase under the control of the β-actin promoter, global expression of WT and D316A AMPKγ1 should be achieved (Fig 1.13).

This model has been characterised with respect to the liver-specific expression of D316A, using mice expressing cre recombinase under the control of the albumin promoter. These mice exhibited significant protection from hepatic steatosis on a lipogenic high-fructose diet, through the phosphorylation of ACC and suppression of gluconeogenic gene expression, resulting in reduced *de* novo lipogenesis and hepatic glucose output (Woods et al., 2017).

This work has focused on the characterisation of the β-actin cre D316A-Tg mouse model, in collaboration with AstraZeneca, to better understand the effects of AMPK activation *in vivo*.

## 1.5 Project Aims

The obesity pandemic and associated metabolic syndrome continues to place extreme pressure on healthcare systems worldwide, both in the Western world, and in developing and semi-developed nations lacking access to dietary and lifestyle advice. Whilst bariatric surgery, diet and exercise remain the most effective treatments and preventative strategies for this multifactorial disease, the rate at which the population, in particular children, are increasing, highlighting the need for significant investment in therapeutics.

AMPK, as a master regulator of energy homeostasis, is often regarded as a promising therapeutic target for obesity and associated diseases, though with few tools available to study this potential *in vivo* in a chronic and specific manner, its true potential is somewhat clouded. Indeed, AMPK has been implicated in many pathways underlying energy balance, positive and negative, including the modulation of food intake and satiety, insulin sensitivity and secretion, lipolysis and *de novo* lipogenesis and adaptation to metabolic stress. As obesity is inherently a disease of energy imbalance, where caloric intake exceeds expenditure, it is unsurprising that AMPK has been implicated in many studies looking for mechanisms underlying its development.

The aim of this thesis is to characterise a global model of constitutive AMPK activation *in vivo*, in collaboration with AstraZeneca, in the context of normal physiology and for the treatment of diet-induced obesity and the metabolic syndrome.

**Aim 1: To confirm the ubiquitous expression of constitutively active AMPKγ1-D316A-FLAG in major tissues.**

The expression of constitutively active AMPK *in vivo* is key to the subsequent assessment of effects on normal physiology, development and adaption to metabolic stress. Therefore, expression must be confirmed in all major tissues and organs, with work relating to this presented in Chapter 3.1.

**Aim 2: To characterise the physiology of the D316A-Tg mouse model.**

AMPK is known to play a role in the development and function of several tissues, including the heart, skeletal muscle, brown adipose tissue and liver. Initial studies, presented in Chapter 3, focus on the characterisation of the D316A-Tg mouse model on a standard chow diet, with reports of cardiac glycogen storage and a cystic kidney phenotype presented in Chapter 4.

**Aim 3: To evaluate the effects of AMPK activation on the progression of diet-induced obesity and associated metabolic disorders.**

To assess AMPK as a viable therapeutic target for the prevention and treatment of obesity and the metabolic syndrome, animals were administered a high-fat diet. Mice were subsequently assessed for food intake and energy expenditure, followed by characterisation of tissue morphology and peripheral lipid accumulation. RNA sequencing was performed on four major metabolically active tissues, in conjunction with histology, qPCR and Western blotting to uncover novel tissue-specific roles of AMPK *in* vivo. Work pertaining to this investigation is presented in Chapter 3.

# 2 CHAPTER 2: MATERIALS AND METHODS

## 2.1 Materials

### 2.1.1 General Reagents

Adenosine triphosphate (ATP), 4-(2-hydroxyethyl)-1-piperazineethanesulfonic acid (HEPES), Tris(hydroxymethyl) aminomethane (Tris), ethylene glycol tetraacetic acid (EGTA), magnesium chloride (MgCl2), sodium fluoride (NaF), sodium pyrophosphate (Na4P2O7), dithiothreitol (DTT), lithium chloride (LiCl), protein A/G-sepharose, sorbitol, β-mercaptoethanol, agarose, glycine, potassium phosphate, hydrogen peroxide ($H_2O_2$), bovine serum albumin (BSA), Gill's haematoxylin, normal goat serum (NGS), DPX, gelatin from cold water fish skin, mixed dNTP (10 mM)and Triton X-100 were obtained from Sigma-Aldrich (Poole, UK).

NaOH, sodium lauryl sulfate (SDS), NaCl, Tween 20, glycerol, ethylenediaminetetraacetic acid (EDTA), ethanol, methanol, glycerol, chloroform, KCl, KH2PO4 and NaHCO3 were acquired from VWR (West Sussex, UK).

Polyvinylidene difluoride (PVDF) membrane and [1-14C] acetic acid sodium salt (NEC084H100/Mc) were from PerkinElmer (Beaconsfield, UK).

RNeasy columns and RNeasy kit from Qiagen (Crawley, UK).

BioMix Red master mix and SensiMix SYBR-HiROX were from Bioline (London, UK).

Random primers were acquired from Promega (Southampton, UK).

DMEM, Penicillin/Streptomycin, optiMEM, and trypsin were from Gibco (Paisley, UK).

BioRad Protein assay kit and x20 MOPS running buffer were acquired from BioRad (Hertfordshire, UK).

BCA Protein Assay Kits (Peirce) and 10% and 4-12% Nu-PAGE Novex Bis-Tris protein gels were acquired from Thermo Fisher Scientific.

DNA primers were generated by Sigma-Genosys (Havrehill, UK).

Skimmed milk powder was obtained from (Oxoid, Thermo Scientific).

VECTASTAIN Elite ABC Kit, VectaShield Mounting Medium and DAB Substrate Kit were from Vector Laboratories (Peterborough, UK).

Triglyceride assay was obtained from Sentinel Diagnostics.

### 2.1.2 Buffers

All chemicals for buffers were obtained from commercial sources and were of at least reagent grade.

**SDS-PAGE Buffer** – 50 mM Tris-HCl, pH 8.4, 400 mM glycine, 0.1% (w/v) SDS.

**MOPS Buffer** – 100ml 20x MOPS, 900ml dd$H_2O$.

**Tris/Glycine Transfer Buffer** – 25 mM Tris, 192 mM glycine, 20% methanol.

**Sample Buffer** – 50 mM Tris-HCl, pH 7.4, 2.5% (w/v) SDS, 1% (v/v) β-mercaptoethanol, 10% glycerol, 0.05% (w/v) bromophenol blue.

**Homogenisation Buffer** – 50 mM Tris, pH 7.4, 50 mM sodium fluoride, 5mM sodium pyrophosphate, 1 mM EDTA, 250 mM mannitol, 1 mM dithiothreitol, 4 µg/ml trypsin inhibitor, 0.1 mM phenylmethylsulfonyl fluoride, 1 mM benzamidine.

**HBA** – 50 mM Hepes pH 7.4, 50 mM sodium fluoride, 5 mM sodium pyrophosphate, 1 mM EDTA, 10% (v/v) glycerol, 1 mM dithiothreitol, 4 µg/ml trypsin inhibitor, 0.1mM phenylmethylsulfonyl fluoride, 1 mM benzamidine.

**Hepes Lysis Buffer (HBA/1% Triton X-100)** – 50 mM Hepes pH 7.4, 50 mM sodium fluoride, 5 mM sodium pyrophosphate, 1mM EDTA 10% (v/v) glycerol, 1% Triton X-100 (v/v), 1 mM dithiothreitol, 4µg/ml trypsin inhibitor, 0.1 mM phenylmethylsulfonyl fluoride, 1 mM benzamidine.

**HGE –** 50 mM Hepes pH 7.4, 1mM EDTA 10% (v/v) glycerol, 1% Triton X-100, 1 mM dithiothreitol, 4µg/ml trypsin inhibitor, 0.1 mM phenylmethylsulfonyl fluoride, 1 mM benzamidine.

**Sodium Citrate Buffer** – 10 mM sodium citrate, 0.05% Tween 20, pH 6.0.

**Phosphate-Buffered Saline (PBS) –** 137 mM NaCl, 2.7 mM KCl, 4.3 mM Na2HPO4, 1.4 mM, KH2PO4, pH 7.4.

**PBS-Tween (PBT)** – PBS, 0.1% Tween20

**TAE** – 40 mM Tris, 20 mM acetic acid, 1 mM EDTA, pH 8.0

**Adipocyte media-** DMEM, 1g/L glucose, 25mM HEPES, sodium pyruvate, phenol red, 10% fetal bovine serum

**Adipocyte respiration media**- As above, no serum

### 2.1.3 Antibodies

The primary antibodies used in this work are listed in the table below.

*Table 2.1 Primary Antibodies*

*Abbreviations: WB, Western blotting; IHC, Immunohistochemistry; IP Immuno*

| Antibody | Raised in | Dilution | Supplier | Product no. | Application |
|---|---|---|---|---|---|
| **ACC** | Mouse | 1/1000 | Millipore | 05-1098 | WB |
| **pACC$^{Ser79}$** | Rabbit | 1/1000 | CST | #3661 | WB |
| **β-Actin** | Rabbit | 1/1000 | CST | #4968 | WB |
| **β-Actin** | Mouse | 1/1000 | Sigma | A3853 | WB |
| **pAMPKα$^{Thr172}$** | Rabbit | 1/1000 | CST | #2535 | WB |
| **AMPKβ1/β1 Sip2** | Rabbit | 1/1000 | In-house | N/A | IP |
| **AMPKγ1** | Rabbit | 1/1000 | Novus | Y308 | WB |
| **CD31/PECAM1** | Rabbit | 1/50 | Abcam | Ab28364 | IHC |
| **CKMT2** | Rabbit | 1/1000 | Abcam | Ab55963 | WB |
| **COXIV** | Rabbit | 1/1000 | CST | 3E11 | WB |
| **FLAG** | Rabbit | 1/1000 | CST | D6W5B | WB/IP |
| **GS** | Rabbit | 1/1000 | CST | 3893 | WB |
| **pGS$^{Ser7}$** | Sheep | 1/1000 | Dundee | N/A | WB |
| **Ki67** | Rabbit | 1/250 | Abcam | Ab16667 | IHC |
| **PGC1α** | Rabbit | 1/1000 | Abcam | Ab54481 | WB |
| **TOM20** | Rabbit | 1/200 | Santa Cruz | FL-145 | IHC/IF |
| **Total OXPHOS** | Mouse | 1/1000 | Abcam | Ab110413 | WB |
| **UCP1** | Rabbit | 1/1000 | Abcam | Ab10983 | WB |
| **Vinculin** | Mouse | 1/1000 | Sigma | V9131 | WB |

The secondary antibodies used in this work are listed below.

**Western Blotting (LI-COR imaging system):** IRDye 680LT Goat anti-Rabbit, IRDye800CW goat anti-Rabbit, IRDye 680LT Goat anti-Mouse, IRDye 800CW Goat anti-Mouse used at a dilution of 1/20,000, obtained from LI-COR Biotechnology (Cambridge, UK).

**Immunohistochemistry:** Biotinylated Goat anti-Rabbit, biotinylated Goat anti-Mouse, used at a dilution of 1/200. Obtained from Vector Laboratories LTD (Peterborough, UK)

**Immunofluorescence:** Goat anti-Rabbit, Alexa Fluor® 633 conjugate used at a dilution of 1/200. Obtained from Invitrogen, Thermo Scientific (Loughborough, UK).

### 2.1.4 Primers

DNA primers were designed using Primer Blast and ordered from Sigma-Genosys (Haverhill, UK). Those used in genotyping are displayed in Table 2.2 and those used for qPCR in table 2.3

*Table 2.2 Genotyping DNA Primers*

Abbreviations: WT, Wild type (non-Tg); Het, heterozygous; Hom, homozygous; bp, base pairs;

| Genotyping | Sequence 5'-3' | Product Size(s) (bp) |
|---|---|---|
| **AMPKγ1** | **F1 (across FLAG-tag)** GGACGACGATGACAAGTGAG<br>**F2** CACGTTTCCGACTTGAGTTG<br>**R** TAAGCCTGCCCAGAAGACTC | **WT**: 365<br>**Het**: 365 and 498<br>**Hom**: 498 |
| **Actin Cre** | **F** CGTACTGACGGTGGGAGAAT<br>**R** CCCGGCAAAACAGGTAGTTA | 178 |
| **IL2 (internal control, Cre)** | **F** CTAGGCCACAGAATTGAAAGATCT<br>**R** GTAGGTGGAAATTCTAGCATCATCC | 324 |

*Table 2.3 Quantitative PCR primers (Sybr)*

| qPCR Primers (Mouse) | Sequence 5'-3' | Product Size (bp) |
|---|---|---|
| **Agrp** | **F** ACAACTGCAGACCGAGCAGAA<br>**R** CGACGCGGAGAACGAGACT | |
| **Atp2a1 (SERCA)** | **F** ATTGGCAAGATCCGAGACCA<br>**R** GACAGGATCGTTGAAGTGGC | 156 |
| **Atp1a4 (NaKATPase)** | **F** TCACTTCTTCCTCTGGCTGG | 171 |

| | | |
|---|---|---|
| | **R** AGAACCGGAGATGGCATACG | |
| **Aqp1** | **F** CTGGCCTTTGGTTTGAGCAT<br>**R** CCACACACTGGGCGATGAT | 151 |
| **Cart** | **F** CGAATTCCGATCTACGAGAAGAA<br>**R** CCTGGCCCCTTTCCTCACT | 84 |
| **Casr** | **F** CTGACCAGCGAGCCCAAAA<br>**R** GCTGCTACTCCAAAATGGATAGG | 73 |
| **Ckmt2** | **F** CTCACGGGCAGTTTGATGAG<br>**R** GATCCTGCTCCGTCATCTCA | 201 |
| **Cox4i1** | **F** TGGGAGTGTTGTGAAGAGTGA<br>**R** GCAGTGAAGCCGATGAAGAAC | 273 |
| **Eno3** | **F** TGCGTCCACTGGCATCTAC<br>**R** CAGAGCAGGCGCAATAGTTTTA | 151 |
| **Enac** | **F** CAGCCTAGAAACTCCCTGCT<br>**R** CTGGGCTAGAACGGAAGGAT | 210 |
| **Fas** | **F** TGCTCCCAGCTGCAGGC<br>**R** GCCCGGTAGCTCTGGGTGTA | 107 |
| **Gapdh** | **F** AGGTCGGTGTGAACGGATTTC<br>**R** TGTAGACCATGTAGTTGAGGTC | 123 |
| **Hprt** | **F** CAGTCCCAGCGTCGTGATTA<br>**R** TGGCCTCCCATCTCCTTCAT | 168 |
| **Myog** | **F** GGAAGTCTGTGTCGGTGGAC<br>**R** CCTCGAAGGCCTCATTCACT | 84 |
| **Neb** | **F** GCTGGATGTATGGCACTGTG<br>**R** GCCCTGGTGTACTGAAGTCT | 154 |
| **Npy** | **F** GTGTTTGGGCATTCTG<br>**R** TTCTGTGCTTTCCTTCAT | 193 |
| **Pgc1α** | **F** TATGGAGTGACATAGAGTGTG<br>**R** CCACTTCAATCCACCCAGAAA | 134 |
| **Pkd1** | **F** TCTGGATGGGCTTCAGCAA<br>**R** AGCGGGAAGGCAGTGGAT | 172 |
| **Pkd2** | **F** AGACTTCTCGGTGTATAACGCAAA<br>**R** CACCCGTTGCTGGGAACT | 77 |

| | | |
|---|---|---|
| **Polr2a** | **F** CTTCTCTCCCAGTGCTGCAT<br>**R** GGGGATGTATGGGCTTGAGG | 115 |
| **Pomc** | **F** TATGAAAACGCCCCCAGAAC<br>**R** CGGGAGAACAAGTTTCATTTCC | 72 |
| **Pparγ** | **F** TGAAAGAAGCGGTGAACCAC<br>**R** AGCTGATTCCGAAGTTGGTG | 119 |
| **Tnnc2** | **F** GCTGCCTTTGACATGTTCGA<br>**R** GTCCACCTCCTCGATGATGG | 129 |
| **Ucp1** | **F** AGCCATCTGCATGGGATCAAA<br>**R** GGGTCGTCCCTTTCCAAAGTG | 103 |

## 2.2 Animal Studies

### 2.2.1 Declaration

All experiments involved in the generation of transgenic animals were approved by Gothenburg Ethics Committee. All *in vivo* studies were performed in accordance with the UK Animals (Scientific Procedures) Act (1986) and approved by the Animal Welfare and Ethical Review Board at Imperial College London.

### 2.2.2 Animal Models

The animal strains used in these studies are listed below, with associated nomenclature.

***Table 2.4 Animal Models***

| Strain | Nomenclature | Source |
|---|---|---|
| **C57BL/6J** | Bl6 | The Jackson Laboratory (JAX) |
| **129sv** | 129sv | Envigo |
| **Prkag1-AMPKγ1-WT$^{flox/STOP/flox}$/β-Actin Cre** | WT-Tg | AstraZeneca, Mölndal, Sweden |
| **Prkag1-AMPKγ1-D316A$^{flox/STOP/flox}$/β-Actin Cre** | D316A-Tg | AstraZeneca, Mölndal, Sweden |

| | | |
|---|---|---|
| **Prkag1-AMPKγ1-D316A$^{flox/STOP/flox}$/CAGGCre$^{ERT}$** | D316A-Tg$^{TMX}$ | AstraZeneca, Mölndal, Sweden/JAX |
| **129sv/Prkag1-AMPKγ1-D316A$^{flox/STOP/flox}$/β-Actin Cre** | D316A-Tg$^{129sv}$ | Envigo/AstraZeneca, Mölndal, Sweden/JAX |

### 2.2.3 Diet Administration

Unless otherwise stated, all animals were maintained on an RM3 chow breeding diet (Special Diet Services, Essex UK), with a nutrient profile of 11.48% energy from oil, 27.28% from protein and 61.24% from carbohydrate. High-fat diet was obtained from TestDiet (St. Louis, US), with 46.1% calories from fat, 18.1% from protein and 35.8% from carbohydrates.

Unless otherwise stated, animals were group housed in individually ventilated cages and fed *ad libitum* and weighed weekly when on an experimental protocol as per licence requirements.

### 2.2.4 Blood sampling

Animals were weighed, warmed (tail vein only) and blood samples of less than 100µl taken from either the tail vein or saphenous vein whilst animals were restrained. Terminal blood samples were taken via cardiac puncture under terminal anaesthesia (isofluorane). Blood was collected in a heparin coated tube, centrifuged to separate serum from red blood cells and stored at -80$^{o}$C. Whole blood for VetScan analysis was used fresh and never frozen.

### 2.2.5 Glucose Tolerance

Animals were weighed prior to fasting to calculate glucose dose. Animals were then fasted overnight. Animals were warmed to 38$^{o}$C to dilate the tail vein, prior to a pre-GTT bleed of 150µl from the lateral tail vein. Glucose was injected IP at time-point zero and blood samples of approximately 10µl were taken 15, 30, 60 and 120 minutes following initial warming. Animals were then fed 120 minutes after glucose injection. Glucose concentrations were measured using a glucose assay (Sigma), or using a glucometer.

### 2.2.6 Comprehensive Laboratory Animal Monitoring System (CLAMS)

Animals were singly housed for one week prior to entry, to acclimatise to housing conditions. Animals were fed *ad libitum* in all studies using this system. Animals were weighed prior to being placed into designated cages, with even distribution of genotypes between each rack. All studies conducted began on a Monday morning, and ended on the following Friday, with animals then checked on the Friday evening. Recordings were taken at 22 minute intervals between these times. Raw files generated were used to extract $VO_2$, $VCO_2$, XTOT (horizontal movement) and ZTOT (vertical movement), along with calculated RER. Measurements for $VO_2$ and $VCO_2$ were calculated by built in software (Oxymax) and normalised to bodyweight prior to extraction, to give a unit of ml/kg/h. Un-normalised values were also extracted for additional analysis, to remove bodyweight as an additional variable, given that animals maintained on a high-fat diet were divergent with respect to genotype.

### 2.2.7 Feeding studies (BioDAQ)

To monitor food intake in HFD-fed animals, mice were singly housed in BioDAQ food intake monitoring cages (Research Diets Inc.), measuring the ad libitum feeding activity over a period of one week. Mice were fed the same 45% HFD from gated hoppers mounted outside of the cage to reduce variability. Data was recorded using the BioDAQ DataViewer.

### 2.2.8 Ultrasound and Echocardiogram

Animals were anaesthetised using isofluorane and placed on their back with a rodent face mask securely placed to ensure constant delivery of anaesthesia during the procedure. The abdomen was then shaved and colourless, warmed ultrasound gel applied to the skin and to the transducer before scanning. Kidneys were imaged with VisualSonics Vevo®LAZR System, using the liver as a marker of orientation and density.

### 2.2.9 ECGenie (Electrocardiogram)

The ECGenie was acquired from Mouse Specifics, Inc. (MA, US). This equipment features interchangeable, disposable footplate electrodes on a recording platform, designed to rapidly acquire an ECG trace from awake, unrestrained rodents. Animals were weighed, placed onto the recording platform and an ECG recording taken for sufficient time to ensure a complete trace. ECG recordings were then interpreted using

EzCG software supplied by Mouse Specifics Inc. with data extracted pertaining to the PQRST interval and heart rate for each animal. Studies performed by Laura Wilson.

### 2.2.10 Tamoxifen Administration for the Induction of D316A-Tg Expression

Tamoxifen was purchased from Sigma-Aldrich and dissolved in corn oil at a concentration of 20mg/ml overnight at 37°C in the dark (foil wrapped). Solubilised Tamoxifen was stored at 4°C until day of use. On the day of administration, the solution was warmed to 37°C to ensure suspension. Mice were weighed and injected intraperitoneally with 150µl Tamoxifen/corn oil once every 24 hours for 4 consecutive days. Injected mice were housed separately from un-injected controls to avoid transfer of Tamoxifen through skin contact. Expression of D316A-Tg protein was confirmed by Western blotting up to 8-weeks post-induction.

### 2.2.11 Genotyping

To identify animals positive for both the AMPK-D316A-FLAG gene and Cre recombinase, ear biopsies were taken at 3 weeks of age. Biopsies were digested in 0.5M NaOH and heated in 10 minute cycles at 100°C. Samples were then neutralised using 0.5M Tris, pH8.

Primer sets were designed to amplify both the wild type and the FLAG-tagged sequences (Table), allowing detection of both heterozygous and homozygous animals. DNA from digested samples was amplified by PCR using Bioline Reddymix (2x Reddymix master mix containing Taq DNA polymerase, ThermoScientific). DNA preparations were separated and analysed by agarose gel electrophoresis on a 2% agarose gel made with tris-acetate-EDTA (TAE) containing 0.2µg/ml ethidium bromide for 50 minutes at 120v, resulting in two detectable bands, the larger indicating the presence of the FLAG sequence and the smaller the endogenous AMPKγ1. Primer sequences were also designed to detect Cre recombinase expression (Table). An IL2 internal control was used for this PCR to distinguish between a Cre negative sample and a failed PCR reaction.

In addition to initial genotyping, post mortem tail biopsies were collected to confirm the genotype of each animal used for study.

## 2.3 General Methods

### 2.3.1 Dissection and tissue preservation

All terminal bleeds were taken via cardiac puncture under terminal anaesthesia (PJM). Mice were culled using an overdose of anaesthesia (Isofluorane) followed by cervical dislocation, or using rising concentrations of $CO_2$ in a designated chamber, followed by cervical dislocation (AP). Organs were dissected, weighed, halved and placed into either 4% paraformaldehyde for histology, or snap frozen in liquid nitrogen for later homogenisation. For cryostat sectioning, samples were frozen in OCT freezing medium and stored at -80$^{o}$C.

### 2.3.2 Homogenisation of whole tissue

Frozen tissues were weighed, thawed and homogenised using an Ultra-Turrax homogeniser in 10x w/v ice cold homogenisation buffer containing 50mM Tris, 50mM NaFl, 5mM NaPP, 1mM EDTA and 0.25M mannitol. Phosphatase inhibitors (1mM DTT, 157µg/ml benzamidine, 4µg/ml trypsin inhibitor and 0.1mM PMSF) were added immediately before use.

Homogenates were centrifuged at 13,000rpm for 15 minutes to separate the soluble fraction, which was then removed and stored separately. Protein content of soluble fractions was quantified using a BCA assay. Sample were diluted 1 in 20 with dd$H_20$ and 25µl was added to 200µl BCA working reagent and incubated at room temperature for 15 minutes. Absorbance was read at 542nm and quantified using a BSA standard curve. Samples were stored at -80$^{o}$C until use.

For RNA extraction, samples were thawed on ice to preserve RNA integrity, weighed and homogenised in 1ml/100mg Trizol reagent. For adipose studies, samples were then stored overnight at -20$^{o}$C to remove the lipid fraction, which was then stored at -80$^{o}$C for future work if required.

### 2.3.3 RNA extraction

To 1ml homogenate, 200µl chloroform was added (400µl for adipose) and mixed at room temperature for 15 minutes, then centrifuged at 13000rpm for 15 mins. The clear aqueous phase was transferred to an RNAse-free Eppendorf and 0.53 x volume of ethanol absolute was added. The preparations were then transferred to RNAeasy Mini Columns (Qiagen) and spun at 13000rpm for 1 minute. Columns were then washed using buffer RW1, followed by brief centrifugation at 13000rpm. Columns were then

washed twice with buffer RPE (diluted). RNA was eluted in 50µl RNase free $H_2O$ and quantified using the Nanodrop photospectrometer. Samples were frozen at -80$^oC$ until use.

### 2.3.4 cDNA synthesis

To obtain cDNA from RNA preparations, 3µg RNA was incubated with 1µl random hexamers (50ng/µl), 1µl 10mM dNTP mix and DEPC $H_2O$ to 10µl. Samples were incubated at 65$^oC$ for 5 minutes on a thermal cycler. 10µl cDNA synthesis mix (containing 2µl 10xRT buffer, 4µl 25mM $MgCl_2$, 2µl 0.1M DTT, 1µl RNase Out and 1µl Superscript II (Qiagen)) was added to each sample and cycled as follows: 10mins 25$^oC$, 50mins 85$^oC$, then onto ice until cool. 1µl RnaseH was added to each sample and incubated at $37^0C$ for 10mins.

### 2.3.5 Quantitative polymerase chain reaction (qPCR)

To check primer linearity, 5µl cDNA from each sample were pooled and serially diluted to give a standard curve. To quantify gene expression, specific primers were designed to the sequence of DNA corresponding to the gene of interest. For each PCR reaction, 5µl cDNA was added to 10µl 2x SYBR-HiROX (Bioline), 1.6µl forward and reverse primer mix and $ddH_2O$ to a total reaction volume of 20µl. The qPCR plate was analysed using an Opticon thermal cycler with Opticon monitor software to generate c(t) values for each reaction.

To quantify gene expression, c(t) value replicates were checked for primer efficacy (%) and consistency. Average c(t) values were then calculated for each sample, and quantified using a linear equation (y=mx+c) previously determined from the standard curve, corresponding to the gene of interest. The equation was solved for X, with Y as c(t) value. This value was then transformed using 10^X, as the standard curve was generated on a logarithmic scale. This process was repeated for all genes, including a designated housekeeping gene. The choice of housekeeping gene was particularly important when comparing genotypes with an additional variable, namely diet, as many common housekeeping genes were altered between diet and genotype with one factor clearly influencing the other. Unless otherwise stated, all experiments were normalised to Polr2a, an RNA polymerase which has been shown to remain stable across dietary interventions.

Gene expression was then presented as both a ratio to the expression of the housekeeping gene for the experiment, and as fold change over the designated control.

### 2.3.6 Gel electrophoresis and Western blotting

Fifty micrograms of protein from homogenised tissue samples was added to 5x sample buffer and heated above 70$^{o}$C, with the exception of protein for mitochondrial analysis, which were not boiled according to the Abcam data sheet. Samples were loaded into a 10% SDS PAGE or 4-12% Bis-Tris gel and run at 200v for 60 minutes. Separated proteins were transferred to a PVDF membrane (Millipore Immobilon-FL Transfer membrane, pore size 0.45uM) at 100v for 90 minutes. Membranes were Ponceau stained to check transfer and blocked in 4% BSA for 1 hour at room temperature. Primary antibodies were diluted 1:1000 unless otherwise stated in 4% BSA-TBS-T (10mM Tris-HCl pH 7.4, 150mM NaCl, 0.1% Tween-20) and incubated with the membrane for 4 hours at room temperature or overnight at 4$^{o}$C. Membranes were then washed in TBS-T and incubated with a fluorescent secondary antibody (LI-COR) for 1 hour at room temperature. Fluorescence was imaged using the Odyssey Imaging System (LI-COR Biosciences) and quantified using ImageStudio 4.0.

### 2.3.7 Immunohistochemistry

Upon dissection, organs were harvested, weighed and placed in 4% paraformaldehyde for 24hours, then transferred first to 50% then 70% ethanol. Samples were then wax embedded and sectioned to a thickness of 4 microns. Slides were rehydrated using Acquaclear, 100% and 70% EtOH and boiled in sodium citrate antigen retrieval solution (for 1L: 2.96g sodium citrate (Sigma-Aldrich), 5ml 10% Tween-20, to 1L with dd$H_2O$) for 5 minutes in a pressure cooker. Antigen retrieval was not required for PAS and H+E stains.

#### *2.3.7.1 DAB staining*

Sections were then incubated for 20 minutes with 0.3% $H_2O_2$ to block endogenous peroxidase activity, washed with PBS and blocked for 1 hour with 10% normal goat serum in PBS (NGS-PBS) at room temperature. Sections were then incubated overnight at 4$^{o}$C with primary antibody at a predetermined concentration. Sections were washed three times with PBS-tween (0.1%) and incubated with biotinylated goat secondary antibody for 1 hour at room temperature in a humidified chamber. Samples

were then stained using Vectastain DAB reagent, counterstained with haematoxylin and dehydrated in 70%, 100% EtOH and Acquaclear. Dehydrated slides were then mounted using DPX mounting liquid.

*2.3.7.2 Periodic Acid-Schiff (PAS) and Haematoxylin and Eosin (H+E)*

All PAS and H+E staining was performed by Lorraine Lawrence (Imperial College London Histology), with the exception of haematoxylin-only staining of adipose tissue.

For PAS staining, sections were deparaffinised as described above, and immersed in Periodic Acid Solution (Sigma-Aldrich) for 5 minutes at room temperature. Slides were then rinsed and immersed in Schiff's reagent (Sigma-Aldrich) for 15 minutes at room temperature. Slides were then washed in running tap water for 5 minutes and counterstained with Gill's Haematoxylin Solution (No.3) for 90 seconds, rinsed, dehydrated, cleared and mounted using DPX mounting liquid.

*2.3.7.3 Immunofluorescence*

Tissues were deparaffinised and antigen retrieval performed as described previously. Slides were washed in TBS and non-specific binding blocked by incubation with 0.2% (w/v) fish skin gelatin (FSG) for 1 hour at room temperature. Sections were then incubated with primary antibody at an assay dependent concentration in 0.2% FSG overnight at 4$^{o}$C. Slides were washed in TBS-Tween (0.1%) and incubated with an Alexa Fluor conjugated secondary antibody (488 green or 633 red) for 1 hour at room temperature. After subsequent washes with TBS-T, sections were incubated with DAPI to stain nuclei for 5 minutes, rinsed under running water and mounted using VectaShield immunofluorescent mounting medium. Immunofluorescence-stained sections were imaged using a Leica TCS SP5 confocal microscope at 200Hz, with a 200x (dry) 400x and 630x (oil immersion) optical zoom and analysed using LASAF software (Leica).

### 2.3.8 Glycogen Assay

To assess the accumulation of glycogen in harvested tissues, 100ul 60% KOH was added to 100uL of tissue homogenate in homogenisation buffer and heated to 100$^{o}$C for 1 hour. Samples were allowed to cool before adding 1ml 100% EtOH and 2µl 4M LiCl and left to precipitate at 4$^{o}$C overnight. Samples were centrifuged at 3000g for 30mins and the supernatant discarded. Pellets were resuspended in 50µl 4M HCl and boiled for 90 minutes. Samples were neutralised with 50µl 4M $K_2CO_3$ and the glucose

content quantified using a Glucose Oxidase Kit (Sigma-Aldrich). Briefly, 25µl tissue digest was added to 100µl assay reagent made according to manufacturer's instructions. After 15 minutes, the reaction was stopped using 100µl $H_2SO_4$ and the plate read at 540nm. In addition to tissue samples, a glycogen standard curve was also taken through the assay to ensure the assay worked correctly and to allow the quantification of glucose from a known amount of glycogen. A glucose standard curve was also used to quantify the amount of glucose produced from each reaction.

## 2.3.9 Enzyme Linked ImmunoSorbent Assay (ELISA)

### *2.3.9.1 Leptin*

Mouse Leptin ELISA kits were purchased from CrystalChem (Netherlands, Cat# 90030). Serum samples to be used for ELISA protocols was separated from red blood cells by centrifugation as described previously. Serum samples were defrosted on ice whilst the plate was prepared according to manufacturer's instructions. In brief, the supplied, antibody-coated microplate was assembled, washed and prepared using 45µl sample diluent, 50µl guinea pig anti-mouse leptin serum and 5µl of sample or working mouse leptin standard per well. The plate was then incubated overnight at 4$^{o}$C, washed and 100µl of anti-guinea pig IgG enzyme conjugate added to each well. The plate was then incubated for 3 hours at 4$^{o}$C, washed thoroughly and 100µl enzyme substrate solution applied for 30 minutes at room temperature, avoiding light exposure. The enzyme reaction was stopped with the provided enzyme reaction stop solution. Absorbance was measured at A450, with A630 values subtracted, and leptin concentration calculated from the resulting standard curve, using a higher-grade polynomial.

### *2.3.9.2 Adiponectin*

Mouse Adiponectin ELISA kits were purchased from CrystalChem (Netherlands, Cat# 80569). Serum samples were defrosted on ice and diluted 1:10000 according to the supplied protocol. 100µl of diluted sample, control or undiluted standard were added to each well of the supplied antibody-coated microplate and incubated for 1 hour at room temperature. Wells were then aspirated, washed and 100µl antibody-POD conjugate added. The plate was then shaken at 350rpm for 1 hour at room temperature. Wells were washed as before,100µl of substrate solution added and the plate incubated at room temperature, avoiding exposure to light, for 30 minutes. The reaction was stopped using 100µl stop solution and the absorbance measured at

A450, with A620 values subtracted. Adiponectin concentrations were calculated from the resulting standard curve, using a higher-grade polynomial and multiplying by the dilution factor (10,000) to give a final concentration in ng/ml.

#### *2.3.9.3 Insulin*

Ultra-Sensitive Mouse Insulin ELISA kits were purchased from CrystalChem (Netherlands, Cat# 90080). Serum samples were defrosted on ice whilst the plate was prepared according to manufacturer's instructions. The supplied, antibody-coated microplate was assembled and prepared using 95µl sample diluent and 5µl of sample or working mouse leptin standard per well. The plate was then incubated for 2 hours at 4ºC, washed and 100µl of anti-insulin enzyme conjugate added to each well. The plate was then incubated for 30 minutes at room temperature, washed thoroughly and 100µl enzyme substrate solution applied for 40 minutes at room temperature (low/wide range assay), avoiding light exposure. The enzyme reaction was stopped with the provided enzyme reaction stop solution. Absorbance was measured at A450, with A630 values subtracted, and leptin concentration calculated from the resulting standard curve, using a higher-grade polynomial.

#### *2.3.9.4 Homeostatic Model Assessment (HOMA-IR and HOMA-B)*

The HOMA-IR and HOMA-B for chow and HFD-fed mice were calculated from fasting glucose measurements (mmol/L) and fasting serum insulin concentrations (ng/ml converted to µU/L) as per the following equations:

HOMA-IR: (Fasting insulin x Fasting glucose) / 22.5

HOMA-B: (20 x Fasting insulin) / (Fasting glucose – 3.5)

### 2.3.10 Triglyceride Assay

To measure liver triglyceride content, 200mg wet tissue (snap frozen at harvest) was homogenised in 10x volume of 100% EtOH and incubated overnight at 4ºC to extract lipid. Following extraction, 500µl was removed and diluted into 1ml EtOH and mixed overnight at 4ºC. A further 500µl were taken and diluted as before, followed by centrifugation at 13000rpm for 10 minutes. The cleared supernatant was transferred to a fresh 1.5ml Eppendorf for analysis using a Triglyceride TG enzymatic colorimetric assay (Sentinel Diagnostics, Cat# 17624) according to manufacturer's instructions. In brief, triglycerides liquid was warmed to room temperature and a standard curve

constructed from a 143mg/dl triglyceride stock. In a 96-well flat bottomed plate, 2.5µl sample was added to 10µl PBS and 300µl triglyceride liquid. The plate was incubated at 37ºC for 10 minutes with gentle shaking, and absorbance read at 546nm. Total triglyceride content was determined as % of tissue wet weight using the standard curve.

### 2.3.11 Immunoprecipitation (for Western blotting)

AMPK was immunoprecipitated for the detection of FLAG-tagged protein by Western blotting. Lysate of 100µg total protein was added to 10µl of 50% protein-A sepharose (Sigma), 2µl of a 1/10 dilution of Sip2 antibody (AMPKβ) and made up to a volume of 200µl with homogenisation buffer. Samples were vortexed at 4ºC for 1.5-3 h and centrifuged at 13000g for 1 minute to pellet the immune complexes. The resulting pellet was washed once with homogenisation buffer and once with HGE and the remaining buffer removed with a Hamilton syringe. Samples were then solubilised in sample buffer for Western blot analysis for FLAG expression.

## 2.4 RNA sequencing

### 2.4.1 RNA Extraction and Quality Assessment

RNA was extracted from brown adipose, white adipose (subcutaneous), skeletal muscle (gastrocnemius) and liver from 6 WT-Tg and 6 D316A-Tg mice, fed a high fat diet for 16 weeks, as described previously and quantified using the Nanodrop photospectrometer. A total of 2µg of RNA in 60µl RNase-free $H_2O$ per sample were sent to AstraZeneca (Mölndal, Sweden) for quality assessment using a BioAnalyzer RNA kit (Agilent CA, US). An RNA Integrity Number (RIN) score of >7 was required for sequencing.

### 2.4.2 RNA Sequencing Analysis Pipeline

RNA-Seq FASTQ files were received from Mölndal and initial quality control checks performed (Appendices-Fastq QC) using FastQC to assess overall read quality, %GC content and sequence duplication. Reads were mapped to the mouse genome mm10 using STAR alignment tool. Generated BAM (Binary Alignment Map) files were then viewed in an interactive genome viewer (IGV) to confirm alignment. As a quality control step at this point, the D316A mutation was confirmed in all 6 D316A-Tg samples from each tissue sequenced. All WT-Tg samples were confirmed by a correct AMPKγ1 sequence in all samples. BAM files were then converted to a counts table and quality

assessed to confirm sufficient coverage along genes, and to identify any unmapped reads. and values normalised using DESeq2 to account for gene length, variation in library size and any batch effects that may affect analysis. Outliers were identified and removed (dispersion plot), as well as those with a consistently high P value. A principle component analysis was then generated as a quality control step, to assess the clustering of samples in terms of gene expression. A list of differentially expressed genes was generated, expressed as Log2 fold change over the control sample (WT-Tg), with an adjusted P value for each gene.

### 2.4.3 Manual annotation with Online Gene/Pathway Analysis

Using original DESeq2 output Excel files, genes were listed in order of Log2FC, with an adjusted p value threshold of 0.05 and a biological threshold of +/-1.5 FC over WT-Tg. Genes with a high fold change were then manually annotated for function using the Ensembl Gene ID to search the GeneCard database, which combines known gene IDs with aliases and descriptions of function from other online databases such as UniProt to provide detailed information on gene function and annotated pathways.

### 2.4.4 Ingenuity Pathway Analysis

The resulting tables of differentially expressed genes were uploaded into Ingenuity Pathway Analysis (IPA) (Qiagen Bioinformatics, US). IPA licence (Qiagen) was provided by AstraZeneca (Cambridge, UK). All data sets were uploaded and thresholds set to exclude genes with an adjusted p value greater than 0.05. A biological threshold was not set for this analysis. Pathway, gene annotation and upstream regulation analyses were exported to Excel for presentation and further interpretation and graphical presentation.

## 2.5 Mitochondrial respiration in subcutaneous white adipocytes

### 2.5.1 White adipocyte isolation (whole cell suspension)

Mice for mitochondrial isolation were culled using rising concentrations of $CO_2$ followed by cervical dislocation. Bodyweights were recorded and biopsies taken for post-mortem genotyping. White subcutaneous (inguinal) adipose tissue was removed from the dorsal lumbar region of the animal, weighed and washed twice in ice-cold HBSS. WATsc pads were pooled with respect to genotype, with 3-4 animals used per genotype per experiment. Pooled adipose was then minced in a 6cm petri-dish using sharp dissecting scissors until resembling a fine paste. Minced adipose was then

transferred to a 15ml Falcon tube containing 9.8ml HBSS, 0.2ml 50mg/ml Collagenase type II and 0.025g BSA, warmed to 37ºC. The adipose was digested at 37ºC for 30-40 minutes, passed through a 100µm filter and mixed 1:1 with warmed suspension medium (DMEM modified with HEPES, 1g/L glucose (low), L-glutamine, sodium pyruvate, 10% FBS and phenol red) (ThermoFisher, Cat# 12320032). The resulting cell suspension was kept at 37ºC during transport. Studies using this cell suspension were conducted in collaboration with the laboratory of Professor Michael Duchen at University College London (Mitochondrial Biology, Anatomy Building, UCL, UK).

### 2.5.2 Mitochondrial respiration (OROBOROS O2K)

All mitochondrial respiration studies described were conducted using an OROBOROS Oxygraph-2K high-resolution respirometer (OROBOROS instruments Corp., Austria). On arrival, cells were maintained at 37ºC whilst air calibration of the Oxygraph was performed, using respirometry medium (DMEM as previously described, with omission of 10% FBS). Cells were centrifuged at 500g for 10 minutes to remove serum and lipid (which are known to interfere with O2K measurements), whilst maintaining cell integrity. The resulting pellets were resuspended in 5ml respirometry medium as described previously. Cells were counted using a haemocytometer and counts fed to the DatLab O2K software for normalisation. To begin recording, 2.5ml cell suspension were added to each chamber, with WT-Tg and D316A-Tg run in parallel to provide an accurate comparison. Basal respiration was established approximately 15 minutes after closing the chambers, with an average taken over 5 minutes.

**PA Response:** To establish a response to the addition of palmitate, sodium palmitate (Sigma) was solubilised in 50% EtOH to give a stock 50mM solution and conjugated to ultra-fatty acid-free BSA in a ratio of 6:1 overnight at 37ºC prior to the day of use. The palmitate solution (PA) was warmed to 37ºC and injected into the O2k chambers to a final concentration of 0.25M using a Hamilton syringe. Peak oxygen consumption in response to PA was recorded for each addition.

**Mitochondrial Stress Test:** To assess the mitochondrial function of intact white adipocytes, cell suspensions were then treated with compounds to manipulate the mitochondrial respiratory chain as follows.

1. Leak respiration: To inhibit ATP synthase and establish leak respiration, 1µl of a 1mM Oligomycin stock was injected into each chamber after PA response was established and respiration returned to basal.
2. Maximum uncoupled flux: To assess the maximum uncoupling potential of mitochondria in this system, 1µl of a 5mM stock of the protonophore FCCP was injected into each chamber. FCCP facilitates the movement of protons across the mitochondrial membrane, thus uncoupling oxygen consumption from ATP synthesis.
3. Complex I inhibition: To establish complex I contribution to oxygen consumption, 1µl of a 1mM stock of the complex I inhibitor rotenone was injected into each chamber.
4. Total mitochondrial respiration inhibition (Complex III): To establish a value for non-mitochondrial respiration, 1µl of a 1mM stock of the complex III inhibitor Antimycin A was injected into each chamber.

Data was quantified within the DatLab software and analysed in Microsoft Excel. Non-mitochondrial respiration values were subtracted from all readings prior to interpretation. For each measurement, a minimum of three separate biological replicates were performed, with 3-4 animals pooled per replicate on separate days. All values were normalised to cell number within the chamber, and then to protein concentration of the final cell suspension, using a BCA protein assay.

## 2.6 Statistical analyses

All data in figures presented as mean ± standard error of the mean (SEM). Differences between datasets were analysed by one-tailed Student's t tests with statistical significance defined as a p value of 0.05 or less. To compare three or more data sets, a one-way analysis of variance (one-way-ANOVA) was used, followed by Bonferroni's range test to measure significance between means. To compare the interaction between two variables with two or more groups per variable (e.g. Effect of diet and genotype on gene expression), a two-way analysis of variance (two-way ANOVA) was performed, followed by a Bonferroni's Multiple Comparisons Test to determine statistical significance between groups based on one variable. For the analysis of CLAMS metabolic cage data, animal weights were used to calculate oxygen consumption and carbon dioxide production in ml/kg/h only when bodyweight was not significantly different. For analysis of animals with difference in bodyweight, an

analysis of co-variance (ANCOVA) was performed. For RNA sequencing analyses, an adjusted p value threshold was determined at 0.05, normalised using DEseq2. All other statistics were performed using GraphPad Prism 7 software.

# 3 CHAPTER 3: METABOLIC CONSEQUENCES OF GLOBAL AMPK ACTIVATION

In the current global epidemic of diet and lifestyle-induced obesity, the need for therapeutic intervention has never been stronger. However, the complexity and multifactorial nature of this disease makes the identification of molecular targets an inherently difficult task. Laboratory models of obesity and the metabolic syndrome, such as the use of a high fat diet, have proved useful tools to begin to determine cause and effect relationships between behaviour, hormonal signalling and functional alterations on a cellular level. The use of transgenic models to mimic therapeutic intervention under these conditions remains a promising proof of principle approach to drug design, however, these models are not without limitation, and translation to human remains a significant unmet need. With these thoughts in mind, characterisation of the D316A-Tg mouse began on a standard laboratory chow diet, to examine the effect of AMPK activation under normal, non-stressed conditions.

During the course of this work, several cohorts of chow fed animals were monitored for bodyweight, total body composition, feeding behaviour and energy expenditure. At termination, full tissue harvests were performed to assess tissue weight, morphology and lipid content. Within each cohort, animals were sufficiently age-matched to reduce age-related variability such as adiposity and insulin sensitivity, and blood samples were taken throughout studies to evaluate hormone levels and other circulating factors. This chapter introduces the main findings from these experiments, prior to the investigation into the effects of metabolic stress, in the form of high fat diet feeding.

## 3.1 Mouse Model Characterisation

### 3.1.1 Genotyping Strategy

Experimental animals, both WT-Tg and D316A-Tg were chosen based on heterozygous or homozygous expression of the FLAG-tagged transgene, and the expression of cre recombinase (materials and methods; genotyping). Previous studies in our laboratory (Woods et al., 2017) revealed no difference in total AMPKγ1-Tg expression or complex activity between heterozygotes and homozygotes, nor any phenotype separating the WT-Tg from non-transgenic animals. Using this information, both heterozygous and homozygous animals were used for this work, using non-

transgenic animals as a negative control when assessing expression of the AMPKγ1-transgenic protein in later investigations.

### 3.1.2 Confirmation of AMPKγ1-D316A Transgenic Protein Expression *in vivo*

The feasibility of using this global activating mutant relied on the successful, ubiquitous expression and activity of the D316A-Tg AMPK complex *in vivo.* The addition of a FLAG tag allowed detection of the transgenic protein using a number of experimental techniques, including Western blotting and immunoprecipitation, from dissected whole tissue lysates.

Initial confirmation of FLAG expression was carried out on twelve tissues, comparing D316A-Tg to a non-transgenic wild type control. Expression of FLAG tagged AMPKγ1 was then determined by Western blotting, using a primary antibody raised to the FLAG

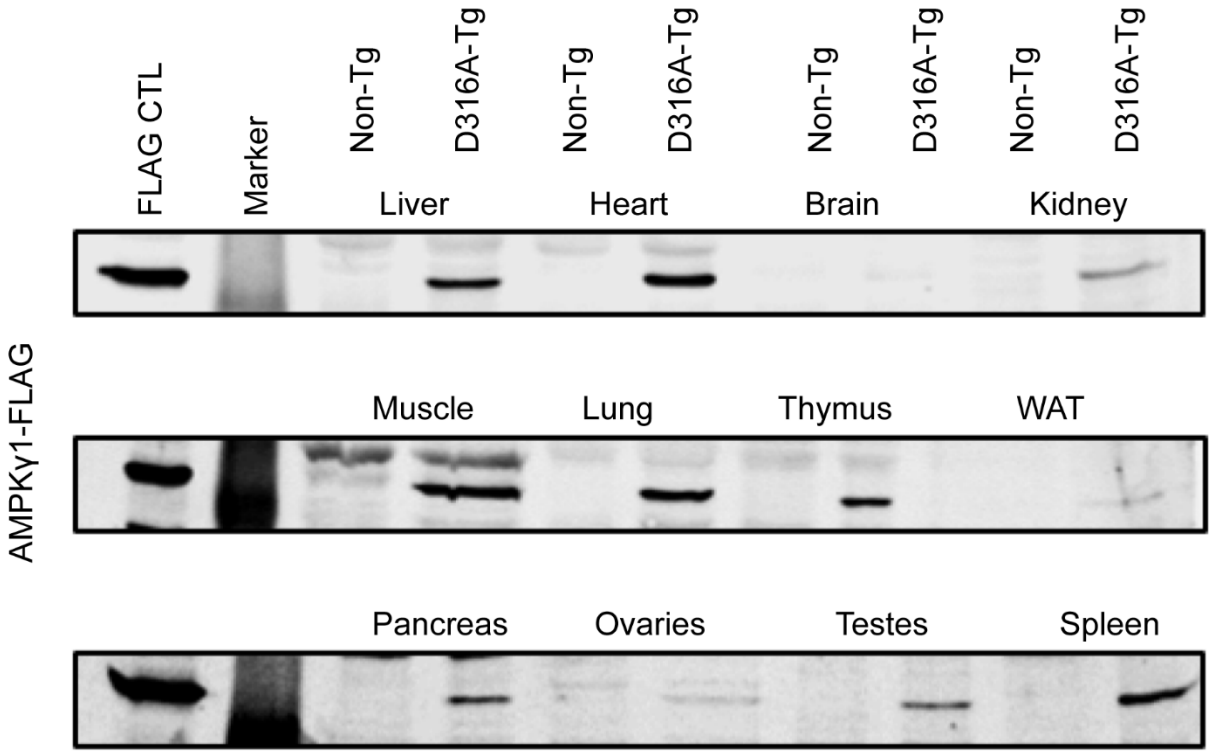



***Figure 3.1 Detection of D316A-Tg FLAG-tagged protein expression in isolated tissues.***

*Western blot highlighting presence or absence of FLAG expression in 12 tissues from non-Tg and D316A-Tg chow-fed mice.*

*FLAG-tagged AMPKγ1 expressed in HEK293 cells (Robin Willows) was used as a positive control.*

peptide epitope, and an appropriate secondary antibody, to enable detection and quantification using the LI-COR Odyssey imaging system.

Using this method, expression of FLAG was confirmed in all tissues chosen (Fig3.1) with the exception of whole brain lysate, which initially presented a strong, non-specific band at approximately 30kda. A subsequent Western blot with increased protein loading was then used to confirm expression in this tissue (Fig 3.2).

As noted previously during initial characterisation of the D316A-Tg in the liver-specific model, the wild type transgenic AMPKγ1 subunit replaced almost all of the endogenous protein, whereas the D316A-Tg protein replaced approximately 50% (Fig 3.2). This was observed in the heart and brain of the global mutant, though is most likely true in all tissues expressing these transgenic proteins. The reasons for this remain unclear; it has been hypothesised that the D316A-Tg protein is perhaps less stable, or is simply a weaker binding partner for the AMPKα and β subunits during complex formation. This was not found to increase total AMPK activity in WT-Tg as shown in hepatocytes (Woods et al., 2017).

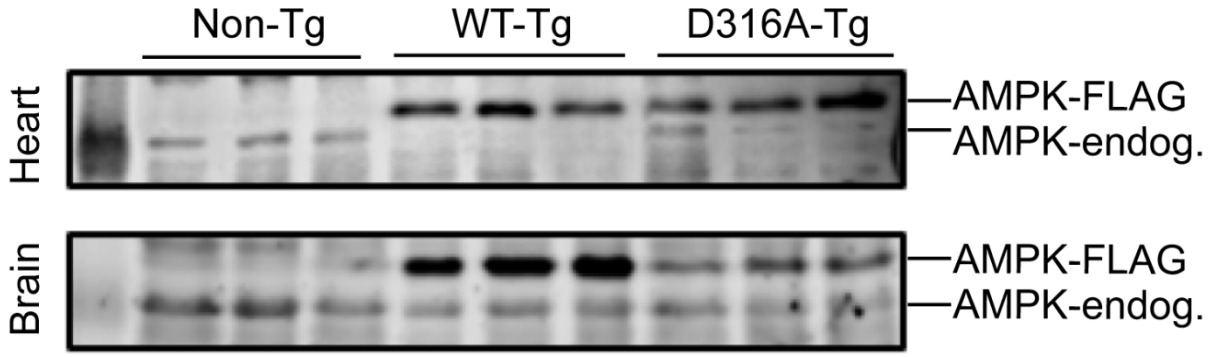



***Figure 3.2 Detection of endogenous AMPKγ1 (AMPK-endog.) and FLAG-tagged WT-Tg and D316A-Tg protein.***

*Western blot analysis of AMPKγ1-FLAG protein expression in whole heart and brain lysates. Non-Tg heart and brain lysates were used as both a positive control for endogenous AMPKγ1 expression and as a negative control for γ1-FLAG.*

Together, these results suggest that although the WT-Tg protein is more efficient at replacing the endogenous γ1 subunit, this does not lead to an increase in total AMPK expression, as the total amount of AMPK complex formed is limited by the amount of the α and β subunits available. Previous studies using this mutation have not found any differences in total AMPK complex formation between WT-Tg and D316A-Tg.

Having confirmed the wide-spread expression of the D316A-Tg protein, attention was then turned to a more in-depth analysis of tissue weight and morphology, as well as metabolic characterisation of the model *in vivo*. The results of these studies are separated into two chapters, as they present fascinating yet distinct phenotypes of this novel mouse model.

## 3.2 Metabolic Phenotyping of the D316A-Tg Mouse Model

### 3.2.1 Bodyweight and total body composition on a chow diet

To establish whether activation of AMPK had an effect on bodyweight gain, chow fed animals were weighed once weekly from 8 weeks of age. Over a subsequent period of 8 weeks, no significant differences in bodyweight were observed between WT-Tg and D316A-Tg animals (Fig 3.3A).

During this period, animals were scanned using echo MRI, to quantify fat and lean mass *in vivo*. At 16 weeks of age, there were no significant differences between genotypes in either parameter, indicating a normal level of adiposity and total lean mass in the D316A-Tg model on a chow diet (Fig 3.3B).

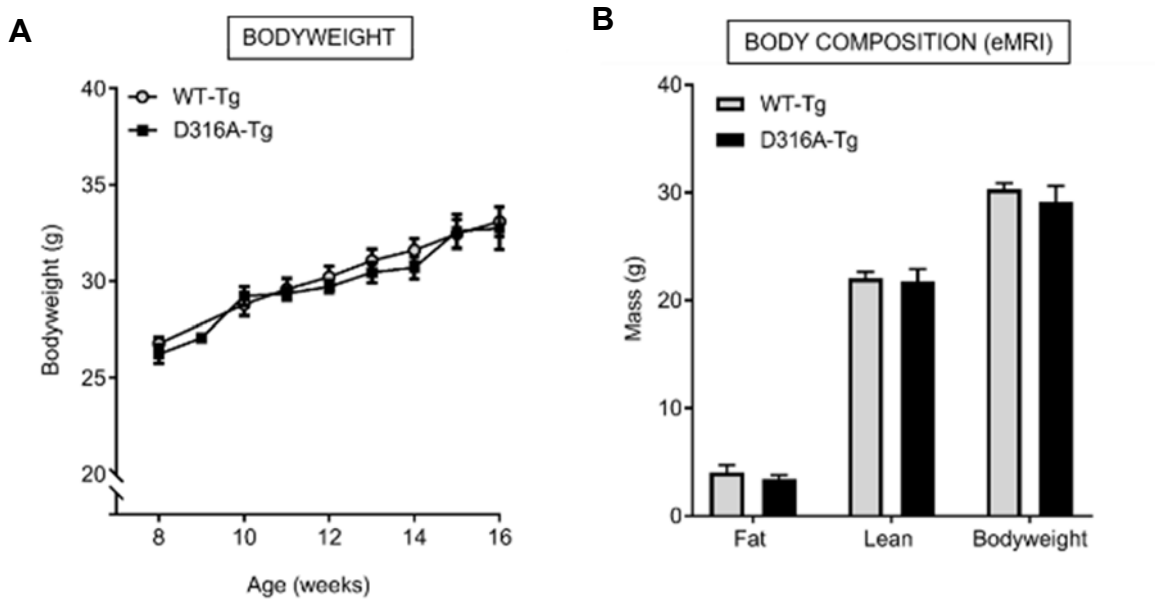



***Figure 3.3 Bodyweight and total body composition on a chow diet.***

***A)*** *Growth curve of WT-Tg and D316A-Tg chow-fed male mice, measured over a period of 8 weeks. Data combined from 3 separate cohorts. N=20, 19.*

***B****) Total body composition of 16-week old WT-Tg and D316A-Tg chow-fed male mice as assessed by echo MRI. N=7, 7. Data are presented as mean ±SEM.*

### 3.2.2 Food intake (chow)

From the monitoring of bodyweight and adiposity in this model, no indications of age-related obesity were observed. However, due to the global expression of the D316A mutation and ubiquitous nature of AMPKγ1 versus γ2, it is possible that any increase in bodyweight through hyperphagia may be compensated for by an increase in energy expenditure in a number of metabolic tissues, a hypothesis previously discussed by Yavari et al. Therefore, to examine the feeding behaviour of D316A-Tg animals on a chow diet, animals were supplied with standard RM3 chow diet, weighed prior to administration. After seven days, food was removed and re-weighed. This pattern was repeated to give a three-week period of food intake measurement. Daily intake was calculated for each week individually, then combined to give an average daily food intake for each genotype. These data indicate no significant difference in food intake between WT-Tg and D316A-Tg animals (Fig 3.4) using this method.

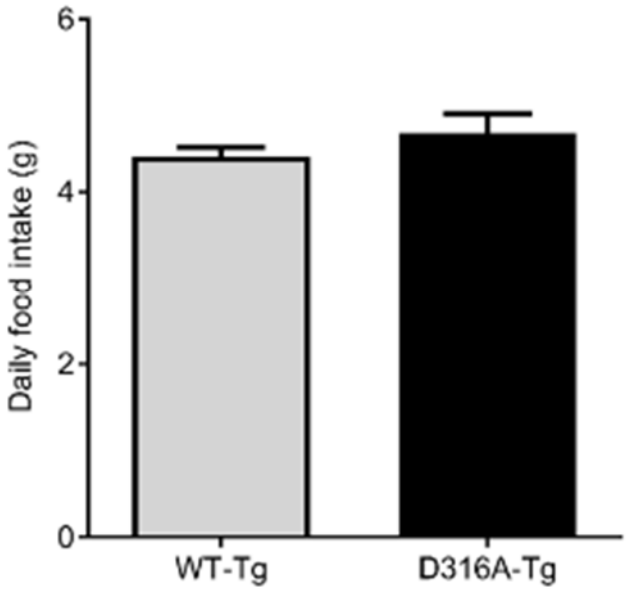



***Figure 3.4 Daily food intake on a chow diet.***

*Average daily food intake of 12-week old chow-fed WT-Tg and D316A-Tg male mice. Food intake was measured over a 3-week period, with food weighed before administration and remaining food re-weighed after 7 days. Average daily intake was then calculated for each week individually and averaged. N=6, 6*

When taking into consideration the equivalence in bodyweight and fat mass, in conjunction with normal feeding behaviour, it may be concluded that activation of AMPKγ1 under the β-Actin promotor does not induce the hyperphagic, obese

phenotype seen in the AMPKγ2 R299Q knock-in model. This observation, however, raises an important question as to whether the D316A-Tg AMPK complex is expressed in the arcuate nucleus (ARC) of the hypothalamus, implicated in the central regulation of energy homeostasis and appetite regulation (Morton et al., 2006). Due to the non-specific nature of FLAG-staining in immunohistochemistry, it was not possible to identify regions of expression in the brain using this method.

In the R299Q AMPKγ2 mouse model, hyperphagic behaviour was reported to be driven by ghrelin-responsive neuronal populations in the ARC, leading to an increase in Agrp activity and a concurrent increase in food intake (Yavari et al., 2016). In this model, both Agrp and Npy gene expression was upregulated in the ARC, with no significant difference in Pomc between wild type and homozygotes.

To investigate the expression of these genes in the D316A-Tg mouse model, qPCR was performed on the whole hypothalamus from four WT-Tg and four D316A-Tg female animals maintained on a chow diet (qPCR performed by Dr. Luis Martins). Though not statistically significant, there was a clear trend towards an increase in both Npy and Pomc mRNA expression in the hypothalamus of D316A-Tg mice. A modest increase in Agrp expression was also observed, with no difference in the expression of CART (Appendices Fig 6.1). Repetition of this experiment with increased animal numbers, as well as the use of both male and female animals, are required to determine the significance of these findings.

### 3.2.3 Glucose Homeostasis (chow)

Due to AMPK being implicated in glucose metabolism, particularly in the context of insulin sensitisation and glucose uptake, glucose handling was evaluated *in vivo* using a glucose tolerance test (GTT), performed on 16-week old male, chow fed mice.

At this time-point, no differences in glucose tolerance were observed; both WT-Tg and D316A-Tg blood glucose levels rose to between 20 and 25mmol/L within 15 minutes of glucose administration, and baseline was reached in both genotypes by 120 minutes with similar clearance profiles (Fig 3.5A).

To determine the effect of AMPK activation on insulin production, 5 WT-Tg and 5 D316A-Tg male animals were subjected to an overnight fasting period, after which a small blood sample was taken (<150µl). Food was then re-administered, and a further

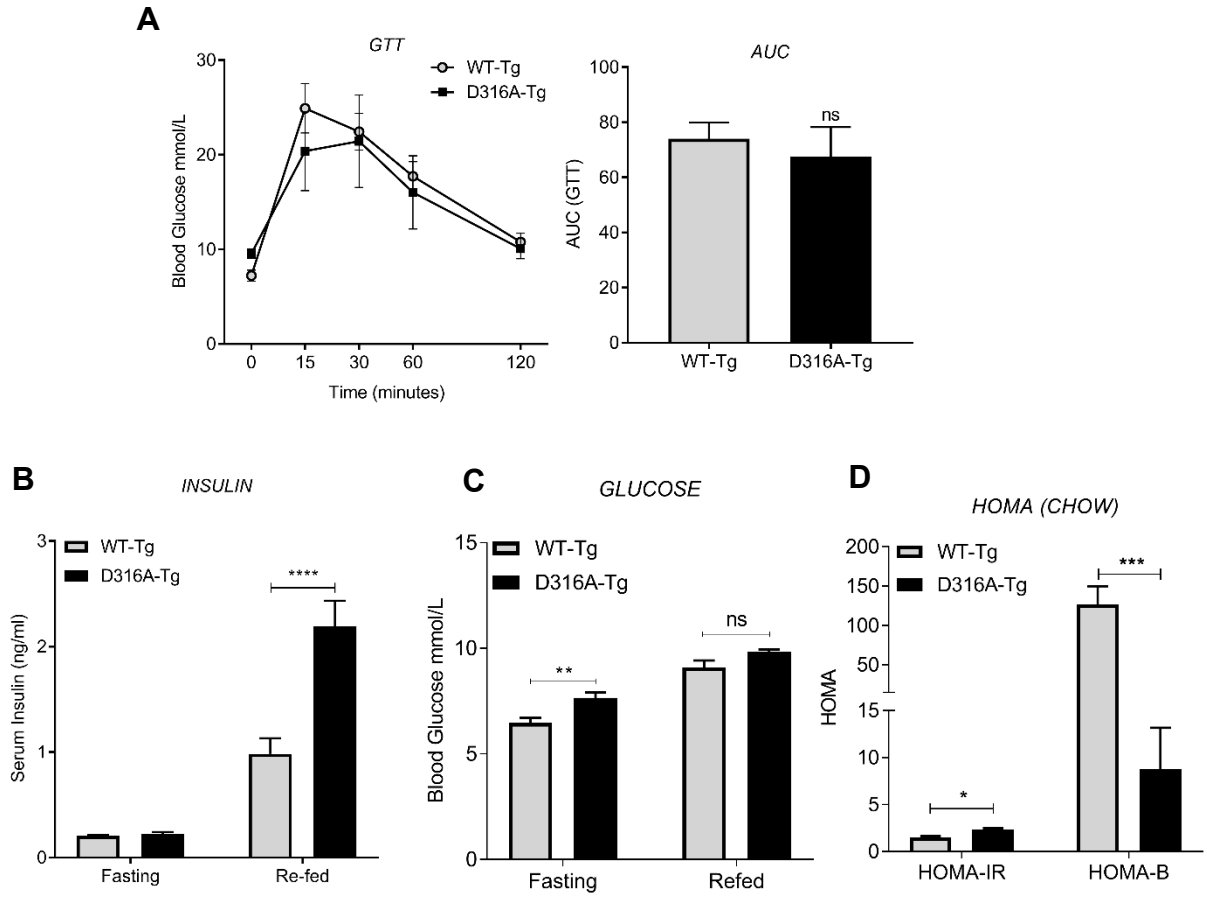



***Figure 3.5 Glucose homeostasis in the D316A-Tg mouse model on a chow diet.***

***A)*** *Glucose tolerance test (GTT) performed on 12-week old male WT-Tg and D316A-Tg fasted chow-fed mice, with AUC. N=5, 4*

***B)*** *Serum insulin concentrations of fasted, refed and ad libitum chow-fed male mice as measured by ELISA. N=5, 8. Data are presented as mean ±SEM. **P<0.01, ****P<0.0001*

***C)*** *Fasting and refed blood glucose of chow-fed mice. N=5, 8. Data are presented as mean ±SEM. **P<0.01, ****P<0.0001*

***D)*** *HOMA-IR and HOMA-B calculated from fasting insulin and fasting glucose measurements of 12-week old male WT-Tg and D316A-Tg chow-fed mice. N=5, 8. Data are presented as mean ±SEM. **P<0.01, ****P<0.0001*

blood sample taken two hours later. Both sample sets were analysed using CrystalChem ELISA kit to quantify total serum insulin concentration.

No differences in serum insulin were observed between WT-Tg and D316A-Tg animals in the fasted state (Fig 3.5B), though blood glucose measurement in this state was significantly higher in the D316A-Tg group (Fig 3.5C). Insulin levels relative to

glucose were calculated as both Homeostatic Model Assessment-IR (HOMA-IR) and HOMA-B to assess insulin resistance and pancreatic beta cell function respectively (Fig 3.5D). A small but significant increase in HOMA-IR was observed in D316A-Tg mice, suggestive of moderate insulin resistance, with a highly significant reduction in beta cell function as suggested by HOMA-B in D316A-Tg chow-fed mice.

After 2 hours of feeding, both genotypes displayed an increase in serum insulin, with the D316A-Tg exhibiting and increase in excess of 2-fold over that seen in WT-Tg animals (Fig 3.6C). This result was somewhat surprising, given previous literature suggesting an impairment in insulin secretion in models of AMPK activation. However, the high re-fed circulating insulin did not correspond to an excessive lowering of blood glucose (Fig 3.6B), suggesting that this model is capable of sufficient glucose clearance, and is not insulin-intolerant. No differences were observed in animals fed *ad libitum*, though there was a trend towards decreased circulating insulin in D316A-Tg animals.

### 3.2.4 Tissue weight (chow)

Thus far, no overt differences in any *in vivo* parameter had been identified on a standard chow diet. This, too, proved true for gross tissue morphology; initial harvest did not reveal any other significant differences in organ weight, colour, appearance or dimension (Fig 3.6). Data from the studies described thus far suggest that D316A-Tg

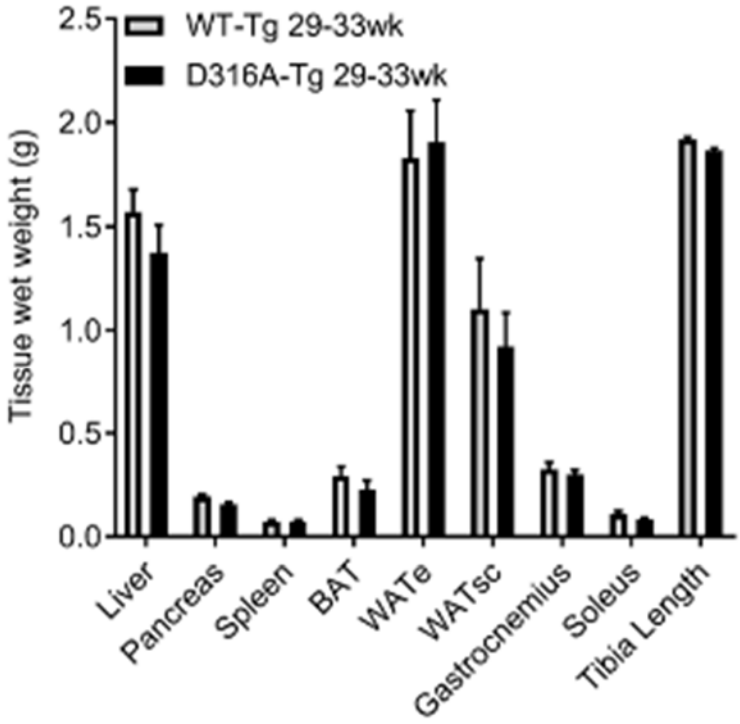



***Figure 3.6 Terminal tissue weights of chow-fed WT-Tg and D316A-Tg mice***

*Tissue weights from WT-Tg and D316A-Tg chow-fed mice at 29-33 weeks of age (n=7, 7). * P<0.05, Data are presented as mean ±SEM.*** P<0.001.*

mice do not exhibit any significant metabolic phenotype. Therefore, to interrogate this model under conditions of metabolic stress, a high fat diet (45% calories from fat) was administered.

### 3.2.5 Bodyweight and total body composition (HFD)

To investigate the effects of AMPK activation on bodyweight, HFD was administered to WT-Tg and D316A-Tg male mice from 8 weeks of age and animals weighed weekly. Data from each cohort were combined to produce a final bodyweight curve from 8 to 16 weeks of HFD-feeding (Fig 3.7A). A separate cohort of HFD-fed female mice were also found to be protected from DIO (Fig 3.7B). All subsequent studies were performed on male animals unless otherwise stated.

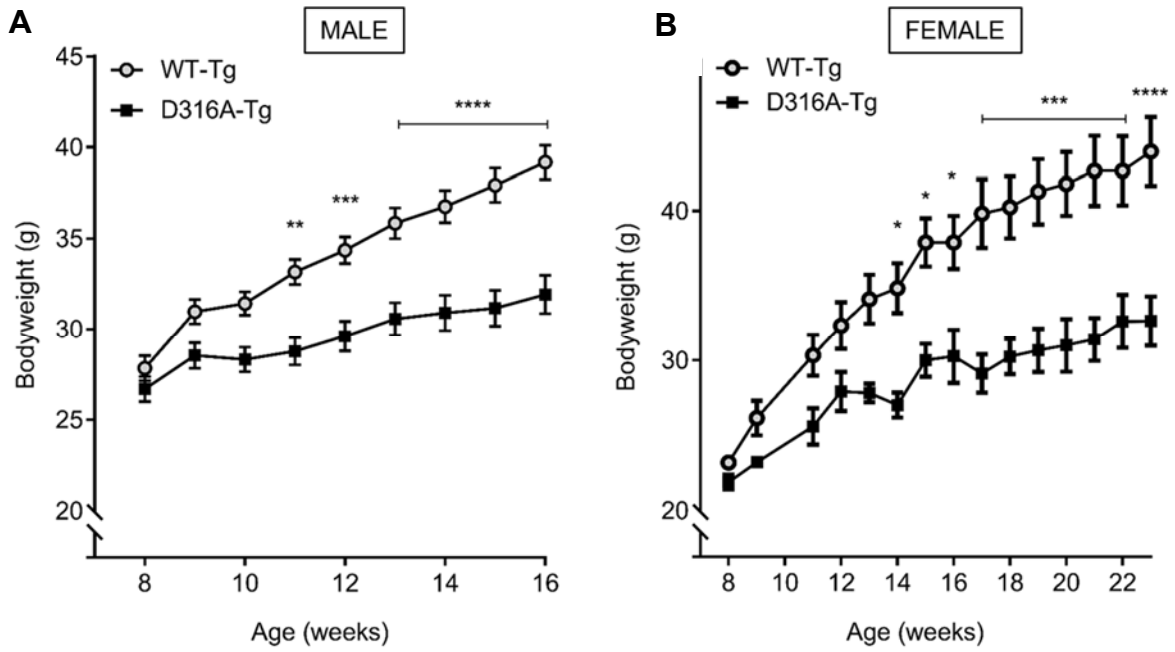



***Figure 3.7 Protection from HFD-induced obesity exhibited by D316A-Tg mice***

***A)*** *Bodyweight curve of WT-Tg and D316A-Tg male mice fed a HFD from 8 weeks of age. N=27, 17, Data are presented as mean ±SEM.**P<0.01, ***P<0.001, ****P<0.0001.*

***B)*** *Bodyweight curve of WT-Tg and D316A-Tg female mice fed a HFD from 8 weeks of age. N=8, 5 Data are presented as mean ±SEM.**P<0.01, ***P<0.001,*

In all cohorts, chronic, global AMPK activation provided complete protection from diet-induced obesity. Wild type animals gained between 3 and 5 grams within the first week of HFD-feeding, with D316A-Tg mice gaining between 1 and 2, similar to that of a chow-fed mouse. This trend was followed for the remainder of the time-course, with D316A-Tg mice consistently gaining 1 to 2 grams per week, and their WT-Tg counterparts gaining approximately 2-4 grams per week. After 4-5 weeks of HFD-feeding, D316A-Tg mice were significantly lighter, and no bodyweight convergence

was observed, with D316A-Tg mice remained on a growth curve similar to that of a chow fed animal until termination.

In addition to a reduction in bodyweight, HFD-fed D316A-Tg mice at harvest appeared significantly leaner, with no excess adiposity as seen in WT-Tg controls (Fig 3.8B). Total body composition was therefore assessed *in vivo* using echo MRI in mice fed HFD for 8 weeks (Fig 3.8A). Data shown are of animals scanned at 8 weeks on a HFD, and are representative of all time-points measured.

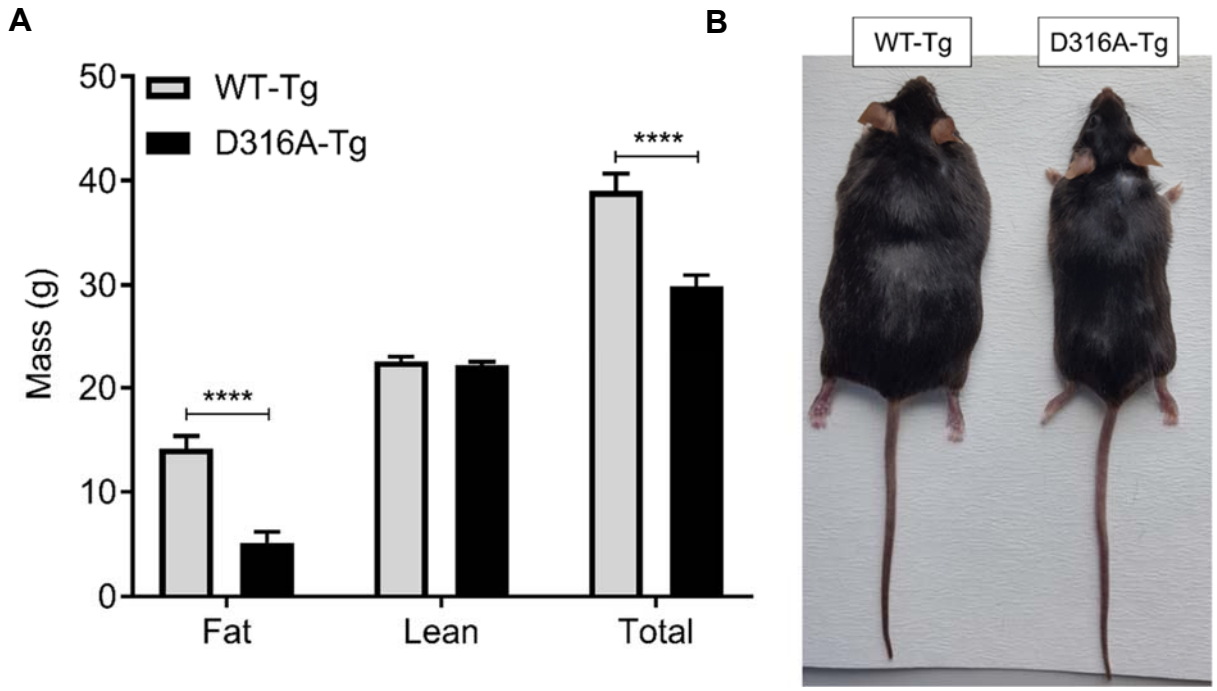



***Figure 3.8 Total body composition of D316A-Tg mice on a HFD.***

***A)*** *Total body composition of 8-week HFD-fed (16-week old) male mice, as assessed by echo MRI. N=8, 7 Data are presented as mean ±SEM.****P<0.0001.*

***B)*** *Representative image of WT-Tg and D316A-Tg 24-week HFD fed (32-week old) male mice at harvest.*

These findings were reflected in terminal tissue weights (Fig 3.13), with significant reduction in liver weight and subcutaneous white adipose (WATsc) mass after 16 and 28 weeks of HFD-feeding. Tissue weights were not presented as a ratio to bodyweight (Appendices, Fig 6.1) as the reduction in bodyweight is entirely due to a reduction in fat mass, not in total body size, as assessed by eMRI in Fig 3.8.

Whilst brown adipose tissue was significantly reduced when analysed separately from other tissues by an unpaired t-test, the total variation in this tissue when compared to that of WATsc or liver was too great to maintain statistical significance in a two-way ANOVA with a multiple comparisons test. Nevertheless, these results suggest that all tissues that become lipid-laden during the progress of obesity are protected from lipid accumulation in the D316A-Tg mouse model, as no differences in lean mass were observed using eMRI (Fig 3.8).

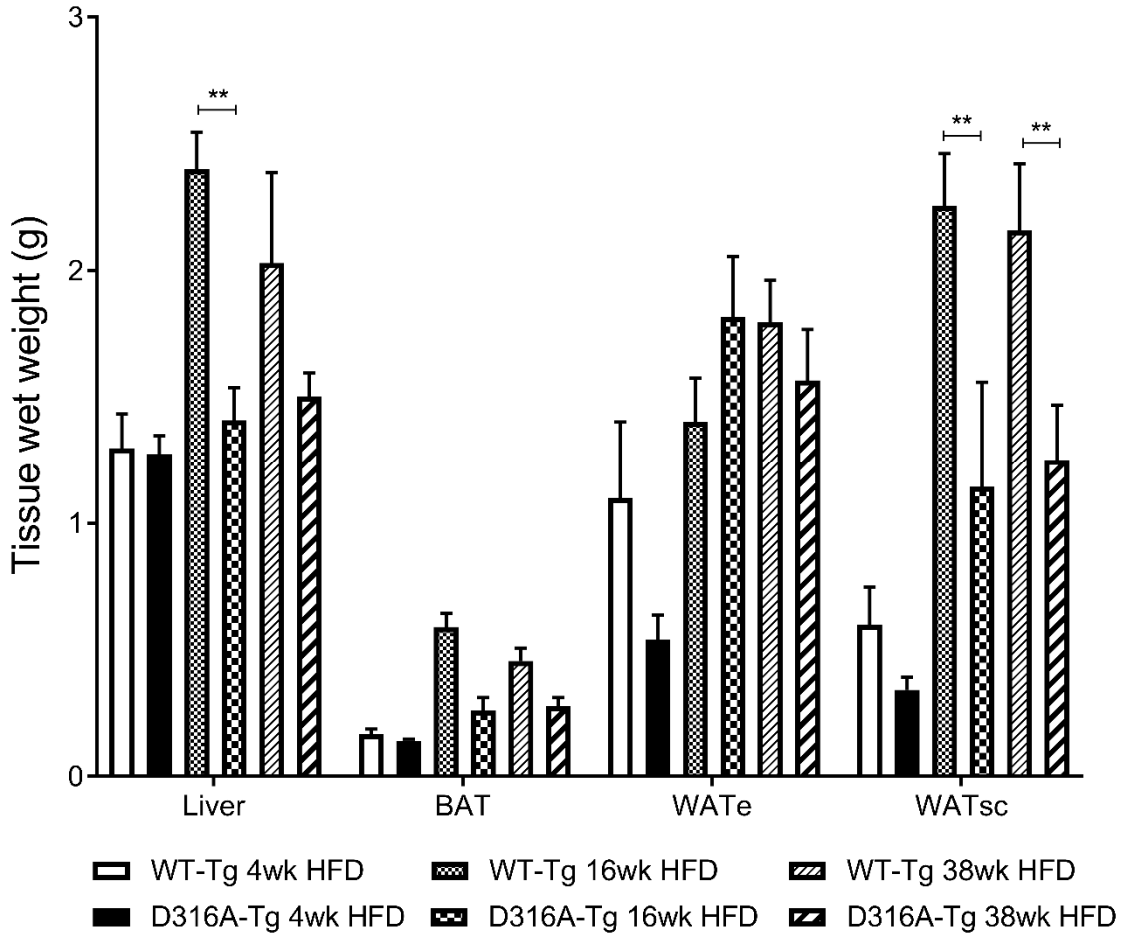



***Figure 3.9 Terminal tissue weights from HFD-fed male WT-Tg and D316A-Tg mice.***

*Tissue weights from 4-week, 16-week and 38-week HFD-fed mice at harvest. 2-way ANOVA with Bonferroni multiple comparisons test was used to determine statistical significance. N=7, 7 (4-week HFD, 12-weeks old). N=8, 6 (16-week HFD, 24-weeks old). N=9, 8 (38-week HFD, 46-weeks old) Data are presented as mean ±SEM. **P<0.01.*

A key feature in the pathogenesis of obesity is the development of hepatic steatosis, or fatty liver. To confirm whether the reduction in liver weight and absence of pale colouration seen in the HFD-fed D316A-Tg mouse model was due to a protection from lipid accumulation, livers from 28-week HFD-fed male mice were paraffin-embedded, sectioned and stained with haematoxylin and eosin (H&E) to observe morphology.

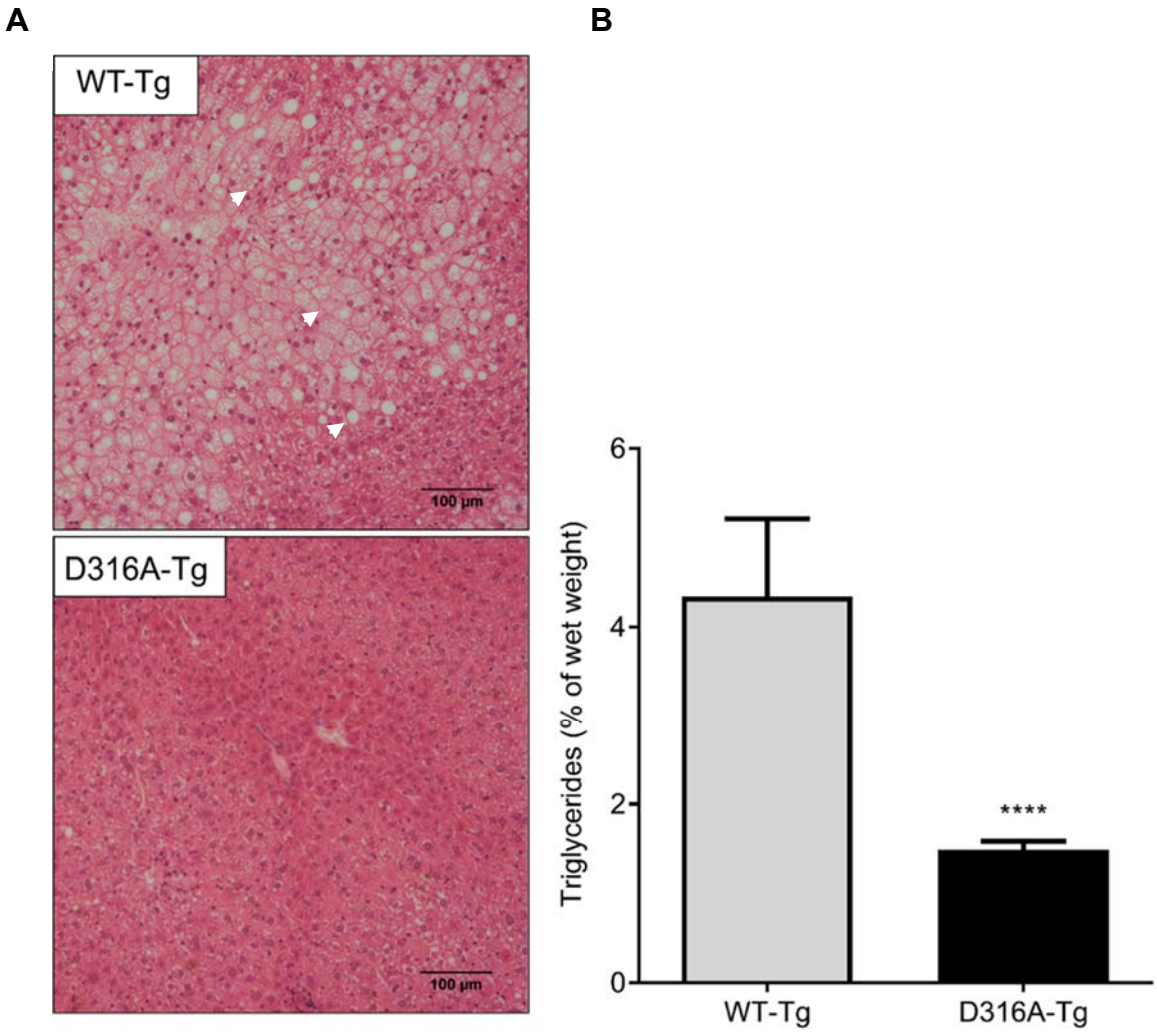



***Figure 3.10 Protection from HFD-induced hepatic steatosis.***

***A)*** *H&E staining of livers from WT-Tg and D316A-Tg mice fed a HFD for 28 weeks. WT-Tg livers are lipid laden, with most hepatocytes containing multilocular lipid droplets (white arrows). Images taken at 10x magnification, scale bar 100µm.*

***B)*** *Quantification of total liver triglyceride content after 28 weeks of HFD feeding (36-weeks old), as a percentage of wet tissue weight. N=9, 9 Data are presented as mean ±SEM.****P<0.0001 student's unpaired t-test.*

WT-Tg livers were found to contain many lipid droplets (white arrows), indicative of the development of hepatic steatosis (Fig 3.10A). In contrast, D316A-Tg livers did not show any lipid accumulation at this time-point. These findings were reflected in the

subsequent quantification of liver triglycerides (Fig 3.10B), with D316A-Tg livers displaying an approximate 75% reduction in total triglyceride content.

A key determinant of the progression of obesity is the balance of food intake with energy expenditure. No differences were observed between WT-Tg and D316A-Tg mice fed a chow diet, suggesting that activation of AMPKγ1 does not alter feeding behaviour. However, it was hypothesised that activation of AMPK in this model may protect from HFD-induced hyperphagia, which would in turn protect, at least in part, from HFD-associated obesity.

### 3.2.6 Food intake (HFD)

The ingestion of highly palatable lipid-dense foods has been shown to stimulate hyperphagia in rodent models of obesity, and is a significant driving force behind the accelerated progression of obesity in overweight human populations (Sharma et al., 2012). It was therefore of interest to continue to investigate the feeding behaviour of D316A-Tg mice on a high-fat diet, despite a lack of phenotype on a chow diet, as the introduction of high-fat content food in the presence of chronic AMPK activation may reveal a previously unidentified axis for the predisposition to HFD-induced hyperphagia and obesity.

This hypothesis was investigated using an automated feeding system (BioDAQ) to establish whether, in addition to any changes in quantity consumed, there were any significant differences in feeding patterns, including meal timing, number of meals and amount consumed per meal.

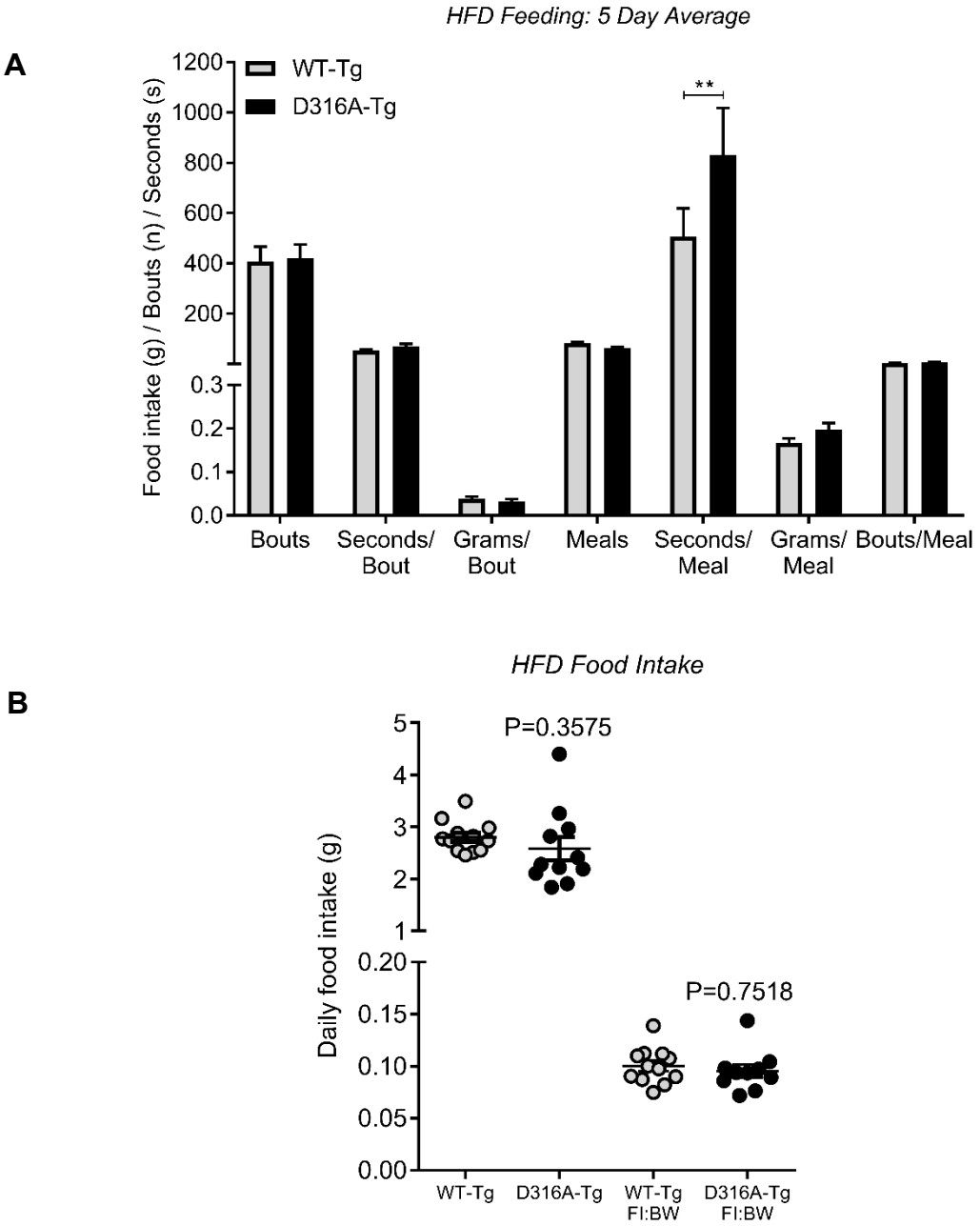



***Figure 3.11 Daily food intake and feeding behaviour of D316A-Tg mice on a HFD.***

***A)*** *BioDAQ automated food monitoring system output analysis of 4 -week HFD-fed WT-Tg and D316A-Tg mice at 12 weeks of age. A bout represents an uninterrupted period of feeding. Seconds per bout indicates the average time (s) of each bout. Grams per bout indicates average food consumption (g) per bout. A meal is defined as a period of food intake, consisting of several bouts, separated by a minimum 5-minute interval. Meals represents an average number of meals per day. Seconds per meal defines the average length of time spent eating per meal. Grams per meal defines the total amount of food consumed on average per meal. All averages calculated over a 5-day period, represented as an average per genotype.*

***B)*** *Average daily food intake over a 5-day period, displayed as raw food intake (FI) and normalised to bodyweight. N= 10, 12, Data are presented as mean ±SEM.**P<0.01.*

Animals were singly housed for one week prior to entry into the BioDAQ automated feeding system, where 45% HFD was provided *ad libitum* via external feeding hoppers connected to computer-monitored scales to provide accurate weight measurement over the course of the experiment. Episodic measurements were also taken pertaining to the number of times animals accessed the food, the length of time spent feeding and the time between feeding bouts. Total food intake per 24 hours was also calculated for each animal after data were extracted. Animals were monitored for a total of 5 days, with bodyweight measurements taken before entry and after extraction.

D316A-Tg mice displayed normal feeding behaviour, comparable to their WT-Tg counterparts in all but one parameter, with equivalent number of bouts, amount of food consumed per bout (Fig 3.11A) and total food intake (Fig 3.11B). However, D316A-Tg mice spent, on average, 5.3 minutes longer at the food hopper (meal (s)), though this was not reflected in the amount of food in grams eaten in the same meal, nor in the number of bouts per meal.

In addition to routine monitoring, a fast-refeed experiment was performed to assess food intake in response to a period of fasting. Significant differences were observed between D316A-Tg and WT-Tg HFD-fed mice only with respect to seconds per meal, as seen previously in animals fed *ad* libitum.

### 3.2.7 Glucose handling and hormonal signalling (HFD)

Though no differences were observed in either *ad libitum* food intake nor consumption in response to fasting, samples were evaluated for circulating factors associated with alterations in adiposity; insulin, leptin, adiponectin and glucose. Although these factors are often linked to change in feeding behaviour, many studies have also demonstrated a link between serum concentrations and adiposity in the context of obesity.

AMPK signalling is commonly described as a downstream mechanism through which insulin, leptin and adiponectin exert their effects, particularly with respect to glucose uptake, fatty acid oxidation and control of food intake. As the D316A-Tg mouse model presents with a reduction in adiposity, bodyweight and resistance to hepatic steatosis, the dynamics of hormonal signalling in response to chronic HFD feeding in this model were investigated.

To investigate the effects of chronic, global AMPK activation on the production of leptin, adiponectin and insulin, serum samples were taken from WT-Tg and D316A-Tg chow- and 16-week HFD-fed mice in the fed state and analysed using high-

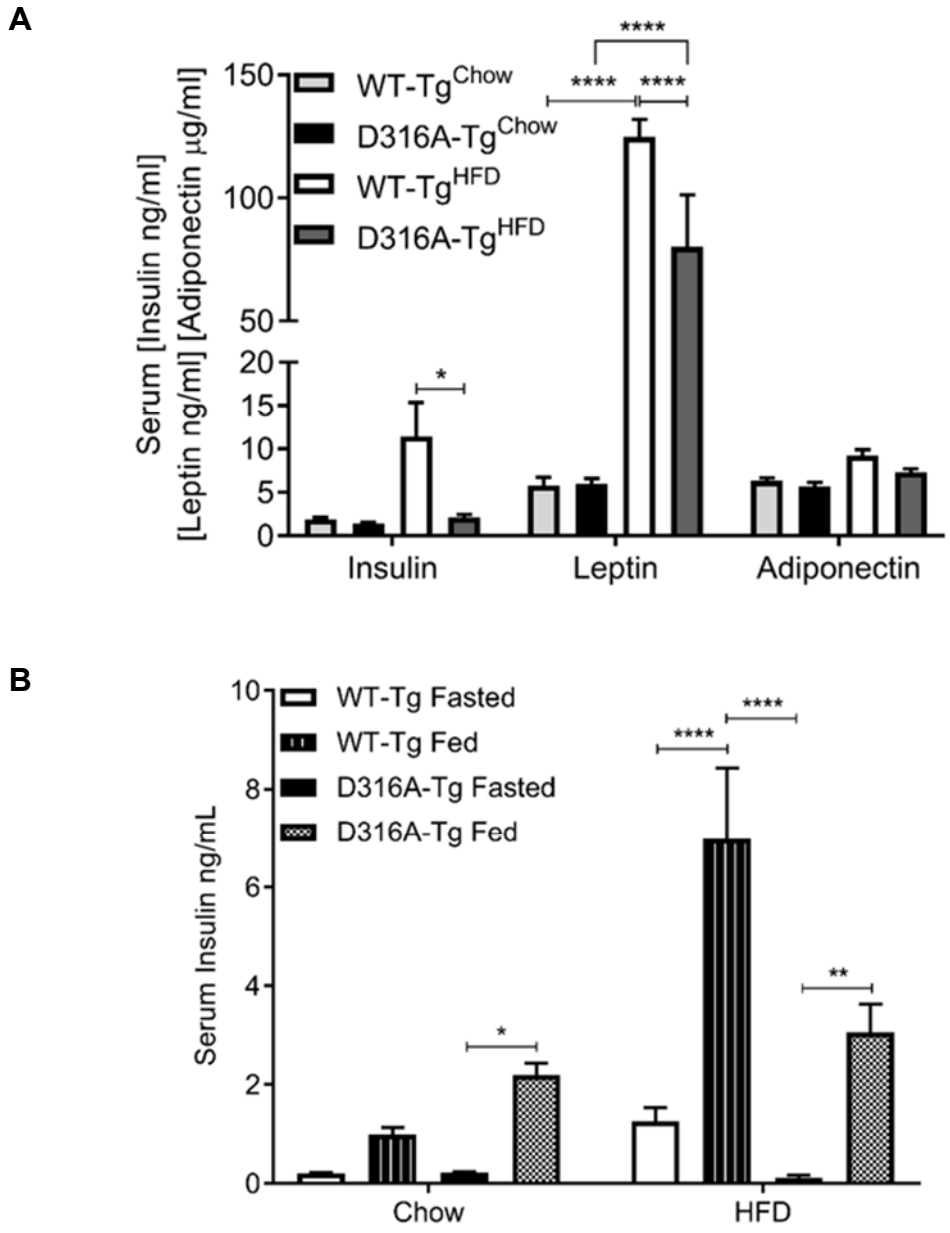



***Figure 3.12 Circulating factors in chow-fed and HFD-fed WT-Tg and D316A-Tg mice.***

***A)*** *Serum concentrations of insulin, leptin and adiponectin in ad libitum, chow-fed and 16-week HFD-fed (24-week old) male mice. N=5, 5, *P<0.05, Data are presented as mean ±SEM.****P<0.0001.*

***B)*** *Fasting and re-fed serum insulin concentration of WT-Tg and D316A-Tg chow- and 16-week HFD-fed (24-week old) mice. N=6, 6, *P<0.05, Data are presented as mean ±SEM.**P<0.01, ****P<0.0001.*

sensitivity ELISA kits (CrystalChem). D316A-Tg chow-fed mice did not exhibit any significant differences in serum insulin, leptin or adiponectin concentrations (Fig 3.12A), suggesting that, under basal conditions, chronic AMPK activation does not alter the normal production of these hormones. High-fat diet feeding lead to a small increase in circulating insulin in WT-Tg, which was not seen in D316A-Tg counterparts. However, this observation did not reach significance using a two-way ANOVA multiple comparisons test (Bonferroni), in part due to the inherent variability of insulin concentration in WT-Tg samples. An independent t-test (unpaired, two-tailed) attributed a p value of 0.0421, though this did not take into consideration overall variability between different serum factors of each individual.

No significant differences in adiponectin concentrations were found between WT-Tg and D316A-Tg HFD-fed mice, nor did obese WT-Tg mice exhibit a reduction in adiponectin concentrations when compared with chow-fed counterparts. In contrast, a significant increase in leptin was observed between WT-Tg chow-fed and HFD-fed mice, indicative of adipose tissue expansion and concurrent obesity-associated leptin resistance. D316A-Tg mice exhibited a reduction (WT-Tg: 124.8ng/ml D316A-Tg: 80.14ng/ml) in circulating leptin when compared with their WT-Tg counterparts, though this value still far exceeded that observed in chow-fed animals.

To further interrogate insulin production in the D316A-Tg mouse model, HFD-fed WT-Tg and D316A-Tg mice were subjected to an overnight (16h) fast, during which circulating insulin levels are known to be reduced in both WT-Tg and D316A-Tg mice on a chow diet.

High-fat diet-fed WT-Tg mice showed elevated fasting-induced insulin concentrations similar to those measured previously in age-matched, chow-fed animals in the fed state (chow: 0.9ng/ml, HFD: 1.2ng/ml) (Fig 3.12B). In contrast, HFD-fed D316A-Tg mice in the fasted state exhibited a pronounced reduction in serum insulin, more-so than their chow-fed counterparts. After 2 hours of feeding, WT-Tg HFD-fed mice exhibited a profound spike in serum insulin concentration, which was comparatively

reduced in D316A-Tg mice, where a similar response to chow-fed counterparts was

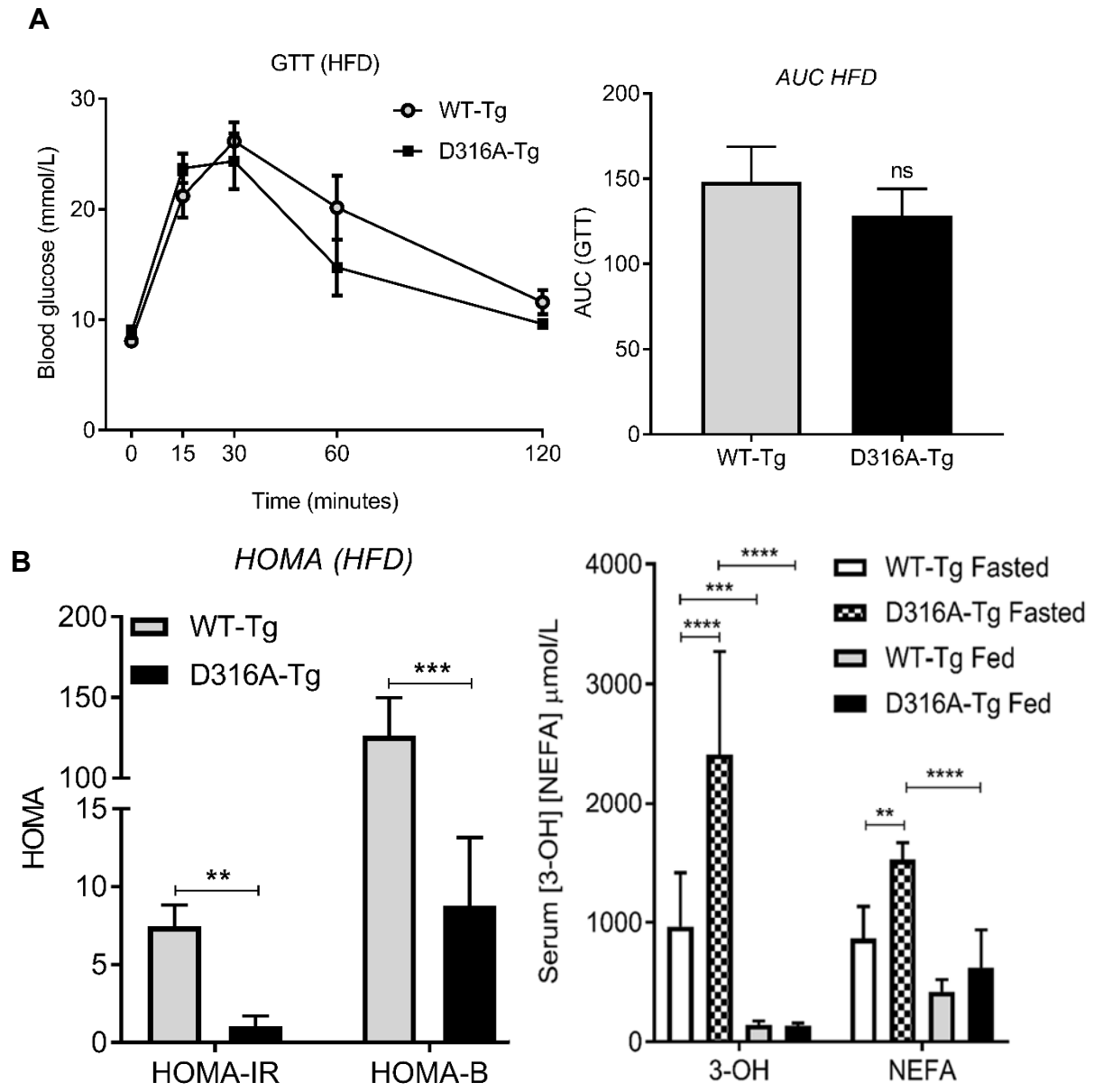



***Figure 3.13 Glucose tolerance and fatty acid metabolism in WT-Tg and D316A—Tg mice.***

***A)*** *Glucose tolerance test performed on 12-week HFD-fed (20-week old) male mice. Glucose was administered via IP injection. Blood glucose concentrations were measured at 0, 15, 30, 60 and 120 minutes after bolus administration. N=8, 6. Data are presented as mean ±SEM.*

***B)*** *HOMA-IR and HOMA-B calculated from fasting insulin and fasting glucose measurements of 12-week HFD-fed (20-week old) male WT-Tg and D316A-Tg chow-fed mice. N=5, 8. Data are presented as mean ±SEM. **P<0.01, ***P<0.001*

***C)*** *Fasted and ad libitum fed serum 3-hydroxybutyrate (ketone) and non-esterified fatty acid (NEFA) concentrations from WT-Tg and D316A-Tg 12-week HFD-fed (20-week old) mice. N= 8, 8 per genotype. Data are presented as mean ±SEM. **P<0.01, ***P<0.001, ****P<0.0001. Samples analysed by AstraZeneca (Cambridge)*

observed.

Given that HFD-fed D316A-Tg mice exhibit a reduction in plasma insulin in response to refeeding, it was hypothesised that these mice may also display improved glucose tolerance. To determine the effect of AMPK activation on glucose tolerance in HFD-fed WT-Tg and D316A-Tg mice by performing a glucose tolerance test (GTT).

Though not significant, a trend towards improved glucose clearance was observed in D316A-Tg mice after 12 weeks of HFD feeding (Fig 3.13A). Interestingly, though all WT-Tg animals at this age displayed a significant increase in adiposity, considerable variability in response to a glucose bolus was observed. A significant reduction in insulin resistance was observed in D316A-Tg mice as assessed by HOMA-IR (Fig 3.13B), with a concurrent and striking decrease in attributed beta cell function (HOMA-B).

To determine whether AMPK activation promoted the mobilisation and metabolism of triglycerides in response to fasting, serum samples were assessed for ketone bodies (3-hydroxybutyrate) and non-esterified fatty acid (NEFA) concentrations in the fasted and *ad libitum* fed state (Fig 3.13C). In response to fasting stimulus, 3-OH serum levels were elevated in both genotypes. D316A-Tg mice exhibited 2-3-fold higher serum 3-OH in response to fasting. Further investigation is required into these parameters on a chow diet. A similar increase was observed in the fasting state with respect to serum NEFA concentrations. D316A-Tg mice exhibited elevated NEFA concentrations in response to fasting than WT-Tg counterparts. No significant differences were observed in the fed state.

Previous studies have demonstrated insulin-independent glucose uptake in the skeletal muscle of rodents and non-human primates using small molecule pan-AMPK activators (Myers et al., 2017, Cokorinos et al., 2017). To determine whether AMPK activation promoted glycogen accumulation in D316A-Tg skeletal muscle in response to HFD-feeding, gastrocnemius and soleus muscles were isolated from HFD-fed WT-Tg and D316A-Tg mice and a glycogen assay performed on whole tissue homogenate. Significant glycogen accumulation was observed in the gastrocnemius muscle of D316A-Tg HFD-fed mice. A simultaneous glycogen assay was performed on isolated soleus muscle but due to low tissue mass and subsequent total protein concentration,

glycogen concentrations from both genotypes fell below the sensitivity of the assay (Fig 3.14A).

To examine further the effects of AMPK activation on glycogen synthesis in skeletal muscle, expression of phosphorylated glycogen synthase, total glycogen synthase

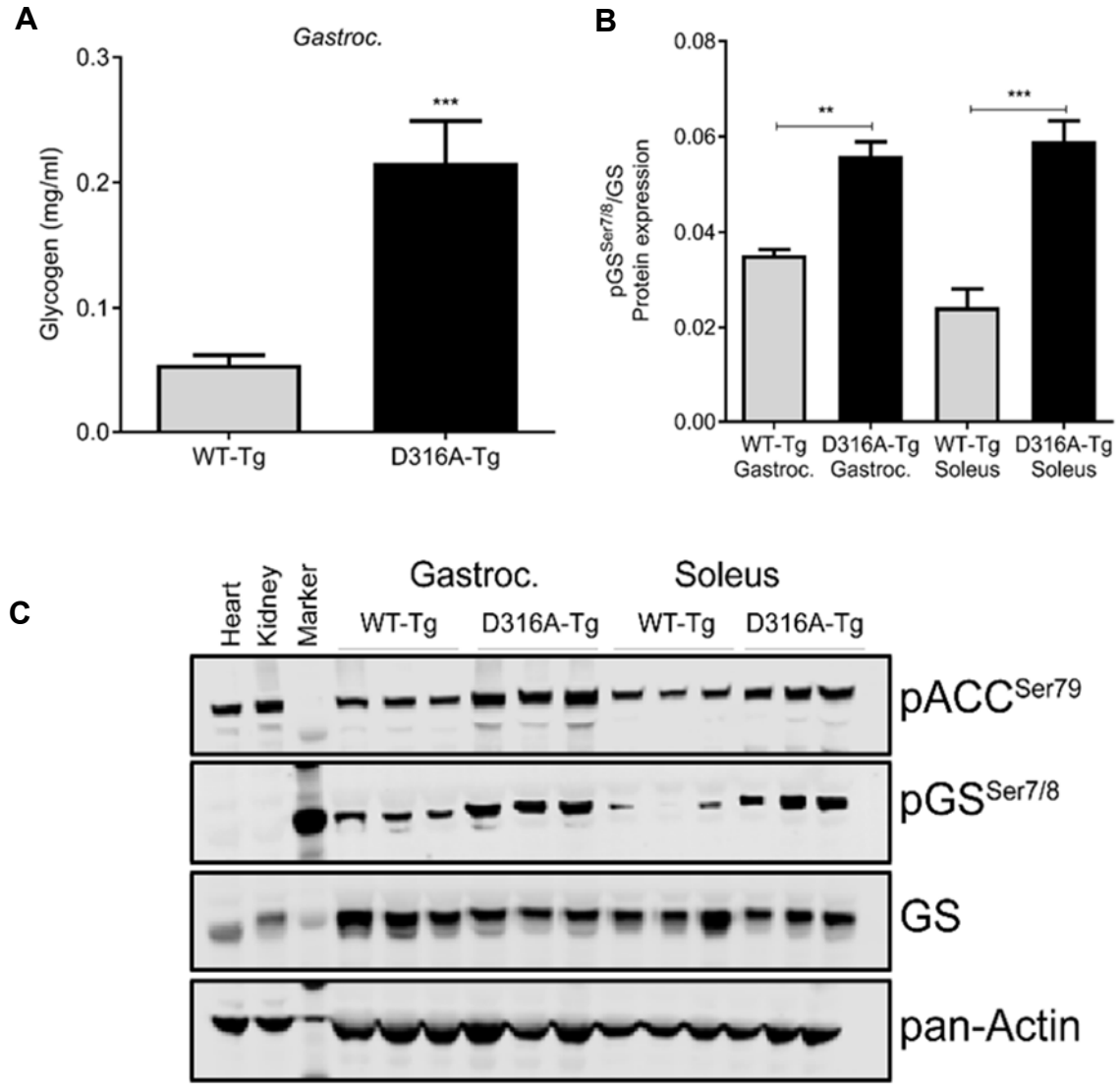



***Figure 3.14 Glycogen accumulation in D316A-Tg skeletal muscle.***

***A)*** *Glycogen content of isolated gastrocnemius muscle from 16-week HFD-fed (24-week old) WT-Tg and D316A-Tg mice. N=6, 6, Data are presented as mean ±SEM.***P<0.001.*

***B)*** *Quantification of glycogen synthase (GS): phospho-glycogen synthase (p-GS) expression in gastrocnemius and soleus muscles isolated from 16-week HFD-fed WT-Tg and D316A-Tg mice. Data are presented as mean ±SEM.**P<0.01, ***P<0.001.*

***C)*** *Representative Western blot showing expression of total GS, p-GS and phosphorylated ACC indicative of AMPK activity. N=3, 3.*

(GS) was assessed by Western blotting (Fig 3.14B and C). AMPK activity was confirmed in both gastrocnemius and soleus muscle by an increase in phosphorylated acetyl-coA carboxylase (Fig 3.14C).

Both gastrocnemius and soleus muscle from HFD-fed D316A-Tg mice showed an increase in the phosphorylation of glycogen synthase on serine 7/8, with no increase in total glycogen synthase expression.

From the studies outlined thus far, it was determined that D316A-Tg mice are protected from HFD-induced obesity and associated hepatic steatosis, with no differences found in food intake. As caloric intake was not altered in this model, it was hypothesised that an increase in energy expenditure (EE) may be responsible for the resistance to DIO. To investigate this hypothesis, HFD-fed animals were monitored using indirect calorimetry.

## 3.2.8 Energy Expenditure (EE)

To determine whether an increase in energy expenditure (EE) was responsible for the resistance to DIO in D316A-Tg mice, EE was measured after 6 weeks of HFD-feeding, to minimise differences in bodyweight seen at later time-points in obese animals, using indirect calorimetry performed in the Comprehensive Laboratory Animal Monitoring

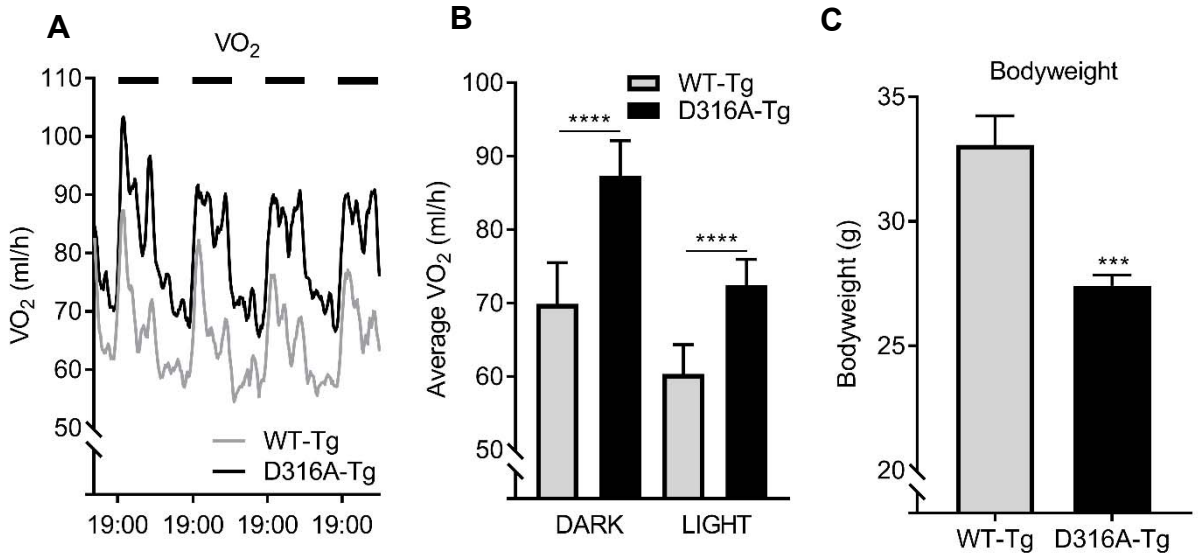



***Figure 3.15 Oxygen consumption ($VO_2$) is increased in D316A-Tg HFD-fed mice.***

***A)*** *$VO_2$ (trace) of WT-Tg and D316A-Tg 6-week HFD-fed (14-week old) male mice. Measurements, recorded in the CLAMS, were taken at 22-minute intervals for a period of 3 days on a 12h light/dark cycle. Dark periods indicated by black bars. N=8, 7.*

***B)*** *Average $VO_2$ area under the curve (AUC) (ml/hr) during dark (active) and light (inactive) periods. N=8, 7, Data are presented as mean ±SEM.****P<0.0001.*

***C)*** *Average bodyweight of WT-Tg and D316A-Tg mice prior to CLAMS entry. N=8, 7, Data are presented as mean ±SEM.****P<0.0001.*

System (CLAMS). This system uses sealed caged with a constant fresh air low and allows calculation of EE from a rate of oxygen consumption and carbon dioxide production with minimal alterations in environment, with all measurements performed in the animal's home cage. Using this method, it was possible to determine oxygen consumption, RER and locomotor activity of singly-housed mice.

D316A-Tg HFD-fed mice exhibit significantly higher oxygen consumption ($VO_2$) than their WT-Tg counterparts (Fig 3.15A), during both light and dark periods (Fig 3.15B), presented as ml/h. Due to difference in bodyweight at this time, statistical significance

was determined using a two-way ANOVA with data not corrected for body weight (Fig 3.15C).

Another parameter frequently described when investigating whole organism energy homeostasis is the respiratory exchange ratio (RER) calculated by dividing the volume of $CO_2$ ($VCO_2$) by the volume of $O_2$ ($VO_2$). This value is often used to estimate the respiratory quotient; the evaluation of the primary fuel source (carbohydrate or fat) being used by the organism, though not directly equivalent over short time periods

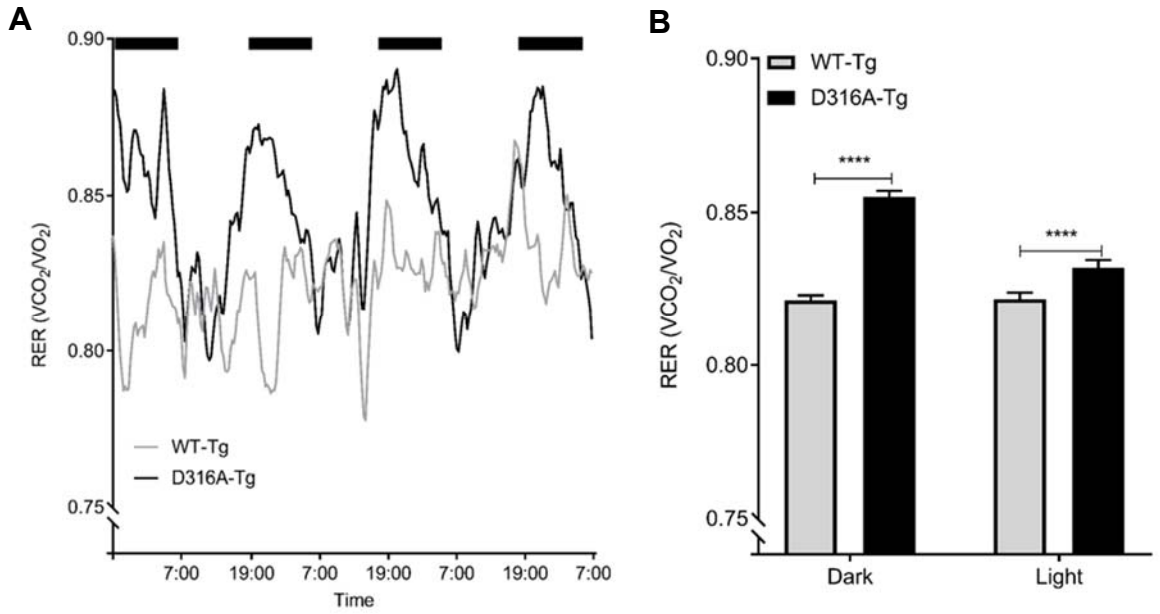



***Figure 3.16 Respiratory exchange ratio (RER) of 6-week HFD-fed (14-week old) WT-Tg and D316A-Tg mice.***

***A)*** *Average RER over a 3-day period, measured in the CLAMS. Dark periods are indicated by black bars. Data smoothed (2nd order) to 5 neighbours.*

***B)*** *3-day average RER (AUC) of WT-Tg and D316A-Tg mice. N=8, 6, Data are presented as mean ±SEM.****P<0.0001*

(Speakman, 2013). An RER of 1 represents pure carbohydrate oxidation, and a value of 0.7 associated with pure fat oxidation.

Over a 5-day period, D316A-Tg mice displayed significantly higher RER in both active and inactive periods when compared to their WT-Tg counterparts, indicative of increased carbohydrate utilisation when fed a HFD (Fig 3.16A). Interestingly, though no significant pattern of cycling was observed in WT-Tg animals between light and dark periods, attributed to the intake of a HFD, D316A-Tg mice appeared to cycle

normally between substrates, utilising carbohydrates during the active (dark) periods and a combination of the two fuel sources during rest (light) periods (Fig 3.16B).

To investigate whether spontaneous locomotor activity was responsible for the increase in $VO_2$ in D316A-Tg mice, XTOT (horizontal) and ZTOT (vertical) beam-break counts were measured in the CLAMS. No significant differences were found between WT-Tg and D316A-Tg HFD-fed mice in the pattern of activity (Fig 3.17A), nor in total movement in either direction (Fig 3.17B), indicating that increased locomotor activity was not responsible for the significant difference in oxygen consumption in D316A-Tg

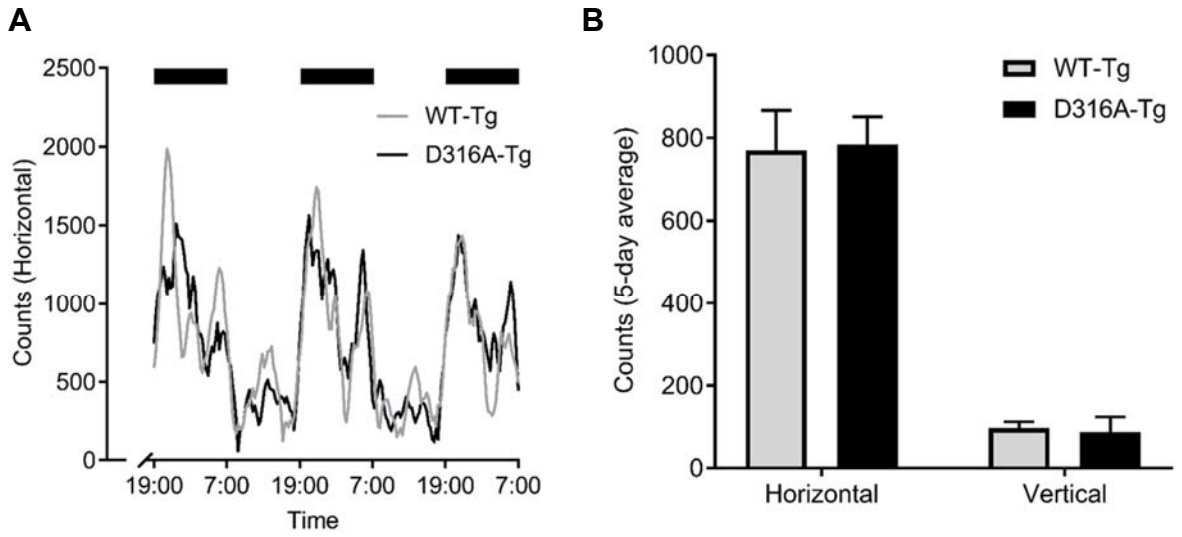



***Figure 3.17 Assessment of spontaneous locomotor activity***

***A)*** *Average horizontal movement of 6-week HFD-fed (14-week old) WT-Tg and D316A-Tg male mice, monitored over a 3-day period in the CLAMS. Data smoothed (2nd order) to 5 neighbours, black bars indicate dark (active) periods.*

***B)*** *Quantification of horizontal and vertical movement assessed by beam breaks (5-day average). N=8, 6. Data are presented as mean ± SEM.*

mice.

With no evidence for increased activity in this system, animals were not assessed for voluntary exercise at this time. However, whether AMPK activation in this manner stimulates voluntary exercise when presented with apparatus, or prolongs periods of forced exercise remains an attractive area of investigation.

In rodents and in humans, energy expenditure can be divided into four compartments; basal metabolism, increased EE in response to food intake, thermoregulation and physical activity (Speakman, 2013). Since D316A-Tg HFD-fed mice did not exhibit alterations in feeding or physical activity, it was hypothesised that AMPK activation may drive thermogenesis in response to HFD-feeding, conferring protection from DIO.

### 3.2.9 Brown Adipose Tissue-Mediated Thermogenesis

A well-established read-out of brown adipose tissue activation *in vivo* is the measurement of core body temperature (Meyer et al., 2017). *To* investigate the effects of AMPK activation on brown adipose tissue functionality *in vivo*, the core temperatures of WT-Tg and D316A-Tg HFD-fed un-anaesthetised mice were taken using a rectal probe.

No significant difference was found between the core temperatures of HFD-fed WT-Tg and D316A-Tg mice over a 3-day period (Fig 3.18), suggesting that BAT-mediated increase in core temperature is not responsible for the elevated oxygen consumption

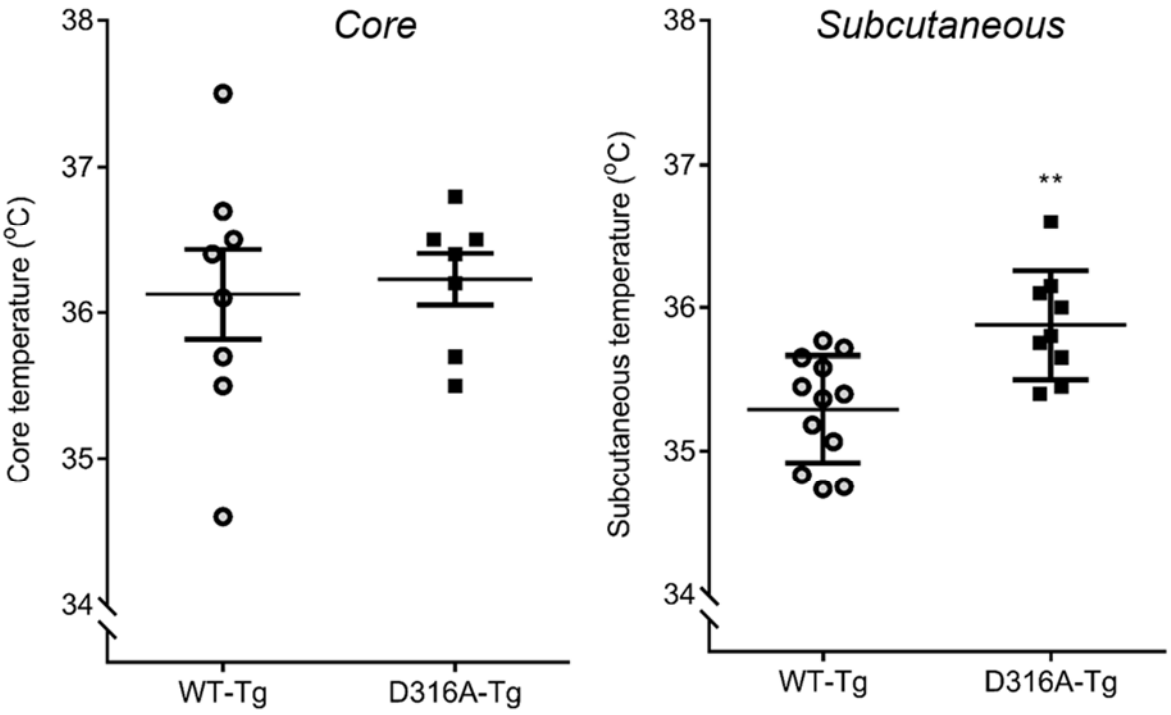



***Figure 3.18 Average rectal (core) and subcutaneous temperature of WT-Tg and D316A-Tg 12-week HFD-fed (20-week old) male mice.***

*Data are displayed as 3-day averages of individual animals, measured in triplicate. N=8, 7, Data are presented as mean ±SEM. **P<0.01.*

seen in D316A-Tg HFD-fed mice. However, a significant difference was observed using subcutaneous temperature probes, inserted into the inguinal or subcutaneous adipose of HFD-fed mice (Fig 3.18), monitored over a period of three days.

To determine whether AMPK activation led to an alteration in the thermogenic capacity of BAT, a β3-adrenoceptor-selective agonist, CL316, 243, was administered intraperitoneally to chow-fed mice whilst being monitored in the CLAMS. Oxygen consumption (ml/kg/h) was measured for 30 minutes prior to CL-agonist administration. A robust increase in oxygen consumption was observed (Fig 3.19A and B) in response to β3-adrenoceptor stimulation in both genotypes, demonstrating normal BAT functionality in D316A-Tg mice. This study was kindly performed by Dr. Luis Martins.

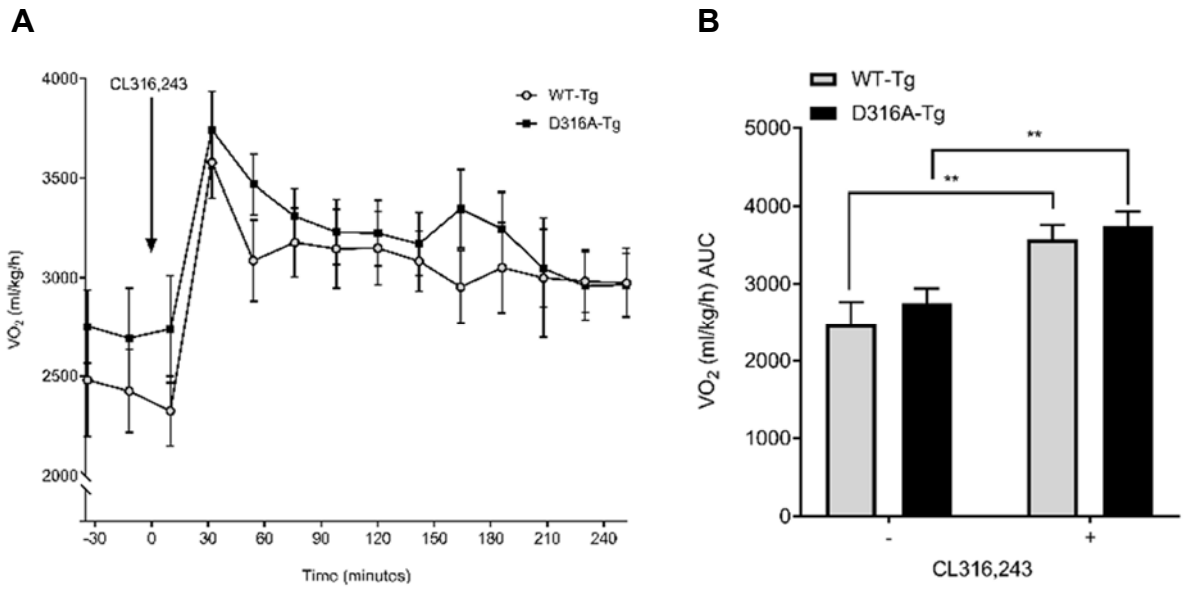



***Figure 3.19 Thermogenic response to the β3-adrenoreceptor agonist CL316, 243***

***A)*** *Trace of average $O_2$ consumption of WT-Tg and D316A-Tg 12-week old chow-fed male in response to IP administration (1mg/kg) of CL316, 243. Injections performed by Dr. Luis Martins and Phillip Muckett.*

***B)*** *Quantification of $VO_2$ before and after CL-agonist administration. N=5-6 per group, Data are presented as mean ±SEM. **P<0.01.*

Animals were culled 6 hours after treatment, and BAT harvested for gene expression analysis. The expression of UCP1 is often regarded as a 'hallmark' of brown adipose tissue, and is responsible for the thermogenic capacity of this highly specialised tissue. However, the expression of UCP1 on the inner membrane of BAT mitochondria is dependent on β3-adrenergic-induction of several cAMP-dependent pathways

responsible for the upregulation of UCP1 mRNA in brown adipocytes (Klingenspor, 2003). To determine whether AMPK activation alters the expression of UCP1 mRNA in response to β3-adrenergic stimulation, BAT mRNA from vehicle-treated and CL316, 243-treated chow-fed mice was extracted, reverse transcribed and analysed for UCP1 expression by qPCR.

Both WT-Tg and D316A-Tg BAT displayed a significant upregulation of UCP1 mRNA in response to CL-agonist treatment, with no difference found between genotypes (Fig 3.20). These results confirm BAT functionality in the D316A-Tg mouse model on a chow diet, in response to β3-adrenergic stimulation. It was confirmed that AMPK activation does not significantly alter the ability of BAT to respond to this stimulus, nor does it promote the expression of UCP1 mRNA and subsequent energy expenditure.

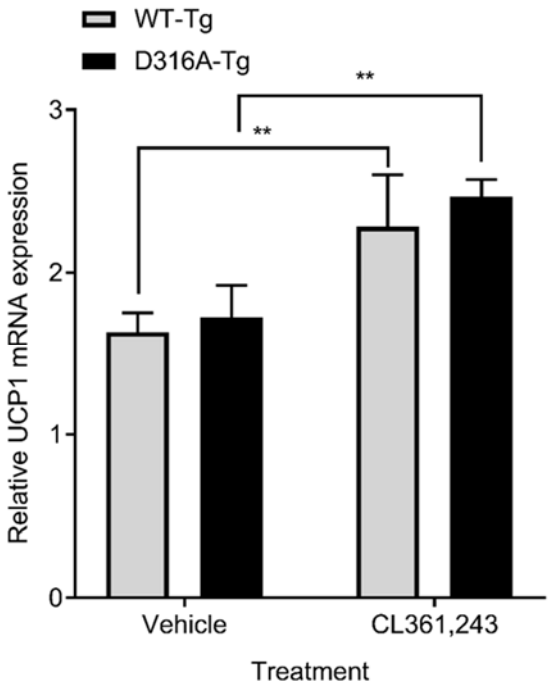



***Figure 3.20 UCP1 expression in response to β3-adrenoceptor stimulation.***

*UCP1 mRNA expression in vehicle and β3-adrenoceptor agonist CL316, 243 treated 12-week old chow-fed male mice. qPCR was performed by Dr. Luis Martins. N=5-6 per group. Data are presented with permission as mean ±SEM. **P<0.01.*

It is widely accepted that BAT-mediated thermogenesis is induced by food intake, particularly when the dietary protein content is low, inducing UCP1 protein expression and associated uncoupling activity (Kevonian et al., 1984, Feldmann et al., 2009). To establish whether AMPK activation in the D316A-Tg mouse model alters response to

HFD-feeding in BAT, interscapular BAT (iBAT) was isolated from 4-week HFD-fed WT-Tg and D316A-Tg mice to assess mitochondrial content and UCP1 expression.

To determine whether the protection from diet-induced lipid accumulation in D316A-Tg brown adipose tissue was associated with alterations in mitochondrial content and UCP1 expression, BAT from chow-fed and HFD-fed mice was assessed by Western blotting.

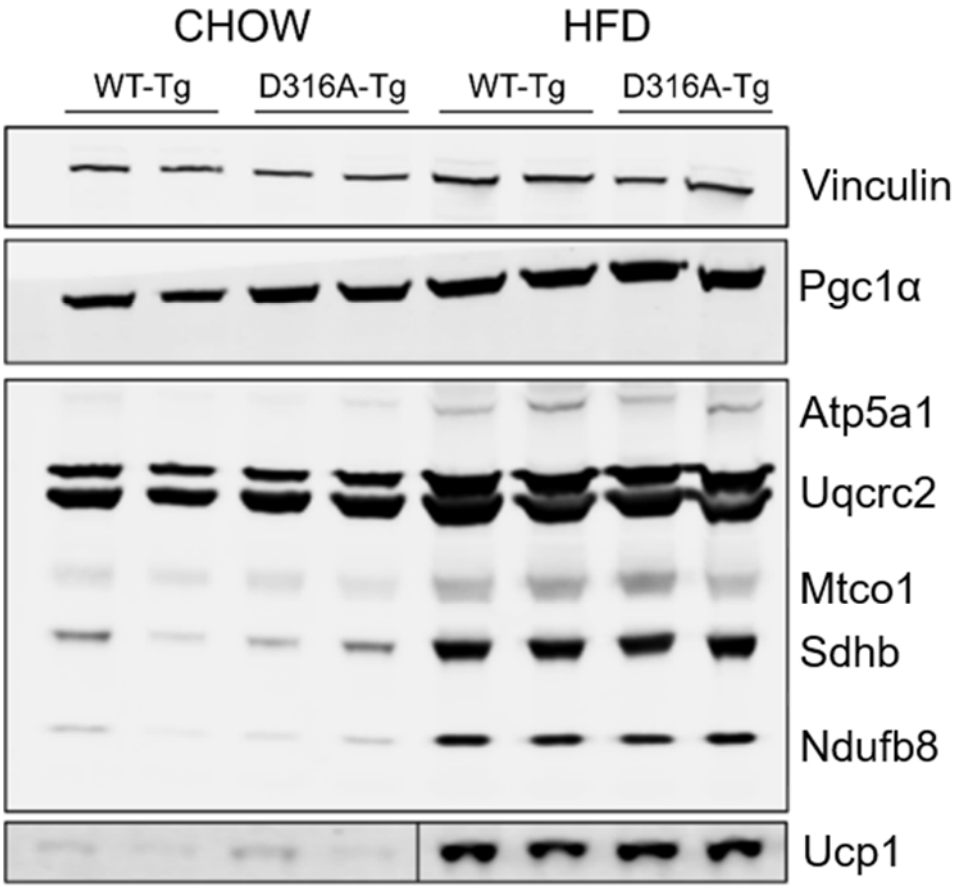



***Figure 3.21 Mitochondrial content and UCP1 expression in chow- and HFD-fed mice.***

*Assessment of BAT mitochondrial respiratory chain complexes CI-V, UCP1 and PGC1α, a master regulator of mitochondrial biogenesis, in whole BAT protein extracts from WT-Tg and D316A-Tg 16-week old chow-fed and 4-week HFD-fed (12-week old) mice by Western blotting. N=4, 4 per diet. Vinculin was used as a loading control.*

*Mitochondrial respiratory chain complexes; Atp5a1, ATP synthase (CV); Uqcrc2, cytochrome b-c1 (CIII); Mtco1, cytochrome c oxidase 1 (CIV); Sdhb, succinate dehydrogenase (ubiquinone, iron-sulphur) (CII); Ndufb8, NADH: ubiquinone oxidoreductase subunit B8 (CI).*

As previously reported by Feldmann *et al.,* administration of HFD robustly induced the expression of UCP1 protein in BAT from both WT-Tg and D316A-Tg mice. However, no genotype-dependent effect was observed on either diet (Fig 3.21). Interestingly, a strong increase in expression of all mitochondrial respiratory chain (mtRC) components was observed in response to HFD-feeding. Samples were also assessed for the expression of PGC1α, a key regulator of mitochondrial biogenesis, responsible for the expression of nuclear encoded subunits of the mitochondrial respiratory chain and UCP1 through co-activation of several factors, including the nuclear respiration factor NRF-1 (Lowell and Spiegelman, 2000). Interestingly, though mtRC proteins were significantly upregulated in response to HFD-feeding, little change was observed in the expression of PGC1α (Fig 3.21).

In addition to BAT development, AMPK has also been implicated in the 'browning' or 'beiging' of inguinal or subcutaneous white adipose (WATsc), characterised by the acquisition of brown-like adipocytes within white adipose depots, expressing classical BAT-specific genes such as UCP1, Prdm16, PGC1α, PPARγ and DIO2. These studies, however, utilise indirect activators of AMPK *in vitro* or employ genetic mutations that indirectly lead to AMPK activation *in vivo* (Chung et al., 2017, Yan et al., 2016).

The D316A-Tg model, exhibiting increased subcutaneous temperature and EE on a HFD, presented a unique opportunity to examine whether AMPK activation promotes the beiging of white adipose and, if so, to determine whether these cells responsible for the protection from DIO observed in this model.

## 3.3 Characterisation of D316A-Tg subcutaneous white adipose tissue

As beige adipocytes share key characteristics with classical brown adipocytes; high mitochondrial content, UCP1 expression and multilocular lipid droplet morphology, it was hypothesised that AMPK activation may drive the differentiation of these cells in response to a high-fat diet, contributing to the increase in EE, subcutaneous temperature and protection from DIO observed in the D316A-Tg mouse model. To investigate this hypothesis, subcutaneous white adipose was isolated from WT-Tg and D316A-Tg after 4, 16, 24 and 28 weeks of HFD-feeding for examination by histology and assessment of mitochondrial content.

### 3.3.1 Tissue weight and morphology

As shown previously, HFD-fed D316A-Tg mice exhibit a reduction in adiposity as assessed by eMRI.

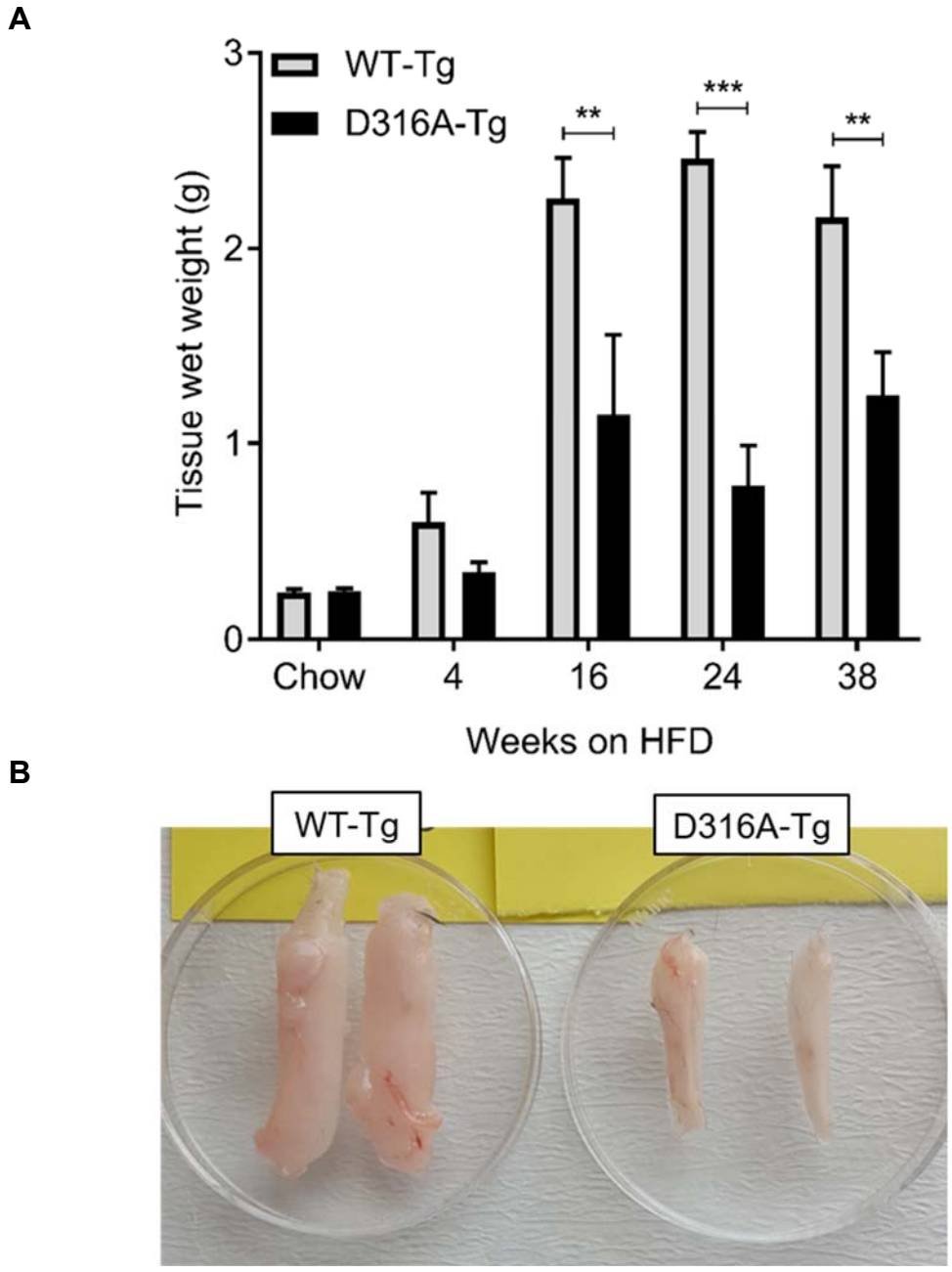



***Figure 3.22 Subcutaneous white adipose tissue (WATsc) mass is reduced in D316A-Tg HFD-fed mice.***

***A)*** *Tissue weight from 16-week old chow-fed and HFD-fed WT-Tg and D316A-Tg mice at harvest. N=7-9 per group, **P<0.01, ***P<0.001.*

***B)*** *Gross image of isolated WATsc from 24-week HFD-fed (32-week old) male mice.*

In addition, subcutaneous white adipose mass was significantly decreased at harvest, when compared to WT-Tg controls after 16 weeks of HFD-feeding, with protection conferred even after 28 weeks on a HFD (Fig 3.22A). The appearance of the WATsc isolated from D316A-Tg HFD-fed mice differed greatly from that of WT-Tg controls, being far smaller in diameter (3.22B).

A reduction in WATsc size and weight is often indicative, as in the D316A-Tg mouse model, of a reduction in total animal adiposity, and can be a consequence of a reduction in total lipid accumulation, as opposed to a change in cell type.

To determine whether the reduction in mass observed in HFD-fed D316A-Tg WATsc was associated with 'beiging', WATsc was isolated from 4-week HFD-fed mice, when the reduction in total WATsc mass was not significantly altered. Haematoxylin-staining of these samples revealed a striking brown-like morphology of D316A-Tg WATsc (Fig 3.23), with a significant proportion of the depot displaying small, hexagonal adipocytes containing multilocular lipid droplets and increased cytoplasmic volume. In contrast, WT-Tg WATsc adipocytes displayed characteristic white adipocyte morphology; a large, round unilocular lipid droplet rendering all other cell contents, including the nucleus, compressed to the cell membrane.

The presence of these 'beige' or brown-like adipocytes is indicative of classical beiging of the WATsc. However, a true beige adipocyte, by definition, must express the hallmarks of brown adipose, namely the expression of UCP1 and an increase in components of the mitochondrial respiratory chain.

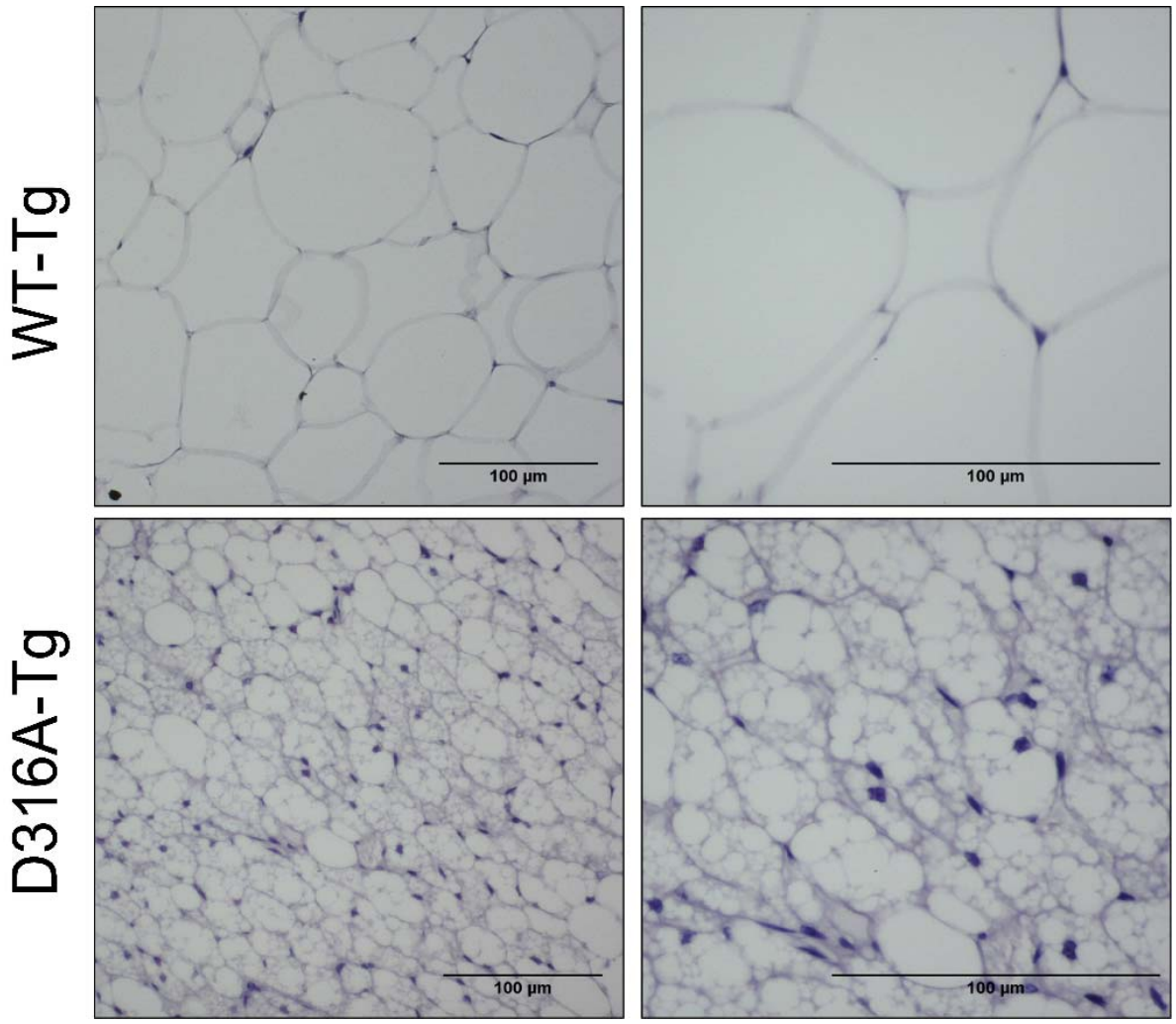



***Figure 3.23 WATsc morphology from WT-Tg and D316A-Tg 4-week HFD-fed (12-week old) male mice.***

*Haematoxylin stained WATsc, magnification at 20x (left) and 40x (right). Scale bar 100µm.*

To determine whether D316A-Tg WATsc contained classical beige adipocytes, whole tissue homogenates from 4-week HFD-fed mice were assessed for PGC1α, mtRC and UCP1 protein expression by Western blotting. Upon examination, D316A-Tg WATsc was found to express remarkably high levels of mtRC proteins when compared to WT-Tg HFD-fed controls, as well as a substantial increase in the expression of PGC1α (Fig 3.24).

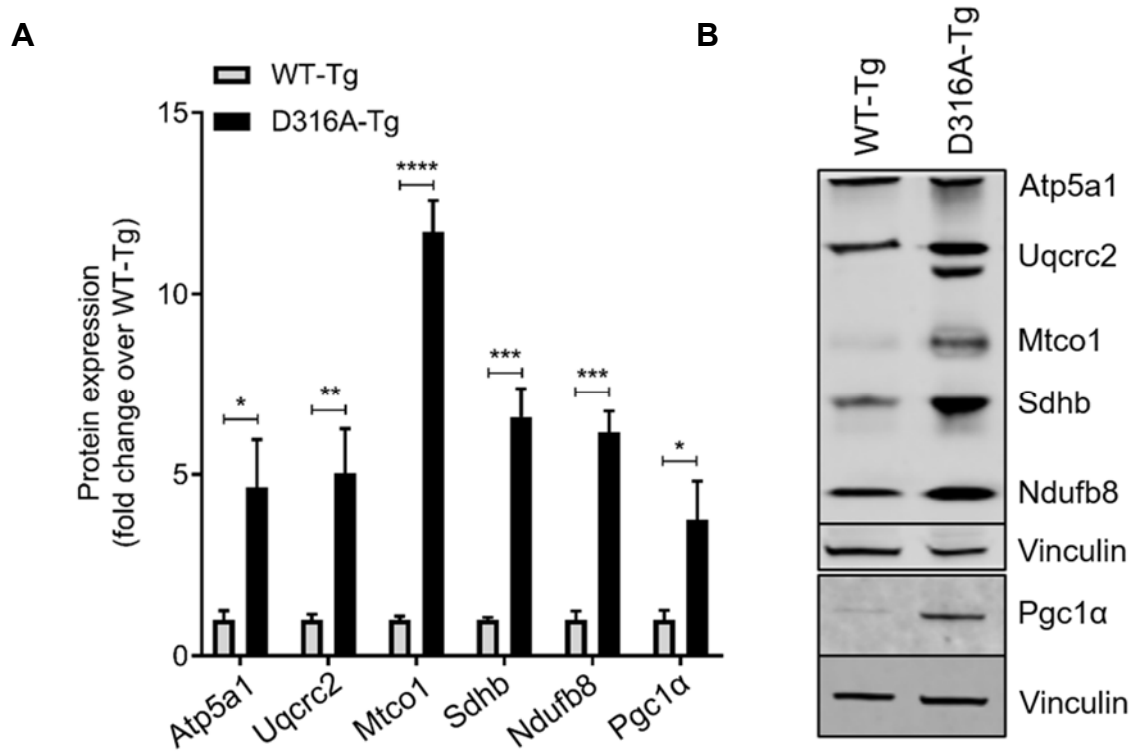



***Figure 3.24 Assessment of mitochondrial biogenesis in HFD-fed D316A-Tg mice.***

***A)*** *Quantification of mitochondrial respiratory chain protein and PGC1α expression in WT-Tg and D316A-Tg WATsc from 4-week HFD-fed (12-week old) male mice as assessed by Western blotting. N=3, 3. Data are presented as mean ±SEM. *P<0.05, **P<0.01, ***P<0.001, ****P<0.0001.*

***B)*** *Representative Western blot of mtRC proteins complex I to V and respective PGC1α expression in WATsc from 4-week HFD-fed (12-week old) WT-Tg and D316A-Tg mice. N= 1, 1. All protein expression was normalised to the housekeeping protein Vinculin and expressed as fold change over WT-Tg controls.*

*Mitochondrial respiratory chain complexes; Atp5a1, ATP synthase (CV); Uqcrc2, cytochrome b-c1 (CIII); Mtco1, cytochrome c oxidase 1 (CIV); Sdhb, succinate dehydrogenase (ubiquinone, iron-sulphur) (CII); Ndufb8, NADH: ubiquinone oxidoreductase subunit B8 (CI).*

The presence of high levels of respiratory chain complexes in conjunction with PGC1α suggested substantially enhanced mitochondrial biogenesis, concurrent with the observed morphology in Fig 3.23.

Classical brown and beige adipocytes also exhibit these characteristics, with additional expression of UCP1 at mRNA and protein level to contribute to enhancement of energy expenditure. To determine whether the observed increase in mitochondrial content facilitated increased expression of UCP1 in this model, the same samples were evaluated for UCP1 content by qPCR and Western blotting. Surprisingly, despite the characteristics outlined above, no increase in UCP1 mRNA expression was found

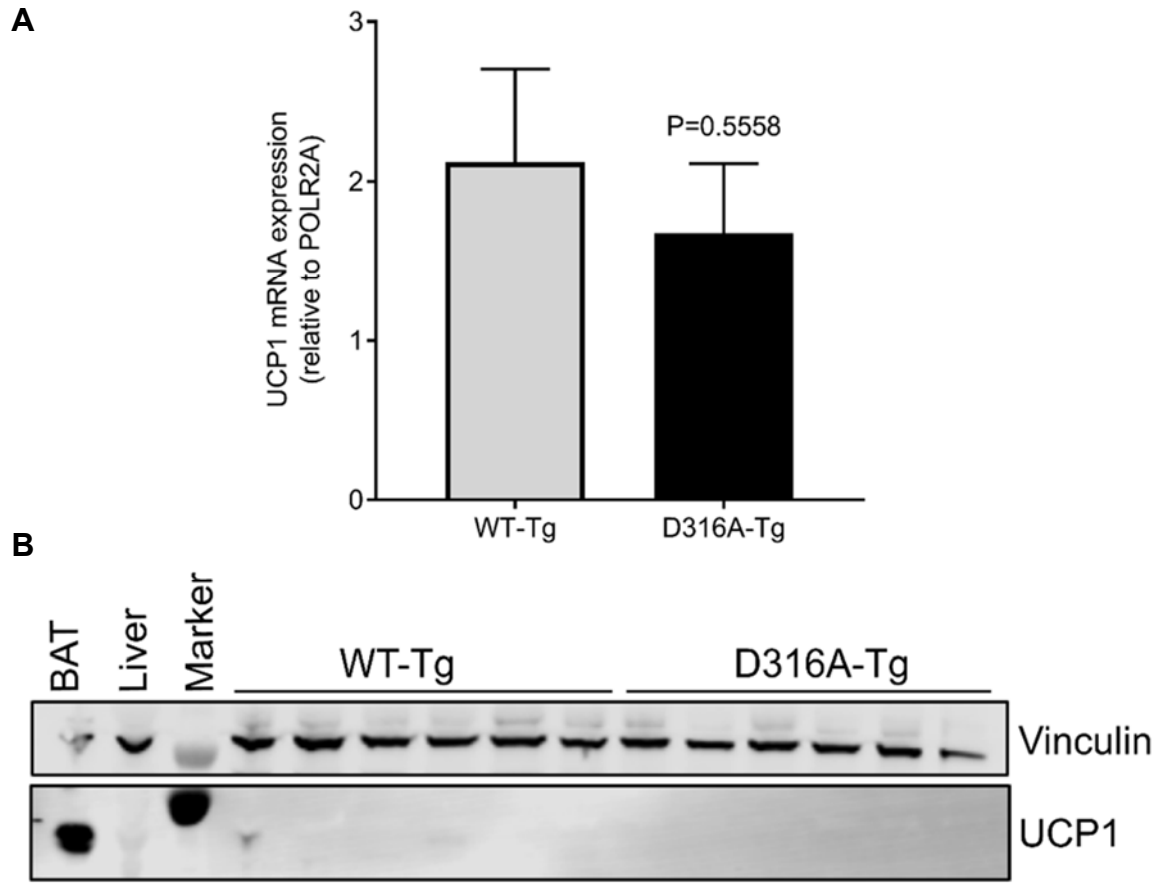



***Figure 3.25 Expression of UCP1 in WATsc from 4-week HFD-fed WT-Tg and D316A-Tg male mice.***

***A)*** *UCP1 mRNA expression in the WATsc of 4-week HFD-fed (12-week old) male mice, expressed relative to the housekeeping gene POLR2A. N=5, 5. Data are presented as mean ±SEM.*

***B)*** *Expression of UCP1 protein in WATsc from 4-week HFD-fed (12-week old) WT-Tg and D316A-Tg mice. Brown adipose tissue was loaded at a lower concentration to serve as a positive control. Liver was used as a negative control.*

in D316A-Tg WATsc at this time-point (Fig 3.25A), nor could expression be detected at protein level (Fig 3.25B).

### 3.3.2 RNA sequencing

To further investigate the possible alternative mechanisms of energy expenditure in this model, RNA sequencing was performed in collaboration with AstraZeneca on RNA extracted from the WATsc of 16-week HFD fed WT-Tg and D316A-Tg male mice. Liver, gastrocnemius and brown adipose tissue isolated from the same animals were also sequenced, to further examine the effects of chronic AMPK activation on the transcriptome of these tissues.

Four key tissues were chosen for sequencing based on their previously described roles in the control of energy homeostasis, thermogenesis and association with protection from DIO. In addition, selection was based on prior knowledge of the role of AMPK in these tissues, with data publicly available from tissue-specific transgenic overexpression, knock-outs and genetic manipulation of AMPK subunits. The selected tissues; liver, BAT, WATsc and gastrocnemius muscle, were isolated from 16-week HFD-fed WT-Tg and D316A-Tg mice (6 animals per group), snap-frozen to preserve RNA integrity and RNA extracted from all samples at the same time, to reduce variation in efficiency and environmental conditions. Isolated RNA was sent to AstraZeneca (Mölndal, Sweden) for integrity analysis, library construction and sequencing.

### 3.3.3 Principal Component Analysis

As an initial assessment of such large data sets as were generated in this study, a principal component analysis (PCA) was performed. In this study, the variables, or ‘principal components’ (PC) were defined as genotype (WT- or D316A-Tg) and tissue. Data points were clustered based on percentage contribution of variation; in simple terms, the less variation between samples, the closer they will cluster and vice versa. By this definition, samples from the same tissue type cluster together as variability in gene expression is low. In contrast, tissues that do not share common gene expression, an example being liver and muscle, appear distant from each other.

A PCA analysis, whilst not intended as a direct measure of gene expression, can provide information about large, diverse data sets such as these when evaluating the effects of genetic manipulation of a PC, in this case genotype. As hypothesised, a divergence was observed between samples taken from liver and those from brown adipose, white adipose and muscle (Fig 3.26). Perhaps also not unexpected was the association between brown adipose and muscle samples, both highly metabolically active and sharing a common Myf5$^{+}$ progenitor cell. However, within these three tissues; liver, muscle and BAT, little divergence was observed between WT-Tg and D316A-Tg samples, suggesting that no overt changes in gene expression had taken place.

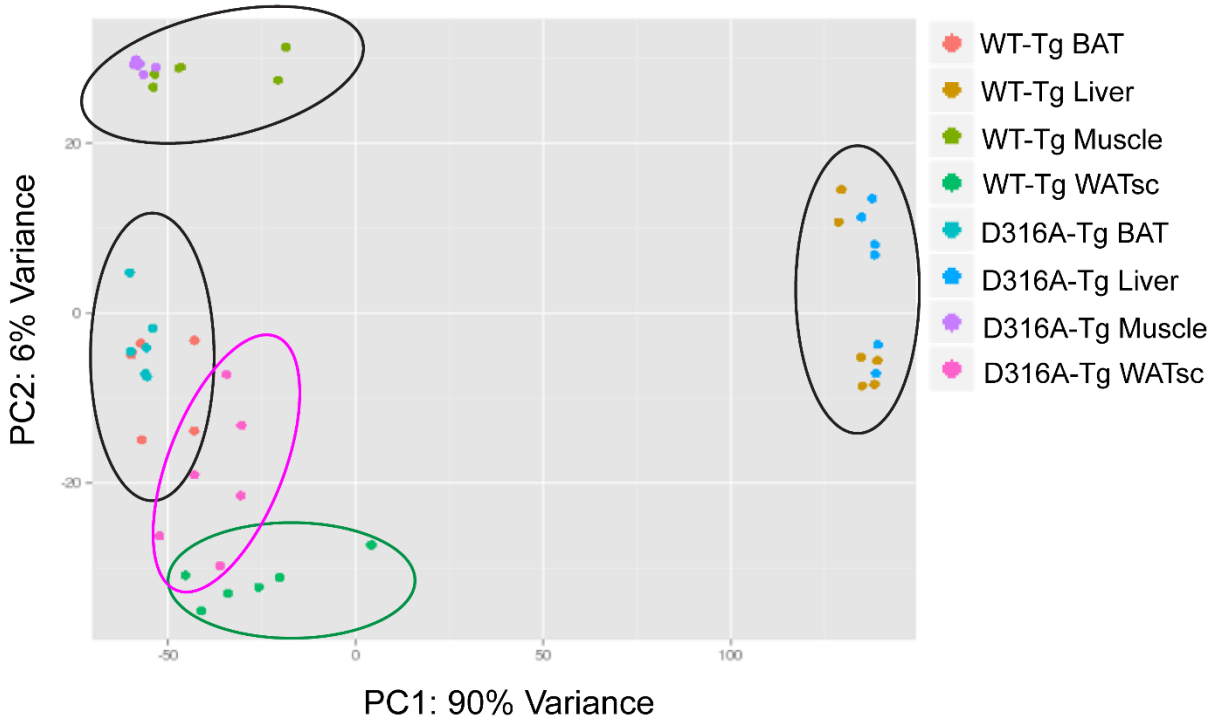



***Figure 3.26 Principal component analysis***

*PCA plot of all RNA sequencing data from BAT, liver, muscle and WAT WT-Tg and D316A-Tg 16-week HFD-fed (24-week old) male mice. N=6, 6 for each tissue.*

In contrast, significant differences were observed, even at this early stage, between the WATsc from WT-Tg samples, forming a distinct group from other tissue clusters (green circle), and D316A-Tg WATsc, grouping closely with BAT and muscle (magenta circle) (Fig 3.26). Interestingly, upon further investigation, the D316A-Tg WATsc sample most closely associated with WT-Tg samples was isolated from the animal

with the greatest adiposity as measured by eMRI, suggesting that the degree of variation observed within D316A-Tg WATsc samples is influenced by total adiposity.

Following this analysis, differentially expressed genes (DEGs) from each tissue were collated and presented in a heat map, to determine whether samples from the same genotype exhibited similar alterations in gene expression profiles. Expression profiles were calculated based on a Log2 fold change over an average of WT-Tg samples, with a large increase in gene expression represented by red colouration and reductions by blue (Fig 3.27). Each column within a heat map represents a biological replicate, in this case an individual animal. With data presented in this form, it was observed that, in all tissues, there were considerable differences in gene expression between WT-Tg and D316A-Tg samples.

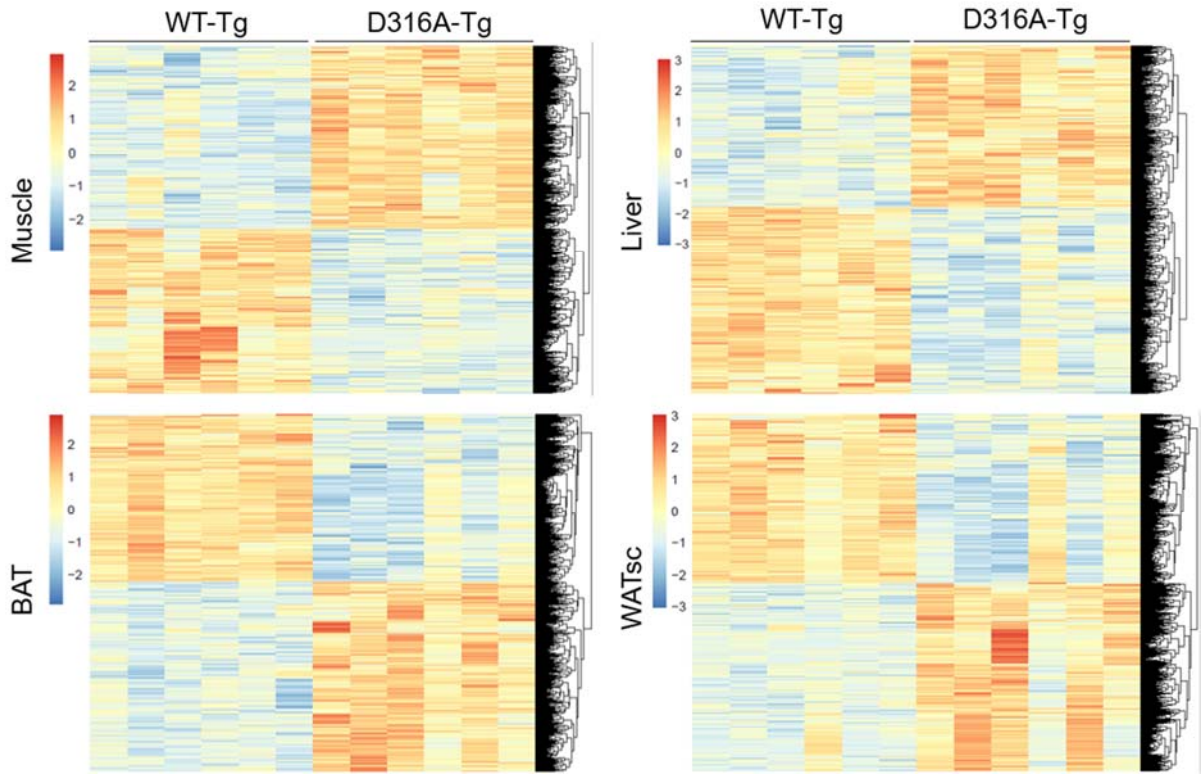



***Figure 3.27 Differentially expressed genes in sequenced tissues***

*Heat map depiction of differentially expressed genes from muscle, liver, BAT and WATsc of WT-Tg and D316A-Tg 16-week HFD-fed (24-week old) male mice. Scale bar indicates Log2FC enrichment over mean WT-Tg expression. N=6, 6.*

Whilst the majority of these changes could be attributed to protection from lipid accumulation, particularly in the liver and brown adipose, a significant proportion of those DEGs in the subcutaneous white adipose samples could not be attributed to any

classical adipocyte-associated transcriptional program. By manual annotation, it was discovered that these genes were, in fact, associated with a shift towards a muscle-like transcriptome, including genes involved in skeletal muscle development, differentiation and metabolism. This exciting and unexpected observation prompted deeper investigation into D316A-Tg WATsc DEGs and their associated pathways, using complementary statistical tools and pathway analysis software provided by Ingenuity Pathway Analysis (IPA, Qiagen).

### 3.3.4 WATsc RNA sequencing

From observations made by manual annotation of differentially expressed genes in each tissue, it was clear that the most striking changes were exhibited by D316A-Tg WATsc. The analysis of liver, muscle and BAT DEGs was performed using IPA software as described for WATsc, with several interesting changes observed, though

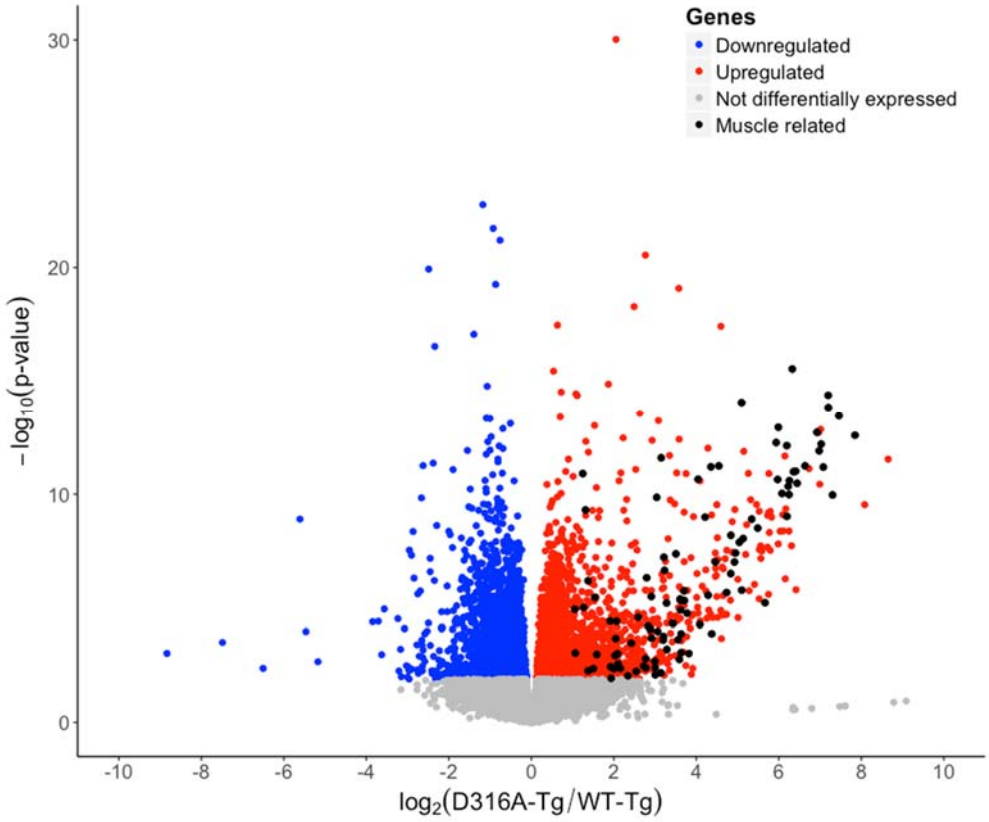



***Figure 3.28 Volcano plot: WATsc***

*Volcano plot highlighting differentially expressed genes identified in WATsc from 16-week HFD-fed D316A-Tg mice. All genes are expressed as Log2 fold change over mean WT-Tg expression. N=6, 6. P<0.05. Plot kindly generated by Sanjay Khadayate.*

none that presented as unique a profile as that of the WATsc. Work pertaining to the results of the RNA sequencing of the other tissues is ongoing.

To evaluate the pattern of differentially regulated genes in D316A-Tg WATsc, individual genes were graphed using a volcano plot, plotting the Log2 fold change against the $Log_{10}$ P value to determine significance (Fig 3.28). Using this method, gene changes that were significantly ($P<0.05$) upregulated, versus mean WT-Tg values, were highlighted in red, with significant downregulation highlighted in blue. Genes that were not differentially expressed, as determined by significance, were depicted in grey. It was found that no one GO term encompassed all of the manually annotated muscle-related genes described previously. Therefore, a combination of analyses was used to determine gene function and associated pathways, including GO analysis conducted using IPA analysis software, DAVID online GO analysis tool and manual annotation using online resources; UniProt, GENECARDS, STRING and MouseMine. Using this method, over 200 differentially expressed in D316A-Tg were categorised as muscle-related, highlighted in black (Fig 3.28).

To begin assembly of these genes into known pathways, DEGs were entered into Ingenuity Pathway Analysis software. This analysis package allowed gene changes to be associated with known upstream regulators, binding partners, interacting pathways and downstream targets, providing detailed analyses and predictions based on published literature.

| ID | Molecules in Network | Score | Focus Molecu | Top Diseases and Functions |
|---|---|---|---|---|
| 1 | ↑ACTN2, ↑Actn3, Alpha Actinin, ↑AMPD1, ↑ANKRD2, ↑CAPN3, ↑ENO3, ERK1/2, ↑KLHL40, ↑KLHL41, ↑LDB3, ↑LMOD3, ↑MYBPC1, ↑MYBPC2, ↑MYH7, ↑MYL1, ↑MYOM1, ↑MYOM2, Myosin, ↑MYOT, ↑MYOZ3, ↑MYPN, ↑NEB, ↑NRAP, ↑Pdlim3, ↑TCAP, ↑TMOD4, Tni, ↑TNNI2, ↑TNNT3, ↑TRIM63, Tropomyosin, ↑WNK2, ↑XIRP1, ↑XIRP2 | 64 | 30 | Skeletal and Muscular System Development and Function, Developmental Disorder, Skeletal and Muscular Disorders |
| 2 | ↑ABRA, ↑AKAP6, Akt, ↑ATP2A1, cacn, ↑CACNA1S, ↑CACNB1, ↑CACNG1, ↑CACNG6, Calcineurin protein(s), calpain, CaMKII, ↑CASQ1, ↑CAV3, ↑CKM, ↑CKMT2, ↑CLCN1, ↑Cmya5, creatine kinase, ↑DES, ↑IP6K3, ↑JPH2, ↑JSRP1, L-type Calcium Channel, ↑MB, MEF2, ↑NOS1, ↑PFKM, PRKAA, ↑PVALB, Ryr, ↑RYR1, ↑SGCA, ↑TRDN, ↑TRIM72 | 49 | 25 | Skeletal and Muscular System Development and Function, Organ Morphology, Cell Morphology |
| 3 | 26s Proteasome, ↑ACSL6, AMPK, ↑AQP4, ↑ASB10, ↑CAP2, ↑CFD, ↑COX6A2, ↑CYP2E1, ↑CYP2F1, ↑ELANE, hemoglobin, ↑HFE2, Hsp70, IgG, IgG1, ↑IGHM, IL1, Immunoglobulin, ↑IRF4, ↑KLHL38, Ldh (complex), ↑MLF1, NADPH oxidase, NFkB (complex), Nos, ↑PCK1, ↑PPP1R3A, Pro-inflammatory Cytokine, ↑PRTN3, ↑RIPK4, RNA polymerase II, ↑RORC, ↑SLC2A3, ↑TNFRSF19 | 39 | 21 | Cell-To-Cell Signaling and Interaction, Respiratory Disease, Tissue Morphology |
| 4 | ↑ASB5, ↑ASB14, ↑ASB15, CUL2, DLG4, DMD, DNMT1, ↑E230001N04Rik, EDRF1, ↑Fam13a, GSTP1, HSP90AA1, ↑IGFN1, ↑KCNA7, ↑KCNJ12, ↑LDB3, Lin7a, LIN7A, ↑MYADML2, ↑MYH1, MYH8, ↑MYL1, ↑MYLK4, ↑OBSCN, ↑PHKG1, phosphorylase, ↑PYGM, ↑RPL3L, SRF, ↑SYNPO2L, ↑TCAP, ↑TMOD4, TOX3, TUFM, ↑VWA7 | 39 | 21 | Skeletal and Muscular System Development and Function, Cellular Assembly and Organization, Cellular Development |

***Figure 3.29 IPA Network analysis of differentially expressed genes in D316A-Tg WATsc.***

*Representative output of IPA pathway analysis performed on DEGs between WT-Tg and D316A-Tg WATsc.*

The extent of the analysis provided by this software made it possible to determine bona fide networks of genes associated with skeletal muscle development, assembly

and metabolism, with three of the top four identified networks defined as skeletal muscle-associated (Fig 3.29).

It has been previously demonstrated that brown adipocytes and muscle cells share a common progenitor cell, and can be manipulated *in* vitro to exhibit skeletal muscle characteristics, through the deletion of Prdm16, a key suppressor of the myogenic lineage in BAT (Seale et al., 2008). Furthermore, disruption of the Prdm16/EHMT1 complex *in vivo* has been shown to promote muscle gene expression in BAT, highlighting the fine control of this lineage in mature tissue to maintain a brown-cell phenotype (Ohno et al., 2013).

To further characterise the transcriptome of this tissue, a second gene ontology analysis was performed, this time focussing on the top 100 significantly upregulated genes. Of these 100, almost all were directly associated with skeletal muscle processes (Fig 3.30A) including contraction, development and calcium signalling. From these 100 upregulated genes, 40 were selected based on known function, common upstream regulators and previously published data outlined above, examining the ability of brown adipose to exhibit muscle-like gene signatures in response to genetic manipulation (Fig 3.30B).

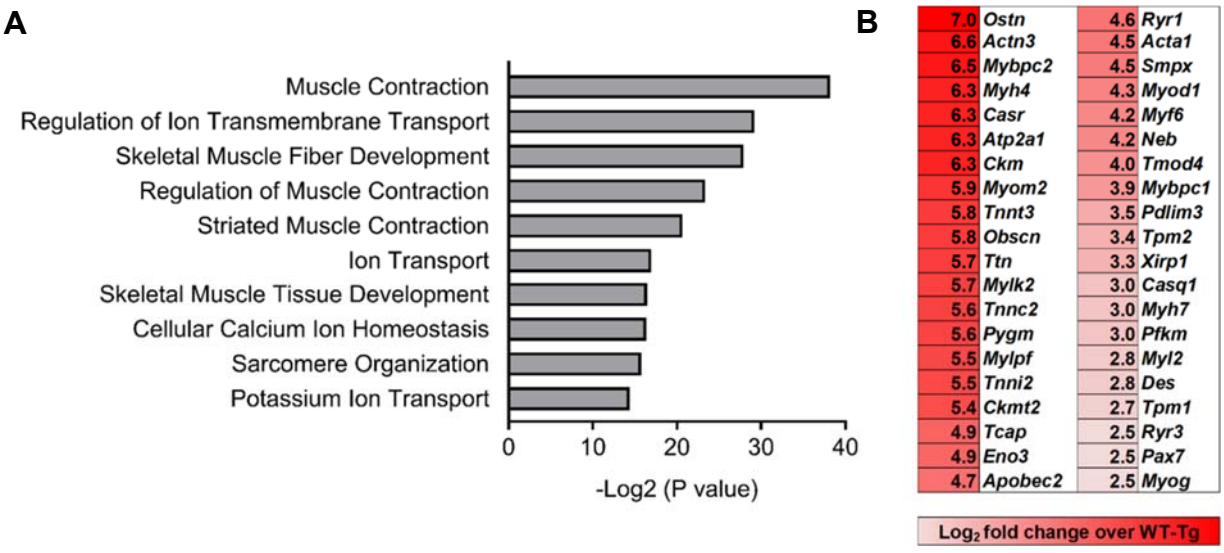



***Figure 3.30 Characterisation of muscle gene expression in D316A-Tg WATsc.***

***A)*** *Gene ontology enrichment analysis based on top 100 differentially expressed genes.*

***B)*** *Log2 fold change of 40 selected genes in D316A-Tg WATsc associated with skeletal muscle differentiation, fibre assembly and metabolism.*

### 3.3.5 Confirmation of DEG expression by qPCR

The data presented thus far provide insight into the substantial evidence for the initiation of a skeletal muscle-associated transcriptional programme in the WATsc of D316A-Tg HFD-fed mice. To confirm these findings, qPCR was performed on randomly selected genes from the top 100 DEGs identified by RNA sequencing. Expression of creatine kinase (Ckmt2), nebulin (Neb), enolase 3 (Eno3) and troponin C2 (Tnnc2) was increased in WATsc from 16-week HFD fed D316A-tg mice (Fig 3.31). The expression of Tnnc2 was deemed not significant based on high variability, with one sample exhibiting a 17-fold increase in expression over WT-Tg controls.

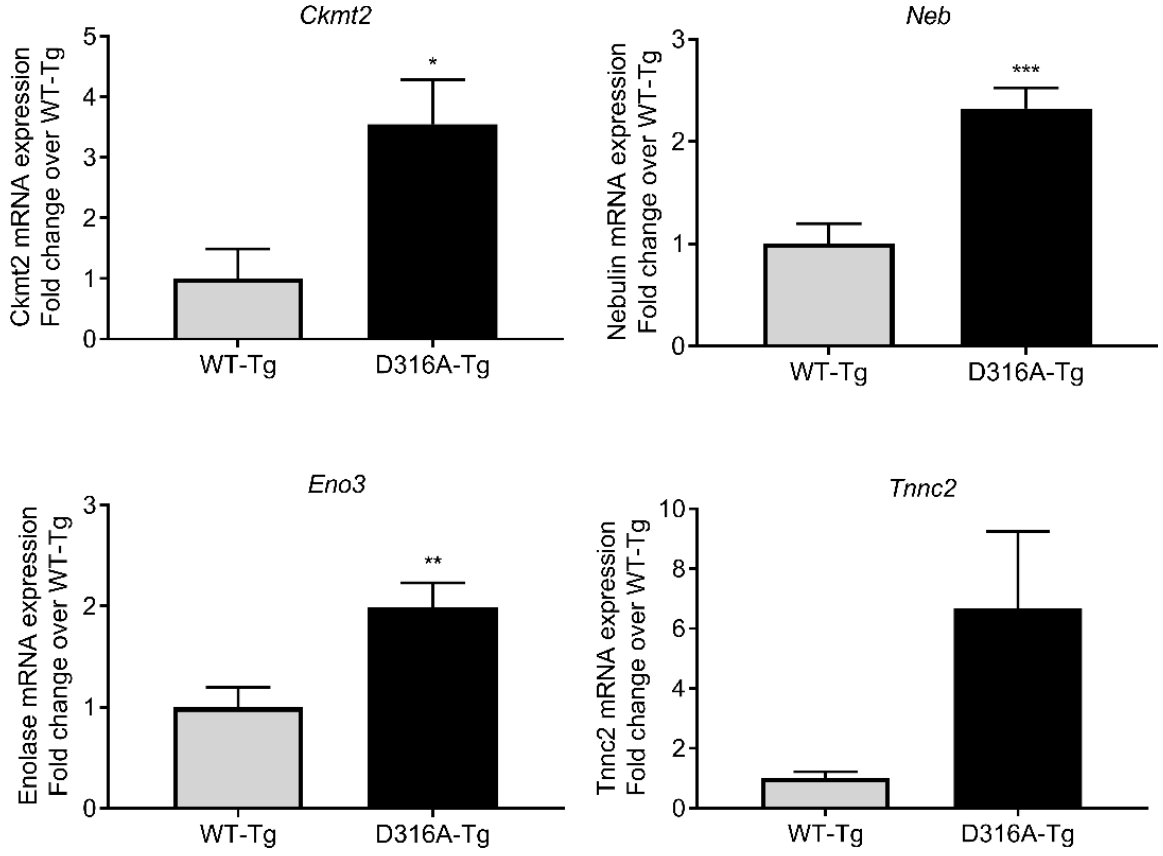



***Figure 3.31 Differentially expressed gene confirmation by qPCR***

*Confirmation of DEG expression in WATsc from 16-week HFD-fed (24-week old) D316A-Tg mice by qPCR. N=6, 6, Data are presented as mean ±SEM. *P<0.05, **P<0.01, ***P<0.001.*

Of the genes identified here, several have since been associated with a creatine-driven futile cycle in beige adipocytes, in a cold-exposed UCP1 knock-out mouse model, namely creatine kinase (Ckm) and creatine kinase, mitochondrial, muscle

(Ckmt2) (Kazak et al., 2015). Though these genes were significantly upregulated in D316A-Tg WATsc, no difference was observed in the expression of UCP1 using RNA sequencing, further substantiating previous evidence that the increased EE, exhibited by the D316A-Tg mouse model, is not UCP1-mediated. Additionally, these findings suggest that alternative thermogenesis can be driven by other mechanisms other than the ablation of UCP1.

Given that creatine metabolism has since been shown to drive energy expenditure in the WAT of cold-acclimatised mice when UCP1 is absent, Western blotting was performed to assess the expression of creatine kinase (mitochondrial) (Ckmt2) in D316A-Tg WATsc at the protein level. In addition, samples from chow-fed mice were assessed, to establish whether expression is driven by HFD-feeding, or is attributable to AMPK activation alone.

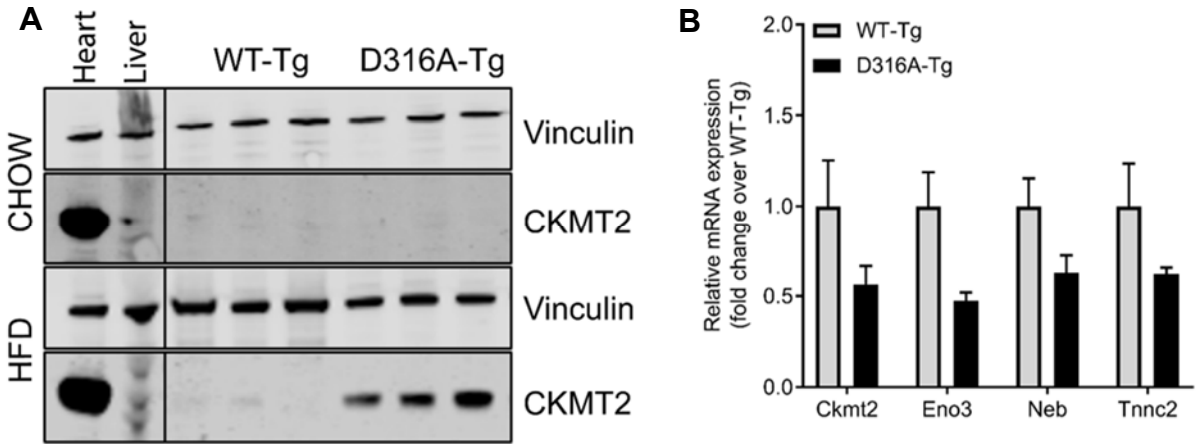



***Figure 3.32 Creatine kinase protein expression in chow and HFD-fed mice***

***A)*** *Expression of creatine kinase (Ckmt2) in WATsc from 16-week old chow-fed and 16-week HFD-fed (24-week old) WT-Tg and D316A-Tg mice as assessed by Western blotting. Heart homogenate was used as a positive control for Ckmt2 expression. N=3, 3 per diet.*

***B)*** *Expression of selected DEG mRNA in WATsc from 16-week old chow-fed WT-Tg and D316A-Tg mice assessed by qPCR. No significant differences were observed. N=6, 6. Data are presented as mean ±SEM.*

Interestingly, no expression of Ckmt2 was detected in chow-fed WT-Tg or D316A-Tg samples, but was robustly expressed in WATsc from 16-week HFD-fed D316A-Tg mice (Fig 3.36A). This finding was confirmed by qPCR analysis showing no increase in Ckmt2 mRNA in WATsc isolated from WT-Tg and D316A-Tg chow-fed mice (Fig

3.33B). Upon further investigation, none of the previously selected muscle-related genes were found to be expressed by D316A-Tg WATsc from mice fed a chow diet (Fig 3.32B), suggesting that the muscle-specific transcriptional programme may initiated by exposure to a HFD.

To investigate this hypothesis, attention was focussed on the nature of the WATsc from chow-fed D316A-Tg mice, to establish whether the brown-like adipocyte morphology seen in HFD-fed WATsc samples was also prompted by HFD-feeding.

### 3.3.6 Characterisation of D316A-Tg WATsc on a chow diet

To establish whether brown-like adipocyte morphology was present in WATsc from 16-week old chow-fed D316A-Tg mice were stained with haematoxylin to highlight cell morphology. The WATsc from D316A-Tg chow-fed mice exhibited significant

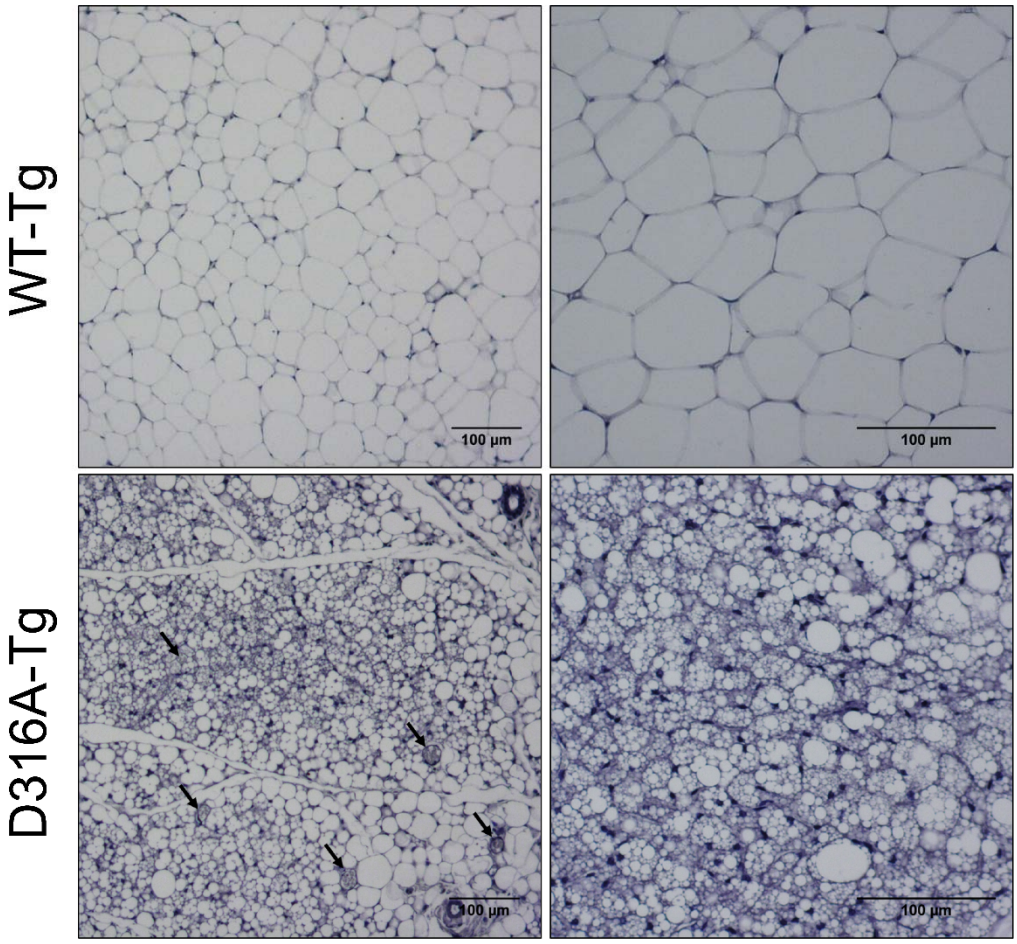



***Figure 3.33 'BAT-like' morphology of D316A-Tg WATsc on a chow diet***

*Haematoxylin staining of WATsc from chow-fed WT-Tg and D316A-Tg 16-week-old male mice. Scale bar 100µm, magnification at 10x (left) and 20x (right).*

development of hexagonal-shaped multilocular adipocytes characteristic of brown adipose tissue, resembling an inversion of classical 'beiging', with only patches of mature white adipocytes (Fig 3.33). In addition, all samples exhibited a striking increase in micro-vascularisation, a well-established feature of brown adipose (Fig 3.33, black arrows).

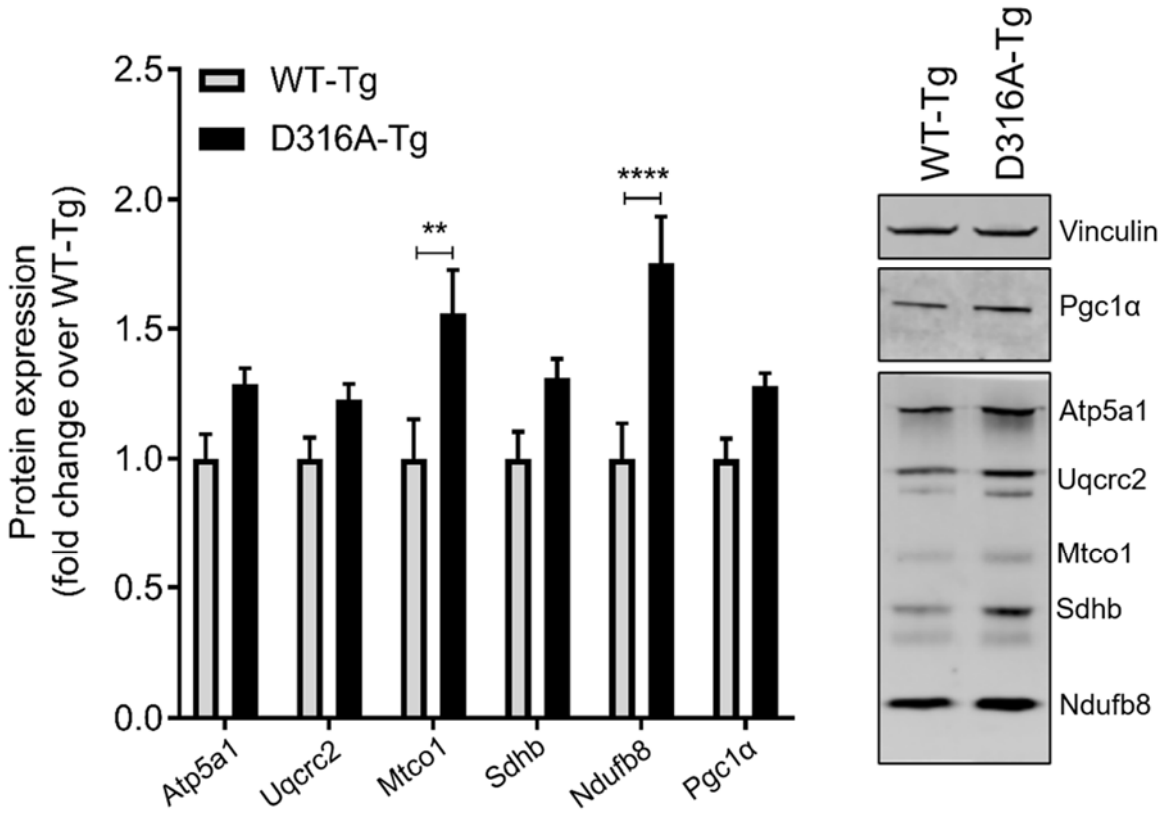



***Figure 3.34 Mitochondrial biogenesis in chow-fed D316A-Tg mice***

*Quantification and representative Western blot of mtRC and PGC1α protein expression in WATsc from 16-week old chow-fed WT-Tg and D316A-Tg mice. N=4, 4. Data are presented as mean ±SEM. **P<0.01, ****P<0.0001.*

*Mitochondrial respiratory chain complexes; Atp5a1, ATP synthase (CV); Uqcrc2, cytochrome b-c1 (CIII); Mtco1, cytochrome c oxidase 1 (CIV); Sdhb, succinate dehydrogenase (ubiquinone, iron-sulphur) (CII); Ndufb8, NADH: ubiquinone oxidoreductase subunit B8 (CI).*

Given that D316A-Tg WATsc exhibited several features of brown adipose, yet chow-fed D316A-Tg mice exhibit no overt metabolic phenotype, either basally or in response to β3-adrenergic stimulation, it was important to establish whether this morphology was indicative of mitochondrial content as seen in HFD-fed D316A-Tg mice. To investigate this, whole WATsc homogenates from 16-week-old chow-fed WT-Tg and

D316A-Tg mice were assessed for mtRC protein expression by Western blotting. Interestingly, though a significant upregulation of complexes four and one were detected, this morphology did not confer as great an increase in mtRC protein expression as seen on a HFD, perhaps due in part to a reduction in the respiratory chain components and PGC1α in the adipose of WT-Tg HFD-fed mice (Fig 3.38). To assess mitochondrial content irrespective of respiratory chain components, paraffin-embedded WATsc from chow-fed and HFD-fed mice were stained using immunofluorescence, for the presence of the outer mitochondrial membrane protein TOMM20/TOM20 (Translocase of the Outer Mitochondrial Membrane).

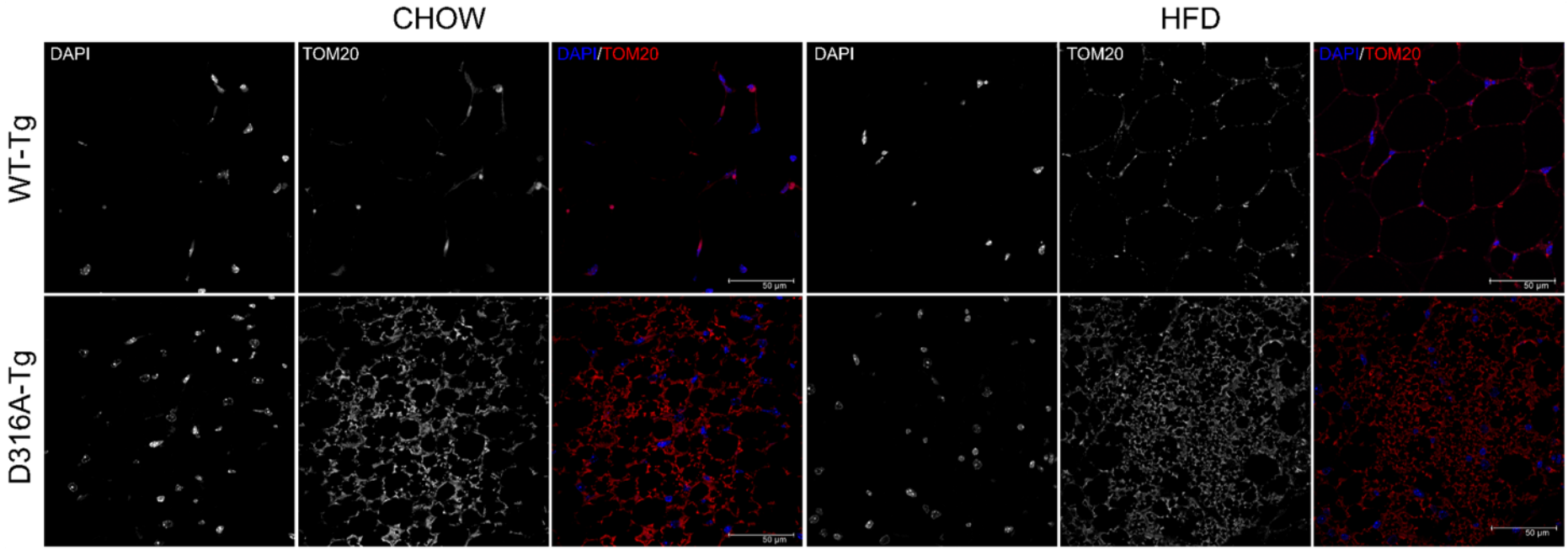



***Figure 3.35 Mitochondrial content in WATsc of chow- and HFD-fed D316A-Tg mice***

*Immunofluorescent staining of mitochondrial membrane protein TOM20 (red) in WATsc from chow-fed and 4-week HFD-fed WT-Tg and D316A-Tg mice. Nuclei were identified by DAPI nuclear staining (blue). Scale bar 50µm.*

WATsc from both chow-fed and HFD-fed D316A-Tg mice displayed a significant increase in TOM20 staining when compared to WT-Tg counterparts (Fig 3.35). Interestingly, mitochondrial staining in chow-fed WT-Tg mice was intensified in regions surrounding the nucleus, with little staining in any other region of the cell. In contrast, WT-Tg WATsc on a HFD exhibited an increase in staining at the cell membrane, though the number of cells in the field of view appeared reduced. No quantification of this parameter has been performed to date, though further investigation into the effects of HFD-feeding on mitochondrial dynamics in WT-Tg and D316A-Tg WATsc is ongoing.

Given that D316A-Tg WATsc on a chow diet exhibits several hallmarks of brown adipose, including multilocular adipocytes, increased mitochondrial content and vascularisation, it was hypothesised that these cells were in fact brown adipocytes, as opposed to 'beige', and may be derived from $Myf5^{+}$ precursors.

To determine whether WATsc isolated from chow-fed D316A-Tg mice reflected a classical brown adipose depot, samples from 16-week-old chow-fed mice were analysed for UCP1 and Prdm16 expression, in conjunction with PPARγ expression, known to promote brown adipocyte development through its co-activator PGC1α and interaction with Prdm16, using qPCR. In addition, samples were also analysed from HFD-fed mice, to determine whether the presence of dietary lipid may alter the gene expression profile of these cells to promote myogenic gene expression *in vivo*.

Interestingly, a small but significant upregulation of UCP1 mRNA was observed in chow-fed D316A-Tg WATsc (Fig 3.36), consistent with high mitochondrial content, though this was not detected at protein level.

No significant increase in UCP1 expression was observed after 4 weeks of HFD-feeding, as confirmed previously. However, on a chow diet, D316A-Tg WATsc exhibited a 6.15-fold increase in Prdm16 expression, a key regulator of the brown adipocyte phenotype and suppressor of the myogenic transcription factor myogenin (MyoG) (Kajimura et al., 2009).

A similar increase was seen in the expression of PPARγ (6.7-fold), a principal regulator of both brown adipocyte thermogenesis and development when in the presence of other BAT-specific transcription factors, as well as the development of white adipocytes when expressed alone (Tontonoz et al., 1994).

A 15-fold increase in expression in PPARγ was observed between WT-Tg WATsc on a chow and a HFD, consistent with WAT expansion. Perhaps the most surprising finding, however, was the further enhancement of PPARγ expression in D316A-Tg WATsc on a HFD, with no concurrent increase in any other brown-adipose related genes at this time point, and a small decrease observed in total Prdm16 and UCP1 expression (Fig 3.36).

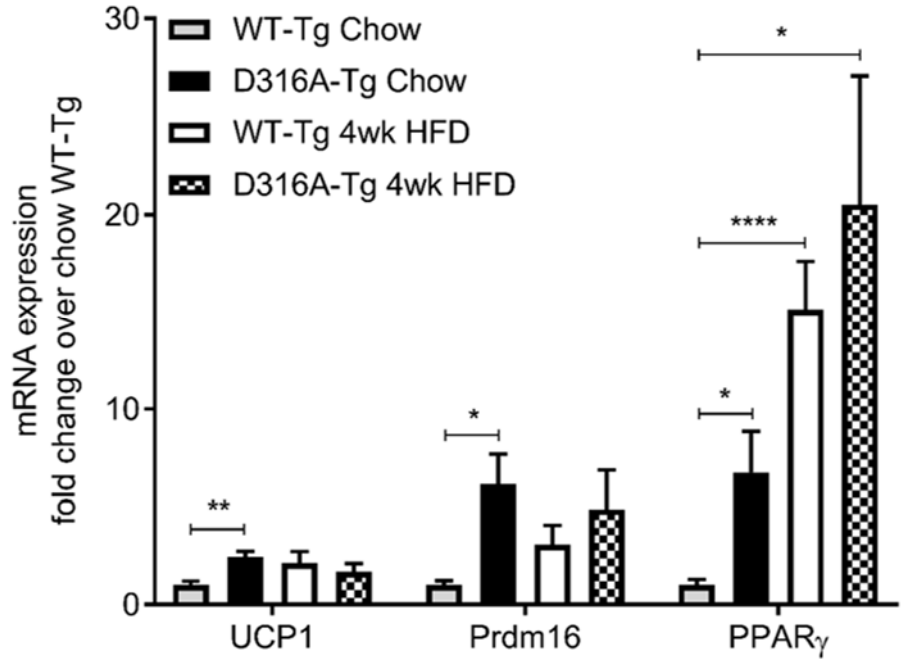



***Figure 3.36 BAT-associated gene expression in D316A-Tg WATsc***

*Expression of brown adipose related genes in WATsc from chow- and 4-week HFD-fed (12-week old) WT-Tg and D316A-Tg mice. Gene expression presented as fold change over mean chow-fed WT-Tg. N=6, 6 per diet. Data are presented as mean ±SEM. *P<0.05, **P<0.01, ****P<0.0001.*

### 3.3.7 Lineage determination in D316A-Tg WATsc

From analysis of RNA-sequencing data, it was determined that, in addition to several genes associated with energy expenditure, there was a significant shift towards early myoblastic gene expression, with the presence of Myf6, MyoD1, Pax7 and the myogenic transcription factor MyoG. If indeed the WATsc of D316A-Tg chow-fed mice more closely resembled BAT, the expression of the myogenic lineage and MyoG itself would require active repression. In classical BAT, this repression is mediated by the Prdm16/EHMT1 complex (Inagaki et al., 2016).

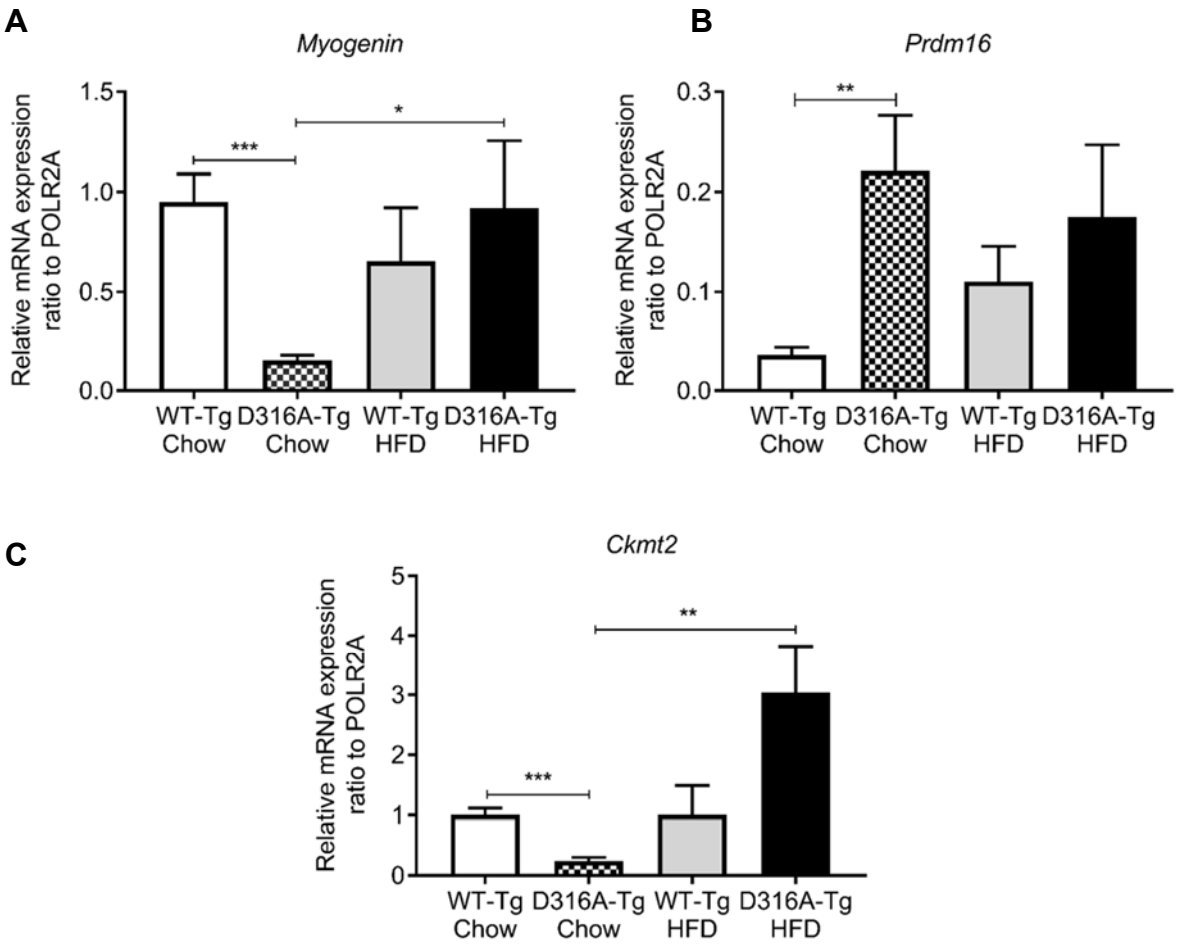



***Figure 3.37 Evidence for a BAT-muscle transition in D316A-Tg WATsc***

*Expression of MyoG, Prdm16 and Ckmt2 in isolated WATsc from chow-fed and 4-week HFD-fed WT-Tg and D316A-Tg male mice. Data are presented relative to the housekeeping gene Polr2a. N=6, 6 per diet. Data are presented as mean ±SEM. *P<0.05, **P<0.01, ***P<0.001.*

As a preliminary investigation into this hypothesis, mRNA expression of MyoG in the WATsc of chow-fed and HFD-fed D316A-Tg mice was assessed by qPCR. it was found that D316A-Tg WATsc exhibited complete repression of myogenin expression on a chow diet (Fig 3.37A), with a concurrent increase in Prdm16 expression when compared to WT-Tg controls (Fig 3.7B). After 4 weeks of HFD-feeding, this repression was removed, coinciding with the onset of expression of Ckmt2 (Fig 3.37C).

Deletion of either Prdm16 or EHMT1 leads to the development of *bona fide* muscle cells *in vitro*, characterised by the expression of MyoG, MyoD and Ckm, also upregulated in D316A-Tg WATsc.

To begin to examine whether the disruption of the Prdm16/EHMT1 complex may also be a driving factor in the D316A-Tg mouse model in response to HFD-feeding, differentially expressed genes from RNA-sequencing performed on EHMT1 KO embryonic BAT was compared to that of WATsc from HFD-fed D316A-Tg mice. Of the 25 genes published by Ohno *et al.,* 18 were also found to be significantly upregulated in the WATsc of D316A-Tg HFD-fed mice (Fig 3.38) (Ohno et al., 2013).

Of the 18 common genes found, MyoG and Myf6 were identified as regulators of the skeletal muscle transcriptional programme, with others such as calsequestrin (Casq1) and ryanodine receptors 1 and 3 (Ryr1, Ryr3) involved in a well-known calcium futile cycle involving SERCA in skeletal muscle. Other regulators of calcium cycling and homeostasis in skeletal muscle were also found to be upregulated in D316A-Tg WATsc upon HFD-feeding, including the calcium receptor Casr and phospholamban (Pln), previously implicated in alternative thermogenesis in UCP1$^{-/-}$ cold acclimatised mice (Ukropec et al., 2006).

| Unique to D316A-Tg | Common | Unique to EHMT1 KO |
|---|---|---|
| Actn2 | Acta1 | Actc1 |
| Actn3 | Casq1 | Agt |
| Apobec2 | Mybpc1 | Flnc |
| Atp2a1 | Mybpc2 | Myh8 |
| Atp2b3 | Myf6 | Myl6b |
| Casr | Myh7 | Smtnl1 |
| Ckm | Myl2 | Tnnc1 |
| Ckmt2 | Mylpf | |
| Des | Myog | |
| Eno3 | Myom2 | |
| Mrln | Neb | |
| Myh2 | Pdlim3 | |
| Myh4 | Ryr1 | |
| Myl1 | Ryr3 | |
| Mylk2 | Tcap | |
| Mylk4 | Tpm2 | |
| Myod1 | Ttn | |
| Myom1 | Xirp1 | |
| Myoz1 | | |
| Myoz2 | | |
| Myoz3 | | |
| Mypn | | |
| Obscn | | |
| Ostn | | |
| Pax7 | | |
| Perm1 | | |
| Pfkm | | |
| Pygm | | |
| Smpx | | |
| Tmod4 | | |
| Tnnc2 | | |
| Tnni2 | | |
| Tnnt3 | | |
| Tpm1 | | |
| Trp73 | | |

***Figure 3.38 Overlap of gene expression between D316A-Tg WATsc and EHMT1 KO BAT.***

*Comparison of EHMT1 KO muscle-related genes (18) with the top 53 muscle-related genes defined by similar gene ontology in the WATsc of HFD-fed D316A-Tg mice. Of the genes presented by Ohno et al., 2013, 18 were common to both EHMT1 KO BAT and D316A-Tg WATsc.*

To confirm whether these cells were classical brown adipocytes on a chow diet, D316A-Tg WATsc was stained with the endothelial cell marker PECAM1/CD31, also a marker of classical BAT (Rosso and Lucioni, 2006) by DAB immunohistochemistry. The pattern of staining observed was unprecedented, with many cells staining strongly for CD31 (Fig 3.39). in addition to the anticipated staining of the vasculature (blue arrows). No specific staining was observed in WT-Tg WATsc (inset), nor in the observable mature white adipocytes within D316A-Tg WATsc.

Though preliminary, the expression of PECAM1 in a large proportion of multilocular adipocytes in WATsc suggests D316A-Tg WATsc more closely resembles classical BAT than WAT, though negative for UCP1 expression.

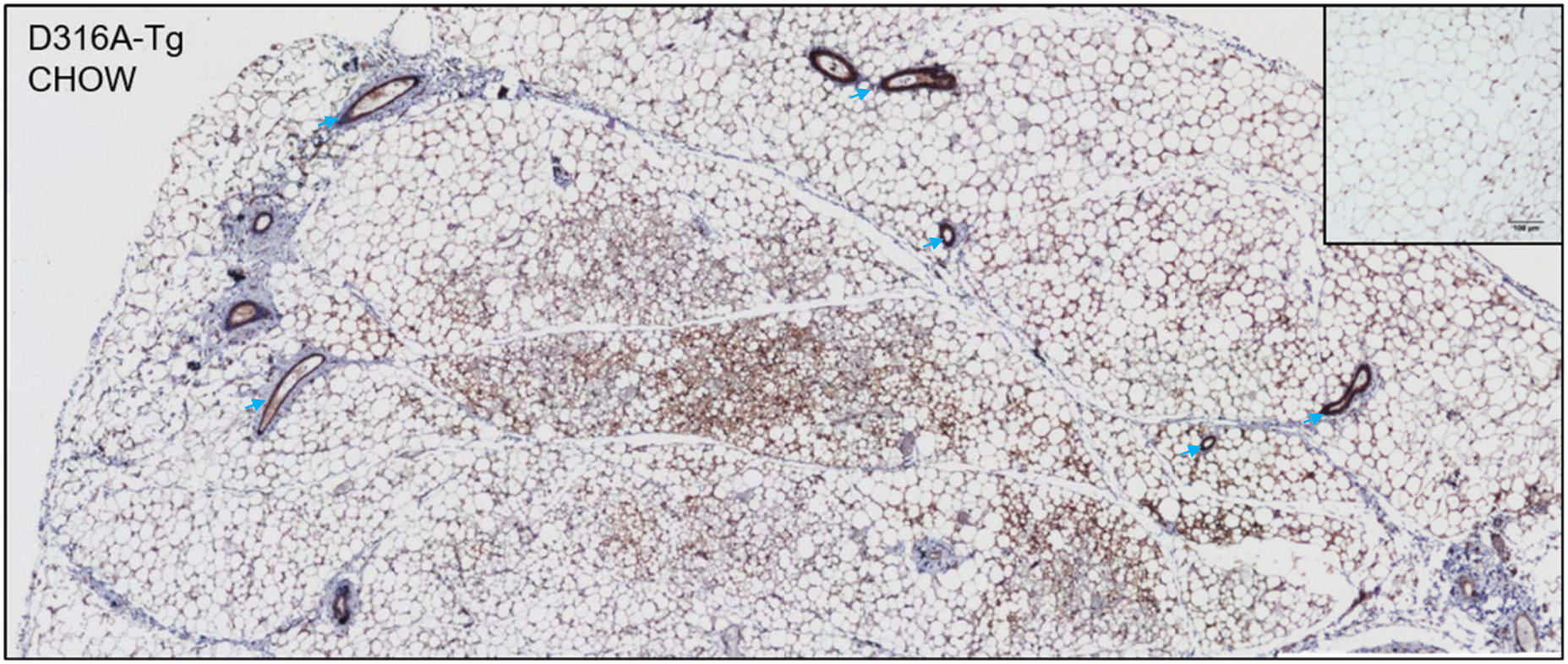



***Figure 3.39 Evidence for the endothelial origin of D316A-Tg WATsc.***

*PECAM1 staining for cells of endothelial cell origin (BAT) in WATsc from 16-week-old chow-fed D316A-Tg mice. Blue arrows indicate vasculature thought to provide a stem cell niche.*

### 3.3.8 Mitochondrial activity (O2K)

One aspect of the D316A-Tg mouse model that provided an intriguing avenue of exploration was the observation that, on a chow diet, mitochondrial content of the WATsc did not confer any overt metabolic phenotype. It was hypothesised that the presence of lipid due to HFD feeding stimulated D316A-Tg WATsc mtRC protein expression, mitochondrial respiration and subsequent ATP synthesis. To examine this hypothesis, whole adipocytes were isolated from the WATsc of chow-fed WT-Tg and D316A-Tg mice and oxygen consumption measured using an OROBOROS Oxygraph-2K high-resolution respirometer.

Whole WATsc cell suspensions from chow-fed WT-Tg and D316A-Tg male mice were analysed for basal respiratory rate, maximum uncoupling potential (FCCP) and response to mtRC inhibitors Oligomycin, Rotenone and Antimycin A. No significant differences were found in basal respiration, nor in response to Oligomycin, used to induce ‘leak’ respiration via inhibition of $F_0$ ATP synthase. In addition, no differences were found in response to the addition of the FCCP, a weak acid protonophore capable of uncoupling oxidation from phosphorylation, or after complex I inhibition with rotenone (Fig 3.40). On the basis of these results, it was concluded that, in the absence of substrate, D316A-Tg WATsc mitochondria are neither dysfunctional nor more active than their WT-Tg counterparts. To evaluate the potential for mitochondrial respiration in response to substrate, initial experiments were performed using sodium palmitate solution.

The addition of palmitate solution (PA) to WT-Tg WATsc cell suspension did not elicit any significant increase in oxygen consumption. An increase in oxygen consumption was observed in D316A-Tg WATsc, though due to high variability was not statistically significant. Nevertheless, this result was reproduced on two other occasions, suggesting that simply the presence of lipid substrate is sufficient to stimulate mitochondrial respiration in D316A-Tg WATsc.

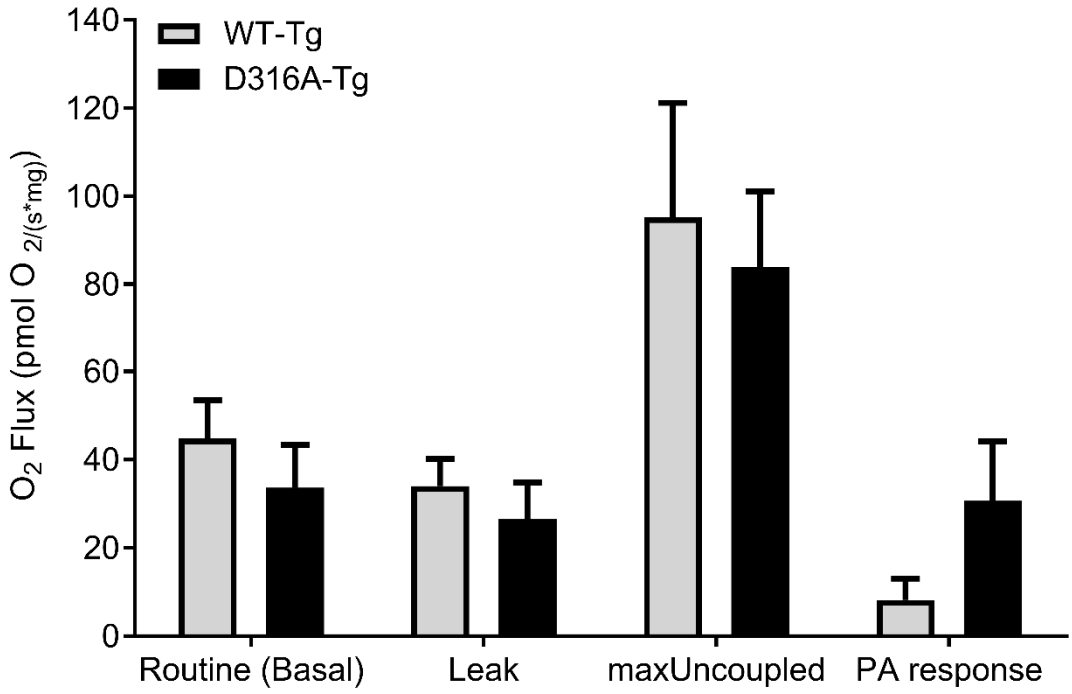



***Figure 3.40 Mitochondrial respiration and response to palmitate in D316A-Tg WATsc***

*Mitochondrial stress test in whole WATsc cell suspensions from chow-fed WT-Tg and D316A-Tg 10-12-week old mice. Basal respiration was determined prior to the addition of Oligomycin to induce leak respiration. Maximum uncoupled respiration determined by addition of FCCP. $O_2$ consumption (increase over basal respiration) in response to the addition of palmitate (PA). N=4, 4 per experiment. Data presented as the mean ±SEM of 5 independent experiments.*

Though these results are promising, further investigations into the effects of fatty acids on mitochondrial metabolism in D316A-Tg WATsc are ongoing, with emphasis on the ability of HFD-feeding to stimulate both mitochondrial respiration and alternative thermogenesis in this model.

## 3.4 Tamoxifen Inducible Model

To further validate AMPK as a therapeutic target *in* vivo, it was necessary to establish whether activation of AMPK in this manner could reverse the negative effects of HFD-feeding in adult mice

To examine the effects of AMPK activation in adult mice, D316A-Tg$^{flox/STOP/flox}$ were paired with a tamoxifen-inducible CAGGCre-ER$^{TM}$ mouse expressing cre-recombinase driven by the chicken beta actin promotor/enhancer coupled with the cytomegalovirus immediate-early enhancer (The Jackson Laboratory). Tamoxifen administration in progeny of this pairing resulted in the global expression of the D316A-Tg protein, as assessed by Western blotting. D316A-Tg$^{TMX}$ was detected in whole kidney, liver and heart, and in immunoprecipitates (IP) of FLAG-eluted kidney homogenates from non-Tg (WT$^{TMX}$) and D316A-Tg$^{TMX}$ mice, 3-weeks post-induction (Fig 3.41).

All terminal studies presented were conducted on mice at 10-weeks post induction, where it was subsequently determined that D316A-Tg expression could not be detected, suggesting that further induction was required to maintain expression.

To investigate the effect of the induction of AMPK activation on bodyweight, 8-week-

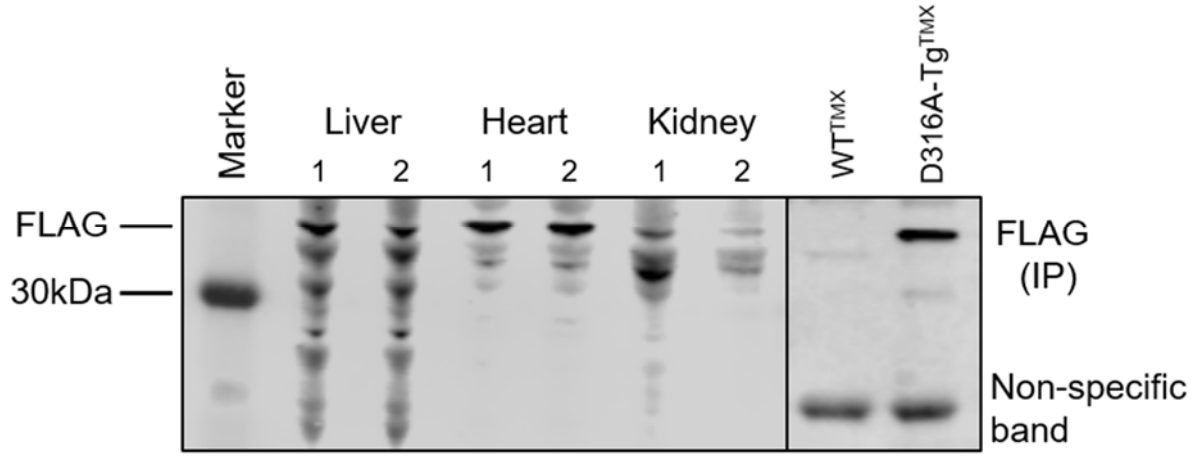



***Figure 3.41 Detection of tamoxifen-induced D316A-Tg-FLAG expression.***

*Confirmation of D316A-Tg FLAG expression in liver, heart and kidney isolated from two D316A-Tg$^{TMX}$ mice (1+2). Immunoprecipitation of FLAG-tagged D316A-Tg protein from WT (non-Tg) and D316A-Tg$^{TMX}$ kidney homogenate.*

old non-transgenic (WT$^{TMX}$) and D316A-Tg$^{TMX}$ mice were fed a 45% calories from fat HFD for 4 weeks prior to Tamoxifen administration (TMX). No differences were

observed in bodyweight prior to injection. Both genotypes exhibited significant acute reduction in bodyweight in response to TMX, as previously reported (Ye et al., 2015), which was stabilised 2 weeks post-IP and normal growth restored after 4 weeks (Fig 3.42).

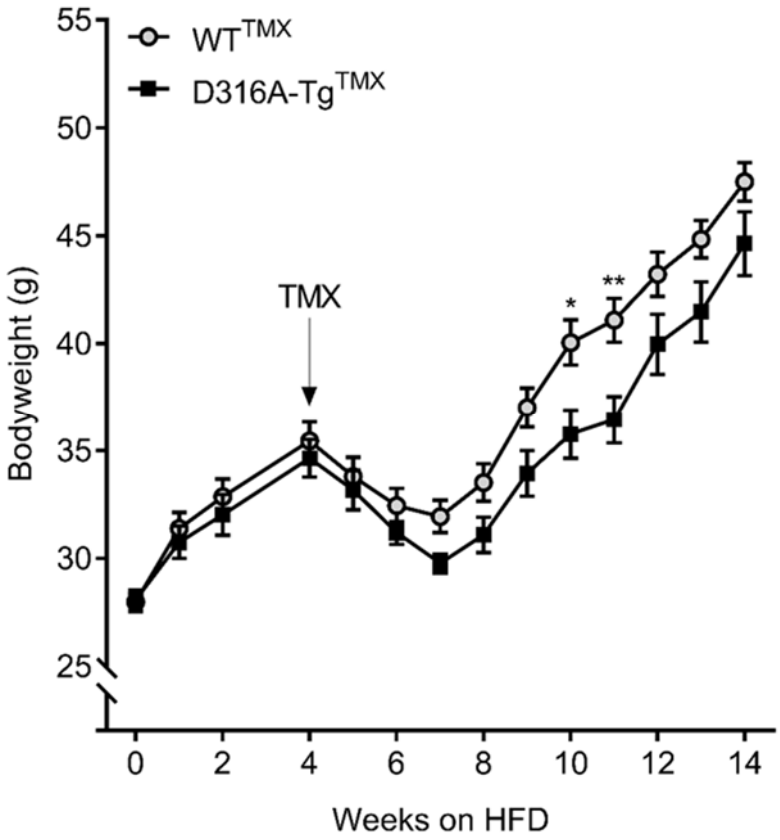



***Figure 3.42 Bodyweight curve of HFD-fed WT$^{TMX}$ and D316A-Tg$^{TMX}$ male mice.***

*Animals were fed a HFD for 4 weeks prior to tamoxifen administration (TMX). N=9, 9, Data are presented as mean ±SEM. *P<0.05, **P<0.01.*

The bodyweight of D316A-Tg$^{TMX}$ mice remained significantly lower than WT$^{TMX}$ mice for a further three weeks before convergence was observed. The study was terminated after 14 weeks of HFD feeding, 10 weeks post induction. No FLAG expression was detected at this time point.

To determine whether the reduction in bodyweight was attributable to a reduction in adiposity, total fat mass was assessed by echo MRI (eMRI). No difference in fat mass was observed prior to tamoxifen administration. After 5 weeks, D316A-Tg$^{TMX}$ mice

exhibited protection from HFD-induced adiposity, with no significant fat mass gain during this period (Fig 3.43).

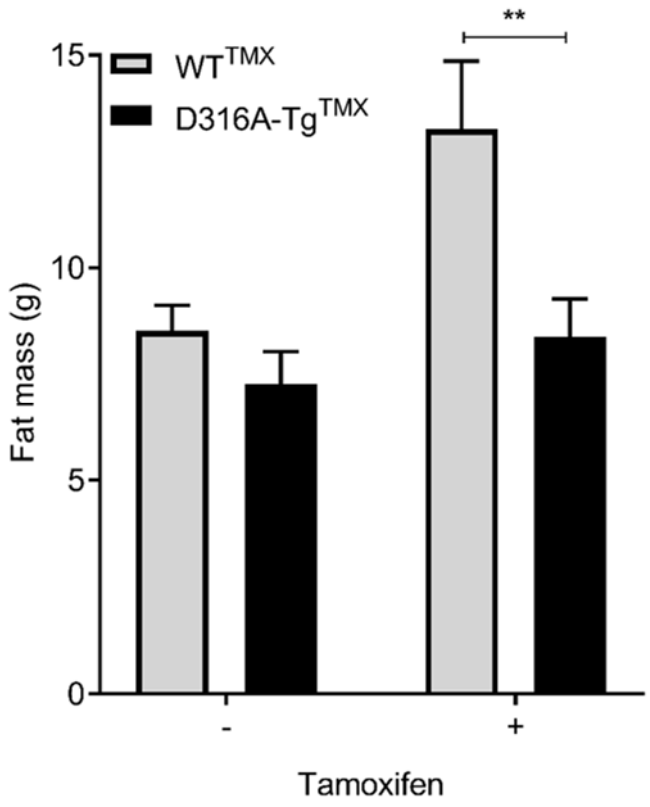



***Figure 3.43 Total body composition of WT$^{TMX}$ and D316A-Tg$^{TMX}$ HFD-fed mice.***

*Total body composition as assessed by eMRI, before and 5 weeks after TMX administration. N=9, 9. Data are presented as mean ±SEM. **P<0.01.*

Terminal blood samples were taken after 14 weeks of HFD-feeding and assessed for circulating insulin. As seen in non-inducible D316A-Tg HFD-fed mice, D316A-Tg$^{TMX}$ mice exhibited significantly lower circulating insulin concentration than WT$^{TMX}$ HFD-fed counterparts (Fig 3.44A), as well as complete protection from liver triglyceride accumulation (Fig 3.44B) after 14 weeks of HFD-feeding, suggesting that, though no FLAG expression could be detected at this time, transient activation of AMPK conferred by D316A-Tg mutation is sufficient to protect from HFD-associated hepatic steatosis.

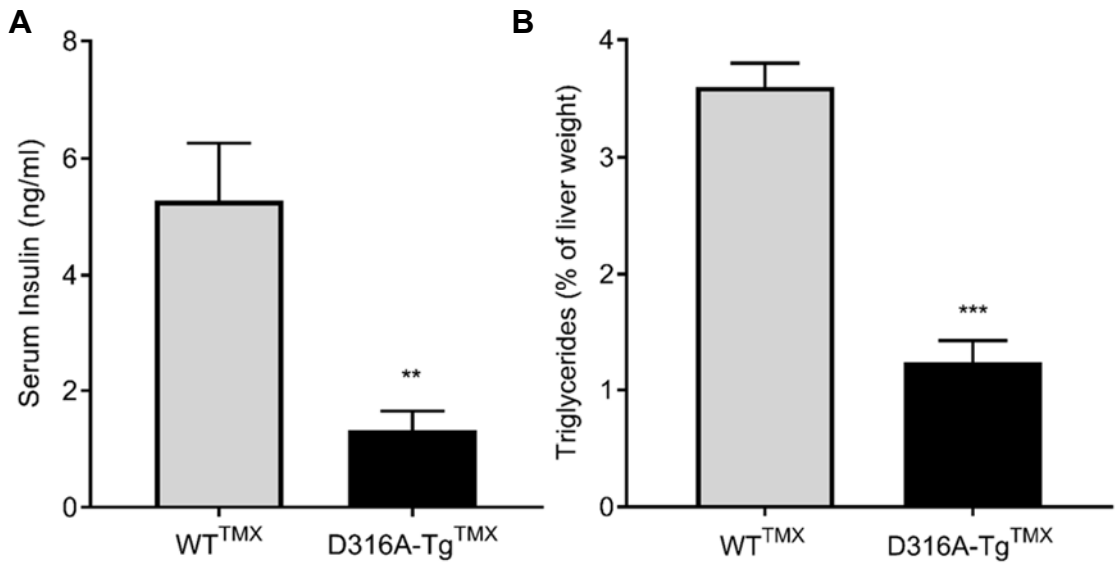



***Figure 3.44 Protection from HFD-associated hyperinsulinaemia and hepatic steatosis in D316A-Tg$^{TMX}$ mice.***

***A)*** *Serum insulin concentrations of ad libitum HFD-fed WT$^{TMX}$ and D316A-Tg$^{TMX}$, 10 weeks after administration of tamoxifen. N=5, 5. Data are presented as mean ±SEM. **P<0.01.*

***B)*** *Liver triglyceride content of HFD-fed WT$^{TMX}$ and D316A-Tg$^{TMX}$ mice 10 weeks post induction. Triglyceride concentrations are presented as a percentage of tissue wet weight. N=4, 4, Data are presented as mean ±SEM. ***P<0.001.*

To determine whether D316A-Tg$^{TMX}$ mice were protected from peripheral lipid accumulation, brown and subcutaneous white adipose depots were isolated, fixed and stained for visualisation of morphology.

WT$^{TMX}$ HFD-fed mice exhibited adipocyte hypertrophy in WATsc and considerable lipid accumulation in brown adipocytes, consistent with DIO (Fig 3.45, left). In contrast, D316A-Tg BAT did not display any excess lipid accumulation, with morphology comparable to a chow-fed mouse. Whilst no cells exhibiting a brown-like morphology were observed in D316A-Tg$^{TMX}$ WATsc, a considerable reduction in adipocyte size was apparent (Fig 3.45, right), as well as an increase in vascularisation; a previously described feature of D316A-Tg WATsc (Fig 3.50).

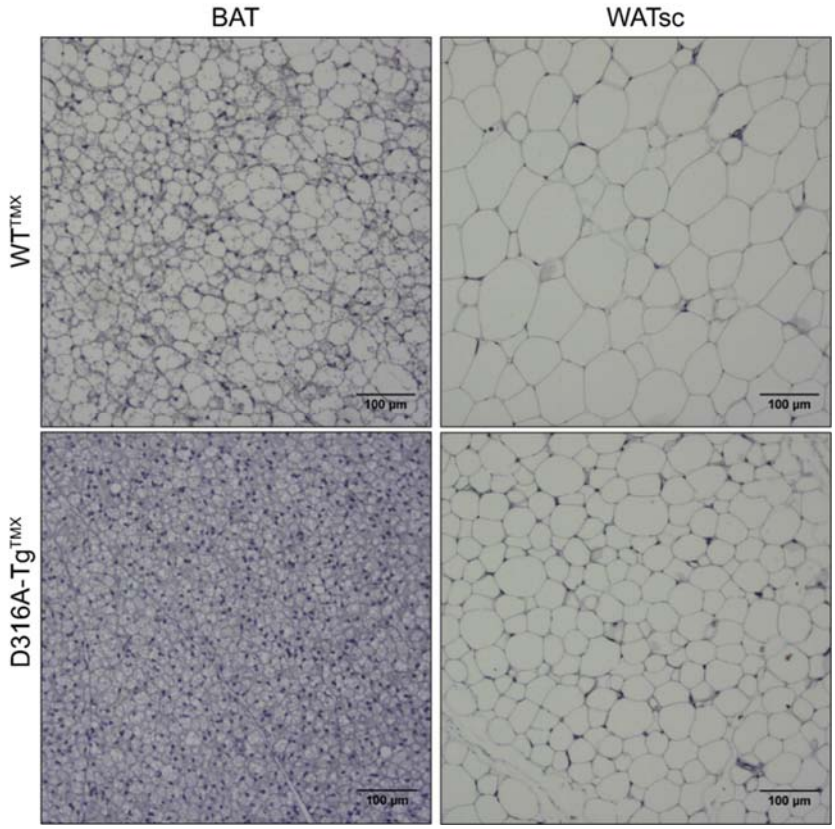



***Figure 3.45 Resistance to lipid accumulation in D316A-Tg$^{TMX}$ BAT and WATsc.***

*Haematoxylin staining of BAT and WATsc from 14-week HFD-fed WT$^{TMX}$ and D316A-Tg$^{TMX}$ mice. Scale bar 100µm.*

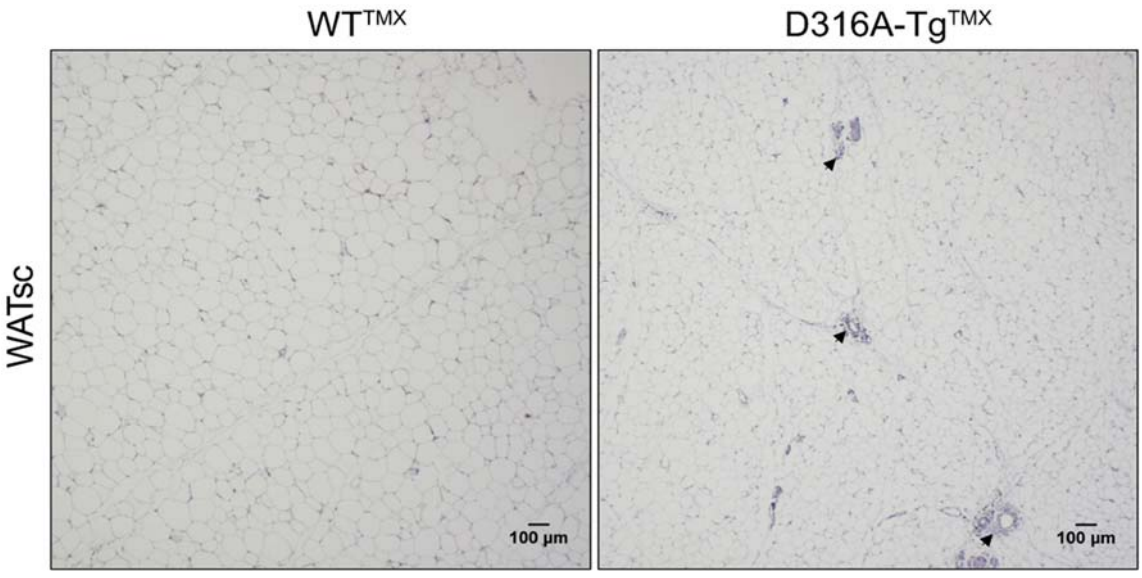



***Figure 3.46 Vascularisation of D316A-Tg$^{TMX}$ WATsc***

*Representative field-of-view containing regions of vascularisation in haematoxylin stained of WATsc from 14-week HFD-fed D316A-Tg$^{TMX}$ mice. WT$^{TMX}$ WATsc did not display any significant vascularisation in any section examined. Scale bar 100µm.*

To determine whether the decrease observed in WATsc adipocyte size was associated with an increase in mitochondrial content, whole WATsc homogenate was assessed for mtRC protein expression by Western blotting (Fig 3.47). After 14 weeks of HFD-feeding, WATsc from D316A-Tg$^{TMX}$ mice showed significant upregulation of complex V (ATP synthase) and complex II (succinate dehydrogenase) of the mitochondrial respiratory chain.

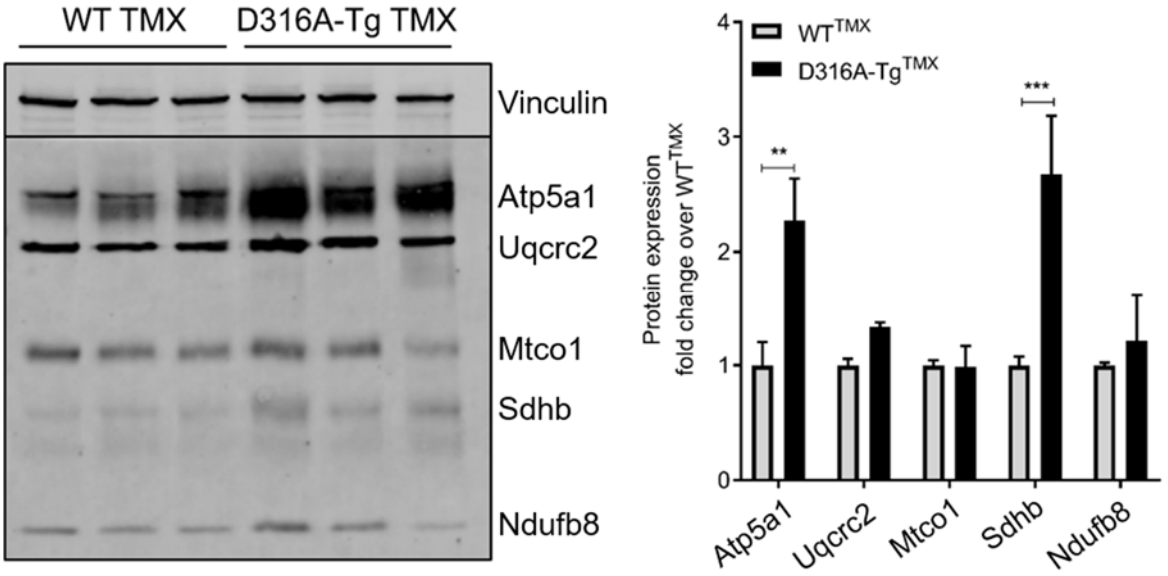



***Figure 3.47 Mitochondrial biogenesis in D316A-Tg$^{TMX}$ WATsc.***

*Representative Western blot and quantification of mitochondrial respiratory chain protein expression in WT$^{TMX}$ and D316A-Tg$^{TMX}$ WATsc after 14 weeks of HFD-feeding. N=6, 6, Data are presented as mean ±SEM. **P<0.01, ***P<0.001.*

*Mitochondrial respiratory chain complexes; Atp5a1, ATP synthase (CV); Uqcrc2, cytochrome b-c1 (CIII); Mtco1, cytochrome c oxidase 1 (CIV); Sdhb, succinate dehydrogenase (ubiquinone, iron-sulphur) (CII); Ndufb8, NADH: ubiquinone oxidoreductase subunit B8 (CI).*

Given that D316A-Tg$^{TMX}$ WATsc exhibited features similar to those of WATsc from non-inducible D316A-Tg HFD fed mice, mRNA was extracted and the expression of key brown adipocyte genes PGC1α and PPARγ assessed by qPCR. In addition, samples were assessed for the mRNA expression of muscle-related genes Ckm, Atp2a1 (SERCA) and Casr, all of which were identified as differentially expressed in D316A-Tg WATsc by RNA sequencing. The expression of both PGC1α and PPARγ was significantly upregulated in D316A-Tg$^{TMX}$ WATsc after 14 weeks of HFD-feeding, 10-weeks post induction (Appendices, Fig 6.3A). The expression of selected muscle-

related genes was also increased, though not statistically significant (Appendices, Fig 6.3B).

## 3.5 Discussion

### 3.5.1 Protection from Diet Induced Obesity

The D316A-Tg mouse model presents an attractive tool with which to ask questions of AMPK in the context of diet-induced obesity, with AMPK activity increased approximately 2-3 fold (Woods et al., 2017), similar to that induced by exercise (Narkar et al., 2008). In addition, activation does not rely on the uptake of compounds into specific tissues, which has been described as a potential barrier to the therapeutic benefits of available activators. It also enables animals to be monitored non-invasively, without the need for injection, oral administration or ingestion of a compound, all of which may induce additional stress and variation, thus interfering with results.

Many previous studies have explored protection from DIO, with varying degrees of resistance achieved through genetic, pharmacological and physical manipulation. However, most report only a modest protection, with animals gaining 50% less than the control HFD-fed group. A recent study described protection from DIO by disruption of the MDM2-RP11-p53 pathway, leading to enhanced repression of HFD-induced p53 expression. However, this study reports an approximate 20% reduction in HFD-induced bodyweight gain, with animals still exhibiting increased weight gain over their chow-fed counterparts (Liu et al., 2017).

Others show similar protection from HFD-induced obesity by inducing defects in key metabolic pathways, such as autophagy via a skeletal muscle-specific Atg knockout, leading to enhanced production of the mitokine Fgf21 from the liver (Kim et al., 2013). However, these animals also displayed a reduction in bodyweight on a chow diet, with significant muscular atrophy as a result of impaired autophagy. This finding was ameliorated by producing a liver-specific Atg knock-out, which produced a similar protection from bodyweight gain on a HFD (Kim et al., 2013), with a small reduction on a chow diet, exacerbated by HFD-feeding.

The D316A-Tg mouse model, therefore, presents a unique case of complete protection from HFD-induced bodyweight gain, with D316A-Tg mice following an almost identical bodyweight curve to their chow-fed counterparts, with no overt phenotype on a chow diet.

The normalisation of organ weight to bodyweight in HFD-fed mice introduced an interesting paradigm into this work, as it is a method which has attracted scrutiny and

is a topic of debate within the field of metabolism, particularly in rodents. The D316A-Tg mouse is significantly lighter in terms of body mass after 4-5 weeks of HFD-feeding, though slight differences between cohorts over the course of this work have been noted. However, significant tissue weight divergence is not seen at this time point, despite alterations in lipid accumulation (histological analysis) and cell morphology (adipose). After 16-weeks of HFD-feeding, significant differences are observed in both total bodyweight and fat mass, as assessed by eMRI. However, no differences in lean mass were observed in any cohort, either on a chow diet or a high fat diet. Adipose tissue wet weight reflected this divergence, with WT-Tg HFD-fed mice consistently exhibiting a higher WATsc mass than D316A-Tg counterparts. The process of normalising to total bodyweight on a HFD, whilst still yielding significant results, is not reflective of the significant protection from DIO in this model, as the reduction in body mass is directly reflected by a reduction in fat mass. Several studies have discussed the importance of correcting for body mass when examining metabolic parameters such as $VO_2$, with clear evidence for the removal of body mass correction in favour of a 'per mouse' measurement. In this instance an analysis of co-variance (ANCOVA) may be used (Tschop et al., 2011).

D316A-Tg mice also exhibit significant protection peripheral lipid accumulation, including hepatic steatosis, a key feature of the metabolic syndrome, associated with DIO. Indeed, the prevalence of hepatic steatosis is approximated at 30% in developed countries, and is a risk factor for the development of type 2 diabetes and non-alcoholic steatohepatitis (NASH) (Rinella, 2015).

As the development of hepatic steatosis is often secondary to increased adiposity, the reduction in liver triglyceride accumulation in the D316A-Tg mouse model may therefore be a consequence of reduced total organism adiposity, mediated by amelioration of energy imbalance by AMPK in WATsc. Indeed, this hypothesis is supported by the findings from the liver-specific activation of AMPK, expressing D316A-Tg protein under the control of albumin-cre, specific to mature hepatocytes, which did not confer protection from HFD-induced hepatic steatosis (Woods et al., 2017). However, in this model, animals were protected from liver triglyceride accumulation driven by a lipogenic, high fructose diet, through the direct inhibition of *de novo* lipogenesis by ACC phosphorylation. These findings suggest that the deposition of lipid in hepatocytes after HFD-feeding is driven predominantly by

saturation of existing lipid storage space in designated adipose depots, and is not driven by *de novo* lipogenesis in the liver. In contrast, fructose is metabolised exclusively by the liver, and contributes to a significantly higher rate of *de novo* lipogenesis. The global D316A-Tg mouse model exhibited a striking decrease in total adiposity, supporting the aforementioned hypothesis that the protection from hepatic lipid accumulation is secondary, as opposed to the driving force behind protection from DIO.

The role of AMPK in glucose homeostasis has been implicated in a number of glycogen storage diseases, including the previously discussed AMPKγ2 R531G mutation leading to human WPW, as well as a naturally occurring Redenement Napole ($RN^-$) mutation in the skeletal muscle-specific AMPKγ3-containing complex in Hampshire pigs. Pigs, mice and humans harbouring this mutation (R255Q) exhibit marked glycogen accumulation in glycolytic skeletal muscle (Milan et al., 2000), though, unlike AMPKγ2 mutations, the resulting phenotype is largely non-pathological. In addition, the AMPKγ2 R531G mutation led to an impairment in pancreatic β-cell function, characterised by a decrease in insulin secretion (Yavari et al., 2016).

The D316A-Tg mouse model, whilst exhibiting complete protection from DIO, showed no significant improvement in glucose tolerance as assessed by GTT. However, an important factor rarely discussed when using animal models for glucose handling studies is the inherent glucose tolerance associated with the chosen rodent strain. The C57Bl/6J mouse strain used in these studies, acquired from The Jackson Laboratory, has been reported to be relatively glucose intolerant (Freeman et al., 2006) due to a deletion in the nicotinamide nucleotide transhydrogenase locus. This deletion has also been reported to reduce insulin secretion from pancreatic beta-cells, contributing to the hyperglycaemic phenotype of these animals (Shimomura et al., 2009). However, this strain is by no means glucose intolerant when compared to genetically modified, glucose intolerant strains, such as KK/HlJ and NON/LtJ, which display a phenotype associated with type 2 diabetes.

The D316A-Tg mouse did, however, present with significant reduction in insulin secretion in response to HFD feeding. Whilst this finding suggests a protection from obesity-induced insulin resistance, the calculation of the HOMA-IR was indicative of slight basal insulin resistance in chow-fed mice, and a significant reduction in beta cell

function on a HFD. Further studies are required, and are ongoing, into the insulin secretion capacity of D316A-Tg pancreatic islets, with initial results suggesting, as observed by several groups (Fu et al., 2013, da Silva Xavier et al., 2003), that chronic AMPK activation inhibits insulin secretion.

Interestingly, though no significant difference in glucose tolerance was observed in this model, D316A-Tg mice exhibited significant glycogen accumulation in skeletal muscle after HFD-feeding, associated with lower blood glucose levels, indicative of enhanced glucose uptake. Though ongoing studies using a muscle-specific D316A-Tg mouse model (Mef2C-cre) did not recapitulate the protection from DIO associated with the global D316A-Tg mouse model, it will be of considerable interest to determine whether these animals also display an increase in glycogen accumulation and, in line with compound studies, amelioration of insulin resistance.

### 3.5.2 Food intake

Given the reported hyperphagic phenotype of the R299Q mouse model of chronic AMPKγ2 activation, it was of particular interest to examine the feeding behaviour of D316A-Tg mice on both standard chow diet and during high-fat feeding (Yavari et al., 2016). Animals were monitored for total food intake as well as the frequency and duration of feeding using an automated, highly accurate laboratory animal feeding system; the BioDAQ. Given that D316A-Tg mice on a chow diet did not exhibit any differences in feeding, nor did they develop age-related obesity as seen in the R299Q mouse model, it was hypothesised that the observed protection from DIO may be driven in part by alterations in foraging behaviour as a result of HFD-feeding, as opposed to total food intake.

Interestingly, a significant increase in the amount of time animals spent ‘foraging’, i.e. time spent at the hopper, was observed, though total amount of food ingested was unchanged. This result, though preliminary, is of particular interest given the observed stimulation of both orexigenic and anorexigenic peptide mRNA expression in the hypothalamus. It is possible that AMPK activation in one neuronal population may promote food-seeking behaviour, whilst simultaneous expression in the opposing population may inhibit the food-consuming behaviour. However, further work is required to establish whether this unique behaviour is reproducible, and if so, whether specific expression of AMPK in one neuronal population is sufficient to stimulate

foraging, and sole expression in the other to stimulate food intake, or whether expression in both populations is required for this complex behaviour. It is also of importance to establish the roles of specific AMPK isoforms within these neuronal populations, given that the R299Q mouse model exhibits activation of γ2-containing complexes only, whereas the D316A-Tg confers activation to complexes of γ1.

It is possible that these isoforms may have highly-specified roles within certain neurons that cannot be compensated for by others, and under normal conditions would be subject to tight regulation within certain cellular compartments until required. However, as noted by Yavari *et al.,* AMPK activators currently in use are not isoform specific, and, in the case of the small molecule activator 991, have also been shown by members of our laboratory to preferentially activate γ2-containing complexes (Willows et al., 2017a). Therefore, considerable attention should be paid to the potentially opposing roles of AMPK complexes in the regulation of food intake and feeding behaviour when developing small molecule activators capable of crossing the blood-brain barrier.

Interestingly, no differences in food intake have been reported by any recent study using the pan-AMPK small molecule activators MK8722 or PF-739, suggesting that activation of AMPK in this manner does not alter food intake *in vivo* (Myers et al., 2017, Cokorinos et al., 2017). However, it is possible that these compounds either do not enter the hypothalamus, or do not confer preferential activation of γ2-containing complexes as seen with 991. Further work will utilise the D316A-Tg protein expressed specifically in SF-1 neurons involved in the regulation of food intake and energy expenditure, particularly in response to HFD-feeding (Kim et al., 2011).

### 3.5.3 Energy expenditure and thermogenesis in the D316A-Tg mouse model

The role of energy expenditure in the pathogenesis of obesity has been explored at great lengths, primarily focussed on the contribution of the skeletal muscle and the brown adipose. Many efforts have been made to target these pathways, given that therapeutics to target food intake and nutrient absorption are plagued with side effects, including nausea, depression, diarrhoea and the potential for misuse (Halford and Blundell, 2000). Therefore, the development of therapeutics towards promoting energy

expenditure has proved a more attractive route to treating obesity, predominantly through the activation of BAT.

Several studies have implicated AMPK signalling in the promotion of BAT-mediated thermogenesis, both in the hypothalamus and in brown/beige adipocytes *in vivo* (Yan et al., 2016, Chung et al., 2017, Lopez et al., 2010). Though it has been established that AMPK is critical for the development and maintenance of brown adipose tissue, and is required for acute BAT-mediated thermogenesis, no studies have convincingly demonstrated activation of AMPK directly promoting UCP1 expression and activity in this tissue *in vivo*.

The D316A-Tg model presented with a substantial increase in energy expenditure when challenged with a HFD, when compared to WT-Tg controls, which could have been attributed to the promotion of BAT-mediated thermogenesis. However, no differences were found in core body temperature, a commonly used diagnostic parameter for BAT activation, nor was basal UCP1 expression increased. Furthermore, treatment of chow-fed mice with the classical BAT activator CL316, 243, a β3-adrenergic receptor agonist, failed to activate D316A-Tg BAT more than WT-Tg controls, both in terms of UCP1 expression and activity, suggesting that this pathway, whilst intact, is not responsible for the increase in EE observed in this model.

Whilst it is clear that AMPK coordinates and maintains many key cellular processes in brown adipose tissue (Mottillo et al., 2016, Yang et al., 2016a), the data presented here, together with the studies mentioned above, suggest that chronic AMPK activation does not promote BAT-mediated NST, nor does it significantly alter the expression of UCP1 and mtRC proteins *in vivo*.

These findings are perhaps fortunate, given that the promotion of NST in humans using thermogenic agents has a wide range of side effects, such as a dangerous elevation in core body temperature, involuntary muscle contraction, nausea and sickness. Indeed, several of these agents are routinely used by the general public without sufficient scientific understanding and have no FDA approval, such as caffeine, herbal extracts and ephedrine (Egras et al., 2011, Stohs and Badmaev, 2016). Whilst the safe and controlled activation of BAT remains an attractive therapeutic avenue for the treatment of obesity, the development of such agents for use in humans requires

further understanding of underlying mechanisms and potential long-term consequences before they can be used to treat this disease.

### 3.5.4 'Browning' of the WATsc

Whilst BAT-mediated NST has been acknowledged for decades, the contribution of white adipose (WAT) to metabolism has been considered minor, thought to act predominantly as an energy storage tissue in the form of lipid droplets. Whilst these observations are logical, it is now known that WAT is capable of so much more and has, in fact, been drastically underestimated, both as a secretory organ and as a mediator of energy homeostasis.

The WATsc of the D316A-Tg mouse model presented with a distinct, 'brown' morphology, with a striking increase in micro and macro vasculature. In addition, these depots were rich in mitochondria, as assessed by TOM20 staining, though this did not confer any reduction in bodyweight or adiposity on a chow diet. The gene expression profile of this depot also resembled that of brown adipose, with a substantial increase in Prdm16 and PPARγ, a partnership that strongly drives the BAT lineage in complex with PGC1α, a known target of AMPK (Jager et al., 2007). Furthermore, these 'brown' cells stained heavily for the endothelial cell marker CD31/PECAM1, described as a *bona fide* marker of brown and not beige adipocytes (Rosso and Lucioni, 2006), suggesting that these cells are either true BAT, or a subset of $Myf5^{+}$ precursors resident in the vasculature of all WATsc that have never been successfully differentiated until now.

However, only a very minor increase in UCP1 mRNA expression was observed which, given the considerable difference in morphology, may suggest an active repression of this pathway. Hypothetical repression of UCP1 by AMPK is plausible, given that the role of AMPK is to conserve and generate ATP, whereas the role of UCP1 is primarily to uncouple ATP synthesis in favour of heat production. However, further studies are required to determine whether AMPK is directly responsible for the repression of UCP1, or if its absence can be explained by another compensatory pathway to avoid unnecessary, uncontrolled energy expenditure.

The absence of UCP1 in the presence of such 'browning' was at first confusing given that, at the time, little was written regarding the existence of an alternative thermogenic

programme in WATsc. Therefore, to identify other potential drivers of thermogenesis, RNA sequencing was performed.

Deep-sequencing technologies such as RNA sequencing have been used to progress our understanding of the eukaryotic transcriptome, generating large data sets containing precise measurements of transcript number and isoform specificity (Wang et al., 2009). The D316A-Tg mouse model presented a unique opportunity to study the effects of chronic AMPK activation on the transcriptome of chosen tissues and cell types, as well as allowing the study of potential crosstalk between tissues, as would be potentially invoked by the administration of therapeutics targeting AMPK in a non-tissue-specific manner. Though all four tissues chosen; BAT, WATsc, liver and gastrocnemius muscle, showed many significant changes in gene expression, none were more surprising or exciting than those identified in WATsc.

Over 4000 differentially expressed genes were identified between WT-Tg and D316A-Tg WATsc. Of these, many were not statistically significant, and others exhibited such low fold change that they were not recognised as biologically significant. Through the use of Ingenuity Pathway Analysis software (IPA), alongside a variety of online tools, it was determined that an extraordinary shift towards a muscle-like transcriptome had occurred. Genes upregulated included creatine kinase; both mitochondrial and non-mitochondrial, Atp2a1 (SERCA), calcium sensing receptors, ryanodine receptors and other key regulators of calcium futile cycling known to play a role in muscle metabolism and ATP dissipation.

Given that the expression of BAT genes were high on a chow diet, it was hypothesised that HFD-feeding had triggered a BAT-muscle switch *in vivo*. Indeed, the genes identified exhibited significant overlap with those expressed in EHMT1 knockout BAT, as well as those upregulated in response to Prdm16 ablation, suggesting that this complex may be sensitive to energy status and thus disrupted by HFD-feeding.

Following the identification of this phenotype in the D316A-Tg mouse model, a paper was published from the laboratory of Dr. Spiegelman, describing a novel alternative thermogenic mechanism in WATsc, in $UCP^{-/-}$, cold acclimatised mice. In this study, BAT and beige adipocytes were analysed using proteomics to identify fundamental differences in adaptive thermogenesis between the two cell types. Within the gene ontologies described were those attributable to creatine metabolism, with 8 unique

proteins identified (Kazak et al., 2015). This finding has since led to the identification of creatine kinase (Ckm/Ckmt1/2) as a mediator of creatine futile cycling in WAT depots, which has been shown to drive thermogenesis in beige adipocytes in the absence of UCP1.

The discovery of creatine-driven thermogenesis in WAT has provided a window into the ability of adipose to adapt to metabolic demand, particularly when the predominant thermogenic mechanism is abolished, and is proving to be an exciting theory of energy dissipation under these circumstances (Kazak et al., 2015). However, whilst it has been established that creatine energetics play an important role in beige WATsc adaptive thermogenesis, the mechanism by which WATsc-derived adipocytes retain this muscle-like ability is unknown. Furthermore, whilst the ablation of creatine metabolism in WAT has recently been shown to disrupt adaptive thermogenesis, the mechanism by which creatine kinase facilitates heat production is subject to speculation, with several futile cycles identified downstream of mitochondrial ATP synthesis, capable of dissipating ATP as heat. Creatine futile cycling through Ckm remains a robust mechanism, particularly in the instance of diet-induced thermogenesis, given that adipose-specific deletion of the rate limiting enzyme in creatine biosynthesis, glycine amidinotransferase (GATM) predisposes mice to DIO. In addition, these studies have shown that supplementation of dietary creatine is sufficient to rescue the obese phenotype, suggesting that creatine metabolism is critical for the induction of diet-induced thermogenesis (Kazak et al., 2017).

Whilst these studies clearly demonstrate physiological importance for creatine metabolism in adaptive thermogenesis, currently available models with which to study this ability are limited. The D316A-Tg mouse model presents with a unique opportunity to study the development of brown-like adipocytes in WATsc without genetic manipulation of UCP1 or cold-acclimatisation. Furthermore, RNA-sequencing of the WATsc of this model has revealed other potential mechanisms, other than creatine kinase, downstream of mitochondrial ATP synthesis that have previously been reported, predominantly in muscle, including the expression of Atp2a1, more commonly referred to as $Ca^{2+}$-ATPase, or SERCA.

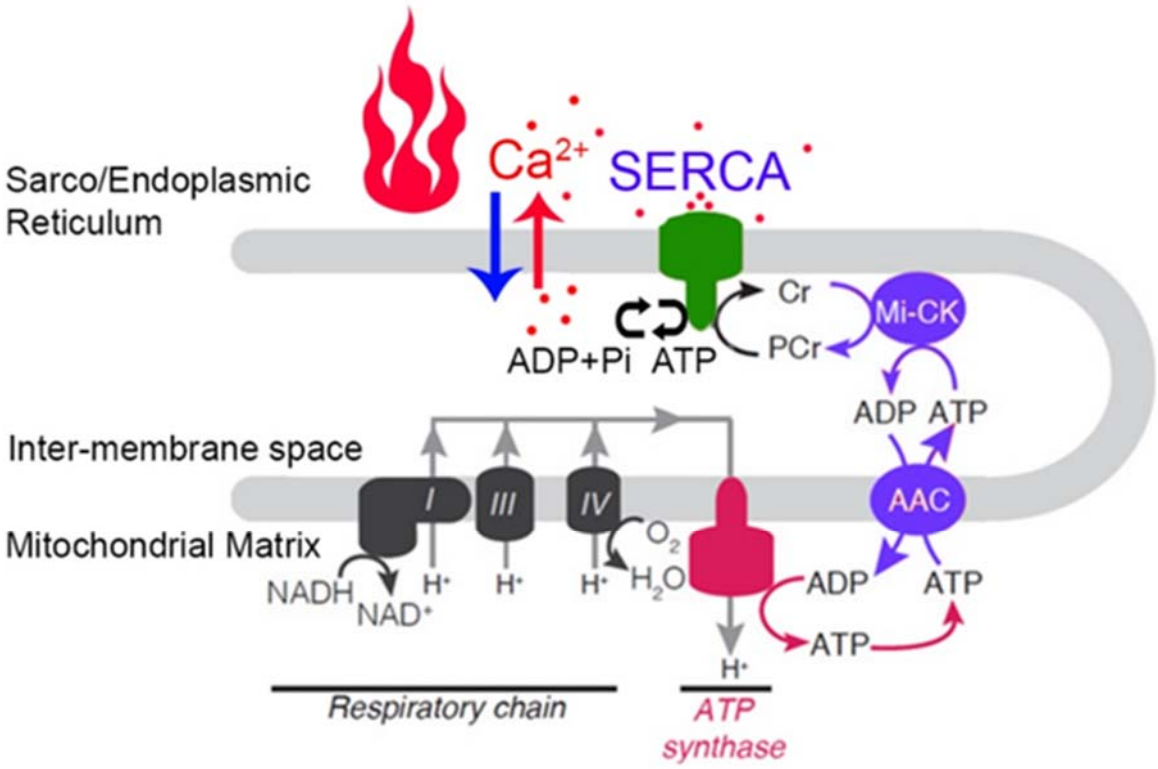



***Figure 3.48 Creatine kinase-SERCA futile cycling***

*Simplified schematic of creatine/calcium futile cycling in mitochondria and the sarco/endoplasmic reticulum. Adapted from Kazak et al., 2015*

*Triacylglycerol packaged in dynamic intracellular lipid droplets (LD) are hydrolysed to glycerol and fatty acids by lipases and enter the mitochondrial respiratory chain. In the absence of UCP1, ATP is produced by ATP synthase, expressed in abundance in D316A-Tg WATsc. ATP is then transported by creatine kinase through the phosphorylation of creatine to phosphocreatine in the intermembrane space, to the sarco/endoplasmic reticulum $Ca^{2+}$-ATPase (SERCA) where it is used to pump calcium ions across the mitochondrial/ER membrane, with each hydrolysis generating approximately -24.7kcal/mol (de Meis, 2003) in the presence of a gradient.*

The D316A-Tg mouse model exhibits increased WATsc mitochondrial content, and upregulation of mtRC proteins in response to a HFD. In the absence of an uncoupling agent, namely UCP1, β-oxidation of fatty acids (FAO) remains coupled to ATP synthesis. However, the upregulation of FAO is insufficient to explain an increase in EE and subsequent protection from DIO in the D316A-Tg mouse model, and the fate of such high ATP concentrations requires resolution.

In skeletal muscle, ATP generated by mitochondrial ATP synthase is subsequently hydrolysed by the sarcoplasmic reticulum $Ca^{2+}$-ATPase, resulting in the transport of $Ca^{2+}$ across the membrane. This cycling of calcium ions between the cytosol and the sarcoplasmic reticulum, mediated by SERCA and ryanodine receptors, releases small amounts of heat with each hydrolysis event (Arruda et al., 2007) (Fig 3.53). This activity has also been shown to subsequently stimulate mitochondrial respiration in order to maintain the cellular ATP concentration (Arruda et al., 2007). Encouragingly, this mechanism has been previously identified in $UCP1^{-/-}$ WATsc from gradually cold acclimatised mice (Ukropec et al., 2006), though since then no further work has been conducted.

The existence of futile cycling in muscle is well studied, but the characterisation of heat production in this system can be attributed to the detailed and elegantly presented work of Professor Leopoldo de Meis (de Meis, 2003, de Meis et al., 2006, de Meis et al., 2005). It is in his work on brown adipose that the connection was made between SERCA and creatine kinase, and is perhaps the missing link between Spiegelman's creatine futile cycling with no thermodynamic conclusion and the enhanced energy expenditure observed (Fig 3.53).

The D316A-Tg mouse model presents both calcium and creatine futile cycling elements that, instead of working independently, may work in tandem to create a muscle-like ATP production and dissipation system in WATsc as well as in the BAT observed by de Meis. For this system to enhance EE, mitochondrial ATP synthesis must not be limiting, which, in the D316A-Tg mouse model on a HFD, it is not. Indeed, the presence of HFD-associated lipid may be the driving force behind the production of ATP to such high concentrations that this system is recruited over time in WATsc. In an effort to investigate this, WATsc cell suspensions from chow-fed mice were prepared and analysed using the OROBOROS O2k high-resolution respirometer,

featuring a Clark-type electrode capable of detecting minute changes in $O_2$ flux. To simulate a HFD, a palmitate: BSA conjugate (PA) was added to determine whether $O_2$ consumption would be stimulated as has been shown in BAT. From these preliminary investigations, it was clear that D316A-Tg adipocytes were considerably more responsive to PA than WT-Tg cells, supporting the hypothesis that HFD feeding may drive ATP synthesis in a mitochondrial-rich environment, as the D316A-Tg WATsc provides.

However, there were several pitfalls associated with this experiment that require attention, perhaps the most prominent being the necessity to separate lipid-laden cells from denser populations. It was found that the presence of lipid interfered with electrode readings by forming a cluster at the top of the chamber, particularly prevalent in WT-Tg samples due to a high proportion of mature adipocytes. Therefore, to establish any readings, these cells had to be removed. In a mature WATsc depot of WT-Tg mice, these cells make up between 85-95% of the tissue by observation alone, and, within the animal, would be the subset of cells contributing to normal metabolism. By removing this population of cells, one immediately biases the metabolic rate of the WT-Tg population, with the remaining cells being of vascular and precursor origin, likely to have a far higher rate of $O_2$ consumption than their mature neighbours. By normalising to cell number, these cells now present a false reading for the basal metabolism associated with WT-Tg WATsc, resulting in unnaturally high basal $O_2$ consumption. It is not known whether the ‘brown-like’ adipocytes in D316A-Tg WATsc are sufficiently dense as to be obtained in the pellet, and further work is required to characterise the different fractions generated by centrifugation. However, the basal rate obtained for these cells was considerably lower than WT-Tg counterparts, perhaps because of the aforementioned bias, or because these cells are indeed retained in the pellet, but have a low basal metabolism until stimulated. Nevertheless, a strong and reproducible induction of $O_2$ consumption was observed in these cells which may become significant once the bias surrounding the WT-Tg rate is removed. It is therefore possible that the presence of HFD may stimulate mtRC protein expression and subsequent ATP synthesis in BAT-like cells which under normal conditions, do not contribute to basal metabolism much more than a white adipocyte. The futile cycling system, therefore, acts as a buffer to the high ATP concentrations then generated by active mitochondrial FAO, driven initially by AMPK.

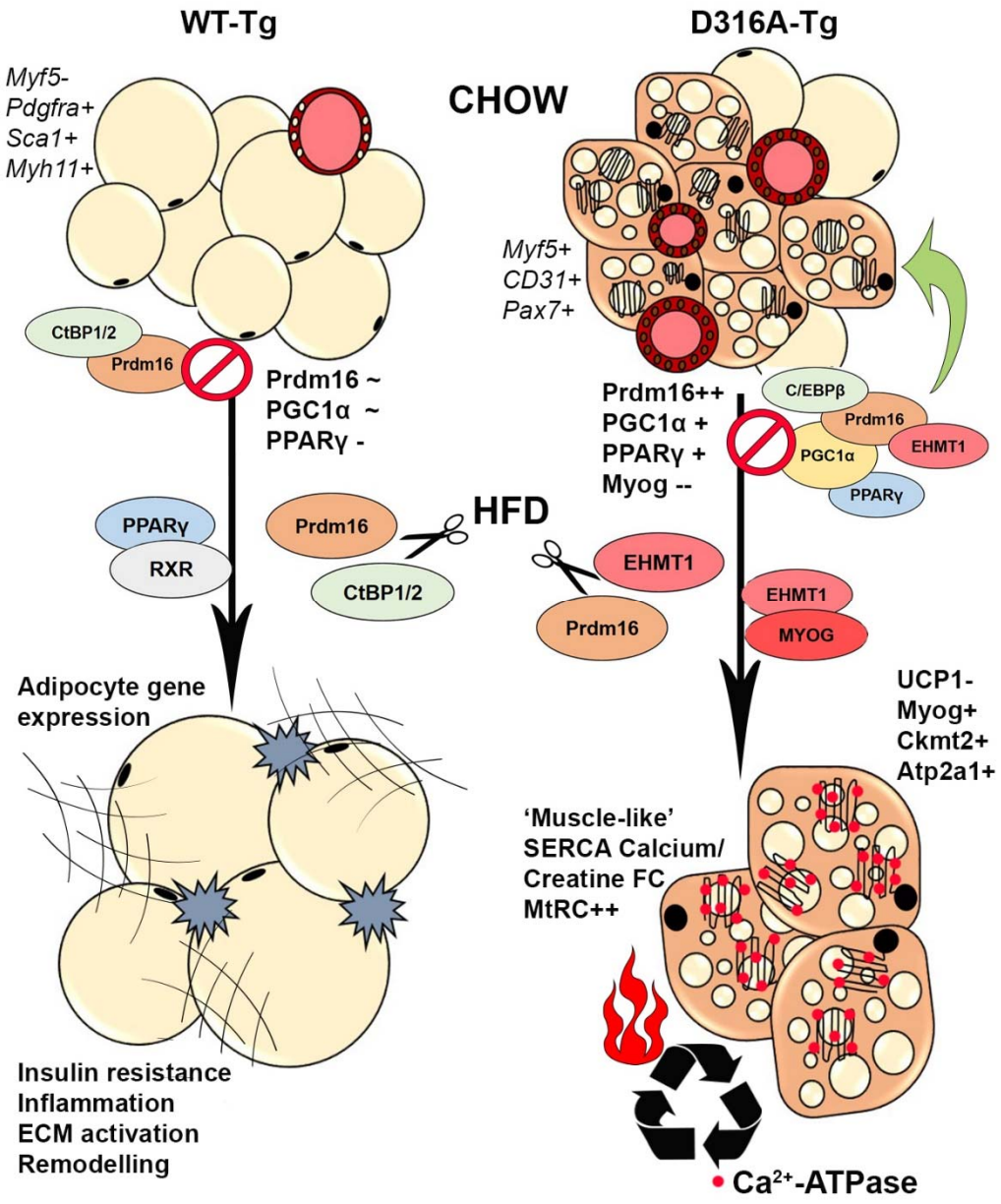



***Figure 3.49 Hypothesis: AMPK promotes Myf5⁺ cell development in WATsc, facilitating Ckmt2/SERCA futile cycling.***

*AMPK promotes the development of BAT-like WATsc on a chow diet, characterised by high mitochondrial content, Prdm16, PPARγ, PGC1α, concurrent with Myogenin repression, known to be driven by EHMT1/Prdm16 complex formation (Ohno et al., 2013, Seale et al., 2011, Seale et al., 2008). HFD-feeding modifies Prdm16, disrupting the EHMT1 complex. In white adipocytes, this relieves the repression of WAT expansion gene programmes driven by PPARγ/RXR (Kajimura et al., 2008), resulting in the activation of ECM-resident fibroblasts and immune cells, leading to fibrosis, chronic inflammation and insulin resistance. In D316A-Tg BAT-like WATsc, disruption of the Prdm16/EHMT1 complex removes repression of myogenin (MyoG), promoting muscle gene expression (Ckmt2, Atp2a1, Ryr1/3, Pln). SERCA/Ckm2-mediated calcium futile cycling generates heat and promotes high mitochondrial respiration (Arruda et al., 2007).*

Spiegelman and others have shown that futile cycling of creatine/phosphocreatine is recruited only in the absence of UCP1, at least in beige adipocytes, though new evidence is coming forward suggesting that creatine dynamics plays more than just a compensatory role in white adipose (Kazak et al., 2017). Since the absence of UCP1 is a feature of WATsc of HFD-fed D316A-Tg mice, it is possible that its absence also plays a role in the promotion of futile cycling, but is more likely to be as a result of the BAT-muscle switch, which has been shown to inhibit UCP1 expression even in classical BAT (Ohno et al., 2013).

If these hypotheses are correct, then within the D316A-Tg WATsc exists an elegant mechanism by which high mitochondrial activity, stimulated by HFD-feeding, is supported by prior acquisition of mitochondrial mass, through the activation of AMPK. The work of Leopoldo de Meis demonstrated that, in BAT, the outer mitochondrial membrane is fused to the endoplasmic reticulum, with sarco/endoplasmic reticulum $Ca^{2+}$-ATPase (SERCA1) expression found in both structures. Indeed, the ER was found to exhibit budding-like structures which formed contact points with the mitochondria, facilitating a calcium futile cycle almost identical to that of muscle, but not observed in mitochondria from other tissues such as liver (de Meis et al., 2010). Indeed, this body of work also identified the 'open/closed' status of ryanodine $Ca^{2+}$ channels as a mediator of heat production in this system.

The presence of SERCA1 and ryanodine receptors, alongside calsequestrin and phospholamban; key proteins involved in the holding and release of intracellular calcium to regulate SERCA activity, in D316A-Tg WATsc suggest that this mechanism may be responsible for increased EE in this tissue. AMPK activation has been shown to activate SERCA through the phosphorylation of phospholamban, suggesting that AMPK activation, in the presence of substrate, may drive this futile cycle through more than one pathway (Schneider et al., 2015).

The involvement of both SERCA and creatine kinase in this system is well established in skeletal and cardiac muscle, with the high energy phosphoryl transfer of ATP to phosphocreatine and vice versa (Fig 3.53), known as the creatine kinase circuit, used to buffer high ATP concentrations and facilitate effective ATP transport to sites of consumption (de Groof et al., 2002). It is therefore possible that the observed increase in creatine kinase, SERCA and associated calcium cycling elements are all involved

in futile cycling in D316A-Tg WATsc, facilitated by high mitochondrial content and activity driven by HFD-feeding.

It is an attractive hypothesis that AMPK activation *in vivo* is sufficient to induce an alternative thermogenic programme resembling that of traditional skeletal muscle, without the need for cold acclimatisation or UCP1 ablation. However, the precise underlying mechanism may not be so straightforward. Indeed, it has been shown that simple expression of these muscle-genes is not sufficient to sustain thermogenesis in BAT, and it is therefore perhaps the development of 'almost-functional' BAT in WATsc depots prior to HFD-feeding that facilitates this response whilst retaining viability. The results presented here strongly support this hypothesis, with a convincing BAT signature on a chow diet and active repression of MyoG, a known target of the Prdm16/EHMT1 complex. Removal of this repression, as observed after just 4 weeks of HFD-feeding, is sufficient to then induce the expression of Ckmt2 and other futile cycling elements (Fig 3.54).

However, the primary development of these cells in WATsc promoted by AMPK activation requires a considerable amount of investigation. The origins of subcutaneous versus other WAT depots has only recently been explored in detail, with some unexpected and exciting results. It has been shown that these depots closely resemble the tissues to which they associate, with studies identifying a mesothelial source for all 'visceral' fat, encompassing gonadal, perirenal, epicardial, retroperitoneal, omental and mesenteric depots, but not for BAT or subcutaneous WAT, which exhibited no mesothelial markers (Chau et al., 2014). Despite lying directly on top of skeletal muscle, most lineage tracing studies maintain that the WATsc is not derived from the $Myf5^{+}$ lineage, at least, not after commitment. As shown in Fig 3.55, and as described previously, mature rodent WATsc contains only 6% $Myf5^{+}$ precursors under normal conditions, whereas BAT, renal WAT and asWAT all contain high proportions of these cells (Sanchez-Gurmaches and Guertin, 2014). It would therefore be of interest to determine the relative proportion of $Myf5^{+}$ precursors in D316A-Tg WATsc, and whether AMPK is directly responsible for the alteration of cell fate. If this WATsc does indeed more closely resemble BAT or a depot rich in $Myf5^{+}$ precursors, this would provide a substantial basis for subsequent 'browning' and a HFD-induced muscle transcriptional programme. It is also of interest to determine whether the increase in vasculature seen in D316A-Tg WATsc drives the development

of such a depot during development, as has been eluded to previously, and whether AMPK plays a role in this *in utero*.

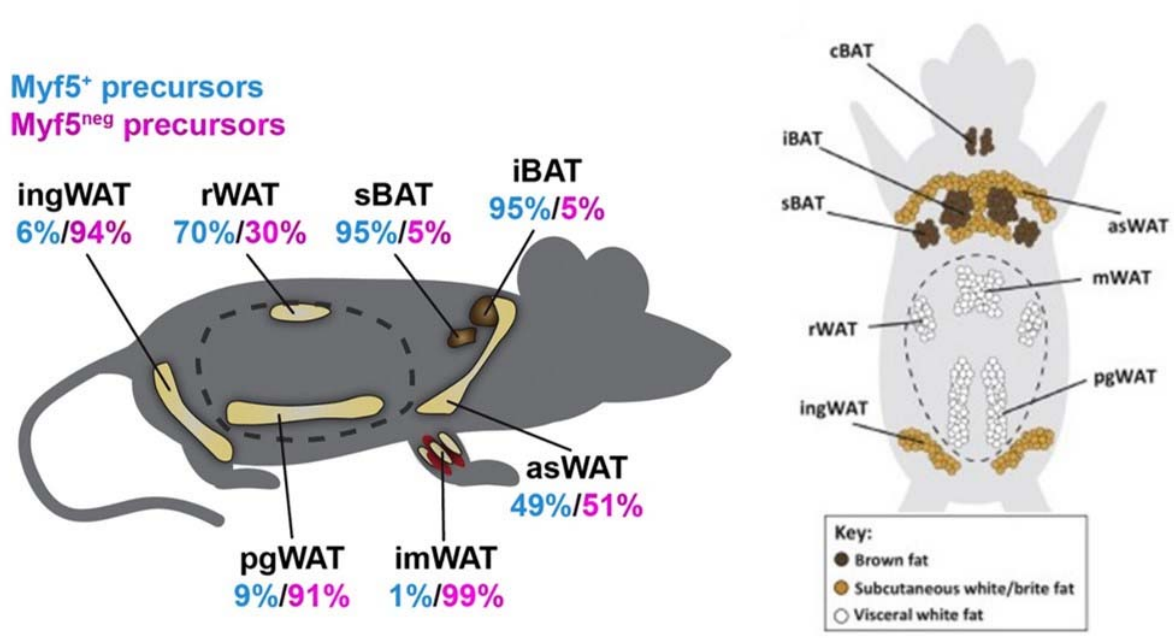



***Figure 3.50 Location and proportion of Myf5⁺ BAT and WAT depots in wild type mice, adapted from Sanchez-Gurmaches and Guertin, 2014.***

*Location of Myf5⁺ stem cell populations within discreet murine adipose depots as determined by in vivo fluorescent lineage tracing. Inguinal white adipose (ingWAT) expressing approximately 6% Myf5⁺ and 94% Myf5⁻ adipocytes, with classical BAT (i/sBAT) containing 95% Myf5⁺cells. Adapted from (Sanchez-Gurmaches and Guertin, 2014).*

The use of a tamoxifen-inducible model of D316A-Tg expression provided insight into the potential use of AMPK activation as a treatment for DIO and the metabolic syndrome. D316A-Tg$^{TMX}$ mice exhibited a reduction in bodyweight gain, adiposity and liver triglyceride accumulation on a HFD, as well as significant upregulation of PGC1α and PPARγ RNA. The expression of mtRC proteins was also increased in WATsc, coinciding with an increase in vascularisation and a reduction in adipocyte size. Whilst this model served as a proof of concept for the use of AMPK activators *in vivo*, several caveats were identified. Perhaps the most influential of these was the reduction in bodyweight associated with tamoxifen administration, which impacted on normal HFD-induced bodyweight gain for approximately 4 weeks. However, 10 weeks post-administration, lipolysis could be detected in WT-Tg WATe (Appendices Fig 6.2), the depot primarily affected by tamoxifen (Ye et al., 2015), potentially distorting any

investigations using this model of AMPK activation. A second caveat of this model is the apparent loss of induction after approximately 8 weeks, suggesting that further administration was required to sustain D316A-Tg expression. The reasons for loss of expression in this model are unknown, and future studies will address this issue by either repeat administration or through a different route, such as incorporation into the diet. This, however, may not be necessary as, in collaboration with AstraZeneca, studies will be conducted to test novel small molecule activators of AMPK *in vivo*.

In conclusion, D316A-Tg mice exhibit complete protection from DIO and associated metabolic syndrome, through increased EE potentially driven by creatine kinase/SERCA-mediated alternative thermogenesis in WATsc on a HFD, as a result of a BAT-muscle switch, independent of UCP1. In addition, a new role for AMPK in the determination of cell fate has been suggested, though further work is required to determine the underlying mechanism. Whether these cells are deserving of a name independent of BAT, WAT, beige or brite is perhaps for the scientific community to decide, as they present with a phenotype that cannot be attributed to any other cell, and may be derived from precursors previously thought to have no function in WATsc.

### 3.5.5 Future work: Metabolic consequences of AMPK activation

Further work is required to confirm several of these hypotheses, in particular the identification of contact points between the ER and mitochondria in WATsc and the expression of SERCA in the ER/mitochondrial outer membrane. WATsc samples have been taken for examination by electron microscopy (EM) as was performed by de Meis on BAT, to evaluate this hypothesis. Western blotting and immunofluorescence have been tested to detect SERCA on the ER/mitochondrial membrane, but further work is required to optimise this system for WATsc, particularly when using paraffin-embedded tissue, as high levels of auto-fluorescence and antibody specificity in this tissue may result in false positives. Once optimised, immunofluorescence can also be used to define populations of stem cells resident in the D316A-Tg WATsc vasculature, allowing quantification of $Myf5^{+}$ and $Pdgfr\alpha^{+}$ precursors within this depot. In future, it would be of interest to use cell lineage tracing to track these populations of cells *in vivo*, to determine the origin of BAT-like cells in WATsc, as performed in cold exposure studies described previously (Chau et al., 2014).

The vascularisation of D316A-Tg WATsc is of particular interest, as mentioned previously, due to its role as a stem cell niche. If the development of such intricate vascularisation is a precursor to the development of BAT-like cells in WATsc, it may then indicate that the increase in vasculature in D316A-Tg$^{TMX}$ WATsc may be the beginning of this process. This would have considerable impact on the development of therapeutics to target the adipose, and would provide an exceptional readout for the efficacy and specificity of any compound administered. To investigate the development of vascularisation in D316A-Tg, a robust experimental procedure for visualising this must first be implemented. One particular protocol describes a technique with which to do this *in situ*, by perfusing tetramethylrhodamine-labelled dextran into the tail vein of awake mice. The dextran is allowed to perfuse for 15 minutes before culling, followed by whole-mounting of extracted WATsc, using BAT and muscle as controls. Tissue mounts are subsequently incubated with primary antibodies to vascular markers such as PECAM1, with white adipocytes labelled by incubation with 4,4-difluoro-4-bora-3a,4a-diaza-s-indacene-3-dodecanoic acid (BODIPY) 558/568 $C_{12}$ and visualised by confocal microscopy. A 3D image can then be constructed using Z-stack images to obtain a complete model of WATsc vascularisation (Xue et al., 2010). Successful implementation of this protocol will allow the subsequent study of developing WATsc in D316A-Tg mice, alongside the development of BAT-like adipocytes. This technique also facilitates the use of other primary antibodies to proteins such as Myf5, SERCA, creatine kinase and UCP1, to determine the proportion of stem cells and induction metabolically active BAT-like cells within this highly flexible depot after HFD-feeding.

The acquisition of the OROBOROS respirometry system will allow further investigation into the effects of lipid on oxygen consumption in isolated D316A-Tg WATsc adipocytes, in an optimised system whereby the presence of lipid is not an interference. In addition, the development of a cell culture model, by identifying and isolating precursors responsible for the generation of BAT-like adipocytes in WATsc, will facilitate investigations into the effect of lipids on gene expression in cells expressing D316A-Tg. The development of this model will also facilitate experiments using small molecule activators such as AZ991, to study the role of AMPK activation in Myf5$^{+}$ precursors found in wild-type WATsc and BAT. Furthermore, a cell culture model would allow the use of *in vitro* techniques such as manipulation of gene

expression by CRISPR or siRNA to remove key components of these identified pathways, or to disrupt complexes known to promote either muscle or BAT lineages (EHMT1/Prdm16).

The key to the development of successful *in vitro* models with which to investigate these novel roles for AMPK is the correct identification of the precursor(s) responsible for the observed phenotype. Several additional mouse models have therefore been developed surrounding this project, which have not been described here, primarily because they have been conducted by other members of the laboratory, and/or because they are ongoing. However, these models are a key feature of the future work on AMPK activation *in vivo* and *in vitro* using the D316A mutation, so will be briefly discussed with emphasis on future experiments.

*Adiponectin-Cre*

Many studies have used the mature adipocyte-specific adiponectin-cre mouse model to study adipocyte development and metabolism *in vivo*. Adiponectin is produced exclusively by mature brown and white adipocytes, and is not expressed in the germ line. Therefore, this model was selected to determine whether mature white adipocytes were responsible for the 'browning' of the WATsc in the global D316A-Tg mouse model through trans- or de-differentiation, as had been hypothesised by several groups prior. Indeed, many studies looking at AMPK *in vivo* have chosen the adiponectin-cre mouse, though these have often been models of deletion as opposed to activation. One such study, using this model to delete the tumour-suppressor folliculin (FLCN) reported chronic activation of AMPK, leading to the induction of functional beige adipose tissue through the promotion of PGC1α/estrogen-related receptor (ERRα) signalling (Yan et al., 2016). The extent to which the WATsc of these animals exhibited 'beiging' however is minimal in comparison to the global D316A-Tg mouse model, with a modest but significant decrease in bodyweight. A study was therefore conducted to assess whether expression of the D316A-Tg protein under the control of the adiponectin promotor would mimic the phenotype of the global D316A-Tg model. No significant differences were found in bodyweight, adiposity or peripheral lipid accumulation in this model, suggesting that AMPK activation in this manner is not sufficient to protect from DIO, or induce 'beiging' of the WATsc. The mechanism through which the FLCN model of AMPK activation exerts its effect is therefore

unknown, and the observed increase in AMPK activity may be secondary to another pathway downstream of FLCN, not yet identified. Alternatively, a threshold for AMPK activation may be in place, whereby activation using the D316A-Tg mouse model is not sufficient in magnitude to exert the same effects, though this study did not quantify total AMPK activity, opting instead for the measurement of phosphorylation of ACC, which is known to be maximally induced by relatively low levels of AMPK activity.

*Pdgfrα-Cre*

Following the observation that adiponectin-cre D316A-Tg mice were not protected from DIO, it was of interest to also exclude the possibility that the BAT-like cells are derived from WAT/beige precursors. This mouse model expresses cre-recombinase under the control of the WAT/beige stem cell marker Pdgfrα, the importance of which has been discussed previously. If the specialised cells in the global D316A-Tg mouse model are from a WAT lineage, they should develop in WATsc in this model as well. However, to date, these mice have not displayed any protection from DIO, supporting the hypothesis that these cells are not of WAT/beige origin, and furthermore, activation of AMPK in this manner does not promote classical beiging, though this is still to be confirmed by histology.

*Mef2C-Cre*

As mentioned previously, it was hypothesised that the D316A-Tg global phenotype could be driven by the skeletal muscle. Indeed, studies conducted in collaboration with the laboratory of Professor Dominic Wells revealed considerable mitochondrial biogenesis in D316A-Tg skeletal muscle which could, in theory, contribute to the protection from DIO. To examine both this hypothesis and to draw comparisons to those studies recently published using small molecule AMPK activators, the D316A-Tg mouse was paired with a muscle-specific cre model; Mef2C. These mice should express D316A-Tg protein in all skeletal muscle, though this is still to be confirmed as studies are ongoing. However, preliminary results show that these mice are not protected from DIO, but do exhibit significant reduction in blood glucose following a fast, indicating a potential increase in glucose uptake into skeletal muscle. Further studies will be conducted on these animals, including glucose tolerance, insulin tolerance and assessment of insulin production by ELISA. At harvest, skeletal muscle will be isolated and assessed for glycogen accumulation, TBC1D1 phosphorylation

and mitochondrial biogenesis; features of models treated with small molecule AMPK activators. Future work using the D316A-Tg$^{Mef2C}$ mouse model will also focus on exploring AMPK activation as a potential therapeutic target for mitochondrial dysfunction in skeletal muscle disorders such as muscular dystrophy. For studies such as these, it would be of interest to express D316A-Tg$^{Mef2C}$ in a mouse model of muscular dystrophy, such as the *mdx* mouse, and a collaboration to address this hypothesis is ongoing.

The future of the D316A-Tg mouse model with respect to adipose metabolism and energy expenditure is bright, with no shortage of avenues to investigate. It is hoped that this model will provide fresh insight into the origins and development of WATsc, and highlights the untapped resource that is the plasticity of this depot in adults. In the future, it would be of considerable benefit to investigate these mechanisms in human tissue, particularly for the comparison of WATsc from obese patients to that of athletes, to determine whether exercise-induced chronic AMPK activation confers similar changes to those observed in the D316A-Tg mouse.

# 4 CHAPTER 4: CHARACTERISATION OF THE CARDIORENAL PHYSIOLOGY OF D316A-TG MICE

Emerging roles for AMPK in the hypothalamus, brown adipose and liver have been recently characterised in relation to feeding behaviour, thermogenesis and lipogenesis using the transgenic mouse models described here, in addition to a variety of AMPK knock-out models. One phenotype in particular that exhibits an interesting phenotype is the AMPKγ2$^{RG}$ knock-in model, which, under conditions of a high fat diet, displayed severe kidney injury, glycogen accumulation and cyst formation (Yang et al., 2016b). Interestingly, in the same study, the AMPKγ2$^{NI}$ knock-in model of AMPK activation did not lead to cyst formation. However, this model also did not display cardiac glycogen accumulation, though exhibited some arrhythmia associated with WPW.

The emergence of kidney abnormalities in response to AMPK activation brings to the forefront a striking phenotype of the D316A-Tg mouse model. The following chapter provides an account of the development of a cystic kidney phenotype, associated with renal glycogen accumulation and a possible mouse strain-dependence with respect to severity.

## 4.1 Introduction

The study of the kidney dates back to 384BC, to the work of Aristotle, where he refers to the kidney as “not present for necessity in animals but have the function of perfecting the animal itself” *De Partibus III* (Marandola et al., 1994). He himself did not deem the kidney particularly important, though noted their ability to excrete the fluid that then collects in the bladder, in animals where this liquid forms in abundance.

It is now well established that the primary functions of the vertebrate kidney are to filter and excrete waste from the bloodstream, maintain electrolyte balance and conserve water through reabsorption, through central and local regulation. It achieves this through the use of an intricate network of specialised cell types, organised into multiple tubular structures known as nephrons. Over the last 50 years, the study of the development of the kidney has proved key to the understanding of several developmental processes, such as mesenchymal-epithelial transitions (MET), mesenchymal cell interactions and epithelial cell polarisation (Dressler, 2006).

The morphology and development of the kidney are well documented, though the molecular mechanisms that drive these observed changes are poorly understood. In the immature kidney, developing nephrons are found subjacent to the renal capsule, are identified by characteristic 'comma-shaped' bodies (CSB), derived from the nephrogenic mesenchyme, in a region known as the nephrogenic zone (NZ). As the nephron matures, these cells undergo a mesenchymal to epithelial transition, become 'S-shaped' bodies (SSB), with a defined epithelium at the proximal end, close to the

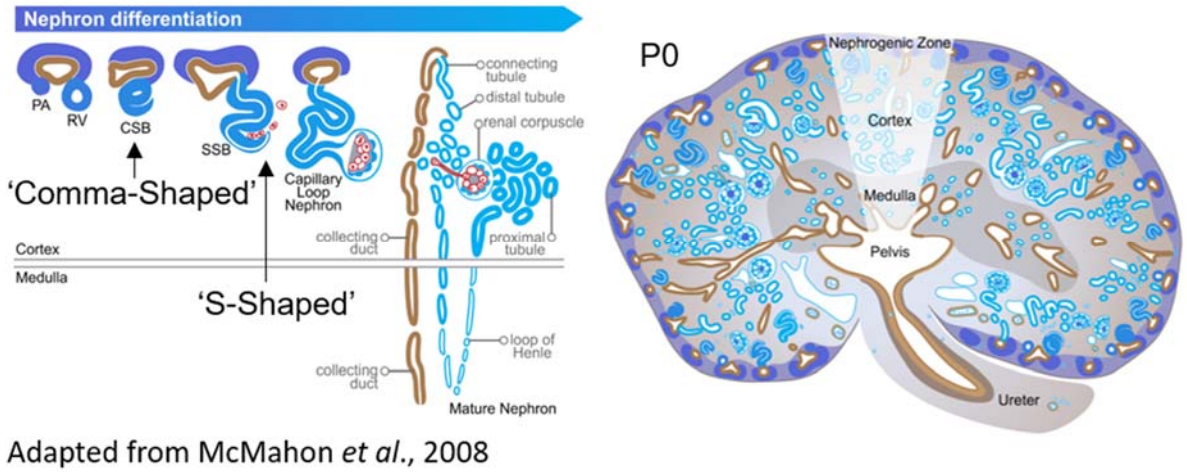



***Figure 4.1 Schematic outlining renal development, outlining murine kidney development.***

*Pre-tubular aggregates (PA) and renal vesicles (RV) are classified as Stage I nephrons. The development of a cleft, leading to 'comma-shaped' bodies (CSB) precedes the development of the Stage II nephron, characterised by 'S-shaped' bodies (SSB). Epithelial layers are established at the proximal end of the nephron, with endothelial cells migrating into the cleft. Loop formation and an immature capillary network denote a Stage III nephron which, together with stage II, can be found in neonates from day -0 (P0) to day-3. By post-natal day 4, healthy kidneys are fully formed. Adapted from McMahon et al., 2008*

NZ, and migratory endothelial cells found moving into the cleft (Fig 4.1, schematic). At birth, the NZ can still be seen, identified by the presence of SSBs and early proximal tubules.

The structure of the mature kidney can be separated into the cortex, the surrounding fibrous capsule and the medulla. The functional unit of the kidney; the nephron (short-loop and long-loop), is comprised of a glomerulus, Bowman's capsule, proximal tubule, loop of Henle, distal tubule and the collecting tubules. Each nephron, of which there

are approximately 1 million per kidney, span the junction between the renal cortex and the medulla. The glomerulus and Bowman's capsule, collectively known as the renal corpuscle, maintain connections between the vascular system (vascular pole) and the proximal tubule (urinary pole). It is here that ultrafiltration of blood plasma takes place, to produce primary urine, at a rate of approximately 125ml per minute in an adult human. The ultrafiltrate then passes to the proximal tubule, lined by simple cuboidal epithelium with a brush border, specialising in the absorption of amino acids, glucose, ions and water. The reabsorption capacity of the proximal tubule is essential for the maintenance of the high glomerular filtration rate sustaining the increased metabolic demands of land vertebrates (Curthoys and Moe, 2014). The proximal tubule then descends, becoming the thin descending limb of the Loop of Henle, lined by simple squamous epithelium. This portion of the nephron is highly water-permeable, and is therefore the primary site of water reabsorption, aided by its relative impermeability to ions (Pannabecker, 2012) and expression of the active water channel aquaporin 1 (AQP1) in the first 10% of this segment. Therefore, by definition, the Loop of Henle constitutes a urine concentrating mechanism, the strength of which can then be regulated in the ascending thin limb (long-loop only). This section has little or no osmotic water permeability, and instead regulates the transport of sodium and chloride ions. The filtrate then proceeds to the thick ascending limb where sodium, potassium and chloride ions are reabsorbed, and is then drained into the distal convoluted tubule (DCT) (Pannabecker, 2012). The DCT is the shortest section of the nephron (5mm in humans), yet plays a crucial role in the regulation of sodium chloride reabsorption, calcium and magnesium handling, and potassium secretion. It is particularly unique in its ability to respond to hormonal stimuli to regulate ion homeostasis, and is therefore also implicated in a number of systemic diseases such as hypertension (Subramanya and Ellison, 2014). Finally, the urine passes into the collecting duct, where the final concentration is determined by the reabsorption of up to 24% of filtered water through the expression of aquaporins in response to hormonal signals (antidiuretic hormone or vasopressin) (Kortenoeven et al., 2015).

The exposure to high pressure and high ion concentrations, together with the high metabolic demands of active tubular transport exert significant strain on the kidney, yet this remarkable organ is extremely resilient, perhaps due to the sheer number of individual nephrons, with approximately 2 million per person. It is possible to lose 75-

80% of kidney function before the patient exhibits renal failure, and as a result, many kidney diseases go undiagnosed in their early stages. However, others leading to rapid obstruction of renal function can be detected much earlier, including perhaps the most famous of all kidney diseases-polycystic kidney disease.

The development and progression of chronic kidney disease (CKD) in humans and laboratory models can be broken down into well-defined stages, though the molecular mechanisms governing the transition between each stage are not so well described (Meng et al., 2014).

The development of CKD, outlined in Fig 4.2 (Wallace, 2011), is commonly initiated by an insult or injury to the nephron, particularly in the glomerulus or proximal tubule. In a healthy kidney, the epithelial renal tubules, located on a tubular basement membrane, are bordered by a small amount of extracellular matrix (ECM) containing resident fibroblasts. In response to injury, inflammatory cells such as macrophages are recruited, and secrete pro-inflammatory cytokines which, in addition to stimulatory factors such as the mitogen FGF-2 (Strutz et al., 2000) released by the damaged renal cells, activate resident myofibroblasts. (Fragiadaki and Mason, 2011, Neilson, 2006) The activation of renal ECM resident fibroblasts in adult tissue leads to ECM synthesis,

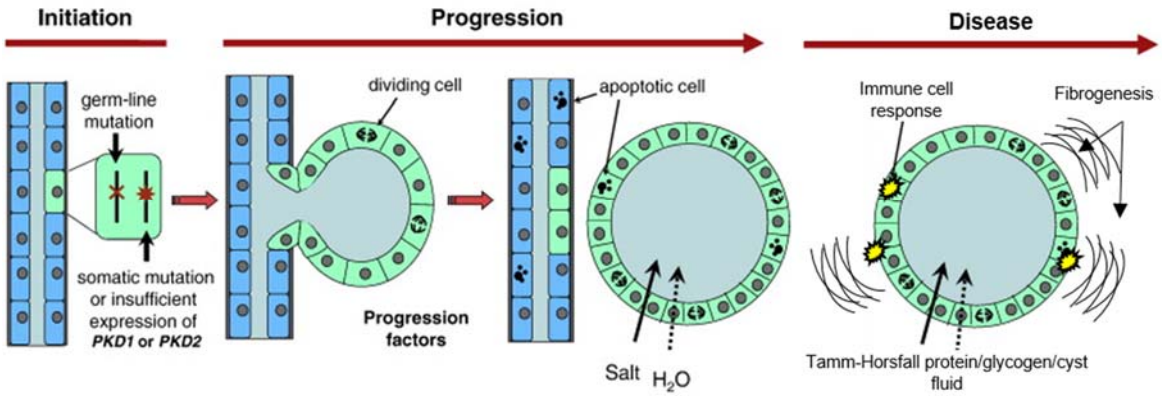



***Figure 4.2 Schematic of cyst development in cystic kidney disease, adapted from Wallace et al., 2011.***

*ADPKD is initiated by a mutation in Pkd1 or Pkd2, leading to absent or mis-expression of polycystin proteins. Downstream signalling changes lead to an increase in epithelial cell proliferation, resulting in tubule expansion and cyst formation. The cyst becomes fully encapsulated by abnormal, proliferative and apoptotic epithelium, and the tubule of origin is obstructed. Surrounding ECM-resident fibroblasts are activated both by infiltrating immune cells and damaged epithelium, facilitating the development of fibrosis surrounding the cyst. Sustained cyst development leads to chronic inflammation, tubule blockage and steady decline in renal function. Adapted from Wallace et al., 2011.*

termed tubulointerstitial fibrogenesis, which replaces the damaged tissue. However, this process is often exacerbated, leading to excessive scar tissue formation (fibrosis), tubular dilation and, in some cases, cyst formation (Strutz et al., 2000).

Cystic kidney diseases are historically separated into two categories, based on genetic or non-genetic (acquired) causality. Simple cysts often arise in ageing populations, detected through abdominal ultrasound. It is estimated that approximately 50% of individuals over 50 years of age have one or more renal cysts, with little or no impact on renal function (Eknoyan, 2009). In contrast, many hereditary cystic kidney diseases such as autosomal dominant and autosomal recessive polycystic kidney disease (AD/ARPKD), present during childhood or early adulthood and cause significant renal impairment, secondary cystic lesions in the periphery, and without transplant, death. Whilst the genetic components associated with these diseases are well documented in both human and laboratory model, little is understood, in comparison, of the molecular mechanisms leading to cyst formation and disease progression. Research into these diseases has outlined a common, proliferative phenotype, linked to several mechanisms downstream of identified mutations. Perhaps the most well studied are indeed the most prevalent; mutations in PKD1 and PKD2 (ADPKD), and in PKHD1 (ARPKD).

PKD1 and 2 encode two, widely expressed membrane glycoproteins; polycystin-1 and 2 respectively and present almost exclusively as disease loci for ADPKD in humans, with a prevalence of 1:400 to 1:1000 live births. ARPKD, in contrast, is linked to mutations in PKHD1, encoding fibrocystin, localised to the primary cilia and basal bodies. Both AR and ADPKD are characterised by de-differentiation of tubular epithelial cells, excessive and prolonged proliferation and fluid secretion (Torres and Harris, 2006). Disruption of several key cellular processes have been implicated in these diseases, though a definitive causal mechanism is yet to be defined between genetic mutations and the development of cysts.

The use of animal models has provided a window into the functions of these proteins in early embryonic development, through to neonatal disease progression and cyst formation. For translational purposes, it is no surprise that the most commonly used model to study these diseases are those with PKD1/2 or PKHD1 mutations. However, several other genetic alterations have been identified as cyst-causing, including the

deletion of oak ridge polycystic kidney disease-associated genes Ift88 and Ift20, leading to the disruption of polycystin 2 (PC2) localisation, and the mis-expression of the cell proliferation gene Nek8 from a specific area of renal cilia to the entire length, associated with increased cyclic AMP levels along the entire nephron (Gascue et al., 2011).

Whilst mutations in PKD1 and 2 can be defined as causal events in human PKD, the phenotypes manifested as a result of other mutations are strikingly similar, and many share common mechanisms leading to cyst development, namely dysregulation of cell proliferation and increased fluid secretion. Subsequent immune cell infiltration, activation of the surrounding ECM-resident fibroblasts and the EMT of tubule epithelium are common to all cystic kidney diseases studies to this extent so far, and are most likely secondary to the development of small cysts obstructing passage of primary urine through individual nephrons.

Here we describe a cystic kidney disease as a result of chronic, global AMPK activation, as opposed to mutation or deletion of genes known to cause PKD. Whether this condition overlaps with the mechanisms underlying previously described cystic kidney diseases remains to be seen.

## 4.2 Observation of kidneys from D316A-Tg mice revealed a cystic phenotype

The cystic kidney phenotype displayed by D316A-Tg mice was apparent upon the harvest of 7-week old chow-fed male animals, on a mixed 129sv/C57Bl/6J, (hereafter referred to as ‘mixed’) background. Kidneys appeared slightly enlarged, though comparable in weight (Fig 4.3A), with fluid-filled cysts covering the renal capsule. Upon histological examination, the degree of cystogenesis was found to be variable between animals, though cysts were present in all animals examined at the time (Fig 4.3B).

In the case of the D316A-Tg kidney, cysts were found dispersed throughout, with no obvious localisation to specific structures, such as glomeruli (Fig 4.3B inset), proximal or distal tubules. At this magnification, cysts appeared numerous, well defined and of varying stages of fibrosis. Larger cysts (black arrows) displayed a thin endothelial cell lining, with a continuous border of fibrotic tissue. Smaller cysts (yellow arrows) did not display the same fibrosis, but instead appear as dilated tubules.

Renal cyst development is often preceded by an insult, such as tubule obstruction or excessive proliferation. To understand the origin of these cysts, and to investigate the

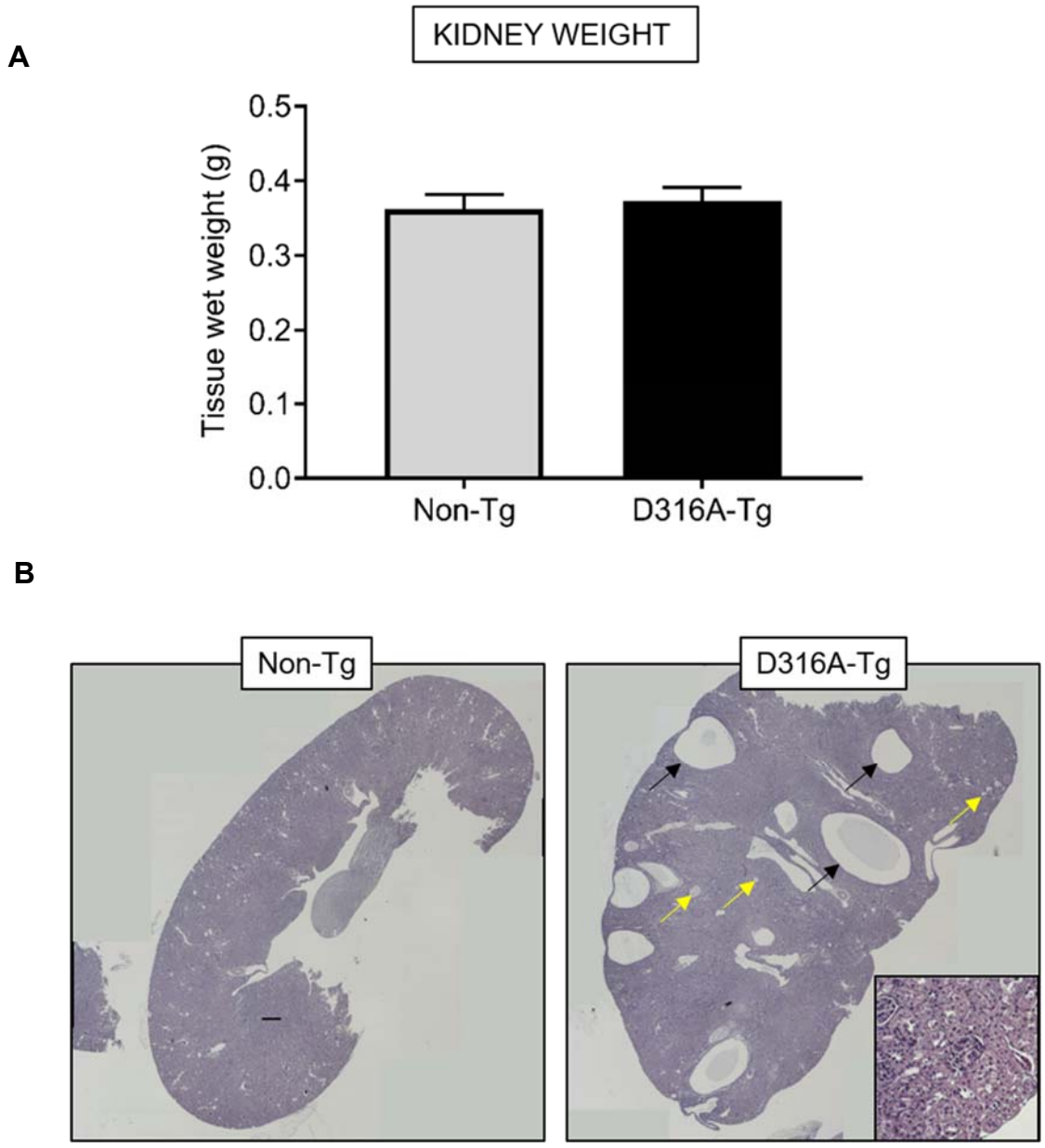



***Figure 4.3 AMPK D316A-Tg, 129sv/C57BL/6J, chow-fed animals display a cystic kidney phenotype on a chow diet***

***A)*** *Kidney wet weight at harvest, from 10 Non-Tg (5 male and 5 female) and 6 D316A-Tg chow-fed mice (3 male and 3 female) at 7-14 weeks of age. N=10, 6. Data are presented as mean ± SEM.*

***B)*** *Representative H+E stained kidneys from 7 week old mice. D316A-Tg mice all presented with cystic kidneys, irrespective of age and sex. Black arrows indicate large, encapsulated cysts with a fibrous border. Yellow arrows indicate smaller, less well defined cysts. All wild type kidneys displayed normal morphology. Composite image magnification at 2.5x, inset magnification 20x.*

progression through to adulthood, kidney development was monitored *in vivo.*

### 4.2.1 Monitoring of the D316A-Tg kidney phenotype in vivo

Using ultrasound, non-transgenic wild-type, WT-Tg and D316A-Tg animals were monitored from 6 weeks of age, for a period of 20 weeks. Using this technique, it was possible to track the development of cysts, their size and position within the kidney, and, importantly, the degree of fibrosis. A total of 4 non-Tg, 4 WT-Tg and 5 D316A-Tg animals were scanned at 6, 10 and 16 weeks of age, with images taken of both kidneys, and of the liver for orientation and density comparison.

The appearance of the kidney from D316A-Tg animals was striking, with almost all of the renal cortex filled with large, fluid filled cysts, identified as large, dark regions (Fig 4.4A, white arrows), by 6 weeks of age. These regions were bordered by a region of increased density, greater than that of normal renal tissue, suggesting fibrosis. No such cystic or fibrotic lesions could be detected in either Non-Tg or WT-Tg kidneys.

An examination conducted at 10 weeks of age confirmed the continued progression of fibrosis, with a dramatic increase in dense tissue surrounding cystic bodies (Fig 4.4A, red arrows). However, the size of both the whole kidney, and of individual cysts appeared reduced, though due to the numerous quantity of lesions, it was not possible to accurately quantify total volume. At 16 weeks of age, kidneys appeared smaller upon scanning, with increased fibrotic tissue density surrounding cystic lesions. Blood samples were taken between scans, at 8, 12 and 18 weeks of age, to be analysed for renal damage markers, including creatinine and blood urea nitrogen (BUN).

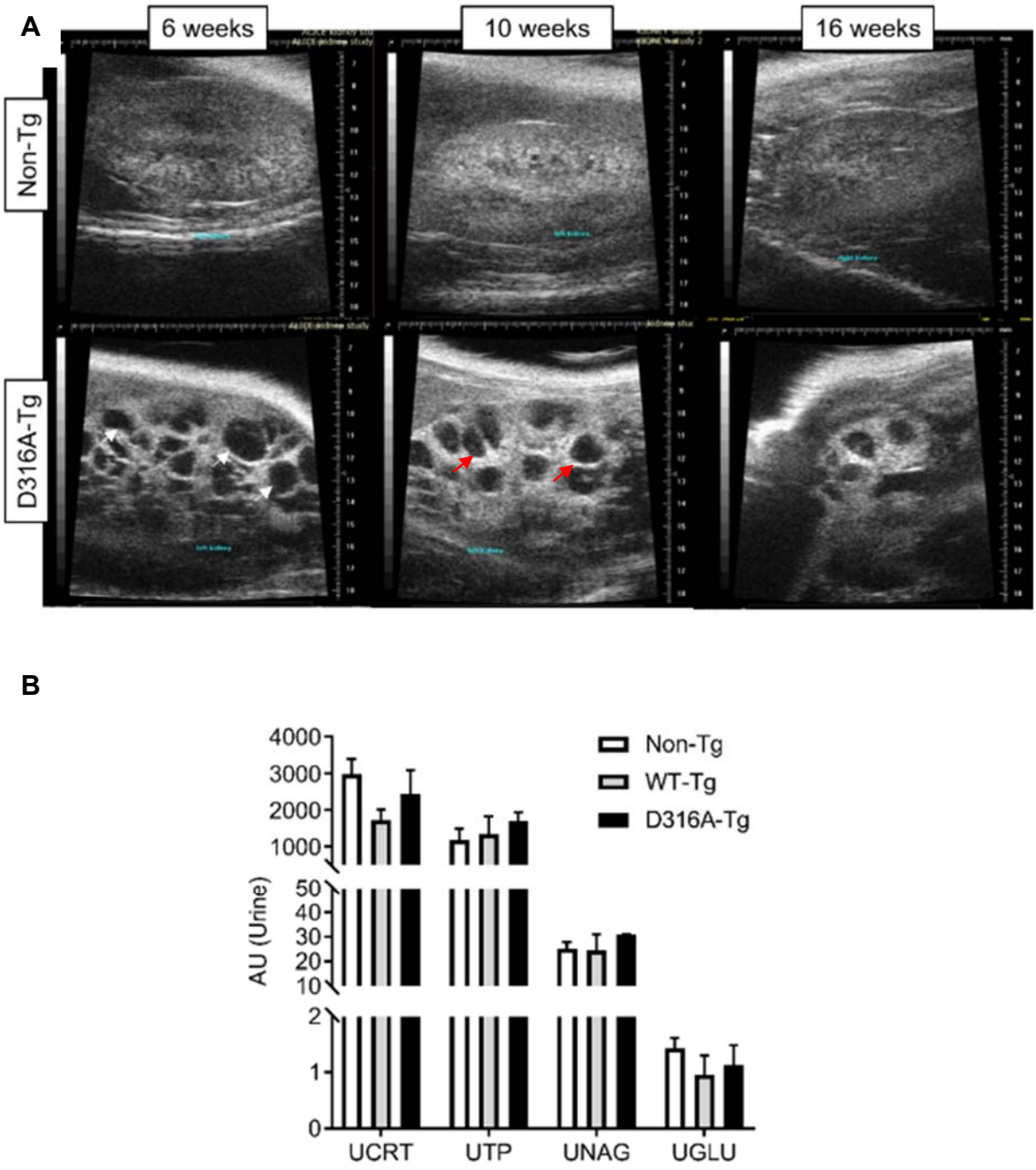



***Figure 4.4 Monitoring of the D316A-Tg cystic kidney phenotype in vivo***

***A)*** *Representative ultrasound images from non-Tg and D316A-Tg male mice at 6, 10 and 16 weeks of age. White arrows indicate the presence of fluid-filled cysts, present only in D316A-Tg animals. Increased tissue density (red arrows) indicates the presence of fibrotic tissue, present at 10 weeks.*

***B)*** *Analysis of urine from 14-week old non-Tg, WT-Tg and D316A-Tg mice (Cambridge). Urine creatinine, (UCRT), total protein (UTP), urine N-acetyl-β-D-glucosaminidase (UNAG) and urine glucose (UGLU), N=5, 2, 3. Data are presented as mean ± SEM.*

Serum samples were analysed using a VetScan VS2 (Abaxis) sample analyser, which, in addition to the above markers, also provided a comprehensive serum biochemistry profile, including glucose, potassium and sodium. Surprisingly, despite the compromised condition of D316A-Tg kidneys from 6 weeks of age, no elevation in BUN or creatinine was detected, nor in any other parameter measured. Urine samples from 14-week old male, non-Tg, WT-Tg and D316A-Tg mice sent to Cambridge (AstraZeneca) were analysed for urine creatinine (UCRT), total protein (UTP), urine glucose (UGLU) and urine N-acetyl-β-D-glucosaminidase (UNAG). No significant differences were identified despite the observed cystic burden (Fig 4.4B).

### 4.2.2 Characterisation of D316A-Tg kidney morphology

The experiments conducted thus far showed that D316A-Tg mice present with a polycystic kidney disease, with cysts present from at least 6 weeks of age. Despite this early-onset, renal function was preserved until at least 16 weeks. Having determined the progression of this phenotype, we then investigated the effects of AMPK activation on the development of the kidney, with animals first harvested at 3 weeks of age. Kidneys from D316A-Tg animals were enlarged, with evidence of cysts,

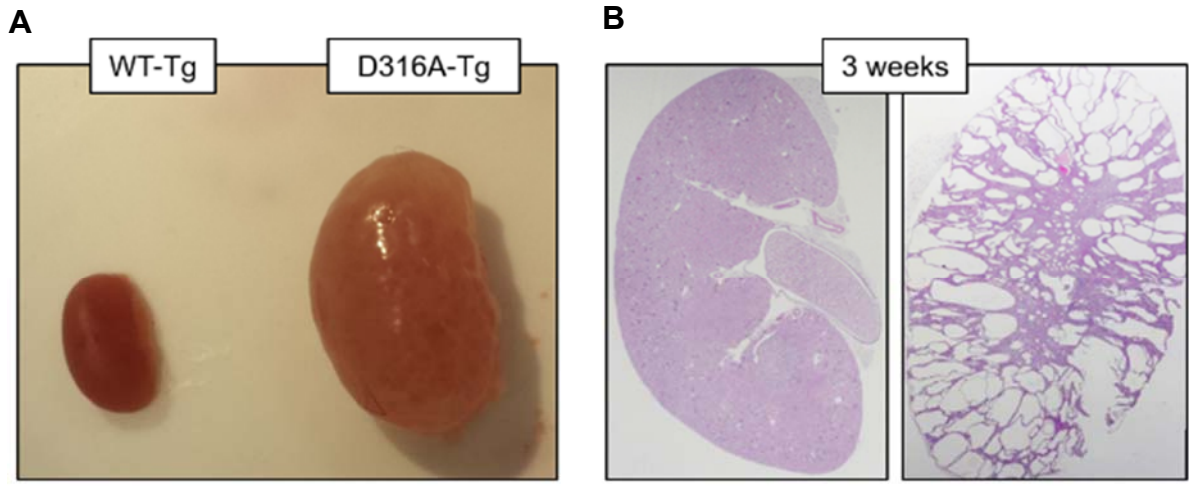



***Figure 4.5 AMPKγ1-D316A-Tg mice develop cystic kidneys from 3 weeks of age***

***A)*** *Comparison of right kidney from WT-Tg (left) and D316A-Tg (right) mice at 3 weeks of age.*

***B)*** *PAS staining of kidneys the same from 3-week old WT-Tg and D316A-Tg mice. Morphology presented is representative of most samples. Some kidneys displayed a lower cystic burden, shown in Fig 4.7. 2.5x magnification, composite image, not to scale.*

with one mouse in particular presenting heavily cystic, fluid-filled renal tissue similar to the morphology seen using ultrasound (Fig 4.5A). Though cysts to this extent were not seen in all animals, all kidneys harvested from D316A-Tg animals at this time point displayed some cystic development.

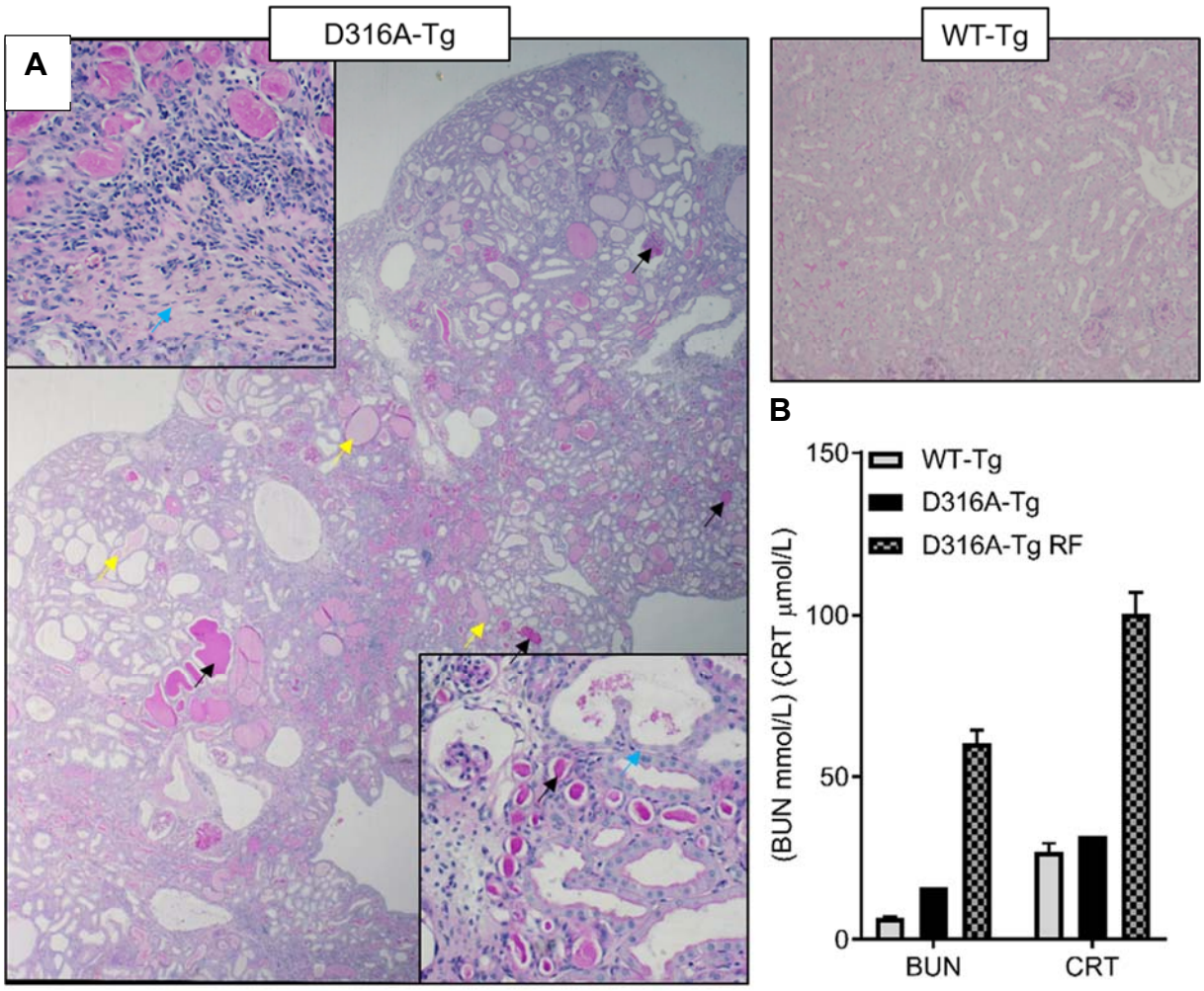



***Figure 4.6 AMPKγ1-D316A-Tg Mice on a mixed background develop chronic kidney disease with associated renal failure (preliminary) at 33 weeks of age.***

***A)*** *PAS staining of WT-Tg and D316A-Tg kidneys from male, 33 week old mice on a chow diet. D316A-Tg kidneys display a significant cystic burden, with tubule dilation, protein (yellow arrows) and glycogen deposition (black arrows). All cysts and tubules can be seen surrounded by fibrotic tissue (blue arrows, insets)*

***B)*** *Blood markers of renal failure three D316A-Tg mice at 33 weeks of age, with representative WT-Tg measurement. Blood Urea Nitrogen (BUN) and creatinine (CRT) were elevated in both animals presenting with signs of renal failure (RF), but were only slightly elevated in the third animal, despite heavily cystic kidneys (n=3, 1, 2). Significance was not attributed due to insufficient numbers in the renal failure group at this time-point. Data are presented as mean ± SEM.*

Histology (PAS staining) of these kidneys revealed a remarkable cystic burden, making up over half of the total kidney volume in some samples. As seen previously, cyst morphology was variable, with larger cysts present in the renal cortex, extending into the medulla, where smaller cysts were of higher abundance. In contrast to those seen at 7 weeks, cysts present at 3 weeks were less defined, bordered by a monolayer comprised of cuboidal epithelial cells, which usually line the proximal and distal tubules within the nephron, suggesting that the cysts originate from blocked or dysfunctional tubules, which then dilate and fill with fluid.

In a parallel study, chow-fed animals were aged to 29-33 weeks, at which point 2 of 3 D316A-Tg mice displayed ill-health in the form of weight loss, inactivity and rapid respiration, indicative of pain.

All three animals were culled and the cause of sickness identified as peritonitis (fluid filled peritoneal cavity), in conjunction with severely cystic kidneys. Blood samples taken via cardiac puncture were analysed using the VetScan, where they displayed elevated creatinine and BUN, indicating renal failure (Fig 4.6B).

The use of PAS staining allowed identification of a proportion of cysts containing polysaccharide deposits (deep magenta), which were later identified as glycogen (Fig 4.6A). These deposits were not limited to cystic bodies, but also found in some glomeruli and the epithelial cells of non-cystic tubules.

### 4.2.3 Kidney development and glycogen accumulation

To identify the events prior to kidney cyst formation in the D316A-Tg model, kidneys from post-natal day 1 (P1), day 4 (P4) and day 7 (P7) pups, were examined for abnormal morphology. Interestingly, no well-formed cysts were found at these time-points (Fig 4.7), though several other abnormalities were observed. These observations are subsequently highlighted at higher magnification in figures 4.8 and 4.9. By 3 weeks (P21), all D316A-Tg kidneys showed cyst development.

Neonatal (P1) kidneys appeared smaller and misshapen than their wild-type counterparts, with a disjointed renal capsule (Fig 4.7,). At higher magnification it was observed that, in non-Tg neonatal kidneys, the nephrogenic zone (NZ), indicated by a dashed line, was well defined, and confined to the edge of the cortex (Fig 4.8). Formed glomeruli (black arrows) and proximal tubules (yellow arrows) were found to be far

more prevalent than S-shaped bodies (SSB), consistent with a maturing renal cortex (Fig 4.1). By P4, non-Tg kidneys exhibited a normal ‘bean’ shaped morphology with a defined cortex and renal capsule. No subsequent changes in non-Tg kidney morphology were observed, consistent with normal kidney development.

In contrast, D316A-Tg P1 kidneys displayed abnormal renal capsule morphology (Fig 4.7), which at higher magnification contained both SSBs (black arrows, right inset) and Comma-shaped bodies (CSB), with no identifiable mature glomeruli. Several glycogen deposits were also identified (Fig 4.8, white arrows) in the epithelial cells of proximal tubules. Nephron formation (outlined in schematic Fig 4.1) appeared stunted, with

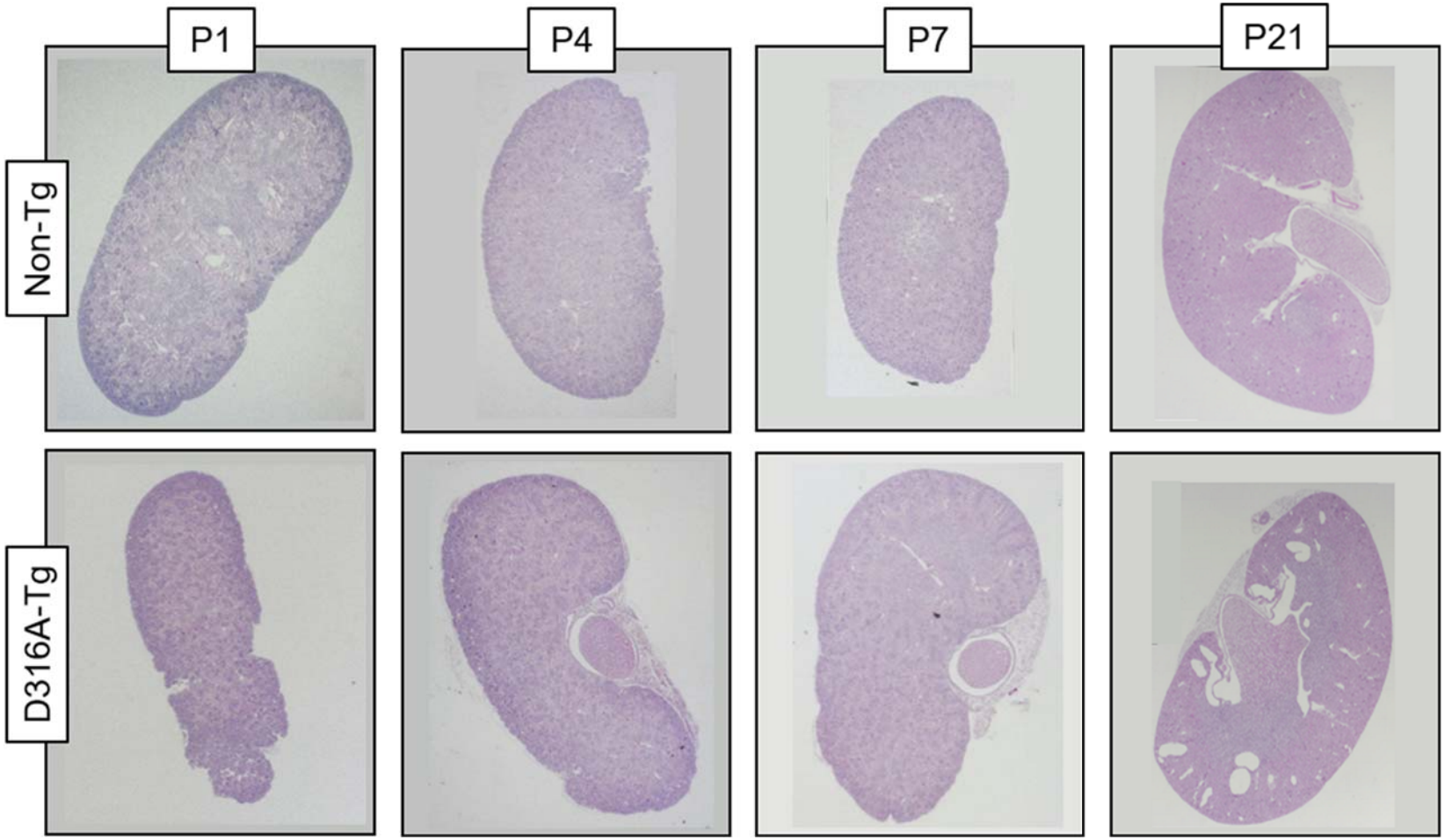



***Figure 4.7 Non-Tg and D316A-Tg kidney development***

*Developmental timeline displaying PAS stained kidneys from neonatal, P4, P7 and P21 (3-week). Abnormal kidney structure observed in new-born animals, with a disjointed renal capsule and irregular distribution of developing nephrons. Cysts were visible in all D316A-Tg kidneys by 3 weeks of age (composite images at 2.5x magnification).*

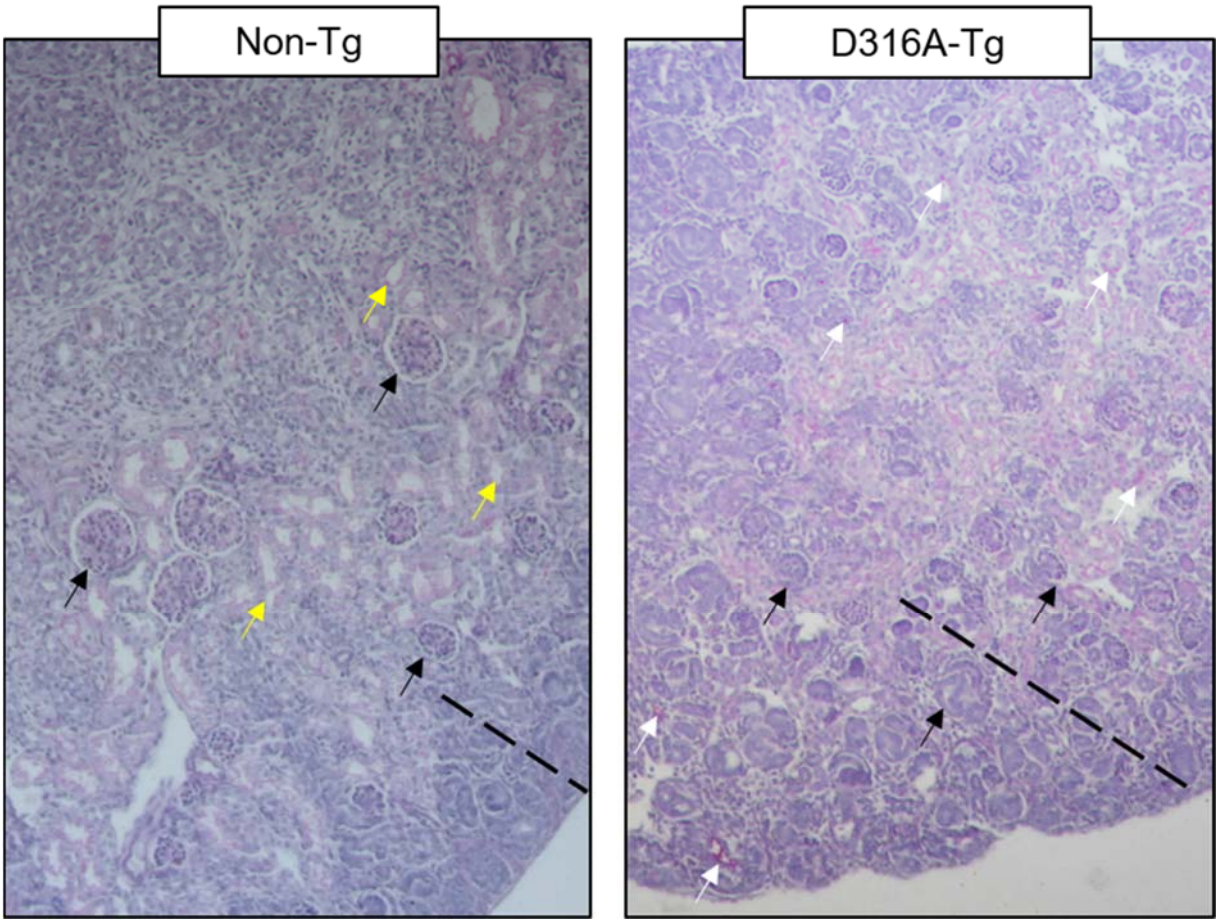



***Figure 4.8 Nephrogenic zone of neonatal (P1) Non-Tg and D316A-Tg kidneys.***

*PAS staining of wild-type kidneys display normal nephron development, with structurally defined glomeruli (black arrows) and proximal tubules (yellow) with minimal magenta staining (polysaccharide) limited to the lining of developing tubules.*

*D316A-Tg kidneys display a wide and disorganised nephrogenic zone (dashed line), many 'S-shaped' bodies (black arrows, right inset), and several pronounced glycogen deposits in early proximal tubules (white arrows). (10x magnification).*

smaller tubules and misshapen glomeruli, indicated by black arrows. By P7, several glomeruli were found to be overcome by glycogen accumulation (Fig 4.9, yellow arrows), and many tubules significantly smaller than their wild-type counterparts. No glycogen deposits of this nature were detected in Non-Tg kidneys. By P21, D316A-Tg mice displayed significant cyst development with protein and glycogen deposition observed within cystic bodies (Fig 4.9).

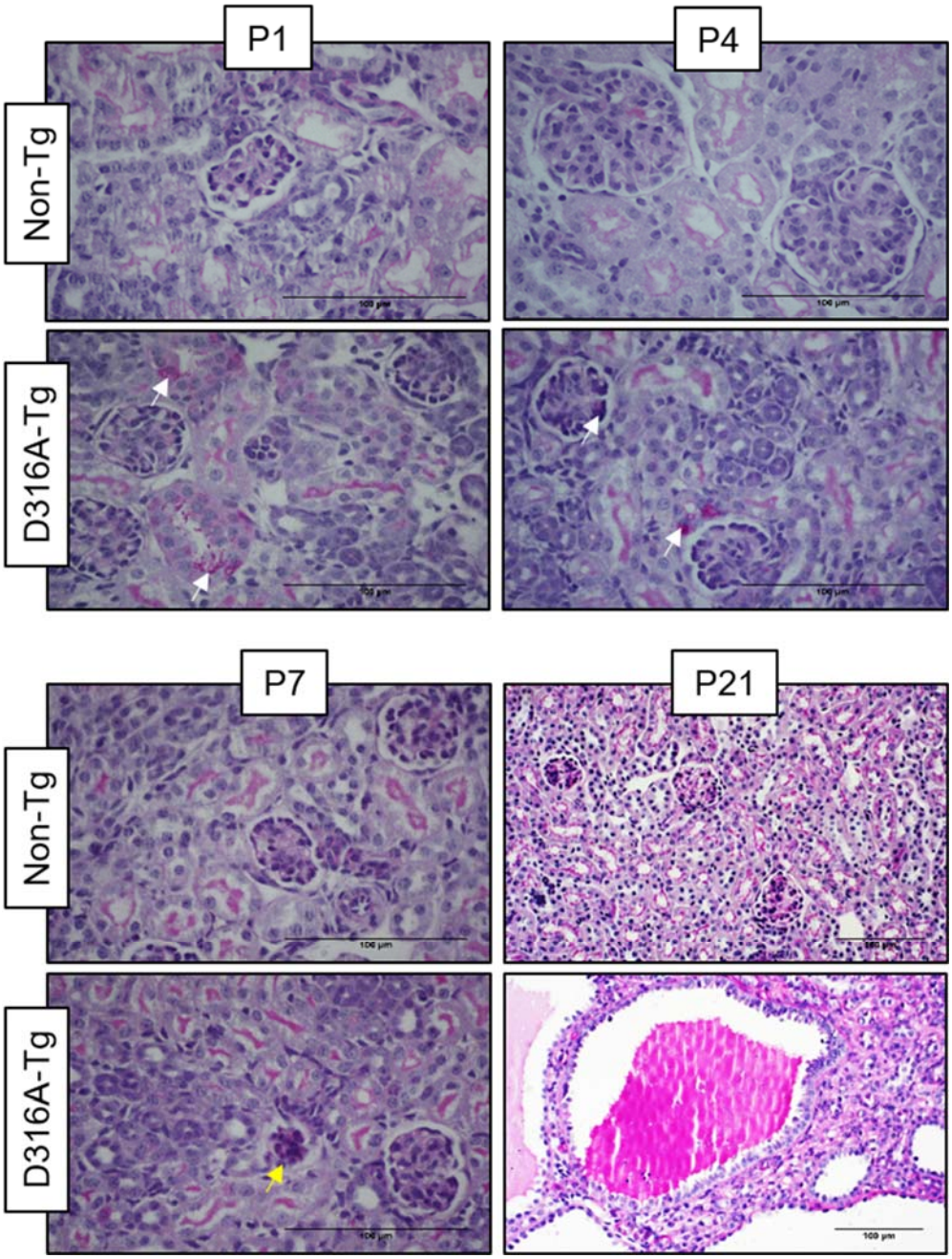



***Figure 4.9 D316A-Tg kidney development and glycogen deposition.***

*PAS staining of Non-Tg and D316A-Tg P1-P21 kidneys. Glycogen accumulation was observed from post-natal day 1 in the tubular epithelium of D316A-Tg kidneys, absent in Non-Tg controls. Nephron development appeared altered, with misshapen glomeruli and further glycogen deposition between post-natal day 4 and 7. By 3-weeks, D316A-Tg kidneys exhibited cystic lesions with luminal glycogen and protein deposition. Images obtained at 40x magnification, scale bar 100μm.*

.

The deposition of glycogen in kidney epithelium has been previously shown to contribute to abnormal proliferation and cyst development (Gjorgjieva et al., 2016). As the nephrogenic zone is of mesenchymal origin, coordinated proliferation is essential for correct development, orientation and function of the renal tubules. Therefore, proliferation in WT-Tg and D316A-Tg kidneys from birth, through to the development of cysts was assessed.

### 4.2.4 Increased Proliferation is a Hallmark of the D316A-Tg Kidney Phenotype

To assess proliferation, WT-Tg and D316A-Tg kidneys were stained (immunohistochemistry) with the proliferation marker Ki67 (Fig 4.9), which is present during all active phases of the cell cycle.

Neonatal kidneys from D316A-Tg mice were smaller, with an elongated and irregular structure, as a result of a less defined renal capsule when compared with WT-Tg tissue (Fig 4.9). When stained with Ki67, a remarkable increase in proliferation was observed. In WT-Tg (normal) kidneys, proliferation was largely confined to the outer edges of the renal cortex, known as the nephrogenic zone, containing numerous 'S-shaped' structures (Fig 4.10 inset i).

Proliferation within the renal pyramid (in the developing medulla) was found to be evenly distributed (inset ii), with identifiable proximal tubular structures, but no discernible separation of the outer or inner medulla. In contrast, D316A-Tg neonatal kidneys presented with increased proliferation, both within the nephrogenic zone and the developing renal cortex.

The pattern of proliferation appeared irregular, with S-shaped proliferative bodies extending into the cortex (inset iii). In addition, proliferation appeared in small, uneven patches throughout the rest of the renal tissue (inset iv).

By post-natal day 4, proliferation within WT-Tg tissue was no longer detected. The glomeruli, proximal and distal convoluted tubules and collecting ducts were well-defined within the renal cortex, and no abnormalities were detected. However, D316A-Tg kidneys continued to exhibit proliferation (Fig 4.11), in both tubular and glomerular epithelial cells.

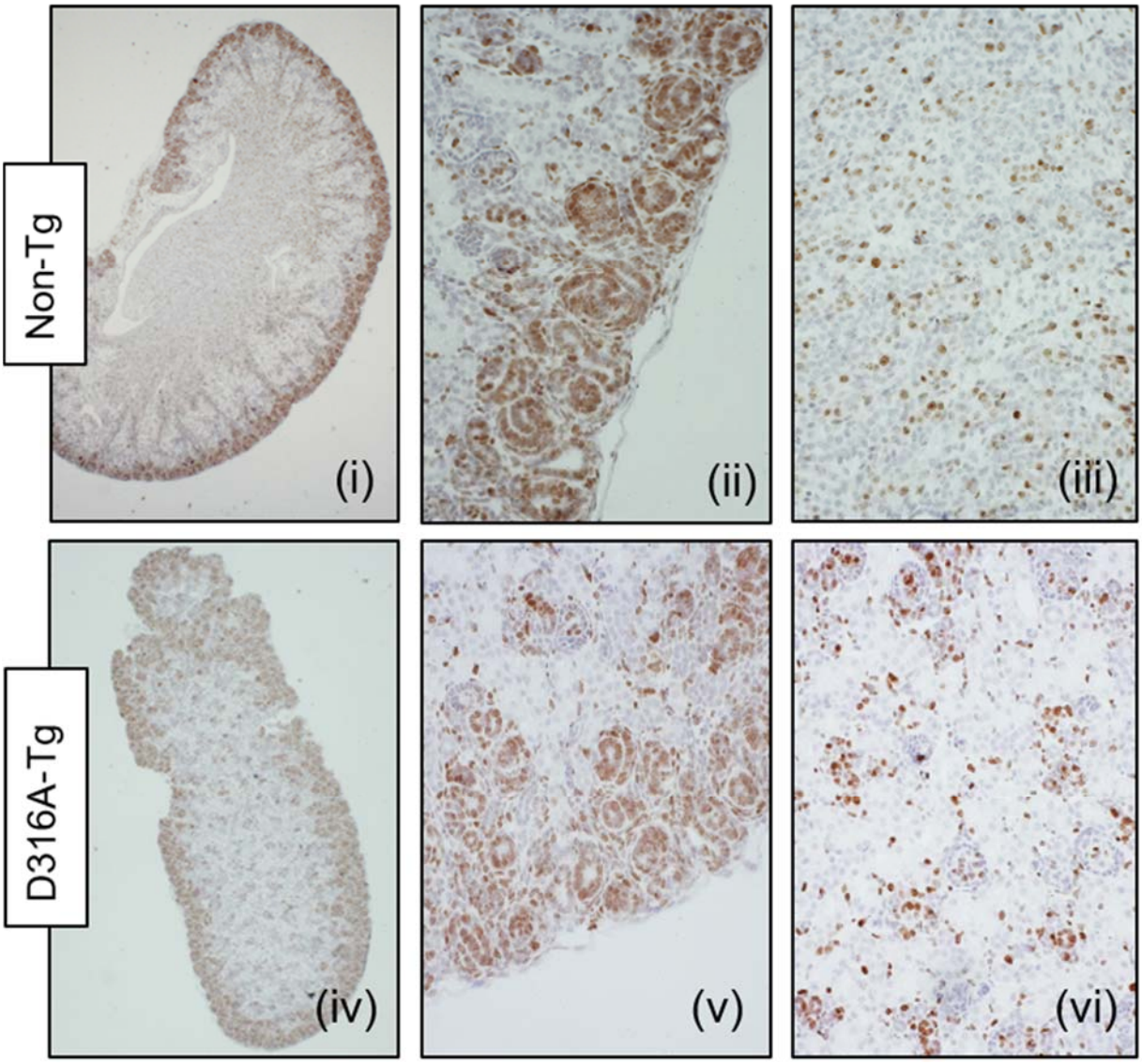



***Figure 4.10 Proliferation in the D316A-Tg developing kidney***

*Ki67 stained kidneys from neonatal WT-Tg and D316A-Tg mice. Composite images outline a defined zone of proliferation in WT-Tg kidneys (i), with developing nephrons showing a common 'S-shaped' morphology, restricted to this region (ii). Proliferating cells found throughout the cortex were evenly distributed (ii), and by 3 weeks of age, none were observed in either region. In contrast, D316A-Tg kidneys displayed a disorganised nephrogenic zone (iv), with S-shaped bodies migrating excessively, in a disorganised manner, into the renal cortex (vi).*

By three weeks, kidneys were heavily cystic with ongoing proliferation. Whilst a significant proportion of these dividing cells were found in the single-cell layer bordering cysts, many were also found lining normal tubules, though no deterioration in function was apparent.

Finally, samples from 33 week old animals were evaluated, including those that had entered renal failure. Consistent with previous time-points, we found areas of proliferation, some associated with cystic lesions, and others in fibrotic areas, indicating a continual activation of the ECM in these animals. One animal (pictured, Fig 4.11, (i)) exhibited a lesion with morphology similar to that of renal adenocarcinoma, a common progression of polycystic kidney disease, due to prolonged exposure of the epithelium to inflammatory stimuli and remodelling of the ECM. Wild-type kidneys did not display any significant proliferation at this time-point.

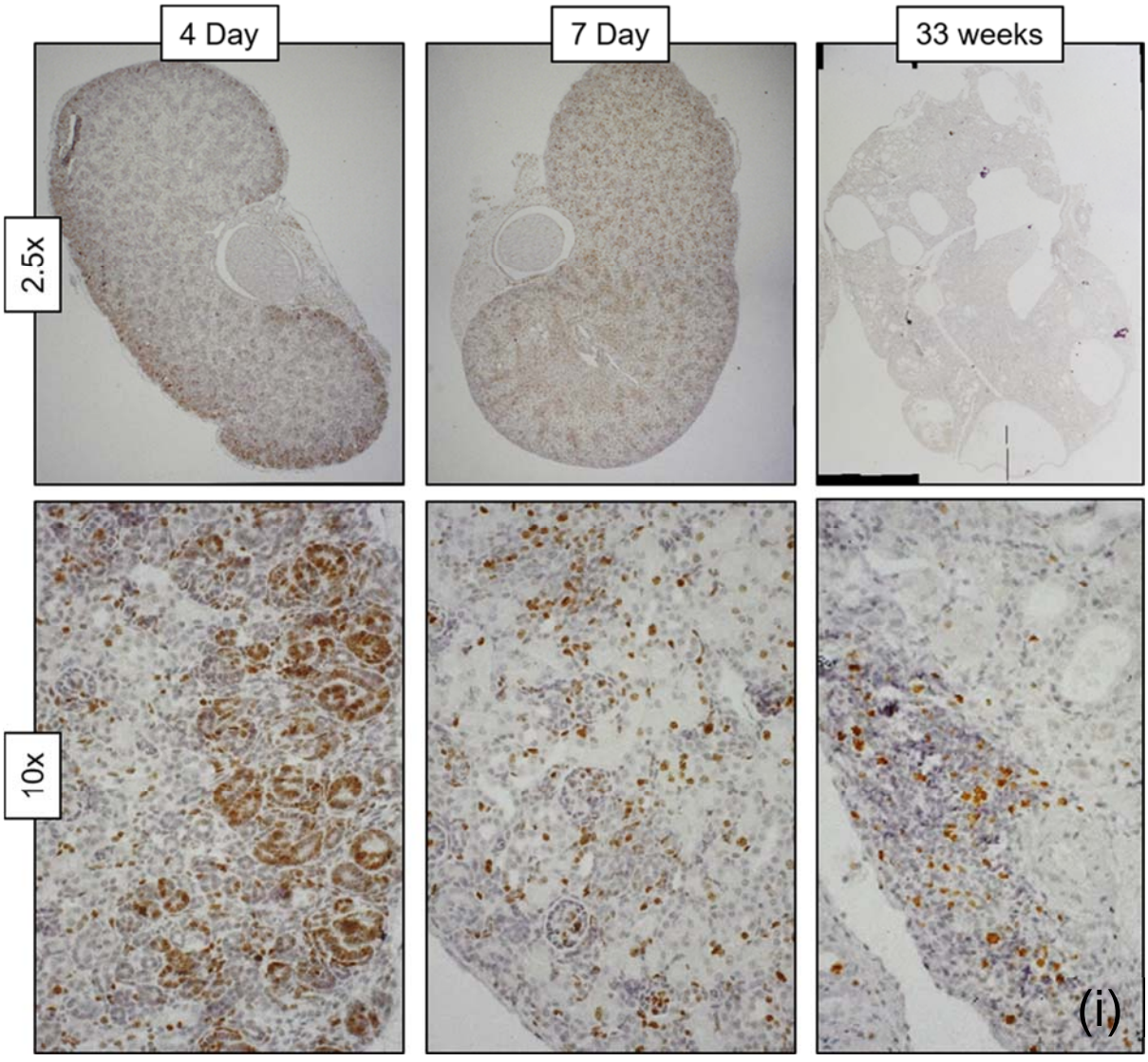



***Figure 4.11 Sustained, irregular proliferation in the D316A-Tg kidney***

*Ki67-stained D316A-Tg kidneys show sustained proliferation from 4 days to 33 weeks of age, with regions of increased cellularity (i) in one animal. No proliferation was detected in WT-Tg kidneys from 4 days of age.*

### 4.2.5 Polycystic kidney disease gene expression

The disruption of Pkd1 and Pkd2 gene expression is known to cause cyst development. To confirm AMPK did not disrupt the expression of Pkd1 and 2, qPCR was performed using primers designed to the wild-type transcripts of Pkd1 Pkd2.

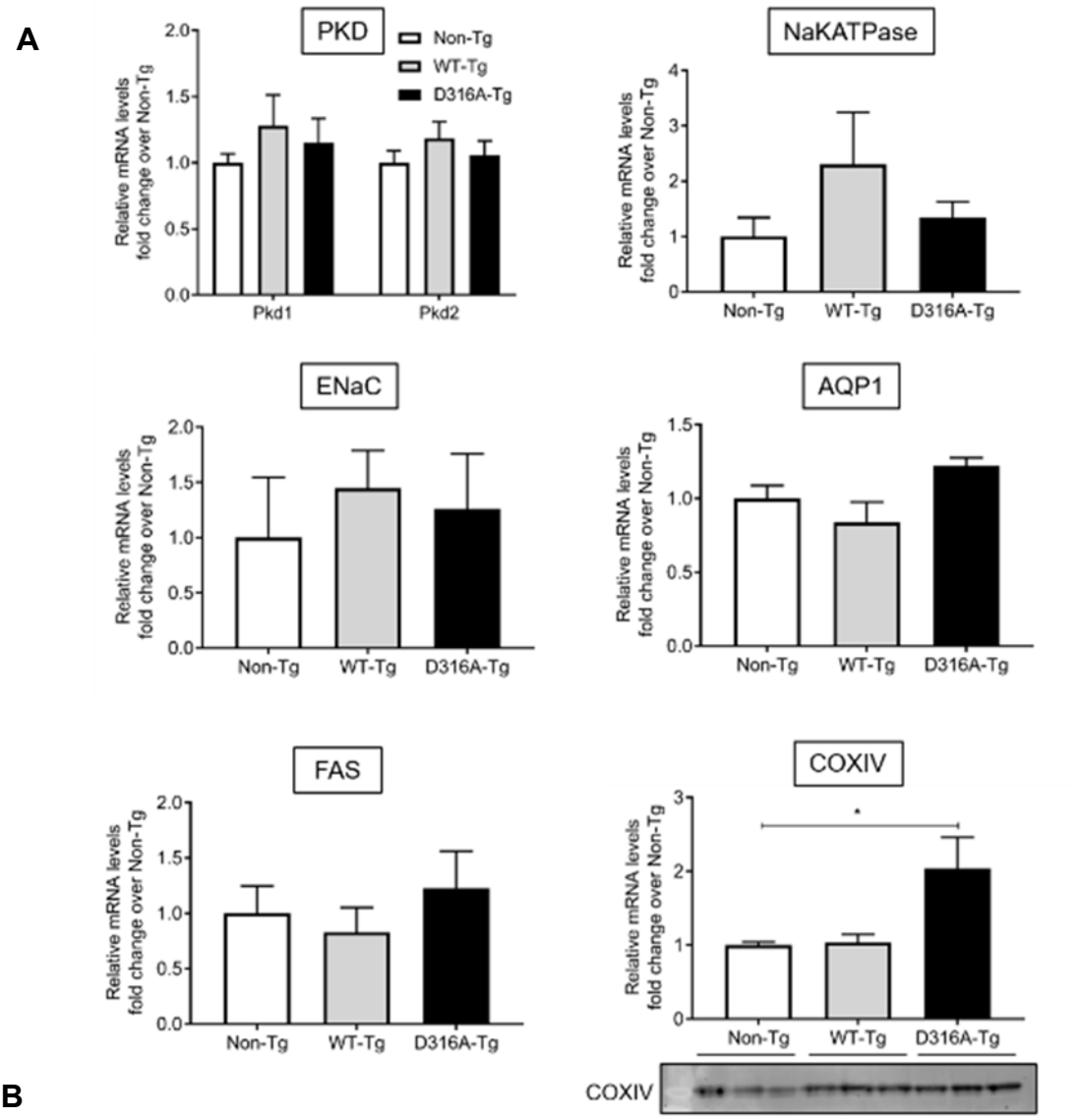



***Figure 4.12 Expression of key genes associated with a cystic kidney phenotype are unaltered in D316A-Tg kidneys at 7 weeks of age.***

***A)*** *mRNA expression of Pkd1 and Pkd2, sodium-potassium ATPase (NaKATPase, epithelial sodium channel (ENaC), aquaporin 1 (AQP1) and fatty acid synthase (FAS) in kidneys from 7-week old male Non-Tg, WT-Tg and D316A-Tg mice. Gene expression was normalised to GAPDH and expressed as a fold change over Non-Tg. No significant differences were observed in these genes. Mitochondrial respiratory complex gene COXIV was significantly upregulated at mRNA level, but no differences were observed at protein level (n=3, 3, 3) as determined by Western blotting* ***(B).*** *Data are presented as mean ± SEM. *P<0.05.*

No significant difference in Pkd1 or Pkd2 gene expression was detected (Fig 4.12A), though this does not exclude the possibility that AMPK activation may alter the expression of these membrane glycoproteins through post-translational modification or translocation. To investigate this hypothesis, expression of a number of other genes associated with tubule dysfunction, fluid secretion and cyst expansion was assessed.

No significant differences were found between Non-Tg, WT-Tg and D316A-Tg kidneys in the expression of the sodium-potassium transporter NaKATPase, the epithelial sodium channel ENaC, the water channel aquaporin 1 (AQP1) or fatty acid synthase (FAS) (Fig 4.12A). However, consistent with AMPK's role in mitochondrial biogenesis, a significant, 2-fold increase in complex 4 of the mitochondrial respiratory chain was observed. Western blotting (Fig 4.12B) revealed that the increase in COXIV mRNA did not translate to protein expression (n=3, 3, 3). Therefore, it was concluded that, despite the development of cysts in all D316A-Tg mice evaluated at this time-point (7 weeks), there were no obvious differences in expression of genes commonly associated with this phenotype.

The investigation into the cause of the D316A-Tg kidney phenotype was cut short, however, when the second cohort of high-fat diet-fed mice were harvested, and did not present with the same severity of kidney cysts as seen in previous chow and high-fat diet cohorts. Subsequent cohorts again showed significant amelioration of this phenotype, some with no detectable cyst development. All animals were confirmed as heterozygous for AMPKγ1-D316A and cre positive by post-mortem genotyping to eliminate the possibility of incorrect genotyping.

It was discussed that, though animals were purchased on a 129sv/C57Bl/6J mixed background, new generations were then steadily backcrossed onto a C57Bl/6J background for several generations, and that the cystic kidney phenotype may be partly dependent on the 129sv mouse strain. To address this question, 129S2/SvHsd mice were purchased from Envigo and crossed with heterozygous, cre positive animals back-crossed onto a C57Bl/6 strain for at least 10 generations.

### 4.2.6 129S2/SvHsd D316A-Tg kidney characterisation

All studies conducted thus far had been conducted with mixed 129S2/SvHsd/C57Bl/6J mice, and as the 129Sv component had been steadily reduced, the severity of the cystic kidney phenotype had reduced accordingly. To determine whether this

phenotype was strain-dependent, a one-generation backcross onto a pure 129S2/SvHsd background was performed.

The first litter produced three wild type and three D316A-Tg heterozygous male mice with a background of at least 50% 129Sv. Animals were maintained on a chow diet for 30 weeks, with blood samples taken at regular intervals to monitor BUN and creatinine levels. An additional backcross was conducted in parallel, with 18 animals genotyped post-mortem as cre positive D316A-Tg heterozygotes.

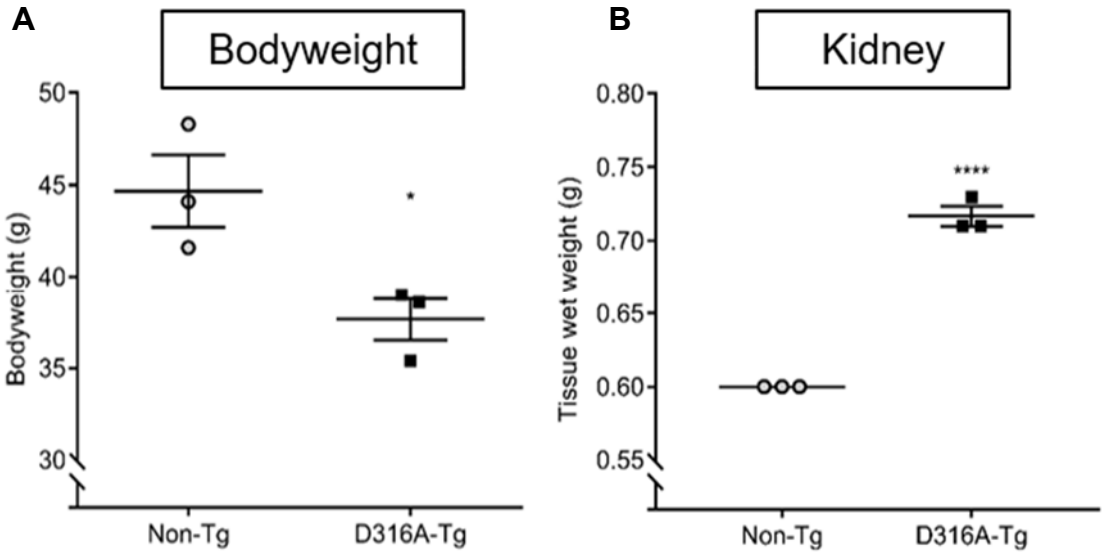



***Figure 4.13 D316A-Tg Mice on a 129Sv background display a severe cystic kidney phenotype on a chow diet.***

**A)** Bodyweight of Non-Tg and D316A-Tg$^{129sv}$ mice measured at 30 weeks of age. N=3, 3. *Data are presented as mean ± SEM.* *P<0.05

**B)** Non-Tg and D316A-Tg$^{129Sv}$ kidney wet weight at harvest. N= 3, 3. *Data are presented as mean ± SEM. ****P<0.0001.*

All D316A-Tg$^{129Sv}$ mice, male and female, presented with a severe cystic kidney phenotype, similar to that of the C57Bl/6, though with significantly less variation in severity between animals. Kidney weight was significantly increased and bodyweight decreased on a chow diet (Fig 4.13). Later experiments determined that this strain-dependent decrease in bodyweight was not seen at earlier time points, and may therefore be due to the impact of compromised renal function at 30 weeks of age.

Kidneys from these animals were then stained using PAS as described previously (Fig 4.14). Of the 18 mice from the parallel study mentioned above, all presented with almost identical cystic morphology.

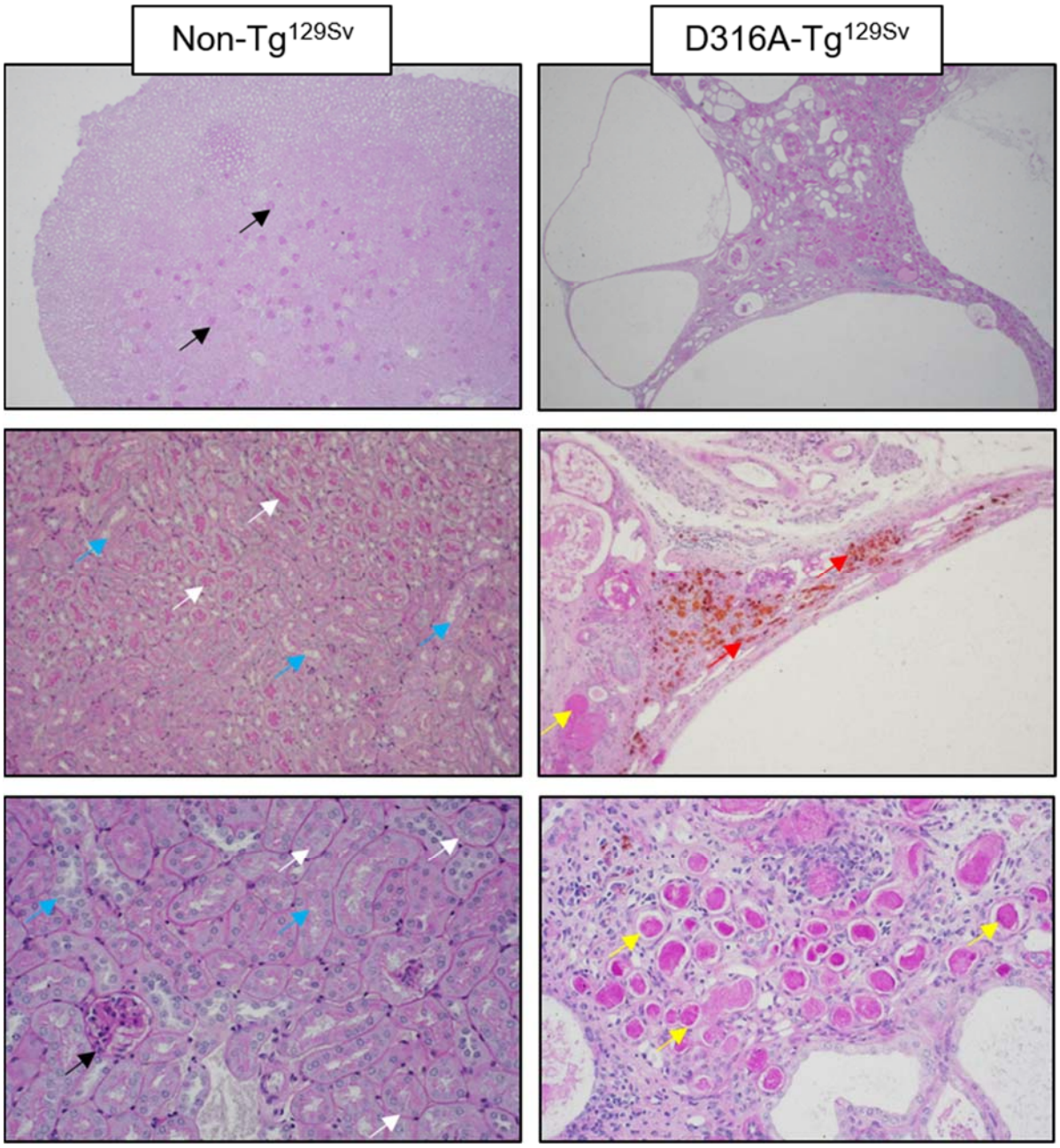



***Figure 4.14 PAS staining of Non-Tg and D316A-Tg 129Sv mice at 30 weeks of age.***

*Non-Tg mice display normal kidney morphology for this strain, with intact glomeruli (black arrows), proximal (white arrows) and distal (blue arrows) tubules, ruling out an age-dependent strain effect. D316A-Tg kidneys appear heavily cystic and fibrotic, with no discernible functional regions. Many tubules appear blocked by polysaccharide (yellow arrows), in addition to brown-stained deposits of unknown origin (red arrows).*

Kidneys were significantly enlarged, with dilated and/or obstructed tubules containing deposits of polysaccharide (Fig 4.14, yellow arrows). Surrounding these cysts and dilated tubules were areas of fibrosis and unidentified mineral deposition (red arrows), with no discernible functional tissue. No cysts or other abnormalities were observed in kidneys from non-Tg mice, instead exhibiting normal glomerular and tubular development (Fig 4.14, white and blue arrows respectively).

An additional feature of these kidneys, not seen to such an extent previously, was the apparent alteration in morphology of the glomeruli, with a considerable dilation of the Bowman's space and shrinkage of the glomerulus itself. These structures also appear to be obstructed by polysaccharide similar to that found in the tubules, though whether this is sufficient to cause the morphological changes in this part of the nephron is currently unknown.

## 4.3 Cardiac phenotyping of the D316A mouse

Since the discovery of causality between AMPKγ2 mutations and WPW in humans, new models of AMPK activation *in vivo* have revealed a number of similarities, and differences, in the phenotypes of rodents and humans. Human WPW is characterised by ventricular pre-excitation, caused by either one or multiple accessory pathways, disrupting the normal contractility of the heart. In addition, patients exhibit dilation of the ventricle, glycogen accumulation and an increase in LV mass (hypertrophic cardiomyopathy) (Oliveira et al., 2003) (Arad et al., 2007).

Current mouse models of AMPKγ2 activation display several overlapping phenotypes associated with human WPW, though few recapitulate all symptoms to the same extent. Whilst numerous studies have further characterised these mutants, there are clear discrepancies between different mutations, isoform activation, and level of complex activity, leading to unique, tissue-dependent phenotypes. Most studies have focussed on the effects of these mutations in the heart and skeletal muscle, in part due to the tissue specificity of the γ2 and γ3 isoforms respectively and that naturally occurring mutations have been identified in these isoforms. Initial experiments were designed to assess these parameters in the D316A-Tg heart.

Upon dissection it was apparent that, on a chow diet, D316A-Tg mice displayed a significant (approximately 1.4 fold) increase in heart weight (Fig 4.15A). To confirm transgenic protein expression, Western blotting was performed on whole heart lysate from chow-fed D316A-Tg male mice, with non-Tg mice used as a negative control for the expression of FLAG-tagged AMPKγ1. The expression of FLAG was detected in all hearts taken from D316A-Tg mice (Fig 4.15B), though no differences were observed in pACC, likely due to the maximal phosphorylation of ACC by AMPK in WT-Tg samples in response to a rise in AMP stimulated by dissection, as reported previously (Zhang et al., 2017, Woods et al., 2017).

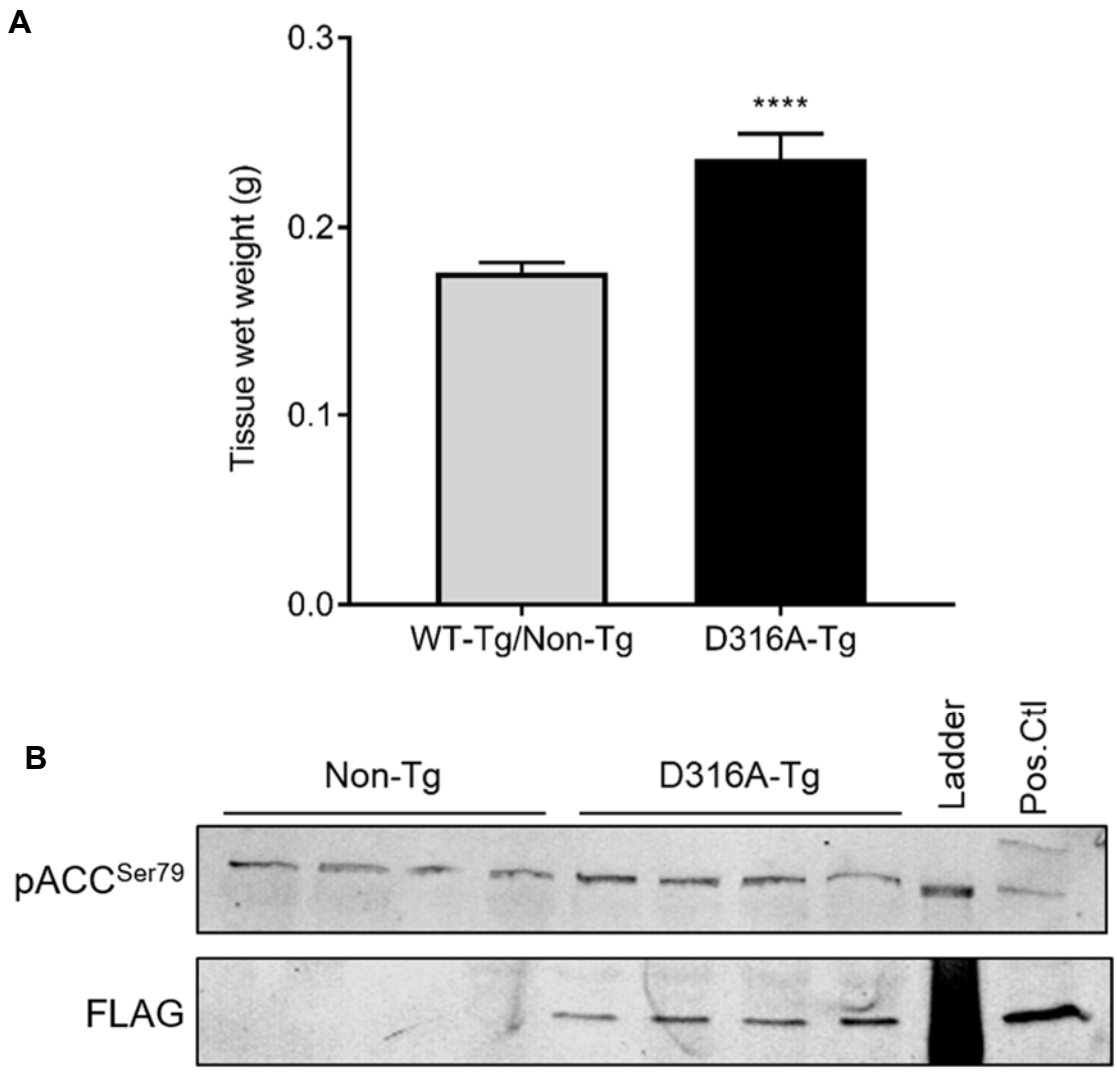



***Figure 4.15 AMPK D316A-Tg chow-fed animals display increased heart weight on a chow diet.***

***A)*** *Heart wet weight from 12-week old male non-Tg/WT-Tg and D316A-Tg animals (n=18, 13) ****p<0.0001.*

***B)*** *Western blot showing expression of phosphorylated acetyl Co-A carboxylase, and AMPKγ1-FLAG in 12 -week old male, chow-fed mice. Non-Tg samples were used as a negative control for FLAG expression, as WT-Tg animals also express FLAG-tagged AMPK. FLAG-tagged AMPKγ1 expressed in HEK293 cells (Robin Willows) was used as a positive control. N= 4, 4. Data are presented as mean ±SEM.*

Patients with HCM-associated WPW present with arrhythmia, ventricular pre-excitation and cardiac hypertrophy, features reportedly mimicked to varying degrees by two AMPKγ2 constitutively active mutant mouse models (Yang et al., 2016b). To establish whether, given the observed increase in heart weight exhibited by the D316A-Tg mouse model, these animals also presented with symptoms of WPW, a

rodent-specific electrocardiogram monitoring system (ECGenie, Mouse Specifics, Inc.), was used to monitor the cardiac activity of awake WT-Tg and D316A-Tg male and female animals. This work was carried out by Laura Wilson, another PhD student in the laboratory.

Human WPW is characterised by an ECG trace with a short PR interval and a distinct associated delta wave; a sloping upstroke within the QRS complex (Mahamat et al., 2016). Using the EzCGenie Analyses software, extracted trace data (Fig 4.16A) associated with the PR and QRS intervals was analysed (Fig 4.16B). Interestingly, no abnormalities in any parameter quantified were identified, including heart rate, suggesting that the cardiac hypertrophy exhibited by this model does not contribute to the development of WPW.

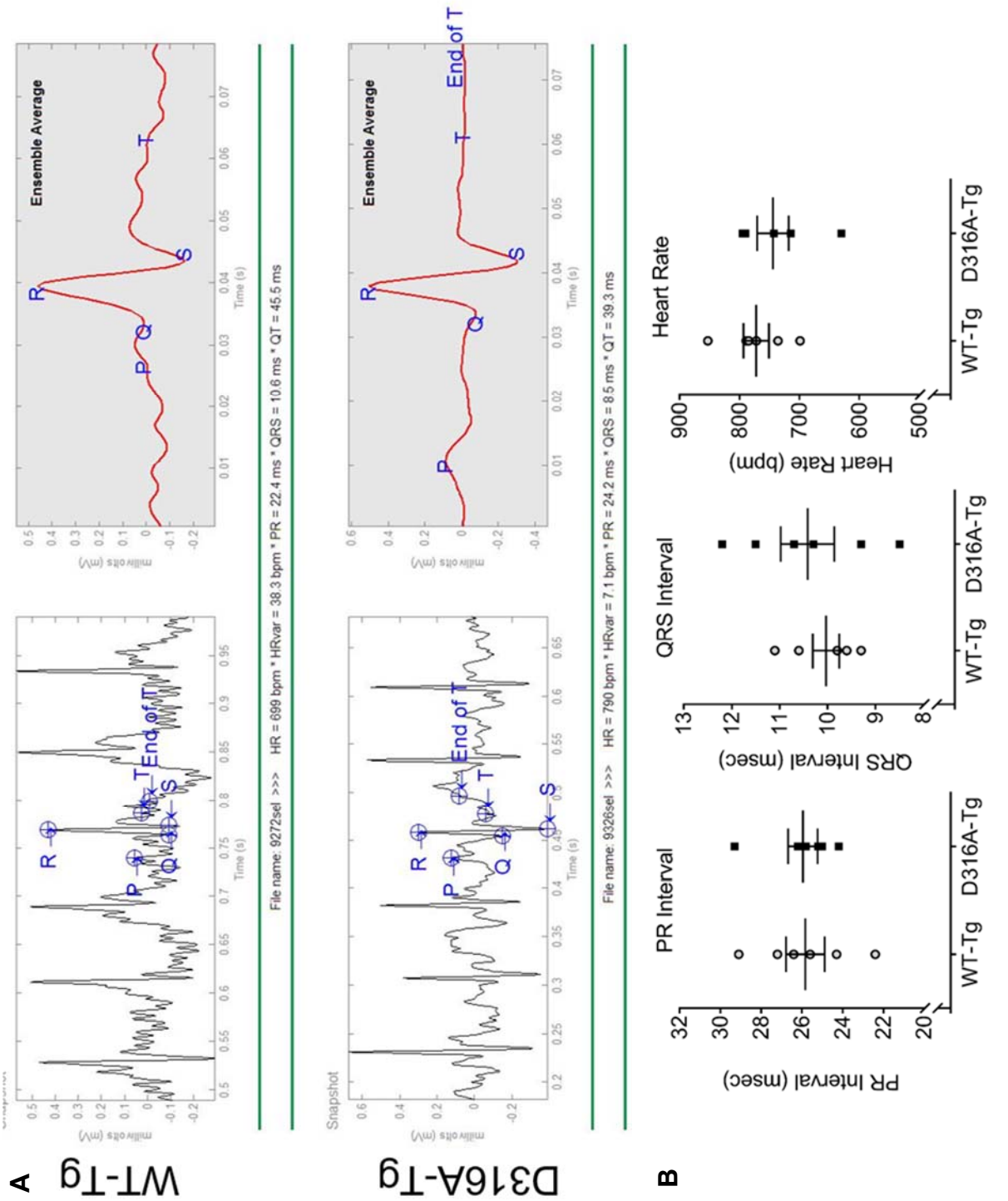



***Figure 4.16 AMPK D316A-Tg chow-fed animals do not exhibit any ECG abnormalities associated with Wolff-Parkinson-White Syndrome***

***A)*** *Example ECG trace supplied by Mouse Specifics Inc. to assist with interpretation of ECG traces, in comparison with a representative trace from WT-Tg and D316A-Tg male mice, PR interval and QRS interval highlighted in red.*

***B)*** *Quantification of ECG trace data; heart rate, PR and QRS interval, extracted from WT-Tg and D316A-Tg mice (n=6,6). Experiment conducted by Laura Wilson Data are presented with permission, as mean ±SEM.*

Given that AMPKγ2 mutations leading to an increase in heart weight and cardiac hypertrophy in humans and rodents also present with and glycogen accumulation, we proceeded to investigate this in the D316A-Tg mouse model.

To further examine the effects of AMPK activation on cardiac hypertrophy and glycogen content, hearts were fixed in 4% paraformaldehyde, wax embedded and sectioned for histological analysis by the Periodic Acid-Schiff method. Examination of D316A-Tg histologically-stained sections did not reveal any significant increase in cell size, nor any dilation of the left ventricle, characteristic of the AMPKγ2 R531G mouse model and WPW human pathology. However, PAS staining revealed striking accumulation of polysaccharide throughout the heart (Fig 4.17A, black arrows) which was not present in in amylase-digested samples, indicating the presence of glycogen.

To quantify total glycogen accumulation in D316A-Tg hearts, a glycogen assay was performed, utilising amyloglucosidase to convert intracellular glycogen to glucose. A significant increase in cardiac glycogen was measured in the hearts of D316A-Tg mice when compared to WT-Tg controls. This finding was exacerbated by HFD feeding (Fig 4.17B). An increase in glycogen accumulation was also observed between chow- and HFD-fed mice, though experiments were not performed at the same time. This finding is supported by several studies (Yang et al., 2016b).

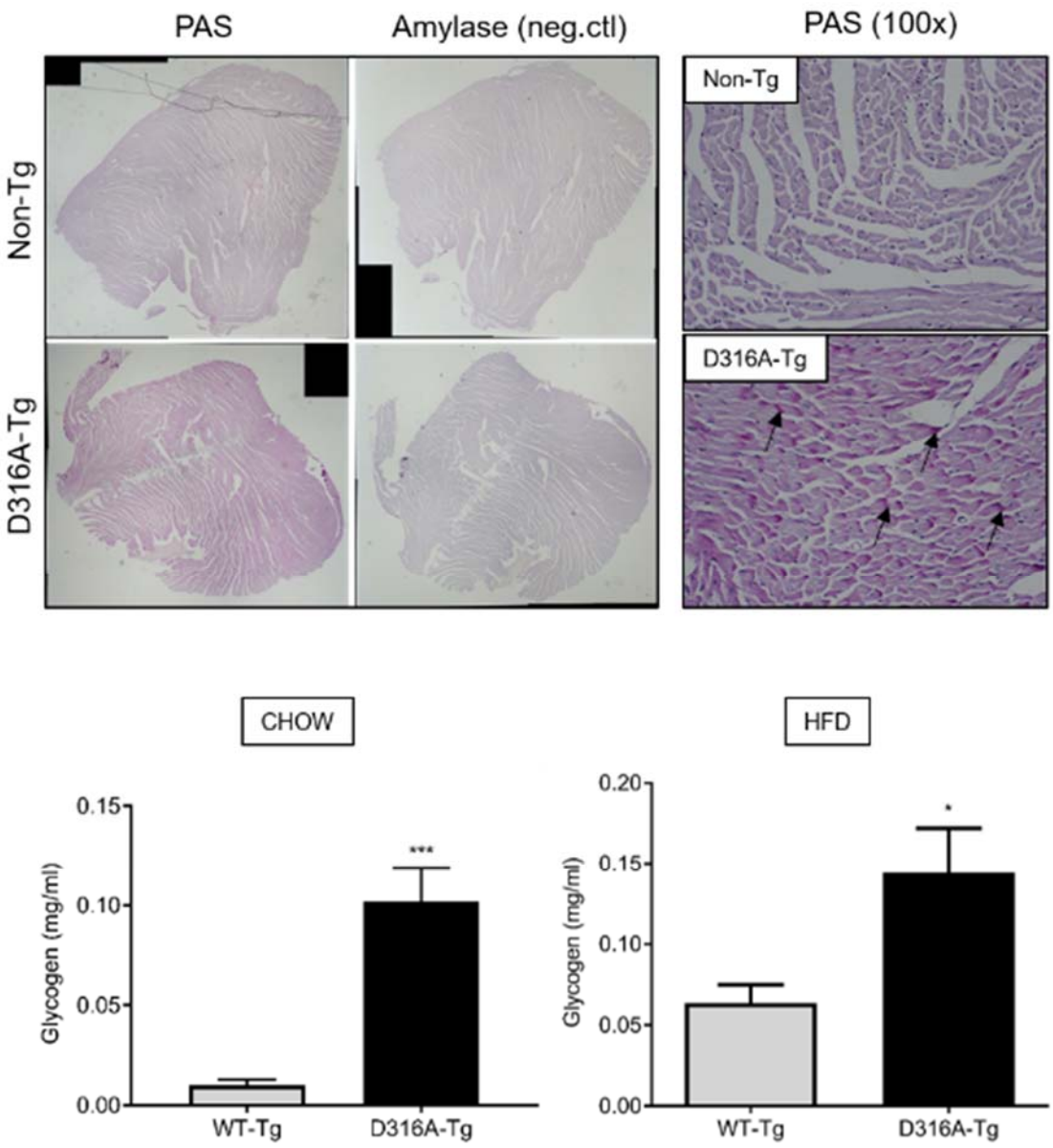



***Figure 4.17 AMPK D316A-Tg chow-fed animals display cardiac glycogen accumulation.***

***A)*** *Periodic Acid-Schiff (PAS) staining of Non-Tg and D316A-Tg heart sections (2.5x magnification, composite image, inset 10x magnification) to stain polysaccharides (deep magenta), including glycogen. An amylase digestion was used to depolymerise glycogen, acting as a negative control to show specific (glycogen) and non-specific (glycoproteins, mucins) staining.*

***B)*** *Glycogen assay to quantify glycogen accumulation in WT-Tg and D316A-Tg hearts. D316A-Tg hearts display significant glycogen accumulation both on a chow and a high-fat diet. N=7, 7, *P<0.05, Data are presented as mean ±SEM.***P<0.001*

To identify whether glycogen accumulation was associated with phosphorylation of glycogen synthase as described previously (section 1.3.3), protein from heart tissue homogenate from WT-Tg and D316A-Tg male mice was assessed for the expression of total glycogen synthase, phosphorylated glycogen synthase, phosphorylated ACC and the housekeeping protein vinculin by Western blotting.

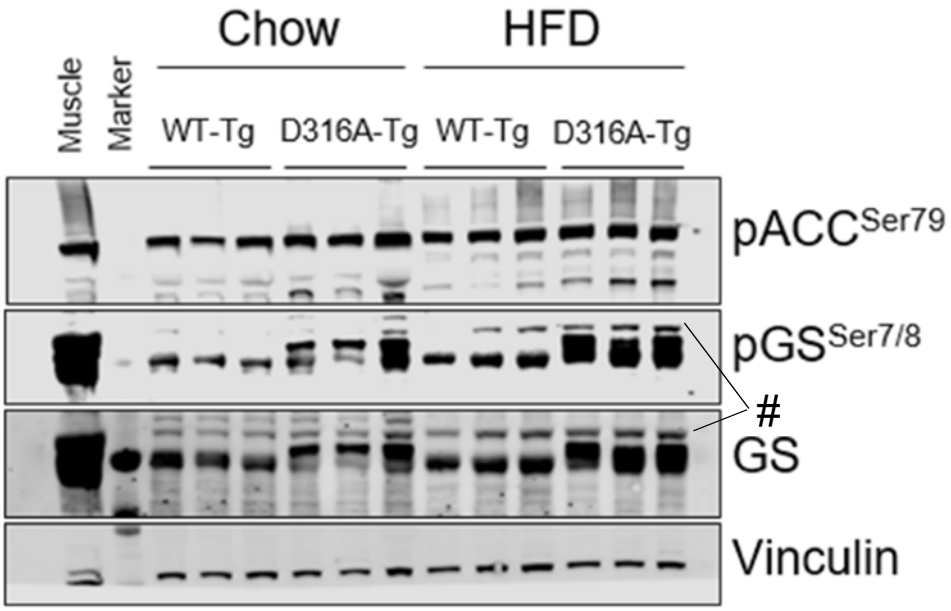



***Figure 4.18 D316A-Tg chow- and HFD-fed mice display enhanced cardiac glycogen synthase phosphorylation.***

*Western blot of heart tissue from 3 WT-Tg and 3 D316A-Tg chow-fed and HFD-fed mice. Membranes were probed for phosphorylation of ACC, glycogen synthase (Ser7) and total glycogen phosphorylase, with vinculin as a loading control. N=3, 3 per diet. Muscle lysate was used as a positive control. # indicates a non-specific band at a higher molecular weight to both GS and pGS$^{Ser7/8}$.*

An increase in phosphorylated (ser7) glycogen synthase was observed in both chow and high fat diet-fed D316A-Tg hearts (Fig 4.18). A mobility shift was observed when using the total-glycogen synthase antibody, often associated with increased phosphorylation. In contrast, this shift was not observed using either antibody in WT-Tg controls.

Under HFD conditions, an increase in phosphorylated GS was observed in both genotypes (Fig 4.18). Together, these data indicate a strong correlation between

AMPK activation and GS phosphorylation on both a chow and a high fat diet. However, to confirm this molecular mechanism, further studies are required; to establish G6P accumulation and to determine the rate of glycogen synthesis in the presence of activated AMPK *in vivo*. Whether increased glucose uptake also plays a role in this model is yet to be determined, with additional work currently being carried out to dissect this phenotype further.

### 4.3.1 D316A-Tg$^{129Sv}$ cardiac hypertrophy and glycogen storage

Interestingly, the cystic kidney phenotype was not the only feature of the D316A-Tg mouse to be exacerbated by the 129Sv background. Of the three animals harvested at 30 weeks of age, one presented with signs of ill health. Upon dissection, it was clear that the mouse was suffering from peritonitis, most likely as a result of heavily cystic kidneys. No other physical abnormalities were observed. All D316A-Tg$^{129Sv}$ mice exhibited similar cardiac hypertrophy (Fig 4.19) and cystic kidneys, but did not show any signs of peritonitis.

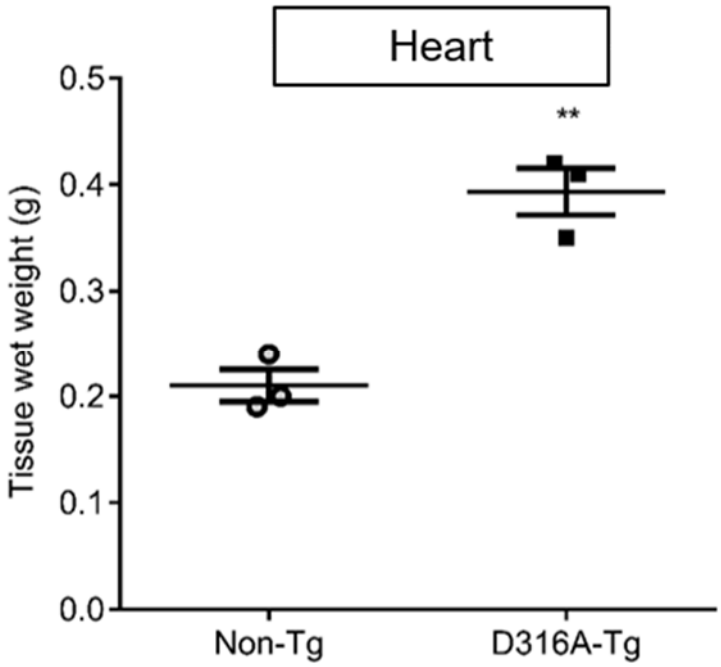



***Figure 4.19 D316A-Tg Mice on a 129Sv background display cardiac hypertrophy and glycogen accumulation, with indication of severe cardiac defects.***

*Heart weight at harvest of male, chow fed mice at 30 weeks of age. N= 3, 3, Data are presented as mean ± SEM.**P<0.01.*

Several interesting pathologies were identified using PAS staining, with both similarities and significant differences to the hearts analysed previously. Figure 4.16 highlights the morphology of a Non-Tg heart (left), the heart of the D316A-Tg animal showing signs of ill health (centre) and an additional D316A-Tg heart from an animal of the same age (30 weeks) with no adverse symptoms (right). Significant glycogen accumulation was observed in both D316A-Tg hearts, with no obvious deposits seen in that of the Non-Tg. Within this parameter, further differences were observed between the centre and right panels.

Glycogen accumulation in the D316A-Tg$^{129Sv}$ heart was comparable in distribution to that of the C57l6 mixed background discussed previously, with small patches (black arrows) distributed evenly throughout the tissue. However, there was a considerable increase in the thickness of the left ventricular wall, as well evidence of remodelling close to the apex.

The most striking differences, however, were seen in the heart taken from the sick animal (Fig 4.20 centre and bottom right, 40x magnification). In addition to a significant increase in glycogen deposition (black arrows), individual cardiomyocytes displayed hypertrophy, a reduction in fibre integrity, with partial or total loss of cytoplasm, and apparent glycogen granule formation (yellow arrows). Once case of suspected atrial hypertrophy was observed (Fig 4.20).

Work on this model is ongoing, with preliminary experiments, conducted by Laura Wilson, showing elevated blood pressure in D316A-Tg$^{129Sv}$ mice. No indication of Wolff Parkinson-White has been observed in these animals.

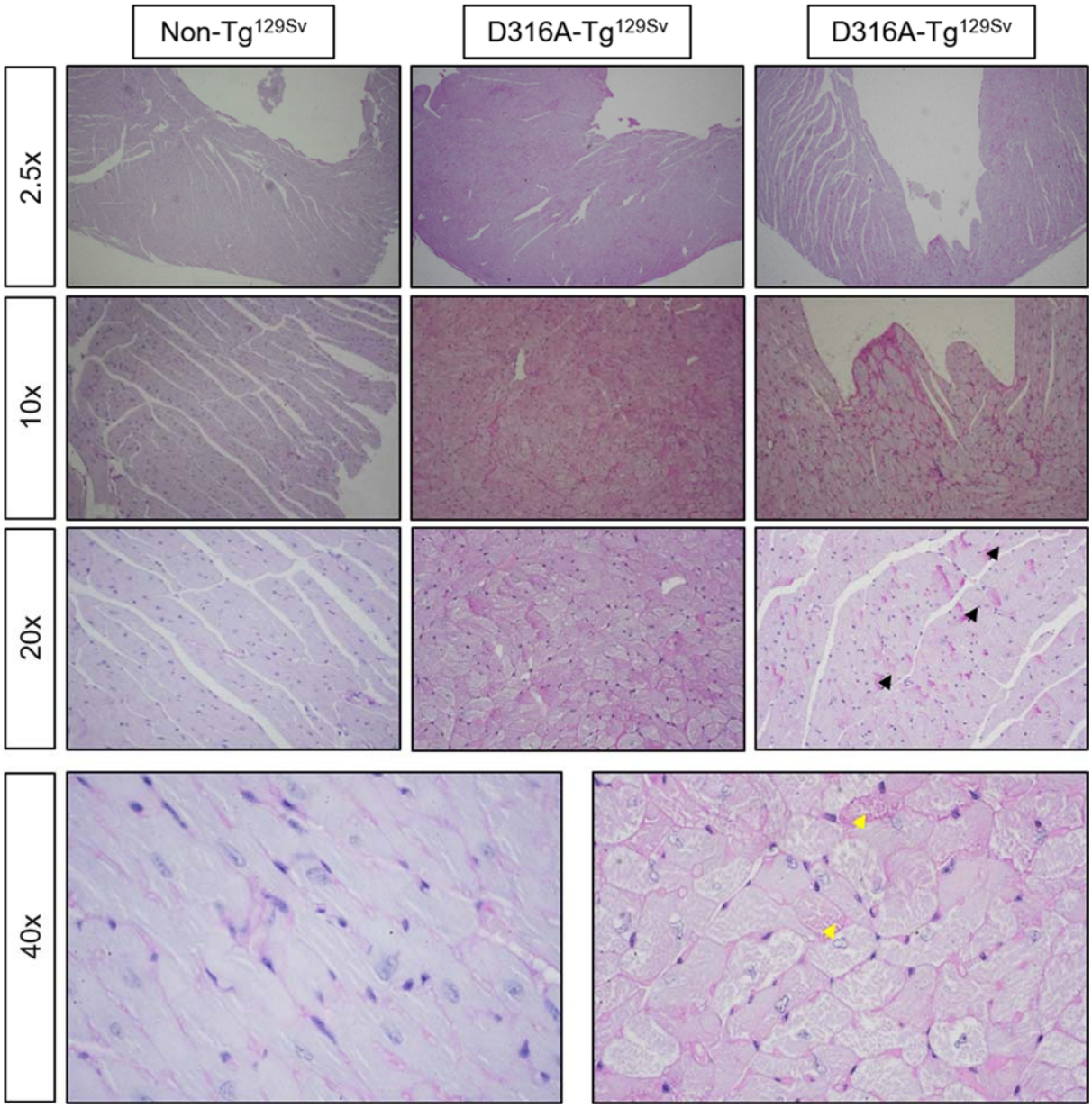



***Figure 4.20 PAS staining of Non-Tg and D316A-Tg$^{129Sv}$ hearts.***

*Deep magenta-stained pockets of glycogen can be seen in almost every cardiomyocyte from D316A-Tg hearts (black arrows), which are not often found in Non-Tg tissue (left). The animal presenting with sickness (centre and bottom right) and an apparently healthy D316A-Tg animal (right), display significant glycogen accumulation, though a striking difference in cell integrity.*

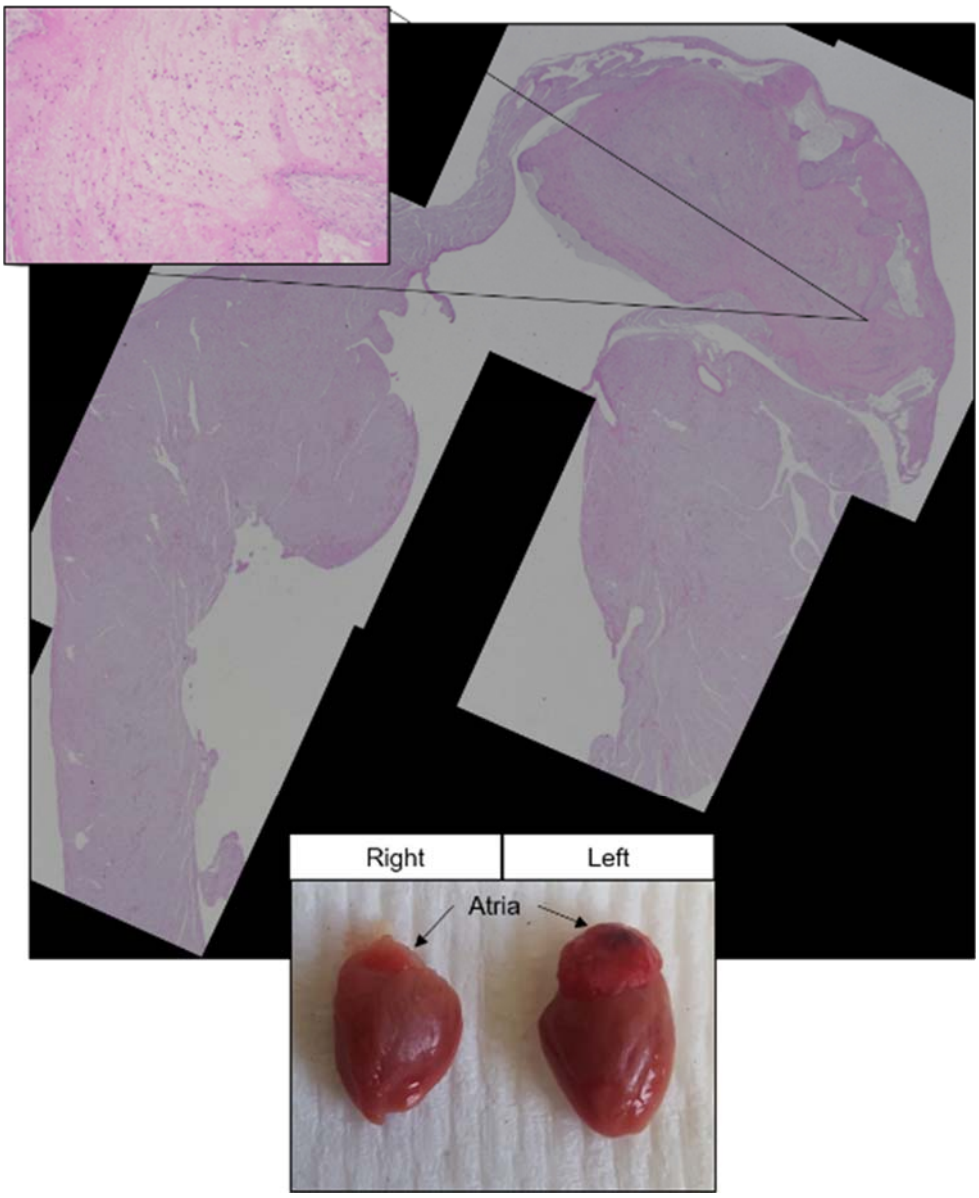



***Figure 4.21 D316A-Tg Mice on a 129Sv background display cardiac hypertrophy and glycogen accumulation, with indication of severe cardiac defects.***

*Enlarged atrium of D316A-Tg mouse with severely cystic kidneys, peritonitis and outward signs of ill health (central panel, Fig 4.16). The left atrium of this subject was found to be obstructed by a large and unstructured mass, thought to be severe hyperplasia of the atrium itself. Composite image at 2.5x magnification, inset 20x magnification.*

## 4.4 Discussion

The D316A-Tg mouse model presents with cardiac glycogen accumulation, independent of ECG abnormalities, with a normal heart rate and cardiac hypertrophy attributable to glycogen storage. Recent studies conducted using novel small molecule activators of AMPK have also reported cardiac glycogen accumulation and concurrent increase in heart weight after 2 weeks in Wistar Han rats and rhesus monkeys, with no abnormal ECG readings (Myers et al., 2017). Authors note that this is also observed in elite athletes, suggesting that these effects may not pose safety concerns in principle, but whether this will remain true in subjects with additional health concerns is subject to further investigation (Myers et al., 2017).

The role of AMPK in WPW is both well characterised and yet poorly understood beyond its contribution to the accumulation of glycogen, which we ourselves have demonstrated is not causative of WPW in this mouse model. Whether this is due to a specific role of AMPKγ2 in the development of this disease, and simultaneous glycogen accumulation is a feature of general AMPK activity, remains to be seen. However, this then provides an exciting window into the role of specific gamma isoforms in this tissue, and is certainly a question that will be addressed in the characterisation of this model in the future.

This work has also revealed a role for AMPK in the development of renal cysts, with a possible mouse-strain effect. Whether this particular phenotype is clinically relevant, however, may perhaps divide opinion, as in an inducible model of AMPK activation described in the previous chapter, this phenotype was not observed, leading to the hypothesis that AMPK activation leads to the development of kidney cysts only when switched on during embryogenesis. This, however, is still subject to investigation using the 129Sv background, as these experiments were conducted using C57Bl/6J animals.

The development of spontaneous kidney cysts is not uncommon, in both humans and laboratory animals. However, these cysts predominantly affect only one kidney, are confined to a specific region within the nephron, and are rarely invasive beyond the original lesion. The D316A-Tg model, however, exhibited multiple, bilateral cyst formation from 3 weeks and fibrosis from 6-7 weeks of age, visible upon ultrasound scanning, with progression through to renal failure in some animals at 33 weeks of

age. Blood sampling during the progression of this disease did not reveal any renal dysfunction prior to end-stage renal failure, identified using the VetScan diagnostic system. However, as the VetScan has limited sensitivity within pre-set biological thresholds, urine samples were additionally sent to AstraZeneca for additional diagnostics.

Clinically, urine samples are often used in addition to blood sampling to detect renal dysfunction, as the kidney provides a barrier to larger, high molecular weight molecules. The lysosomal enzyme N-acetyl-β-D-glucosaminidase (NAG), present in proximal tubule cells, is routinely used to identify tubular injury, as in a healthy subject, the glomerulus provides a barrier to any circulating 200kD enzyme, and it is rapidly cleared from the blood by the liver. However, if the proximal tubule becomes damaged, urinary (U)NAG can be detected in the urine as a result of proximal tubule cell damage (Drake et al., 2002). It is often presented as a ratio to urine creatinine to account for the variability of urine flow rate between patients. Creatinine, a commonly used measure of kidney function, is produced from the breakdown of creatine phosphate in muscle. It is often used as a marker of end-stage renal disease, but inherent variability between patients due to muscle mass, exercise and lifestyle, limits its efficacy in earlier stages of renal dysfunction (Gowda et al., 2010). To establish a more accurate diagnostic, creatinine levels are often presented as a ratio to blood urea nitrogen (BUN). Produced by the liver, urea is filtered and reabsorbed by the kidney, and is often used in conjunction with creatinine to diagnose acute renal failure, through kidney disease or urinary tract obstruction.

Interestingly, none of these parameters were altered in D316A-Tg mice, aside from three animals exhibiting clear renal failure, elevating both BUN and creatinine to concentrations within the range of the VetScan. Despite their routine use in clinics, the markers described above are not often elevated before renal failure in laboratory animals, which occurs when approximately 80% of renal function has been lost. Other, earlier markers of kidney damage have recently been identified, such as the transmembrane glycoprotein Kidney Injury Molecule 1 (KIM1), which is exclusively expressed in damaged proximal tubule epithelial cells, yet absent in healthy renal tissue. However, at the time of these studies, KIM1 and other renal markers were poorly understood in rodents, and reagents to analyse serum and urine samples were

not readily available. Current research using the D316A-Tg model is characterising KIM1 and other more recently identified markers for the cystic kidney phenotype described here.

From the time-points investigated, it was determined that cystogenesis was preceded by a dramatic and irregular upregulation of proliferation, then sustained in both healthy and compromised tissue at 3 weeks of age, at which point wild-type kidneys are fully developed and non-proliferative. Increased or abnormal proliferation of renal tubule epithelial cells is often associated with cystogenesis, tubule dysfunction and fibrosis (Comperat et al., 2006, Nadasdy et al., 1995).

Though many gene changes in Pkd1 and Pkd2 null models have been reported, of particular interest to our laboratory is the impact of alterations in metabolism. A study conducted in 2013 by Rowe *et al.,* described a proliferation-independent increase in metabolism in $Pkd1^{-/-}$ mouse embryonic fibroblasts, with elevated cellular ATP levels in comparison to wild-type cells. Using nuclear magnetic resonance to conduct metabolomics, Pkd1 null cells were found to have a higher rate of aerobic glycolysis, and the increased proliferative capacity of these cells could be brought to the same rate as wild-type cells through glucose deprivation. Interestingly, $Pkd1^{-/-}$ cells also exhibited autophagy defects, with higher rates of apoptosis, dependent to an extent on mTORC2, and could be partially ameliorated with the use of rapamycin. However, this study reported low AMPK activity levels, as demonstrated by reduced phosphorylation of AMPKαThr172, which was attributed to the high levels of ATP within these cells (Rowe et al., 2013). Results from this experiment lead to the conclusion that cystic kidneys exhibit a switch to glycolysis, and that this may present an opportunity for therapeutic intervention in PKD, using drugs such as metformin or AICAR to inhibit mTOR through the activation of AMPK (Rowe et al., 2013).

Results from this study conflict with the phenotype of the D316A-Tg mouse, and it would be of interest to measure the parameters discussed above, particularly through the use of a cell-based model to study ATP concentration and the proliferative index of D316A-Tg renal cells. However, several claims made in the above paper are based on previous studies using metformin to activate AMPK, with only minor reductions in cystic burden. Our findings suggest that far more work is required to understand the

role of AMPK in these diseases, as long term use of these drugs may in fact produce the opposite effect.

The use of Pkd1$^{-/-}$ mouse models by a number of different research groups has significantly expanded our knowledge of disease progression, and provided some interesting insights into the molecular mechanisms underlying pathogenesis. Due to the vast number of studies using these models, there are several contradictions. One such study addresses alterations in metabolism in response to Pkd1 deletion, though findings suggested a defect in fatty acid oxidation as opposed to glycolysis drives the development of cysts in this model (Menezes et al., 2016). Indeed, there are several key differences in research methodology that may explain such discrepancies. For instance, Rowe et al. used the kidney-specific Ksp-Cre; Pkd1$^{flox+}$ model, with measurements taken from animals already exhibiting considerable cystic burden (Rowe et al., 2013), as opposed to the study conducted by Menezes et al., using the same mouse model, but instead mapped the metabolic and transcriptomic profile of kidneys in the process of cyst development. Despite their significantly different results, both studies highlight striking changes in cell metabolism that may contribute to both the initiation and the progression of renal cysts *in vivo*.

If metabolic alterations are indeed a precursor to the proliferation that ultimately causes the development of cysts, it is not surprising that AMPK may play a key role in mediating such a transition. Recently, mitochondrial dysfunction was highlighted as another potential driver of many renal disorders in a review published in 2016 (Emma et al., 2016), particularly in conjunction with tubular defects, as these cells are rich in mitochondria due to the high energy requirements of ion reabsorption (Soltoff, 1986). Many renal diseases exhibit altered mitochondrial dynamics, usually as a result of mitochondrial damage, increased ROS production or defect in mitophagy, all leading to disruption of normal cell metabolism and can result in tubule dysfunction. In a recent study, a possible mechanism through an increase in c-myc expression in Pkd1 and 2-null kidneys was described. It was shown that, in contrast to quiescent kidney epithelial cells, which rely on fatty acid oxidation (FAO) to maintain ATP production, proliferative cells in developing cyst epithelia utilise c-myc-activated glycolysis (glucose) and glutaminolysis (glutamine) to sustain high growth rates, and actively inhibit FAO

through the downregulation of PPARα, a feature of human ADPKD (Hajarnis et al., 2017).

AMPK activation is known to stimulate mitochondrial biogenesis in response to stress, such as exercise, in order to increase ATP synthesis, predominantly through direct phosphorylation of PPARγ-coactivator 1α (PGC1α) (Jager et al., 2007). AMPK has also been implicated in the maintenance of healthy mitochondria by triggering mitophagy (mitochondrial autophagy), by inhibiting the mTOR complex mTORC1, activating the autophagy-activating kinase ULK1, and promoting mitochondrial fission through the phosphorylation of mitochondrial fission factor (MFF) (Zhang and Lin, 2016). All research to date would suggest that AMPK activation would maintain mitochondrial function and turnover, yet in the work presented here suggests AMPK activation drives the development of polycystic kidney disease, with no alteration in mitochondrial complex IV protein expression. Further work is required to determine whether mitochondrial biogenesis or turnover through mitophagy is intact in the D316A-Tg kidney, though it is possible that this phenotype is not driven by alterations in mitochondrial metabolism.

The presence of abnormal proliferation in D316A-Tg kidneys may provide some insight into the mechanism underlying cyst formation. In PAS- stained neonatal kidneys, small deposits of polysaccharide separate from the usual mucins lining the tubular epithelium were detected. It is possible that, in sensitive developing tissue, these (glycogen) deposits may cause injury, leading to an inflammatory response, triggering the cascade described previously.

One of the most common association between AMPK activation and pathology is that of excess glycogen storage in muscle, beginning with the identification of the $RN^-$ mutation in skeletal muscle AMPKγ3 in pigs (Milan et al., 2000). AMPK-associated glycogen storage is also a feature of Wolff-Parkinson White, and was long thought to be a causative factor for the conductance defects seen in this disease. However, recent studies using different animal models of WPW have taken steps to delineate glycogen storage from the other features of this condition, and the results we have presented here support this.

Studies of these diseases have shown that AMPK activation leads to an increase in glucose uptake, resulting in an increase in intracellular glucose-6-phosphate levels that can override the phosphorylation of glycogen synthase and cause accumulation of glycogen (Hunter et al., 2011). It is therefore plausible that chronic, global activation of AMPK leads to glycogen accumulation in the epithelial cells of renal tubules, which may contribute to the development of kidney cysts. Glycogen deposition is a clear feature of the D316A-Tg kidney, particularly in the later stages of the disease, where large deposits are visible within dilated tubules. Accumulation is also visible in neonatal kidneys, between 1 day and 1 week, prior to cyst development. However, it is not clear as to whether the extent of glycogen accumulation in D316A-Tg kidneys prior to cyst development is sufficient to cause the pathology observed from 3 weeks of age, and further studies are required to determine whether this may or may not be a causal mechanism in the D316A-Tg kidney phenotype.

In support of this hypothesis, a recent study using a kidney-specific glucose-6-phosphatase catalytic subunit deficiency model (K.G6pc-/-), a model of glycogen storage disease type I (GSDI) described early-onset nephropathy, with long-term development of renal fibrosis and cyst development (Gjorgjieva et al., 2016). Interestingly, though never reported by patients with GSDI, 22% of patients taking part in this study were found to have polycystic kidneys. In this study, significant glycogen accumulation preceded the fibrosis and cyst development, following an epithelial-to-mesenchymal (EMT) transition of the tubular epithelium after 15 months. The proposed mechanism governing cyst development in this model begins with a build-up of G6P activating, amongst other metabolic pathways, glycogen synthase, leading to glycogen accumulation which triggers an inflammatory response. This response triggers an EMT in renal tubule epithelium, leading to fibrosis, followed by the development of cysts.

Though this mechanism may also be present in the D316A-Tg mouse model, considerable work is required to determine whether the deposits seen in neonatal D316A-Tg renal tubules are sufficient to trigger this response, if proliferation is caused solely by this damage, or whether other underlying mechanisms are involved.

Whilst the role of AMPK in the heart and skeletal muscle is well-defined with respect to glycogen storage, the part it plays in the development of kidney cysts is

controversial, as the only studies using specific activators of AMPK have also reported some incidence of kidney injury, though no reports of significant cyst development. The AMPKγ2$^{RG}$ mouse model, however, does display a similar phenotype to the D316A-Tg mouse model. In this study, mice overexpressing a constitutively active mutation in AMPKγ2 presented with glycogen accumulation, cyst formation and impaired renal function, though only on a high-fat diet (Yang et al., 2016b).

Figure 4.14 outlines the currently accepted model of cyst formation in Pkd1/2 mutants, with adaptations encompassing the hypothesised role of AMPK. In the case of AD/ARPKD, single gene mutations can give rise to a plethora of changes in key cellular pathways, a few of which have been discussed here. It has also been shown that mutations in a number of genes can give rise to very similar phenotypes, leading to hypotheses based on common molecular mechanisms as opposed to those surrounding the expression of the polycystin proteins. The D316A-Tg mouse model provides an exciting new tool with which to study such mechanisms without the need for deletion of the Pkd genes. It is possible that, AMPK plays a crucial role in mediating some of these pathways, and through a yet to be identified mechanism, can lead to the development of kidney cysts. It is therefore of vital importance to understand the role of AMPK in the developing kidney, using the D316A-Tg mouse model, and to determine whether the same activation in a mature kidney may lead to a similar development in humans.

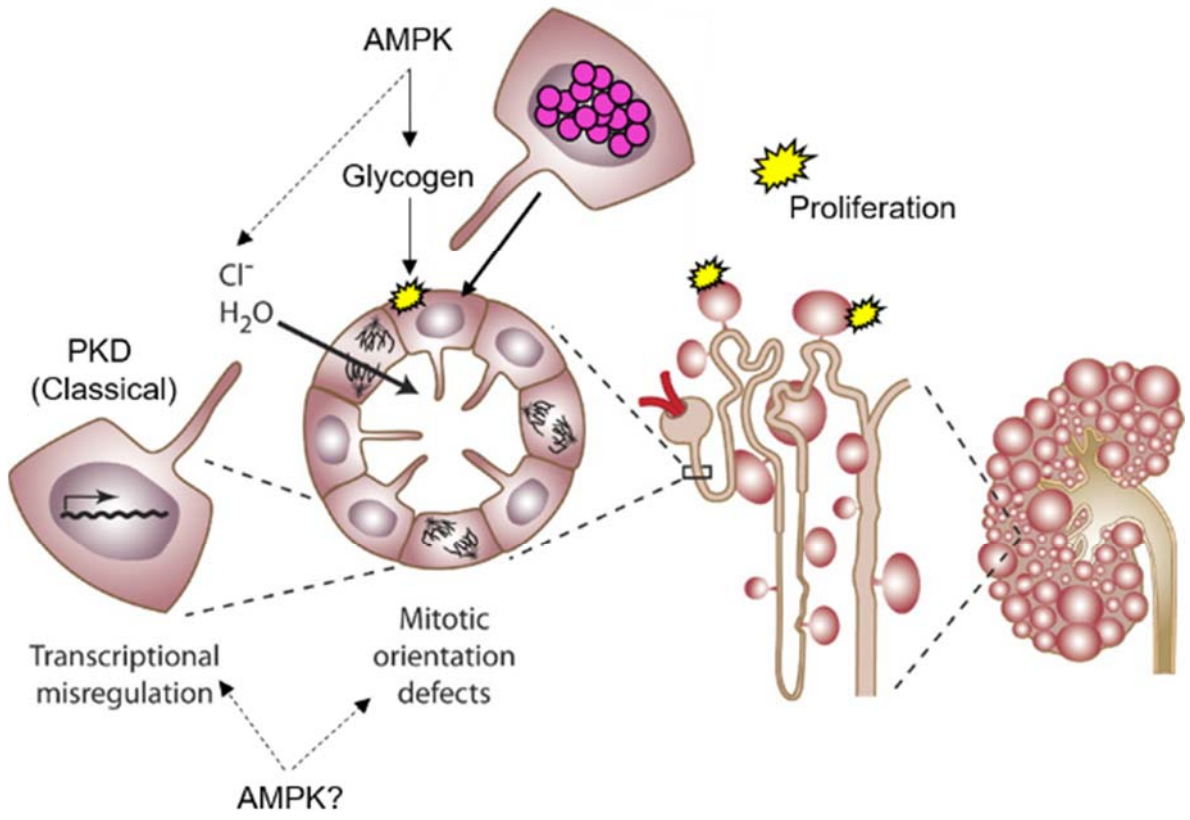



***Figure 4.22 Potential mechanisms for the development of polycystic kidney diseases.***

*Schematic adapted from (Chapin and Caplan, 2010, Oakhill et al., 2012) outlining the currently accepted model of polycystic disease, initiated by defects in Pkd1 and 2, encoding PC1 and 2 respectively. Disruption of these signalling molecules has been shown to increase cell proliferation and alter ion secretion, leading to tubule damage and cyst formation. Chronic renal damage due to ongoing inflammation, proliferation and fibrosis leads, ultimately, to renal failure.*

*Adaptation: Chronic AMPK activation has been shown to induce glycogen deposition in developing nephrons, associated with increased proliferation and cyst formation. Whether AMPK also plays a role in transcriptional regulation and ion secretion in the D316A-Tg mouse model is currently under investigation.*

This work has also identified a possible strain-dependency with respect to kidney cyst severity. In recent years, researchers using different mouse strains to conduct similar experiments have reported significant variations in phenotype or response to therapeutics. Amongst those described were the significant differences between the 129Sv and C57Bl/6 strains, particularly in relation locomotion and, interestingly, renal

pathology (Yang et al., 2005). A study closer to home evaluated the effects of genetic background on response to cyclooxygenase-2 deficiency ($COX2^{-/-}$), using C57Bl/6, 129Sv and BALB/c mice. Surprisingly, kidney abnormalities were significantly more severe on the 129Sv background, with elevated blood pressure, increased urinary Albumin/Creatinine ratio and a high renal injury score. All COX2 deficient animals, male and female, displayed increased BUN, though to a far greater extent in 129Sv subjects. Histology revealed considerable tubule dilation, protein casts (fluid-filled tubules) and renal inflammation, particularly in males, with no evidence of such morphology in either Bl6 or BALB/c animals. However, all three strains still developed renal abnormalities and kidney failure as previously reported by separate groups (Yang et al., 2005).

From these accounts alone, it is clear that some commonly used strains, not necessarily chosen for specific attributes, can have markedly different responses to both behavioural experiments and genetic mutations leading to alterations in cell signalling and metabolism. A similar strain-dependent phenotype was observed in the D316A-Tg mouse model, with a dramatic, early onset cystic kidney phenotype on a mixed C57Bl/6/129Sv background, which lessened in severity (in terms of cystic burden) when animals were crossed further onto a Bl6 background. When animals were then crossed back onto a 129Sv background, the original phenotype was not just restored but greatly exacerbated, with heavily cystic kidneys and elevated blood pressure.

This phenotype bears significant clinical relevance, with no current cure or preventative treatment available for genetic or acquired polycystic kidney diseases. Many studies surrounding AMPK activation and polycystic kidney diseases have drawn conclusions from the use of metformin and AICAR, which may elicit some beneficial effects, though none are significant enough to provide a stand-alone therapeutic target for these diseases. Indeed, there is no sufficient evidence to suggest that direct AMPK activation is beneficial in the prevention of these diseases, and if prolonged treatment with such an activator would have any beneficial effect.

The delineation of the effects of AMPK activation in the development of Wolff-Parkinson White syndrome is of particular interest, with a view to developing isoform specific compounds to avoid deleterious effects such as excessive glycogen

accumulation, atrial fibrillation and left ventricular hypertrophy. Interestingly, cardiac glycogen accumulation was comparable between both D316A-Tg strains; 129Sv and C57Bl/6, suggesting that this may not be only a feature of the 129Sv genetic component, but a *bona fide* feature of AMPK activation. Whether this compromises the health of these animals is not known, though no cardiac defects were observed on either background using ECG, and only time will tell as to whether this parameter affects other parameters, such as exercise capacity or lifespan.

To be able to separate the development of these two potentially confounding phenotypes, consideration has been given to developing a kidney-specific model of AMPK activation, using the Ksp-Cre mouse line expressing cre recombinase in the principle cells of the collecting duct and distal tubule. These animals would be monitored for renal cyst development using ultrasound, as well as echocardiogram to assess left ventricular mass. If cyst development is a precursor to hypertension-related cardiac hypertrophy, mice should exhibit elevated blood pressure and increased left ventricular mass. However, it is still not certain as to whether these animals will develop cystic kidneys, as a preliminary experiment using a different kidney-specific cre (aquaporin-4) did not. This, however, may be due to the strain-specificity of this phenotype, as the AQP4 mice purchased were of a pure C57Bl/6 background, and would therefore dilute further the 129Sv component of the genetic background of the D316A-Tg mouse.

Therefore, the following experiments were designed to address each question in a logical order, beginning with the ongoing monitoring of the D316A-Tg global activating mutant on a 129Sv background:

1. Establish age of onset of kidney cysts and determine whether left ventricular mass is increased at this time point. From studies conducted so far, we have determined that cysts are present from 3 weeks, though due to size constraints, this is 3 weeks below the minimum age for scanning using ultrasound and echocardiogram, so it was not possible to determine these parameters *in vivo*.

2. Repeat the aforementioned time course with the D316A-Tg mouse on a 129Sv background, with additional time-points between 1 and 3 weeks of age to capture the events preceding cyst development.

3. The above will be conducted simultaneously on mice expressing the D316A-Tg mutation specifically in the kidney, as well as a view to expressing this mutation solely in the heart on the same 129Sv background. Together, these experiments will hopefully determine whether one phenotype is responsible, at least in part, for the other.

4. Using a tamoxifen-inducible model, determine whether the induction of AMPK activation during adulthood can give rise to the cystic kidney phenotype seen here. As a preliminary study, pregnant females will be injected intraperitoneally with tamoxifen to induce AMPK activation in utero, to confirm that these animals develop kidney cysts. Following a positive result, animals will be allowed to develop to maturity (8 to 10 weeks of age) before the induction of AMPK activation and monitored as in point 1.

The outcome of the inducible model is of particular interest, as a previous study conducted using this system did not produce kidney cysts, though this may, as with the AQP4-cre, be partially due to the significant reduction in the 129Sv background of these animals. If these animals do not exhibit the cystic kidney phenotype, it may in part confirm the hypothesis that this is a developmental effect of AMPK activation during embryogenesis, and may be less of a concern in the development of AMPK activators as therapeutics for other conditions. Nevertheless, understanding the role of AMPK in the developing kidney may play a key role in elucidating the mechanisms underlying other polycystic kidney diseases, and could in fact present a novel therapeutic target for these diseases. Further investigation of these phenotypes may also elucidate the role of the 129Sv genetic background, and whether the D316A-Tg mouse on this background presents a new model for PKD, irrespective of Pkd1/2, and for glycogen storage diseases in peripheral tissues such as the kidney. Ongoing work on this particular aspect of the D316A-Tg mouse model will provide much needed insight into the true nature of chronic AMPK activation, and whether targeting AMPK *in vivo* will prove safe.

# 5 SUMMARY AND PERSPECTIVES

## 5.1.1 Summary of findings

The prevalence of obesity has now reached staggering heights, with more of the world's population living in countries where more deaths are attributed to obesity than starvation (WHO, 2016). Though preventable in most cases, these figures continue to rise, placing increasing pressure on health care organisations and supporting governments to cover the costs of escalating public demand. Indeed, in a modern society, with cheap, readily available, high calorie foods and beverages, as well as increasing alcoholism and a sedentary lifestyle, it is difficult to comprehend a simple solution without implementation of national policy. Efforts have been made to do so, with promotion of healthy dietary alternatives, exercise goals and improved packaging on foodstuffs highlighting calorie content using an easily interpretable colour-coding system. Despite these steps, the incidence of obesity continues to rise, with the numbers of preventable deaths attributable to obesity and overweight together being second highest only to the use of tobacco (update 2017) (1998).

Over the last 50 years, many efforts have been made by pharmaceutical companies to develop therapeutics to reduce the impact of obesity on health, though with the emergence of cheap appetite suppressants, 'fat-blockers' and off-the-shelf thermogenics, the race to produce evidence-based, safe and effective treatments has been challenging. To date, the most effective strategy for the treatment and prevention of obesity is caloric restriction and exercise, often aided by surgical interventions such as gastric bands or gastric bypass procedures. However, it is often the unobservable strain on internal organs that drives obesity-associated diseases, including atherosclerosis, hepatic steatosis and type 2 diabetes. Therefore, research has focussed on the amelioration and prevention of these secondary pathologies, leaving the reduction in total bodyweight to surgery and lifestyle changes.

Whilst translation remains a significant barrier, many research teams have identified potential molecular targets for the prevention and treatment of obesity, at a rate expected to rise as tools with which to study these pathways improve. In particular, the study of whole-organism energy homeostasis and metabolism has revealed many potential therapeutic avenues, including those axes governing food intake, energy expenditure and gut absorption. As a master regulator of energy homeostasis, AMPK

was, and still is, a key target for the development of anti-obesogenic agents, though without readily available, specific activators, literature surrounding its efficacy is often contradictory. The recent development of such compounds has yielded promising results in both rodents and non-human primates, particularly for the treatment of insulin resistance and type 2 diabetes, though the impact on other features of the metabolic syndrome remain inconclusive (Cokorinos et al., 2017, Myers et al., 2017).

The generation of the D316A-Tg mouse model has revealed some novel and exciting phenotypes that will undoubtedly inform the development of therapeutics targeting AMPK for a wide range of disease pathologies. In this work, a role for AMPK has been described a number of tissues, presented in the table 5.1. However, given the ubiquitous nature of D316A-Tg expression in the β-actin cre mouse model, it is more than likely that many other, subtler phenotypes exist, and will provide the basis for collaboration with any laboratory wishing to investigate AMPK activation in a tissue of interest.

The D316A-Tg mouse model exhibits a rare case of complete resistance to DIO, with no overt metabolic consequence when fed a normal, chow diet. Furthermore, protection is not conferred from the alteration of food intake or physical activity, nor through the promotion of brown adipose tissue thermogenesis. Instead, mice present with enhanced energy expenditure thought to be associated with creatine/calcium futile cycling facilitated by development of BAT-like cells in subcutaneous white adipose on a chow diet, which, on a high-fat diet, transition to a muscle-like metabolic state. This state is characterised by increased mitochondrial fatty acid oxidation, creatine futile cycling and the expression of sarco/endoplasmic reticulum calcium ATPase (SERCA), known to promote sustained thermogenesis in muscle.

Aside from this metabolic phenotype, mice also exhibit a polycystic kidney disease with proliferative origins and strain dependent severity, characterised by the accumulation of glycogen which may drive the development of cysts. The reduction and in many cases the absence of cysts upon the dilution of the 129sv component of the strain may provide further mechanistic insight into the cause of this disease. Examining the key differences between 129sv and C57Bl/6J mice, with respect to kidney metabolism, as well as the development of kidney-specific models of AMPK activation using the D316A-Tg mouse model, will hope to elucidate the role of AMPK

*Table 5.1 Summary of key findings*

| Tissue | Observation | Proposed Mechanism | Comments |
|---|---|---|---|
| **Whole body** | Protection from DIO | Alternative thermogenesis: futile cycling in WATsc | Amelioration of DIO is inducible |
| **Liver** | Protection from hepatic steatosis | Peripheral reduction in lipid accumulation | No protection conferred by liver-specific AMPK activation |
| **BAT** | Normal development and response to β3-adrenergic stimulation.<br><br>Protection from lipid accumulation on HFD | Peripheral reduction in lipid accumulation. | BAT RNA sequencing did not reveal any significant increase in thermogenic gene expression |
| **Muscle** | Mitochondrial biogenesis on a chow diet.<br><br>Glycogen storage on chow and HFD | AMPK activation promoted PGC1α and mtRC protein expression.<br><br>AMPK activation increased glycogen content and GS phosphorylation | Muscle specific D316A-Tg$^{Mef2C}$ model did not exhibit protection from DIO.<br><br>AMPK activation known to increase glucose uptake in skeletal muscle, overriding GS inactivation. |

| | | | |
|---|---|---|---|
| **WATsc** | BAT-like cell development on a chow diet with evidence of endothelial cell origin.<br><br>HFD-induced BAT-muscle switch with expression of myoblastic transition<br><br>Alternative thermogenesis | AMPK activation promoted BAT-like cell development and vascularisation in WATsc depots, possibly through promotion of $Myf5^{+}$ cell lineage.<br><br>HFD-feeding may disrupt key repressor complex Prdm16/EHMT1 leading to MyoG activity and muscle gene expression<br><br>Mitochondrial-generated excess ATP, dissipated by a Ckm-SERCA calcium/creatine futile cycle. | Novel role for AMPK in alteration of cell fate<br>Potential role for ATP-driven gene expression<br><br>Stem cells are conserved in adult human WATsc and may provide a targetable niche. |
| **Heart** | Strain-dependent cardiomyopathy (CM)<br><br>Strain-independent glycogen accumulation<br>No WPW development | Blood-pressure elevation from cystic kidney development on a 129Sv background promotes left ventricular and atrial hypertrophy and eventual loss of cell integrity.<br><br>AMPK drives glucose uptake and glycogen deposition in cardiomyocytes. | Glycogen accumulation common to both strains.<br>CM unique to 129sv background<br><br>AMPKγ1 activation does not cause WPW in the D316A-Tg mouse model |

| | | | |
|---|---|---|---|
| | | No ECG abnormalities | |
| **Kidney** | Cystic kidney development on a 129Sv/C57Bl/6 background | Abnormal and prolonged proliferation in neonatal to 3-week old kidney epithelium.<br><br>AMPK activation drives glycogen accumulation which may contribute to cyst development<br><br>Strain-dependent severity<br><br>Increased blood pressure in the D316A-$Tg^{129Sv}$ mouse model | Not identified in inducible D316A-Tg model on a Bl6 background<br><br>No observable impact on metabolic studies using C57Bl/6 mice |

in this disease, perhaps opening another avenue for the development of therapeutics to treat this disease in humans.

Finally, D316A-Tg mice display strain-independent cardiac glycogen accumulation, in conjunction with a strain-dependent left ventricular and left atrial hypertrophy, thought to be secondary to elevated blood pressure caused by cystic kidneys. Many studies have now reported causality between AMPK activation and glycogen accumulation, both in cardiomyocytes and skeletal muscle. However, these features have been primarily attributed to their respective expression of AMPKγ2 and γ3 isoforms, in which naturally occurring mutations have been found. Cardiac glycogen accumulation is a known feature of Wolff Parkinson-White syndrome, driven by mutations in AMPKγ2 (Arad et al., 2002, Murphy et al., 2005, Yang et al., 2016b, Daniel and Carling, 2002). However, D316A-Tg mice, either on a C57Bl/6J or 129sv background, do not display any features of WPW, suggesting that whilst AMPK activation clearly drives glycogen deposition, this is not a causative feature of WPW-associated arrhythmia and other ECG abnormalities. Indeed, this has also been reported in recent studies using small molecule AMPK activators PF-739 and MK8722, suggesting that these observations are more closely related to exercise-induced cardiac hypertrophy, and may not cause any significant problems *in vivo*. Further work is required to determine this potential overlap, and to understand the long-term consequences in humans.

### 5.1.2 AMPK as a therapeutic target

Supported by the work presented here, AMPK remains a very promising therapeutic target for the treatment of obesity and the metabolic syndrome. The current effort to develop specific, small molecule activators is welcomed by the field, both in translational studies such as those discussed previously, and for the interrogation of pathways identified by models such as the D316A-Tg mouse. The realisation that AMPK activation is not always causative of WPW is particularly encouraging, though the impact on the development of the kidney may cause unforeseen setbacks in the development of therapeutics. To address this issue, focus will be on inducible models of AMPK activation in parallel to studies using small molecule activators, to determine whether this phenotype is primarily of developmental origin, or whether cysts can develop in adulthood. Preliminary studies support the former, though only time will tell

as to whether new small molecules will elicit any deleterious effects on the kidney *in vivo*.

The D316A-Tg mouse model is an invaluable tool for the study of AMPK activation *in vivo*, particularly when used in conjunction with tissue-specific cre lines, and will provide much insight into the role of AMPK in both health and disease. It is hoped that the speculation on the effects of AMPK activation, based on conclusions drawn from knock-out studies, will be re-addressed, as it is clear that the removal of AMPK has many knock-on effects that may not be attributable to its activation, but rather are a consequence of metabolic disruption, impaired development and altered signalling pathways littered with compensatory mechanisms. The successful development of an inducible model of AMPK activation using the D316A-Tg mouse model is crucial for delineating phenotypes associated with chronic and acute AMPK activation, as well as to determine phenotypes that are developmental, as opposed to those with significant translational potential.

Though several phenotypes have been identified using this mouse model that may draw attention from the wider scientific community, the observed plasticity of the subcutaneous white adipose with respect to morphology, metabolism and stem cell fate is of significant importance. Metabolic plasticity is a key feature of stem cell differentiation in response to environmental stimuli, with rapid growth and proliferation associated with enhanced glycolysis and low oxidative phosphorylation (OxPhos), whilst differentiating cells often exhibit a transition to OxPhos. Indeed, metabolism is now considered to play a pivotal role in determining cell fate (Shyh-Chang et al., 2013), and it is therefore of substantial importance to further understand the role of AMPK activation in stem cell metabolism and potential impact on cell fate as observed in D316A-Tg WATsc. If metabolism alone can unlock the potential of stem cells, as has been eluded to, then AMPK will undoubtedly attract significant attention as a potential target for intervention.

### 5.1.3 Closing remarks

The findings presented in this work identify AMPK as an attractive target for the treatment of obesity, diabetes and the metabolic syndrome. Future collaborations, in addition to ongoing work on this novel mouse model will undoubtedly produce many more unexpected roles for this highly conserved metabolic regulator which will, in turn,

inform the development of more stringent, tissue-specific therapeutics. It is hoped that, by promoting collaboration between industry, academia and the clinic, key scientific discoveries such as these can be rapidly associated with unmet clinical need, and developed into effective therapeutics for the benefit of the population.

Since the Nobel prize awarded for the identification and development for induced pluripotent stem cells, there exists a desire to promote awareness of the plasticity of biological systems, driven by observations such as those outlined here, which are both exciting and thought-provoking in nature. There is a tendency, both in science and in broader fields, to reject the extraordinary, in favour of more simple and easily-explainable hypotheses. Whilst the simplest explanation is often the correct one, this does not exclude the possibility that, underneath the simplicity, exists a far more complex system deserving of appreciation.

*“The elation of peering into the depths of nature and being the first to see something new is impossible to describe.”*

*— Jeffery M. Friedman*

# REFERENCES


1983. Nutrition Classics. The Anatomical Record, Volume 78, 1940: Hypothalamic lesions and adiposity in the rat. *Nutr Rev,* 41**,** 124-7.

1998. Clinical Guidelines on the Identification, Evaluation, and Treatment of Overweight and Obesity in Adults--The Evidence Report. National Institutes of Health. *Obes Res,* 6 Suppl 2**,** 51S-209S.

ACHARI, A. E. & JAIN, S. K. 2017. Adiponectin, a Therapeutic Target for Obesity, Diabetes, and Endothelial Dysfunction. *Int J Mol Sci,* 18.

ACKROFF, K. & SCLAFANI, A. 1996. Effects of the lipase inhibitor orlistat on intake and preference for dietary fat in rats. *Am J Physiol,* 271**,** R48-54.

AHIMA, R. S. 2008. Revisiting leptin's role in obesity and weight loss. *J Clin Invest,* 118**,** 2380-3.

ALBALAT, A., GUTIERREZ, J. & NAVARRO, I. 2005. Regulation of lipolysis in isolated adipocytes of rainbow trout (Oncorhynchus mykiss): the role of insulin and glucagon. *Comp Biochem Physiol A Mol Integr Physiol,* 142**,** 347-54.

ALKHOURI, N., DIXON, L. J. & FELDSTEIN, A. E. 2009. Lipotoxicity in nonalcoholic fatty liver disease: not all lipids are created equal. *Expert Rev Gastroenterol Hepatol,* 3**,** 445-51.

ARAD, M., BENSON, D. W., PEREZ-ATAYDE, A. R., MCKENNA, W. J., SPARKS, E. A., KANTER, R. J., MCGARRY, K., SEIDMAN, J. G. & SEIDMAN, C. E. 2002. Constitutively active AMP kinase mutations cause glycogen storage disease mimicking hypertrophic cardiomyopathy. *J Clin Invest,* 109**,** 357-62.

ARAD, M., SEIDMAN, C. E. & SEIDMAN, J. G. 2007. AMP-activated protein kinase in the heart: role during health and disease. *Circ Res,* 100**,** 474-88.

ARRUDA, A. P., NIGRO, M., OLIVEIRA, G. M. & DE MEIS, L. 2007. Thermogenic activity of Ca2+-ATPase from skeletal muscle heavy sarcoplasmic reticulum: the role of ryanodine Ca2+ channel. *Biochim Biophys Acta,* 1768**,** 1498-505.

ASCHENBACH, W. G., HIRSHMAN, M. F., FUJII, N., SAKAMOTO, K., HOWLETT, K. F. & GOODYEAR, L. J. 2002. Effect of AICAR treatment on glycogen metabolism in skeletal muscle. *Diabetes,* 51**,** 567-73.

ASHCROFT, F. M. & RORSMAN, P. 2012. Diabetes mellitus and the beta cell: the last ten years. *Cell,* 148**,** 1160-71.

BARNES, B. R., MARKLUND, S., STEILER, T. L., WALTER, M., HJALM, G., AMARGER, V., MAHLAPUU, M., LENG, Y., JOHANSSON, C., GALUSKA, D., LINDGREN, K., ABRINK, M., STAPLETON, D., ZIERATH, J. R. & ANDERSSON, L. 2004. The 5'-AMP-activated protein kinase gamma3 isoform has a key role in carbohydrate and lipid metabolism in glycolytic skeletal muscle. *J Biol Chem,* 279**,** 38441-7.

BARRE, L., RICHARDSON, C., HIRSHMAN, M. F., BROZINICK, J., FIERING, S., KEMP, B. E., GOODYEAR, L. J. & WITTERS, L. A. 2007. Genetic model for the chronic activation of skeletal muscle AMP-activated protein kinase leads to glycogen accumulation. *Am J Physiol Endocrinol Metab,* 292**,** E802-11.

BECK, B. 2000. Neuropeptides and obesity. *Nutrition,* 16**,** 916-23.

BERG, A. H., COMBS, T. P., DU, X., BROWNLEE, M. & SCHERER, P. E. 2001. The adipocyte-secreted protein Acrp30 enhances hepatic insulin action. *Nat Med,* 7**,** 947-53.

BERRY, R. & RODEHEFFER, M. S. 2013. Characterization of the adipocyte cellular lineage in vivo. *Nat Cell Biol,* 15**,** 302-8.

BHUROSY, T. & JEEWON, R. 2014. Overweight and obesity epidemic in developing countries: a problem with diet, physical activity, or socioeconomic status? *ScientificWorldJournal,* 2014**,** 964236.

BLOCK, B. A. 1994. Thermogenesis in muscle. *Annu Rev Physiol,* 56**,** 535-77.

BOON, H., BOSSELAAR, M., PRAET, S. F., BLAAK, E. E., SARIS, W. H., WAGENMAKERS, A. J., MCGEE, S. L., TACK, C. J., SMITS, P., HARGREAVES, M. & VAN LOON, L. J. 2008. Intravenous AICAR

administration reduces hepatic glucose output and inhibits whole body lipolysis in type 2 diabetic patients. *Diabetologia,* 51**,** 1893-900.

BORGA, M., VIRTANEN, K. A., ROMU, T., LEINHARD, O. D., PERSSON, A., NUUTILA, P. & ENERBACK, S. 2014. Brown adipose tissue in humans: detection and functional analysis using PET (positron emission tomography), MRI (magnetic resonance imaging), and DECT (dual energy computed tomography). *Methods Enzymol,* 537**,** 141-59.

BRUNET, A., SWEENEY, L. B., STURGILL, J. F., CHUA, K. F., GREER, P. L., LIN, Y., TRAN, H., ROSS, S. E., MOSTOSLAVSKY, R., COHEN, H. Y., HU, L. S., CHENG, H. L., JEDRYCHOWSKI, M. P., GYGI, S. P., SINCLAIR, D. A., ALT, F. W. & GREENBERG, M. E. 2004. Stress-dependent regulation of FOXO transcription factors by the SIRT1 deacetylase. *Science,* 303**,** 2011-5.

BURKS, D. J. & WHITE, M. F. 2001. IRS proteins and beta-cell function. *Diabetes,* 50 Suppl 1**,** S140-5.

CAMBRIDGE, V. C., ZIAUDDEEN, H., NATHAN, P. J., SUBRAMANIAM, N., DODDS, C., CHAMBERLAIN, S. R., KOCH, A., MALTBY, K., SKEGGS, A. L., NAPOLITANO, A., FAROOQI, I. S., BULLMORE, E. T. & FLETCHER, P. C. 2013. Neural and behavioral effects of a novel mu opioid receptor antagonist in binge-eating obese people. *Biol Psychiatry,* 73**,** 887-94.

CANTO, C. & AUWERX, J. 2009. PGC-1alpha, SIRT1 and AMPK, an energy sensing network that controls energy expenditure. *Curr Opin Lipidol,* 20**,** 98-105.

CAO, W., DANIEL, K. W., ROBIDOUX, J., PUIGSERVER, P., MEDVEDEV, A. V., BAI, X., FLOERING, L. M., SPIEGELMAN, B. M. & COLLINS, S. 2004. p38 mitogen-activated protein kinase is the central regulator of cyclic AMP-dependent transcription of the brown fat uncoupling protein 1 gene. *Mol Cell Biol,* 24**,** 3057-67.

CARLING, D., CLARKE, P. R., ZAMMIT, V. A. & HARDIE, D. G. 1989. Purification and characterization of the AMP-activated protein kinase. Copurification of acetyl-CoA carboxylase kinase and 3-hydroxy-3-methylglutaryl-CoA reductase kinase activities. *Eur J Biochem,* 186**,** 129-36.

CARLING, D., THORNTON, C., WOODS, A. & SANDERS, M. J. 2012. AMP-activated protein kinase: new regulation, new roles? *Biochem J,* 445**,** 11-27.

CARLING, D., ZAMMIT, V. A. & HARDIE, D. G. 1987. A common bicyclic protein kinase cascade inactivates the regulatory enzymes of fatty acid and cholesterol biosynthesis. *FEBS Lett,* 223**,** 217-22.

CHAPIN, H. C. & CAPLAN, M. J. 2010. The cell biology of polycystic kidney disease. *J Cell Biol,* 191**,** 701-10.

CHAU, Y. Y., BANDIERA, R., SERRELS, A., MARTINEZ-ESTRADA, O. M., QING, W., LEE, M., SLIGHT, J., THORNBURN, A., BERRY, R., MCHAFFIE, S., STIMSON, R. H., WALKER, B. R., CHAPULI, R. M., SCHEDL, A. & HASTIE, N. 2014. Visceral and subcutaneous fat have different origins and evidence supports a mesothelial source. *Nat Cell Biol,* 16**,** 367-75.

CHENG, K. K., LAM, K. S., WANG, Y., HUANG, Y., CARLING, D., WU, D., WONG, C. & XU, A. 2007. Adiponectin-induced endothelial nitric oxide synthase activation and nitric oxide production are mediated by APPL1 in endothelial cells. *Diabetes,* 56**,** 1387-94.

CHUNG, Y. W., AHMAD, F., TANG, Y., HOCKMAN, S. C., KEE, H. J., BERGER, K., GUIRGUIS, E., CHOI, Y. H., SCHIMEL, D. M., APONTE, A. M., PARK, S., DEGERMAN, E. & MANGANIELLO, V. C. 2017. White to beige conversion in PDE3B KO adipose tissue through activation of AMPK signaling and mitochondrial function. *Sci Rep,* 7**,** 40445.

COHEN, P., LEVY, J. D., ZHANG, Y., FRONTINI, A., KOLODIN, D. P., SVENSSON, K. J., LO, J. C., ZENG, X., YE, L., KHANDEKAR, M. J., WU, J., GUNAWARDANA, S. C., BANKS, A. S., CAMPOREZ, J. P., JURCZAK, M. J., KAJIMURA, S., PISTON, D. W., MATHIS, D., CINTI, S., SHULMAN, G. I., SEALE, P. & SPIEGELMAN, B. M. 2014. Ablation of PRDM16 and beige adipose causes metabolic dysfunction and a subcutaneous to visceral fat switch. *Cell,* 156**,** 304-16.

COKORINOS, E. C., DELMORE, J., REYES, A. R., ALBUQUERQUE, B., KJOBSTED, R., JORGENSEN, N. O., TRAN, J. L., JATKAR, A., CIALDEA, K., ESQUEJO, R. M., MEISSEN, J., CALABRESE, M. F., CORDES, J., MOCCIA, R., TESS, D., SALATTO, C. T., COSKRAN, T. M., OPSAHL, A. C., FLYNN, D., BLATNIK,

M., LI, W., KINDT, E., FORETZ, M., VIOLLET, B., WARD, J., KURUMBAIL, R. G., KALGUTKAR, A. S., WOJTASZEWSKI, J. F. P., CAMERON, K. O. & MILLER, R. A. 2017. Activation of Skeletal Muscle AMPK Promotes Glucose Disposal and Glucose Lowering in Non-human Primates and Mice. *Cell Metab,* 25**,** 1147-1159 e10.

COLEMAN, R. A., LEWIN, T. M. & MUOIO, D. M. 2000. Physiological and nutritional regulation of enzymes of triacylglycerol synthesis. *Annu Rev Nutr,* 20**,** 77-103.

COLLABORATION, N. C. D. R. F. 2016. Trends in adult body-mass index in 200 countries from 1975 to 2014: a pooled analysis of 1698 population-based measurement studies with 19.2 million participants. *Lancet,* 387**,** 1377-1396.

COMPERAT, E., FERLICOT, S., CAMPARO, P., ESCHWEGE, P., BA, N., BENOIT, G., BEDOSSA, P. & PARADIS, V. 2006. Expression of epidermal growth factor receptor and proliferative activity of cyst epithelium in human renal cystic diseases. *Urol Int,* 76**,** 269-73.

CONSIDINE, R. V., CONSIDINE, E. L., WILLIAMS, C. J., HYDE, T. M. & CARO, J. F. 1996. The hypothalamic leptin receptor in humans: identification of incidental sequence polymorphisms and absence of the db/db mouse and fa/fa rat mutations. *Diabetes,* 45**,** 992-4.

COOL, B., ZINKER, B., CHIOU, W., KIFLE, L., CAO, N., PERHAM, M., DICKINSON, R., ADLER, A., GAGNE, G., IYENGAR, R., ZHAO, G., MARSH, K., KYM, P., JUNG, P., CAMP, H. S. & FREVERT, E. 2006. Identification and characterization of a small molecule AMPK activator that treats key components of type 2 diabetes and the metabolic syndrome. *Cell Metab,* 3**,** 403-16.

COSTFORD, S. R., KAVASLAR, N., AHITUV, N., CHAUDHRY, S. N., SCHACKWITZ, W. S., DENT, R., PENNACCHIO, L. A., MCPHERSON, R. & HARPER, M. E. 2007. Gain-of-function R225W mutation in human AMPKgamma(3) causing increased glycogen and decreased triglyceride in skeletal muscle. *PLoS One,* 2**,** e903.

COUSIN, B., CINTI, S., MORRONI, M., RAIMBAULT, S., RICQUIER, D., PENICAUD, L. & CASTEILLA, L. 1992. Occurrence of brown adipocytes in rat white adipose tissue: molecular and morphological characterization. *J Cell Sci,* 103 ( Pt 4)**,** 931-42.

CURTHOYS, N. P. & MOE, O. W. 2014. Proximal tubule function and response to acidosis. *Clin J Am Soc Nephrol,* 9**,** 1627-38.

DA SILVA XAVIER, G., LECLERC, I., VARADI, A., TSUBOI, T., MOULE, S. K. & RUTTER, G. A. 2003. Role for AMP-activated protein kinase in glucose-stimulated insulin secretion and preproinsulin gene expression. *Biochem J,* 371**,** 761-74.

DANESCHVAR, H. L., ARONSON, M. D. & SMETANA, G. W. 2016. FDA-Approved Anti-Obesity Drugs in the United States. *Am J Med,* 129**,** 879 e1-6.

DANIEL, T. & CARLING, D. 2002. Functional analysis of mutations in the gamma 2 subunit of AMP-activated protein kinase associated with cardiac hypertrophy and Wolff-Parkinson-White syndrome. *J Biol Chem,* 277**,** 51017-24.

DAVIES, J. K., WELLS, D. J., LIU, K., WHITROW, H. R., DANIEL, T. D., GRIGNANI, R., LYGATE, C. A., SCHNEIDER, J. E., NOEL, G., WATKINS, H. & CARLING, D. 2006. Characterization of the role of gamma2 R531G mutation in AMP-activated protein kinase in cardiac hypertrophy and Wolff-Parkinson-White syndrome. *Am J Physiol Heart Circ Physiol,* 290**,** H1942-51.

DE GROOF, A. J., FRANSEN, J. A., ERRINGTON, R. J., WILLEMS, P. H., WIERINGA, B. & KOOPMAN, W. J. 2002. The creatine kinase system is essential for optimal refill of the sarcoplasmic reticulum Ca2+ store in skeletal muscle. *J Biol Chem,* 277**,** 5275-84.

DE JONG, J. M., LARSSON, O., CANNON, B. & NEDERGAARD, J. 2015. A stringent validation of mouse adipose tissue identity markers. *Am J Physiol Endocrinol Metab,* 308**,** E1085-105.

DE MEIS, L. 2003. Brown adipose tissue Ca2+-ATPase: uncoupled ATP hydrolysis and thermogenic activity. *J Biol Chem,* 278**,** 41856-61.

DE MEIS, L., ARRUDA, A. P., DA COSTA, R. M. & BENCHIMOL, M. 2006. Identification of a Ca2+-ATPase in brown adipose tissue mitochondria: regulation of thermogenesis by ATP and Ca2+. *J Biol Chem,* 281**,** 16384-90.

DE MEIS, L., KETZER, L. A., DA COSTA, R. M., DE ANDRADE, I. R. & BENCHIMOL, M. 2010. Fusion of the endoplasmic reticulum and mitochondrial outer membrane in rats brown adipose tissue: activation of thermogenesis by Ca2+. *PLoS One,* 5**,** e9439.

DE MEIS, L., OLIVEIRA, G. M., ARRUDA, A. P., SANTOS, R., COSTA, R. M. & BENCHIMOL, M. 2005. The thermogenic activity of rat brown adipose tissue and rabbit white muscle Ca2+-ATPase. *IUBMB Life,* 57**,** 337-45.

DEEPA, S. S., ZHOU, L., RYU, J., WANG, C., MAO, X., LI, C., ZHANG, N., MUSI, N., DEFRONZO, R. A., LIU, F. & DONG, L. Q. 2011. APPL1 mediates adiponectin-induced LKB1 cytosolic localization through the PP2A-PKCzeta signaling pathway. *Mol Endocrinol,* 25**,** 1773-85.

DENZEL, M. S., SCIMIA, M. C., ZUMSTEIN, P. M., WALSH, K., RUIZ-LOZANO, P. & RANSCHT, B. 2010. T-cadherin is critical for adiponectin-mediated cardioprotection in mice. *J Clin Invest,* 120**,** 4342-52.

DESSALLE, K., EUTHINE, V., CHANON, S., DELARICHAUDY, J., FUJII, I., ROME, S., VIDAL, H., NEMOZ, G., SIMON, C. & LEFAI, E. 2012. SREBP-1 transcription factors regulate skeletal muscle cell size by controlling protein synthesis through myogenic regulatory factors. *PLoS One,* 7**,** e50878.

DIVAKARUNI, A. S., HUMPHREY, D. M. & BRAND, M. D. 2012. Fatty acids change the conformation of uncoupling protein 1 (UCP1). *J Biol Chem,* 287**,** 36845-53.

DRAKE, P. L., KRIEG, E., TEASS, A. W. & VALLYATHAN, V. 2002. Two assays for urinary N-acetyl-beta-D-glucosaminidase compared. *Clin Chem,* 48**,** 1604-5.

DRESSLER, G. R. 2006. The cellular basis of kidney development. *Annu Rev Cell Dev Biol,* 22**,** 509-29.

DRIDI, S. & TAOUIS, M. 2009. Adiponectin and energy homeostasis: consensus and controversy. *J Nutr Biochem,* 20**,** 831-9.

DUNCAN, R. E., AHMADIAN, M., JAWORSKI, K., SARKADI-NAGY, E. & SUL, H. S. 2007. Regulation of lipolysis in adipocytes. *Annu Rev Nutr,* 27**,** 79-101.

EGAN, D. F., SHACKELFORD, D. B., MIHAYLOVA, M. M., GELINO, S., KOHNZ, R. A., MAIR, W., VASQUEZ, D. S., JOSHI, A., GWINN, D. M., TAYLOR, R., ASARA, J. M., FITZPATRICK, J., DILLIN, A., VIOLLET, B., KUNDU, M., HANSEN, M. & SHAW, R. J. 2011. Phosphorylation of ULK1 (hATG1) by AMP-activated protein kinase connects energy sensing to mitophagy. *Science,* 331**,** 456-61.

EGRAS, A. M., HAMILTON, W. R., LENZ, T. L. & MONAGHAN, M. S. 2011. An evidence-based review of fat modifying supplemental weight loss products. *J Obes,* 2011.

EIZIRIK, D. L., COLLI, M. L. & ORTIS, F. 2009. The role of inflammation in insulitis and beta-cell loss in type 1 diabetes. *Nat Rev Endocrinol,* 5**,** 219-26.

EKNOYAN, G. 2009. A clinical view of simple and complex renal cysts. *J Am Soc Nephrol,* 20**,** 1874-6.

EMMA, F., MONTINI, G., PARIKH, S. M. & SALVIATI, L. 2016. Mitochondrial dysfunction in inherited renal disease and acute kidney injury. *Nat Rev Nephrol,* 12**,** 267-80.

ENERBACK, S., JACOBSSON, A., SIMPSON, E. M., GUERRA, C., YAMASHITA, H., HARPER, M. E. & KOZAK, L. P. 1997. Mice lacking mitochondrial uncoupling protein are cold-sensitive but not obese. *Nature,* 387**,** 90-4.

ESTRADE, M., VIGNON, X. & MONIN, G. 1993a. Effect of the RN(-) gene on ultrastructure and protein fractions in pig muscle. *Meat Sci,* 35**,** 313-9.

ESTRADE, M., VIGNON, X., ROCK, E. & MONIN, G. 1993b. Glycogen hyperaccumulation in white muscle fibres of RN- carrier pigs. A biochemical and ultrastructural study. *Comp Biochem Physiol B,* 104**,** 321-6.

EXPERT PANEL ON DETECTION, E. & TREATMENT OF HIGH BLOOD CHOLESTEROL IN, A. 2001. Executive Summary of The Third Report of The National Cholesterol Education Program (NCEP) Expert Panel on Detection, Evaluation, And Treatment of High Blood Cholesterol In Adults (Adult Treatment Panel III). *JAMA,* 285**,** 2486-97.

FAUST, I. M., JOHNSON, P. R., STERN, J. S. & HIRSCH, J. 1978. Diet-induced adipocyte number increase in adult rats: a new model of obesity. *Am J Physiol,* 235**,** E279-86.

FAVA, E., DEHGHANY, J., OUWENDIJK, J., MULLER, A., NIEDERLEIN, A., VERKADE, P., MEYER-HERMANN, M. & SOLIMENA, M. 2012. Novel standards in the measurement of rat insulin granules combining electron microscopy, high-content image analysis and in silico modelling. *Diabetologia,* 55**,** 1013-23.

FEDORENKO, A., LISHKO, P. V. & KIRICHOK, Y. 2012. Mechanism of fatty-acid-dependent UCP1 uncoupling in brown fat mitochondria. *Cell,* 151**,** 400-13.

FELDMANN, H. M., GOLOZOUBOVA, V., CANNON, B. & NEDERGAARD, J. 2009. UCP1 ablation induces obesity and abolishes diet-induced thermogenesis in mice exempt from thermal stress by living at thermoneutrality. *Cell Metab,* 9**,** 203-9.

FISHER, J. S., GAO, J., HAN, D. H., HOLLOSZY, J. O. & NOLTE, L. A. 2002a. Activation of AMP kinase enhances sensitivity of muscle glucose transport to insulin. *Am J Physiol Endocrinol Metab,* 282**,** E18-23.

FISHER, R. M., THORNE, A., HAMSTEN, A. & ARNER, P. 2002b. Fatty acid binding protein expression in different human adipose tissue depots in relation to rates of lipolysis and insulin concentration in obese individuals. *Mol Cell Biochem,* 239**,** 95-100.

FLATT, J. P. 2011. Issues and misconceptions about obesity. *Obesity (Silver Spring),* 19**,** 676-86.

FOCK, K. M. & KHOO, J. 2013. Diet and exercise in management of obesity and overweight. *J Gastroenterol Hepatol,* 28 Suppl 4**,** 59-63.

FOLMES, K. D., WITTERS, L. A., ALLARD, M. F., YOUNG, M. E. & DYCK, J. R. 2007. The AMPK gamma1 R70Q mutant regulates multiple metabolic and growth pathways in neonatal cardiac myocytes. *Am J Physiol Heart Circ Physiol,* 293**,** H3456-64.

FOSTER, D. O. & FRYDMAN, M. L. 1979. Tissue distribution of cold-induced thermogenesis in conscious warm- or cold-acclimated rats reevaluated from changes in tissue blood flow: the dominant role of brown adipose tissue in the replacement of shivering by nonshivering thermogenesis. *Can J Physiol Pharmacol,* 57**,** 257-70.

FRAGIADAKI, M. & MASON, R. M. 2011. Epithelial-mesenchymal transition in renal fibrosis - evidence for and against. *Int J Exp Pathol,* 92**,** 143-50.

FREEMAN, H. C., HUGILL, A., DEAR, N. T., ASHCROFT, F. M. & COX, R. D. 2006. Deletion of nicotinamide nucleotide transhydrogenase: a new quantitive trait locus accounting for glucose intolerance in C57BL/6J mice. *Diabetes,* 55**,** 2153-6.

FRUHBECK, G., TOPLAK, H., WOODWARD, E., YUMUK, V., MAISLOS, M., OPPERT, J. M. & EXECUTIVE COMMITTEE OF THE EUROPEAN ASSOCIATION FOR THE STUDY OF, O. 2013. Obesity: the gateway to ill health - an EASO position statement on a rising public health, clinical and scientific challenge in Europe. *Obes Facts,* 6**,** 117-20.

FU, A., EBERHARD, C. E. & SCREATON, R. A. 2013. Role of AMPK in pancreatic beta cell function. *Mol Cell Endocrinol,* 366**,** 127-34.

FULLERTON, M. D., GALIC, S., MARCINKO, K., SIKKEMA, S., PULINILKUNNIL, T., CHEN, Z. P., O'NEILL, H. M., FORD, R. J., PALANIVEL, R., O'BRIEN, M., HARDIE, D. G., MACAULAY, S. L., SCHERTZER, J. D., DYCK, J. R., VAN DENDEREN, B. J., KEMP, B. E. & STEINBERG, G. R. 2013. Single phosphorylation sites in Acc1 and Acc2 regulate lipid homeostasis and the insulin-sensitizing effects of metformin. *Nat Med,* 19**,** 1649-54.

GARCIA-ROVES, P. M., OSLER, M. E., HOLMSTROM, M. H. & ZIERATH, J. R. 2008. Gain-of-function R225Q mutation in AMP-activated protein kinase gamma3 subunit increases mitochondrial biogenesis in glycolytic skeletal muscle. *J Biol Chem,* 283**,** 35724-34.

GASCUE, C., KATSANIS, N. & BADANO, J. L. 2011. Cystic diseases of the kidney: ciliary dysfunction and cystogenic mechanisms. *Pediatr Nephrol,* 26**,** 1181-95.

GJORGJIEVA, M., RAFFIN, M., DUCHAMPT, A., PERRY, A., STEFANUTTI, A., BREVET, M., TORTEREAU, A., DUBOURG, L., HUBERT-BURON, A., MABILLE, M., PELISSOU, C., LASSALLE, L., LABRUNE, P., MITHIEUX, G. & RAJAS, F. 2016. Progressive development of renal cysts in glycogen storage disease type I. *Human Molecular Genetics,* 25**,** 3784-3797.

GOLLOB, M. H., GREEN, M. S., TANG, A. S., GOLLOB, T., KARIBE, A., ALI HASSAN, A. S., AHMAD, F., LOZADO, R., SHAH, G., FANANAPAZIR, L., BACHINSKI, L. L. & ROBERTS, R. 2001. Identification of a gene responsible for familial Wolff-Parkinson-White syndrome. *N Engl J Med,* 344**,** 1823-31.

GOWDA, S., DESAI, P. B., KULKARNI, S. S., HULL, V. V., MATH, A. A. & VERNEKAR, S. N. 2010. Markers of renal function tests. *N Am J Med Sci,* 2**,** 170-3.

GUO, F., LIU, S. Q., GAO, X. H. & ZHANG, L. Y. 2016. AICAR induces AMPK-independent programmed necrosis in prostate cancer cells. *Biochem Biophys Res Commun,* 474**,** 277-283.

GUSTAFSSON, A. J., INGELMAN-SUNDBERG, H., DZABIC, M., AWASUM, J., NGUYEN, K. H., OSTENSON, C. G., PIERRO, C., TEDESCHI, P., WOOLCOTT, O., CHIOUNAN, S., LUND, P. E., LARSSON, O. & ISLAM, M. S. 2005. Ryanodine receptor-operated activation of TRP-like channels can trigger critical Ca2+ signaling events in pancreatic beta-cells. *FASEB J,* 19**,** 301-3.

GWINN, D. M., SHACKELFORD, D. B., EGAN, D. F., MIHAYLOVA, M. M., MERY, A., VASQUEZ, D. S., TURK, B. E. & SHAW, R. J. 2008. AMPK phosphorylation of raptor mediates a metabolic checkpoint. *Mol Cell,* 30**,** 214-26.

HAJARNIS, S., LAKHIA, R., YHESKEL, M., WILLIAMS, D., SOROURIAN, M., LIU, X., ABOUDEHEN, K., ZHANG, S., KERSJES, K., GALASSO, R., LI, J., KAIMAL, V., LOCKTON, S., DAVIS, S., FLATEN, A., JOHNSON, J. A., HOLLAND, W. L., KUSMINSKI, C. M., SCHERER, P. E., HARRIS, P. C., TRUDEL, M., WALLACE, D. P., IGARASHI, P., LEE, E. C., ANDROSAVICH, J. R. & PATEL, V. 2017. microRNA-17 family promotes polycystic kidney disease progression through modulation of mitochondrial metabolism. *Nat Commun,* 8**,** 14395.

HALAAS, J. L., GAJIWALA, K. S., MAFFEI, M., COHEN, S. L., CHAIT, B. T., RABINOWITZ, D., LALLONE, R. L., BURLEY, S. K. & FRIEDMAN, J. M. 1995. Weight-reducing effects of the plasma protein encoded by the obese gene. *Science,* 269**,** 543-6.

HALFORD, J. C. 2001. Pharmacology of appetite suppression: implication for the treatment of obesity. *Curr Drug Targets,* 2**,** 353-70.

HALFORD, J. C. & BLUNDELL, J. E. 2000. Pharmacology of appetite suppression. *Prog Drug Res,* 54**,** 25-58.

HAMILTON, S. R., STAPLETON, D., O'DONNELL, J. B., JR., KUNG, J. T., DALAL, S. R., KEMP, B. E. & WITTERS, L. A. 2001. An activating mutation in the gamma1 subunit of the AMP-activated protein kinase. *FEBS Lett,* 500**,** 163-8.

HARDIE, D. G. 2013. The LKB1-AMPK pathway-friend or foe in cancer? *Cancer Cell,* 23**,** 131-2.

HARDIE, D. G., SCOTT, J. W., PAN, D. A. & HUDSON, E. R. 2003. Management of cellular energy by the AMP-activated protein kinase system. *FEBS Lett,* 546**,** 113-20.

HARMS, M. & SEALE, P. 2013. Brown and beige fat: development, function and therapeutic potential. *Nat Med,* 19**,** 1252-63.

HARPER, M. E., GREEN, K. & BRAND, M. D. 2008. The efficiency of cellular energy transduction and its implications for obesity. *Annu Rev Nutr,* 28**,** 13-33.

HAWLEY, S. A., BOUDEAU, J., REID, J. L., MUSTARD, K. J., UDD, L., MAKELA, T. P., ALESSI, D. R. & HARDIE, D. G. 2003. Complexes between the LKB1 tumor suppressor, STRAD alpha/beta and MO25 alpha/beta are upstream kinases in the AMP-activated protein kinase cascade. *J Biol,* 2**,** 28.

HAWLEY, S. A., SELBERT, M. A., GOLDSTEIN, E. G., EDELMAN, A. M., CARLING, D. & HARDIE, D. G. 1995. 5'-AMP activates the AMP-activated protein kinase cascade, and Ca2+/calmodulin activates the calmodulin-dependent protein kinase I cascade, via three independent mechanisms. *J Biol Chem,* 270**,** 27186-91.

HEBEBRAND, J. 2008. Welcome to OBESITY FACTS, the official journal of the European Association for the Study of Obesity (EASO)! *Obes Facts,* 1**,** 4-5.

HILL, J. O., WYATT, H. R. & PETERS, J. C. 2012. Energy balance and obesity. *Circulation,* 126**,** 126-32.

HIMMS-HAGEN, J., MELNYK, A., ZINGARETTI, M. C., CERESI, E., BARBATELLI, G. & CINTI, S. 2000. Multilocular fat cells in WAT of CL-316243-treated rats derive directly from white adipocytes. *Am J Physiol Cell Physiol,* 279**,** C670-81.

HOLLOWAY, G. P., LUIKEN, J. J., GLATZ, J. F., SPRIET, L. L. & BONEN, A. 2008. Contribution of FAT/CD36 to the regulation of skeletal muscle fatty acid oxidation: an overview. *Acta Physiol (Oxf),* 194**,** 293-309.

HONG, S. P., LEIPER, F. C., WOODS, A., CARLING, D. & CARLSON, M. 2003. Activation of yeast Snf1 and mammalian AMP-activated protein kinase by upstream kinases. *Proc Natl Acad Sci U S A,* 100**,** 8839-43.

HU, E., LIANG, P. & SPIEGELMAN, B. M. 1996. AdipoQ is a novel adipose-specific gene dysregulated in obesity. *J Biol Chem,* 271**,** 10697-703.

HUNTER, R. W., TREEBAK, J. T., WOJTASZEWSKI, J. F. & SAKAMOTO, K. 2011. Molecular mechanism by which AMP-activated protein kinase activation promotes glycogen accumulation in muscle. *Diabetes,* 60**,** 766-74.

INAGAKI, T., SAKAI, J. & KAJIMURA, S. 2016. Transcriptional and epigenetic control of brown and beige adipose cell fate and function. *Nat Rev Mol Cell Biol,* 17**,** 480-95.

INOKI, K., ZHU, T. & GUAN, K. L. 2003. TSC2 mediates cellular energy response to control cell growth and survival. *Cell,* 115**,** 577-90.

ITO, K. & SUDA, T. 2014. Metabolic requirements for the maintenance of self-renewing stem cells. *Nat Rev Mol Cell Biol,* 15**,** 243-56.

JAGER, S., HANDSCHIN, C., ST-PIERRE, J. & SPIEGELMAN, B. M. 2007. AMP-activated protein kinase (AMPK) action in skeletal muscle via direct phosphorylation of PGC-1alpha. *Proc Natl Acad Sci U S A,* 104**,** 12017-22.

JAHN, R. & FASSHAUER, D. 2012. Molecular machines governing exocytosis of synaptic vesicles. *Nature,* 490**,** 201-7.

JENSEN, T. E., ROSE, A. J., JORGENSEN, S. B., BRANDT, N., SCHJERLING, P., WOJTASZEWSKI, J. F. & RICHTER, E. A. 2007. Possible CaMKK-dependent regulation of AMPK phosphorylation and glucose uptake at the onset of mild tetanic skeletal muscle contraction. *Am J Physiol Endocrinol Metab,* 292**,** E1308-17.

JEPPESEN, J., ALBERS, P. H., ROSE, A. J., BIRK, J. B., SCHJERLING, P., DZAMKO, N., STEINBERG, G. R. & KIENS, B. 2011. Contraction-induced skeletal muscle FAT/CD36 trafficking and FA uptake is AMPK independent. *J Lipid Res,* 52**,** 699-711.

JEPPESEN, J. & KIENS, B. 2012. Regulation and limitations to fatty acid oxidation during exercise. *J Physiol,* 590**,** 1059-68.

JIANG, Y., HUANG, W., WANG, J., XU, Z., HE, J., LIN, X., ZHOU, Z. & ZHANG, J. 2014. Metformin plays a dual role in MIN6 pancreatic beta cell function through AMPK-dependent autophagy. *Int J Biol Sci,* 10**,** 268-77.

JORGENSEN, S. B., WOJTASZEWSKI, J. F., VIOLLET, B., ANDREELLI, F., BIRK, J. B., HELLSTEN, Y., SCHJERLING, P., VAULONT, S., NEUFER, P. D., RICHTER, E. A. & PILEGAARD, H. 2005. Effects of alpha-AMPK knockout on exercise-induced gene activation in mouse skeletal muscle. *FASEB J,* 19**,** 1146-8.

JUNG, E. J., KWON, S. W., JUNG, B. H., OH, S. H. & LEE, B. H. 2011. Role of the AMPK/SREBP-1 pathway in the development of orotic acid-induced fatty liver. *J Lipid Res,* 52**,** 1617-25.

KAJIMURA, S. 2015. Promoting brown and beige adipocyte biogenesis through the PRDM16 pathway. *Int J Obes Suppl,* 5**,** S11-4.

KAJIMURA, S., SEALE, P., KUBOTA, K., LUNSFORD, E., FRANGIONI, J. V., GYGI, S. P. & SPIEGELMAN, B. M. 2009. Initiation of myoblast to brown fat switch by a PRDM16-C/EBP-beta transcriptional complex. *Nature,* 460**,** 1154-8.

KAJIMURA, S., SEALE, P., TOMARU, T., ERDJUMENT-BROMAGE, H., COOPER, M. P., RUAS, J. L., CHIN, S., TEMPST, P., LAZAR, M. A. & SPIEGELMAN, B. M. 2008. Regulation of the brown and white

fat gene programs through a PRDM16/CtBP transcriptional complex. *Genes Dev,* 22**,** 1397-409.

KALENDER, A., SELVARAJ, A., KIM, S. Y., GULATI, P., BRULE, S., VIOLLET, B., KEMP, B. E., BARDEESY, N., DENNIS, P., SCHLAGER, J. J., MARETTE, A., KOZMA, S. C. & THOMAS, G. 2010. Metformin, independent of AMPK, inhibits mTORC1 in a rag GTPase-dependent manner. *Cell Metab,* 11**,** 390-401.

KAZAK, L., CHOUCHANI, E. T., JEDRYCHOWSKI, M. P., ERICKSON, B. K., SHINODA, K., COHEN, P., VETRIVELAN, R., LU, G. Z., LAZNIK-BOGOSLAVSKI, D., HASENFUSS, S. C., KAJIMURA, S., GYGI, S. P. & SPIEGELMAN, B. M. 2015. A creatine-driven substrate cycle enhances energy expenditure and thermogenesis in beige fat. *Cell,* 163**,** 643-55.

KAZAK, L., CHOUCHANI, E. T., LU, G. Z., JEDRYCHOWSKI, M. P., BARE, C. J., MINA, A. I., KUMARI, M., ZHANG, S., VUCKOVIC, I., LAZNIK-BOGOSLAVSKI, D., DZEJA, P., BANKS, A. S., ROSEN, E. D. & SPIEGELMAN, B. M. 2017. Genetic Depletion of Adipocyte Creatine Metabolism Inhibits Diet-Induced Thermogenesis and Drives Obesity. *Cell Metab*.

KEIPERT, S. & JASTROCH, M. 2014. Brite/beige fat and UCP1 - is it thermogenesis? *Biochim Biophys Acta,* 1837**,** 1075-82.

KEVONIAN, A. V., VANDER TUIG, J. G. & ROMSOS, D. R. 1984. Consumption of a low protein diet increases norepinephrine turnover in brown adipose tissue of adult rats. *J Nutr,* 114**,** 543-9.

KIM, J., YANG, G., KIM, Y., KIM, J. & HA, J. 2016. AMPK activators: mechanisms of action and physiological activities. *Exp Mol Med,* 48**,** e224.

KIM, K. H., JEONG, Y. T., OH, H., KIM, S. H., CHO, J. M., KIM, Y. N., KIM, S. S., KIM, D. H., HUR, K. Y., KIM, H. K., KO, T., HAN, J., KIM, H. L., KIM, J., BACK, S. H., KOMATSU, M., CHEN, H., CHAN, D. C., KONISHI, M., ITOH, N., CHOI, C. S. & LEE, M. S. 2013. Autophagy deficiency leads to protection from obesity and insulin resistance by inducing Fgf21 as a mitokine. *Nat Med,* 19**,** 83-92.

KIM, K. W., ZHAO, L., DONATO, J., JR., KOHNO, D., XU, Y., ELIAS, C. F., LEE, C., PARKER, K. L. & ELMQUIST, J. K. 2011. Steroidogenic factor 1 directs programs regulating diet-induced thermogenesis and leptin action in the ventral medial hypothalamic nucleus. *Proc Natl Acad Sci U S A,* 108**,** 10673-8.

KIM, M., HUNTER, R. W., GARCIA-MENENDEZ, L., GONG, G., YANG, Y. Y., KOLWICZ, S. C., JR., XU, J., SAKAMOTO, K., WANG, W. & TIAN, R. 2014. Mutation in the gamma2-subunit of AMP-activated protein kinase stimulates cardiomyocyte proliferation and hypertrophy independent of glycogen storage. *Circ Res,* 114**,** 966-75.

KJOBSTED, R., TREEBAK, J. T., FENTZ, J., LANTIER, L., VIOLLET, B., BIRK, J. B., SCHJERLING, P., BJORNHOLM, M., ZIERATH, J. R. & WOJTASZEWSKI, J. F. 2015. Prior AICAR stimulation increases insulin sensitivity in mouse skeletal muscle in an AMPK-dependent manner. *Diabetes,* 64**,** 2042-55.

KLINGENSPOR, M. 2003. Cold-induced recruitment of brown adipose tissue thermogenesis. *Exp Physiol,* 88**,** 141-8.

KLOK, M. D., JAKOBSDOTTIR, S. & DRENT, M. L. 2007. The role of leptin and ghrelin in the regulation of food intake and body weight in humans: a review. *Obes Rev,* 8**,** 21-34.

KOO, S. H., FLECHNER, L., QI, L., ZHANG, X., SCREATON, R. A., JEFFRIES, S., HEDRICK, S., XU, W., BOUSSOUAR, F., BRINDLE, P., TAKEMORI, H. & MONTMINY, M. 2005. The CREB coactivator TORC2 is a key regulator of fasting glucose metabolism. *Nature,* 437**,** 1109-11.

KORTENOEVEN, M. L., PEDERSEN, N. B., ROSENBAEK, L. L. & FENTON, R. A. 2015. Vasopressin regulation of sodium transport in the distal nephron and collecting duct. *Am J Physiol Renal Physiol,* 309**,** F280-99.

KURAHASHI, M. & KUROSHIMA, A. 1978. Creatine metabolism in skeletal muscle of cold-acclimated rats. *J Appl Physiol Respir Environ Exerc Physiol,* 44**,** 12-6.

LACLAUSTRA, M., CORELLA, D. & ORDOVAS, J. M. 2007. Metabolic syndrome pathophysiology: the role of adipose tissue. *Nutr Metab Cardiovasc Dis,* 17**,** 125-39.

LAFFEL, L. 1999. Ketone bodies: a review of physiology, pathophysiology and application of monitoring to diabetes. *Diabetes Metab Res Rev,* 15**,** 412-26.

LANG, T., YU, L., TU, Q., JIANG, J., CHEN, Z., XIN, Y., LIU, G. & ZHAO, S. 2000. Molecular cloning, genomic organization, and mapping of PRKAG2, a heart abundant gamma2 subunit of 5'-AMP-activated protein kinase, to human chromosome 7q36. *Genomics,* 70**,** 258-63.

LANTIER, L., FENTZ, J., MOUNIER, R., LECLERC, J., TREEBAK, J. T., PEHMOLLER, C., SANZ, N., SAKAKIBARA, I., SAINT-AMAND, E., RIMBAUD, S., MAIRE, P., MARETTE, A., VENTURA-CLAPIER, R., FERRY, A., WOJTASZEWSKI, J. F., FORETZ, M. & VIOLLET, B. 2014. AMPK controls exercise endurance, mitochondrial oxidative capacity, and skeletal muscle integrity. *FASEB J,* 28**,** 3211-24.

LEE, C. W., WONG, L. L., TSE, E. Y., LIU, H. F., LEONG, V. Y., LEE, J. M., HARDIE, D. G., NG, I. O. & CHING, Y. P. 2012. AMPK promotes p53 acetylation via phosphorylation and inactivation of SIRT1 in liver cancer cells. *Cancer Res,* 72**,** 4394-404.

LEE, J. W., PARK, S., TAKAHASHI, Y. & WANG, H. G. 2010. The association of AMPK with ULK1 regulates autophagy. *PLoS One,* 5**,** e15394.

LERMA-CABRERA, J. M., CARVAJAL, F. & LOPEZ-LEGARREA, P. 2016. Food addiction as a new piece of the obesity framework. *Nutr J,* 15**,** 5.

LEVIN, B. E., DUNN-MEYNELL, A. A. & BANKS, W. A. 2004. Obesity-prone rats have normal blood-brain barrier transport but defective central leptin signaling before obesity onset. *Am J Physiol Regul Integr Comp Physiol,* 286**,** R143-50.

LI, Y., XU, S., MIHAYLOVA, M. M., ZHENG, B., HOU, X., JIANG, B., PARK, O., LUO, Z., LEFAI, E., SHYY, J. Y., GAO, B., WIERZBICKI, M., VERBEUREN, T. J., SHAW, R. J., COHEN, R. A. & ZANG, M. 2011. AMPK phosphorylates and inhibits SREBP activity to attenuate hepatic steatosis and atherosclerosis in diet-induced insulin-resistant mice. *Cell Metab,* 13**,** 376-388.

LIU, S., KIM, T. H., FRANKLIN, D. A. & ZHANG, Y. 2017. Protection against High-Fat-Diet-Induced Obesity in MDM2C305F Mice Due to Reduced p53 Activity and Enhanced Energy Expenditure. *Cell Rep,* 18**,** 1005-1018.

LIU, X., CHHIPA, R. R., POOYA, S., WORTMAN, M., YACHYSHIN, S., CHOW, L. M., KUMAR, A., ZHOU, X., SUN, Y., QUINN, B., MCPHERSON, C., WARNICK, R. E., KENDLER, A., GIRI, S., POELS, J., NORGA, K., VIOLLET, B., GRABOWSKI, G. A. & DASGUPTA, B. 2014. Discrete mechanisms of mTOR and cell cycle regulation by AMPK agonists independent of AMPK. *Proc Natl Acad Sci U S A,* 111**,** E435-44.

LOCHHEAD, P. A., SALT, I. P., WALKER, K. S., HARDIE, D. G. & SUTHERLAND, C. 2000. 5-aminoimidazole-4-carboxamide riboside mimics the effects of insulin on the expression of the 2 key gluconeogenic genes PEPCK and glucose-6-phosphatase. *Diabetes,* 49**,** 896-903.

LOPEZ, M., VARELA, L., VAZQUEZ, M. J., RODRIGUEZ-CUENCA, S., GONZALEZ, C. R., VELAGAPUDI, V. R., MORGAN, D. A., SCHOENMAKERS, E., AGASSANDIAN, K., LAGE, R., MARTINEZ DE MORENTIN, P. B., TOVAR, S., NOGUEIRAS, R., CARLING, D., LELLIOTT, C., GALLEGO, R., ORESIC, M., CHATTERJEE, K., SAHA, A. K., RAHMOUNI, K., DIEGUEZ, C. & VIDAL-PUIG, A. 2010. Hypothalamic AMPK and fatty acid metabolism mediate thyroid regulation of energy balance. *Nat Med,* 16**,** 1001-8.

LOWELL, B. B. & SPIEGELMAN, B. M. 2000. Towards a molecular understanding of adaptive thermogenesis. *Nature,* 404**,** 652-60.

MAEDA, K., OKUBO, K., SHIMOMURA, I., FUNAHASHI, T., MATSUZAWA, Y. & MATSUBARA, K. 1996. cDNA cloning and expression of a novel adipose specific collagen-like factor, apM1 (AdiPose Most abundant Gene transcript 1). *Biochem Biophys Res Commun,* 221**,** 286-9.

MAHAMAT, H. A., JACQUIR, S., KHALIL, C., LAURENT, G. & BINCZAK, S. 2016. Wolff-Parkinson-White (WPW) syndrome: the detection of delta wave in an electrocardiogram (ECG). *Conf Proc IEEE Eng Med Biol Soc,* 2016**,** 3809-3812.

MANNING, S., PUCCI, A. & FINER, N. 2014. Pharmacotherapy for obesity: novel agents and paradigms. *Ther Adv Chronic Dis,* 5**,** 135-48.

MAO, X., KIKANI, C. K., RIOJAS, R. A., LANGLAIS, P., WANG, L., RAMOS, F. J., FANG, Q., CHRIST-ROBERTS, C. Y., HONG, J. Y., KIM, R. Y., LIU, F. & DONG, L. Q. 2006. APPL1 binds to adiponectin receptors and mediates adiponectin signalling and function. *Nat Cell Biol,* 8**,** 516-23.

MARANDOLA, P., MUSITELLI, S., JALLOUS, H., SPERONI, A. & DE BASTIANI, T. 1994. The Aristotelian kidney. *Am J Nephrol,* 14**,** 302-6.

MARIN, T. L., GONGOL, B., MARTIN, M., KING, S. J., SMITH, L., JOHNSON, D. A., SUBRAMANIAM, S., CHIEN, S. & SHYY, J. Y. 2015. Identification of AMP-activated protein kinase targets by a consensus sequence search of the proteome. *BMC Syst Biol,* 9**,** 13.

MEHTA, A., MARSO, S. P. & NEELAND, I. J. 2017. Liraglutide for weight management: a critical review of the evidence. *Obes Sci Pract,* 3**,** 3-14.

MENEZES, L. F., LIN, C. C., ZHOU, F. & GERMINO, G. G. 2016. Fatty Acid Oxidation is Impaired in An Orthologous Mouse Model of Autosomal Dominant Polycystic Kidney Disease. *EBioMedicine,* 5**,** 183-92.

MENG, X. M., NIKOLIC-PATERSON, D. J. & LAN, H. Y. 2014. Inflammatory processes in renal fibrosis. *Nat Rev Nephrol,* 10**,** 493-503.

MEYER, C. W., OOTSUKA, Y. & ROMANOVSKY, A. A. 2017. Body Temperature Measurements for Metabolic Phenotyping in Mice. *Front Physiol,* 8**,** 520.

MICKELSEN, O., TAKAHASHI, S. & CRAIG, C. 1955. Experimental obesity. I. Production of obesity in rats by feeding high-fat diets. *J Nutr,* 57**,** 541-54.

MIHAYLOVA, M. M. & SHAW, R. J. 2011. The AMPK signalling pathway coordinates cell growth, autophagy and metabolism. *Nat Cell Biol,* 13**,** 1016-23.

MILAN, D., JEON, J. T., LOOFT, C., AMARGER, V., ROBIC, A., THELANDER, M., ROGEL-GAILLARD, C., PAUL, S., IANNUCCELLI, N., RASK, L., RONNE, H., LUNDSTROM, K., REINSCH, N., GELLIN, J., KALM, E., ROY, P. L., CHARDON, P. & ANDERSSON, L. 2000. A mutation in PRKAG3 associated with excess glycogen content in pig skeletal muscle. *Science,* 288**,** 1248-51.

MINOKOSHI, Y., ALQUIER, T., FURUKAWA, N., KIM, Y. B., LEE, A., XUE, B., MU, J., FOUFELLE, F., FERRE, P., BIRNBAUM, M. J., STUCK, B. J. & KAHN, B. B. 2004. AMP-kinase regulates food intake by responding to hormonal and nutrient signals in the hypothalamus. *Nature,* 428**,** 569-74.

MINOKOSHI, Y., KIM, Y. B., PERONI, O. D., FRYER, L. G., MULLER, C., CARLING, D. & KAHN, B. B. 2002. Leptin stimulates fatty-acid oxidation by activating AMP-activated protein kinase. *Nature,* 415**,** 339-43.

MONTAGUE, C. T., FAROOQI, I. S., WHITEHEAD, J. P., SOOS, M. A., RAU, H., WAREHAM, N. J., SEWTER, C. P., DIGBY, J. E., MOHAMMED, S. N., HURST, J. A., CHEETHAM, C. H., EARLEY, A. R., BARNETT, A. H., PRINS, J. B. & O'RAHILLY, S. 1997. Congenital leptin deficiency is associated with severe early-onset obesity in humans. *Nature,* 387**,** 903-8.

MORTON, G. J., CUMMINGS, D. E., BASKIN, D. G., BARSH, G. S. & SCHWARTZ, M. W. 2006. Central nervous system control of food intake and body weight. *Nature,* 443**,** 289-95.

MOTA, M., BANINI, B. A., CAZANAVE, S. C. & SANYAL, A. J. 2016. Molecular mechanisms of lipotoxicity and glucotoxicity in nonalcoholic fatty liver disease. *Metabolism,* 65**,** 1049-61.

MOTTILLO, E. P., DESJARDINS, E. M., CRANE, J. D., SMITH, B. K., GREEN, A. E., DUCOMMUN, S., HENRIKSEN, T. I., REBALKA, I. A., RAZI, A., SAKAMOTO, K., SCHEELE, C., KEMP, B. E., HAWKE, T. J., ORTEGA, J., GRANNEMAN, J. G. & STEINBERG, G. R. 2016. Lack of Adipocyte AMPK Exacerbates Insulin Resistance and Hepatic Steatosis through Brown and Beige Adipose Tissue Function. *Cell Metab,* 24**,** 118-29.

MURPHY, R. T., MOGENSEN, J., MCGARRY, K., BAHL, A., EVANS, A., OSMAN, E., SYRRIS, P., GORMAN, G., FARRELL, M., HOLTON, J. L., HANNA, M. G., HUGHES, S., ELLIOTT, P. M., MACRAE, C. A. & MCKENNA, W. J. 2005. Adenosine monophosphate-activated protein kinase disease mimicks

hypertrophic cardiomyopathy and Wolff-Parkinson-White syndrome: natural history. *J Am Coll Cardiol,* 45**,** 922-30.

MYERS, R. W., GUAN, H. P., EHRHART, J., PETROV, A., PRAHALADA, S., TOZZO, E., YANG, X., KURTZ, M. M., TRUJILLO, M., GONZALEZ TROTTER, D., FENG, D., XU, S., EIERMANN, G., HOLAHAN, M. A., RUBINS, D., CONARELLO, S., NIU, X., SOUZA, S. C., MILLER, C., LIU, J., LU, K., FENG, W., LI, Y., PAINTER, R. E., MILLIGAN, J. A., HE, H., LIU, F., OGAWA, A., WISNIEWSKI, D., ROHM, R. J., WANG, L., BUNZEL, M., QIAN, Y., ZHU, W., WANG, H., BENNET, B., LAFRANCO SCHEUCH, L., FERNANDEZ, G. E., LI, C., KLIMAS, M., ZHOU, G., VAN HEEK, M., BIFTU, T., WEBER, A., KELLEY, D. E., THORNBERRY, N., ERION, M. D., KEMP, D. M. & SEBHAT, I. K. 2017. Systemic pan-AMPK activator MK-8722 improves glucose homeostasis but induces cardiac hypertrophy. *Science,* 357**,** 507-511.

NADASDY, T., LASZIK, Z., LAJOIE, G., BLICK, K. E., WHEELER, D. E. & SILVA, F. G. 1995. Proliferative activity of cyst epithelium in human renal cystic diseases. *J Am Soc Nephrol,* 5**,** 1462-8.

NAGATA, D., MOGI, M. & WALSH, K. 2003. AMP-activated protein kinase (AMPK) signaling in endothelial cells is essential for angiogenesis in response to hypoxic stress. *J Biol Chem,* 278**,** 31000-6.

NARKAR, V. A., DOWNES, M., YU, R. T., EMBLER, E., WANG, Y. X., BANAYO, E., MIHAYLOVA, M. M., NELSON, M. C., ZOU, Y., JUGUILON, H., KANG, H., SHAW, R. J. & EVANS, R. M. 2008. AMPK and PPARdelta agonists are exercise mimetics. *Cell,* 134**,** 405-15.

NEDERGAARD, J., MATTHIAS, A., GOLOZOUBOVA, V., JACOBSSON, A. & CANNON, B. 1999. UCP1: the original uncoupling protein--and perhaps the only one? New perspectives on UCP1, UCP2, and UCP3 in the light of the bioenergetics of the UCP1-ablated mice. *J Bioenerg Biomembr,* 31**,** 475-91.

NEILSON, E. G. 2006. Mechanisms of disease: Fibroblasts--a new look at an old problem. *Nat Clin Pract Nephrol,* 2**,** 101-8.

NICHOLLS, D. G. 2001. A history of UCP1. *Biochem Soc Trans,* 29**,** 751-5.

NOV, O., SHAPIRO, H., OVADIA, H., TARNOVSCKI, T., DVIR, I., SHEMESH, E., KOVSAN, J., SHELEF, I., CARMI, Y., VORONOV, E., APTE, R. N., LEWIS, E., HAIM, Y., KONRAD, D., BASHAN, N. & RUDICH, A. 2013. Interleukin-1beta regulates fat-liver crosstalk in obesity by auto-paracrine modulation of adipose tissue inflammation and expandability. *PLoS One,* 8**,** e53626.

OAKHILL, J. S., SCOTT, J. W. & KEMP, B. E. 2012. AMPK functions as an adenylate charge-regulated protein kinase. *Trends Endocrinol Metab,* 23**,** 125-32.

OHNO, H., SHINODA, K., OHYAMA, K., SHARP, L. Z. & KAJIMURA, S. 2013. EHMT1 controls brown adipose cell fate and thermogenesis through the PRDM16 complex. *Nature,* 504**,** 163-7.

OLIVEIRA, S. M., EHTISHAM, J., REDWOOD, C. S., OSTMAN-SMITH, I., BLAIR, E. M. & WATKINS, H. 2003. Mutation analysis of AMP-activated protein kinase subunits in inherited cardiomyopathies: implications for kinase function and disease pathogenesis. *J Mol Cell Cardiol,* 35**,** 1251-5.

OLIVEIRA, S. M., ZHANG, Y. H., SOLIS, R. S., ISACKSON, H., BELLAHCENE, M., YAVARI, A., PINTER, K., DAVIES, J. K., GE, Y., ASHRAFIAN, H., WALKER, J. W., CARLING, D., WATKINS, H., CASADEI, B. & REDWOOD, C. AMP-activated protein kinase phosphorylates cardiac troponin I and alters contractility of murine ventricular myocytes. *Circ Res,* 110**,** 1192-201.

ORCI, L. & UNGER, R. H. 1975. Functional subdivision of islets of Langerhans and possible role of D cells. *Lancet,* 2**,** 1243-4.

OWEN, M. R., DORAN, E. & HALESTRAP, A. P. 2000. Evidence that metformin exerts its anti-diabetic effects through inhibition of complex 1 of the mitochondrial respiratory chain. *Biochem J,* 348 Pt 3**,** 607-14.

PANNABECKER, T. L. 2012. Structure and function of the thin limbs of the loop of Henle. *Compr Physiol,* 2**,** 2063-86.

PAZ-FILHO, G., MASTRONARDI, C., DELIBASI, T., WONG, M. L. & LICINIO, J. 2010. Congenital leptin deficiency: diagnosis and effects of leptin replacement therapy. *Arq Bras Endocrinol Metabol,* 54**,** 690-7.

PEREA, A., CLEMENTE, F., MARTINELL, J., VILLANUEVA-PENACARRILLO, M. L. & VALVERDE, I. 1995. Physiological effect of glucagon in human isolated adipocytes. *Horm Metab Res,* 27**,** 372-5.

PERSEGHIN, G., PETERSEN, K. & SHULMAN, G. I. 2003. Cellular mechanism of insulin resistance: potential links with inflammation. *Int J Obes Relat Metab Disord,* 27 Suppl 3**,** S6-11.

PICARD, F., KURTEV, M., CHUNG, N., TOPARK-NGARM, A., SENAWONG, T., MACHADO DE OLIVEIRA, R., LEID, M., MCBURNEY, M. W. & GUARENTE, L. 2004. Sirt1 promotes fat mobilization in white adipocytes by repressing PPAR-gamma. *Nature,* 429**,** 771-6.

PINHEIRO, I., MARGUERON, R., SHUKEIR, N., EISOLD, M., FRITZSCH, C., RICHTER, F. M., MITTLER, G., GENOUD, C., GOYAMA, S., KUROKAWA, M., SON, J., REINBERG, D., LACHNER, M. & JENUWEIN, T. 2012. Prdm3 and Prdm16 are H3K9me1 methyltransferases required for mammalian heterochromatin integrity. *Cell,* 150**,** 948-60.

POLLAK, N., DOLLE, C. & ZIEGLER, M. 2007. The power to reduce: pyridine nucleotides--small molecules with a multitude of functions. *Biochem J,* 402**,** 205-18.

RAHIER, J., GOEBBELS, R. M. & HENQUIN, J. C. 1983. Cellular composition of the human diabetic pancreas. *Diabetologia,* 24**,** 366-71.

REAVEN, G. M. 1988. Banting lecture 1988. Role of insulin resistance in human disease. *Diabetes,* 37**,** 1595-607.

REDINGER, R. N. 2007. The pathophysiology of obesity and its clinical manifestations. *Gastroenterol Hepatol (N Y),* 3**,** 856-63.

RICH, P. R. & MARECHAL, A. 2010. The mitochondrial respiratory chain. *Essays Biochem,* 47**,** 1-23.

RINELLA, M. E. 2015. Nonalcoholic fatty liver disease: a systematic review. *JAMA,* 313**,** 2263-73.

ROBERTS, C. K., BARNARD, R. J., SINDHU, R. K., JURCZAK, M., EHDAIE, A. & VAZIRI, N. D. 2005. A high-fat, refined-carbohydrate diet induces endothelial dysfunction and oxidant/antioxidant imbalance and depresses NOS protein expression. *J Appl Physiol (1985),* 98**,** 203-10.

ROBINSON, E. & CHRISTIANSEN, P. 2014. The changing face of obesity: exposure to and acceptance of obesity. *Obesity (Silver Spring),* 22**,** 1380-6.

RODGERS, J. T., LERIN, C., HAAS, W., GYGI, S. P., SPIEGELMAN, B. M. & PUIGSERVER, P. 2005. Nutrient control of glucose homeostasis through a complex of PGC-1alpha and SIRT1. *Nature,* 434**,** 113-8.

RODRIGUEZ-DIAZ, R., ABDULREDA, M. H., FORMOSO, A. L., GANS, I., RICORDI, C., BERGGREN, P. O. & CAICEDO, A. 2011. Innervation patterns of autonomic axons in the human endocrine pancreas. *Cell Metab,* 14**,** 45-54.

ROSENBAUM, M. & LEIBEL, R. L. 2010. Adaptive thermogenesis in humans. *Int J Obes (Lond),* 34 Suppl 1**,** S47-55.

ROSSO, R. & LUCIONI, M. 2006. Normal and neoplastic cells of brown adipose tissue express the adhesion molecule CD31. *Arch Pathol Lab Med,* 130**,** 480-2.

ROWE, I., CHIARAVALLI, M., MANNELLA, V., ULISSE, V., QUILICI, G., PEMA, M., SONG, X. W., XU, H., MARI, S., QIAN, F., PEI, Y., MUSCO, G. & BOLETTA, A. 2013. Defective glucose metabolism in polycystic kidney disease identifies a new therapeutic strategy. *Nat Med,* 19**,** 488-93.

ROWLAND, L. A., BAL, N. C. & PERIASAMY, M. 2015. The role of skeletal-muscle-based thermogenic mechanisms in vertebrate endothermy. *Biol Rev Camb Philos Soc,* 90**,** 1279-97.

RUI, L. 2014. Energy metabolism in the liver. *Compr Physiol,* 4**,** 177-97.

RUSSO, G. T., GIORDA, C. B., CERCONE, S., NICOLUCCI, A., CUCINOTTA, D. & BETADECLINE STUDY, G. 2014. Factors associated with beta-cell dysfunction in type 2 diabetes: the BETADECLINE study. *PLoS One,* 9**,** e109702.

RUTTER, G. A., PULLEN, T. J., HODSON, D. J. & MARTINEZ-SANCHEZ, A. 2015. Pancreatic beta-cell identity, glucose sensing and the control of insulin secretion. *Biochem J,* 466**,** 203-18.

SAKAMOTO, K. & HOLMAN, G. D. 2008. Emerging role for AS160/TBC1D4 and TBC1D1 in the regulation of GLUT4 traffic. *Am J Physiol Endocrinol Metab,* 295**,** E29-37.

SANCHEZ-GURMACHES, J. & GUERTIN, D. A. 2014. Adipocyte lineages: tracing back the origins of fat. *Biochim Biophys Acta,* 1842**,** 340-51.

SAVAGE, J. S., FISHER, J. O. & BIRCH, L. L. 2007. Parental influence on eating behavior: conception to adolescence. *J Law Med Ethics,* 35**,** 22-34.

SAVASTANO, D. M. & COVASA, M. 2005. Adaptation to a high-fat diet leads to hyperphagia and diminished sensitivity to cholecystokinin in rats. *J Nutr,* 135**,** 1953-9.

SCARPACE, P. J., MATHENY, M., TUMER, N., CHENG, K. Y. & ZHANG, Y. 2005. Leptin resistance exacerbates diet-induced obesity and is associated with diminished maximal leptin signalling capacity in rats. *Diabetologia,* 48**,** 1075-83.

SCHNEIDER, H., SCHUBERT, K. M., BLODOW, S., KREUTZ, C. P., ERDOGMUS, S., WIEDENMANN, M., QIU, J., FEY, T., RUTH, P., LUBOMIROV, L. T., PFITZER, G., MEDEROS, Y. S. M., HARDIE, D. G., GUDERMANN, T. & POHL, U. 2015. AMPK Dilates Resistance Arteries via Activation of SERCA and BKCa Channels in Smooth Muscle. *Hypertension,* 66**,** 108-16.

SCHONKE, M., MYERS, M. G., JR., ZIERATH, J. R. & BJORNHOLM, M. 2015. Skeletal muscle AMP-activated protein kinase gamma1(H151R) overexpression enhances whole body energy homeostasis and insulin sensitivity. *Am J Physiol Endocrinol Metab,* 309**,** E679-90.

SCHUG, T. T., XU, Q., GAO, H., PERES-DA-SILVA, A., DRAPER, D. W., FESSLER, M. B., PURUSHOTHAM, A. & LI, X. 2010. Myeloid deletion of SIRT1 induces inflammatory signaling in response to environmental stress. *Mol Cell Biol,* 30**,** 4712-21.

SCLAFANI, A. & SPRINGER, D. 1976. Dietary obesity in adult rats: similarities to hypothalamic and human obesity syndromes. *Physiol Behav,* 17**,** 461-71.

SCOTT, J. W., LING, N., ISSA, S. M., DITE, T. A., O'BRIEN, M. T., CHEN, Z. P., GALIC, S., LANGENDORF, C. G., STEINBERG, G. R., KEMP, B. E. & OAKHILL, J. S. 2014. Small molecule drug A-769662 and AMP synergistically activate naive AMPK independent of upstream kinase signaling. *Chem Biol,* 21**,** 619-27.

SEALE, P., BJORK, B., YANG, W., KAJIMURA, S., CHIN, S., KUANG, S., SCIME, A., DEVARAKONDA, S., CONROE, H. M., ERDJUMENT-BROMAGE, H., TEMPST, P., RUDNICKI, M. A., BEIER, D. R. & SPIEGELMAN, B. M. 2008. PRDM16 controls a brown fat/skeletal muscle switch. *Nature,* 454**,** 961-7.

SEALE, P., CONROE, H. M., ESTALL, J., KAJIMURA, S., FRONTINI, A., ISHIBASHI, J., COHEN, P., CINTI, S. & SPIEGELMAN, B. M. 2011. Prdm16 determines the thermogenic program of subcutaneous white adipose tissue in mice. *J Clin Invest,* 121**,** 96-105.

SHABALINA, I. G., PETROVIC, N., DE JONG, J. M., KALINOVICH, A. V., CANNON, B. & NEDERGAARD, J. 2013. UCP1 in brite/beige adipose tissue mitochondria is functionally thermogenic. *Cell Rep,* 5**,** 1196-203.

SHARMA, S., HRYHORCZUK, C. & FULTON, S. 2012. Progressive-ratio responding for palatable high-fat and high-sugar food in mice. *J Vis Exp***,** e3754.

SHIMOMURA, K., GALVANOVSKIS, J., GOLDSWORTHY, M., HUGILL, A., KAIZAK, S., LEE, A., MEADOWS, N., QUWAILID, M. M., RYDSTROM, J., TEBOUL, L., ASHCROFT, F. & COX, R. D. 2009. Insulin secretion from beta-cells is affected by deletion of nicotinamide nucleotide transhydrogenase. *Methods Enzymol,* 457**,** 451-80.

SHYH-CHANG, N., DALEY, G. Q. & CANTLEY, L. C. 2013. Stem cell metabolism in tissue development and aging. *Development,* 140**,** 2535-47.

SIM, A. T. & HARDIE, D. G. 1988. The low activity of acetyl-CoA carboxylase in basal and glucagon-stimulated hepatocytes is due to phosphorylation by the AMP-activated protein kinase and not cyclic AMP-dependent protein kinase. *FEBS Lett,* 233**,** 294-8.

SMITH, J. L., PATIL, P. B. & FISHER, J. S. 2005. AICAR and hyperosmotic stress increase insulin-stimulated glucose transport. *J Appl Physiol (1985),* 99**,** 877-83.

SOLTOFF, S. P. 1986. ATP and the regulation of renal cell function. *Annu Rev Physiol,* 48**,** 9-31.
SPEAKMAN, J. R. 2013. Measuring energy metabolism in the mouse - theoretical, practical, and analytical considerations. *Front Physiol,* 4**,** 34.
STAPLETON, D., MITCHELHILL, K. I., GAO, G., WIDMER, J., MICHELL, B. J., TEH, T., HOUSE, C. M., FERNANDEZ, C. S., COX, T., WITTERS, L. A. & KEMP, B. E. 1996. Mammalian AMP-activated protein kinase subfamily. *J Biol Chem,* 271**,** 611-4.
STEINBERG, G. R. & KEMP, B. E. 2009. AMPK in Health and Disease. *Physiol Rev,* 89**,** 1025-78.
STEINBERG, G. R., O'NEILL, H. M., DZAMKO, N. L., GALIC, S., NAIM, T., KOOPMAN, R., JORGENSEN, S. B., HONEYMAN, J., HEWITT, K., CHEN, Z. P., SCHERTZER, J. D., SCOTT, J. W., KOENTGEN, F., LYNCH, G. S., WATT, M. J., VAN DENDEREN, B. J., CAMPBELL, D. J. & KEMP, B. E. Whole body deletion of AMP-activated protein kinase {beta}2 reduces muscle AMPK activity and exercise capacity. *J Biol Chem,* 285**,** 37198-209.
STOHS, S. J. & BADMAEV, V. 2016. A Review of Natural Stimulant and Non-stimulant Thermogenic Agents. *Phytother Res,* 30**,** 732-40.
STRUTZ, F., ZEISBERG, M., HEMMERLEIN, B., SATTLER, B., HUMMEL, K., BECKER, V. & MULLER, G. A. 2000. Basic fibroblast growth factor expression is increased in human renal fibrogenesis and may mediate autocrine fibroblast proliferation. *Kidney Int,* 57**,** 1521-38.
SUBRAMANYA, A. R. & ELLISON, D. H. 2014. Distal convoluted tubule. *Clin J Am Soc Nephrol,* 9**,** 2147-63.
SUDHOF, T. C. & ROTHMAN, J. E. 2009. Membrane fusion: grappling with SNARE and SM proteins. *Science,* 323**,** 474-7.
TATEYA, S., RIZZO-DE LEON, N., HANDA, P., CHENG, A. M., MORGAN-STEVENSON, V., OGIMOTO, K., KANTER, J. E., BORNFELDT, K. E., DAUM, G., CLOWES, A. W., CHAIT, A. & KIM, F. 2013. VASP increases hepatic fatty acid oxidation by activating AMPK in mice. *Diabetes,* 62**,** 1913-22.
THORNTON, C., SNOWDEN, M. A. & CARLING, D. 1998. Identification of a novel AMP-activated protein kinase beta subunit isoform that is highly expressed in skeletal muscle. *J Biol Chem,* 273**,** 12443-50.
TONTONOZ, P., HU, E. & SPIEGELMAN, B. M. 1994. Stimulation of adipogenesis in fibroblasts by PPAR gamma 2, a lipid-activated transcription factor. *Cell,* 79**,** 1147-56.
TORRES, V. E. & HARRIS, P. C. 2006. Mechanisms of Disease: autosomal dominant and recessive polycystic kidney diseases. *Nat Clin Pract Nephrol,* 2**,** 40-55; quiz 55.
TSCHOP, M. H., SPEAKMAN, J. R., ARCH, J. R., AUWERX, J., BRUNING, J. C., CHAN, L., ECKEL, R. H., FARESE, R. V., JR., GALGANI, J. E., HAMBLY, C., HERMAN, M. A., HORVATH, T. L., KAHN, B. B., KOZMA, S. C., MARATOS-FLIER, E., MULLER, T. D., MUNZBERG, H., PFLUGER, P. T., PLUM, L., REITMAN, M. L., RAHMOUNI, K., SHULMAN, G. I., THOMAS, G., KAHN, C. R. & RAVUSSIN, E. 2011. A guide to analysis of mouse energy metabolism. *Nat Methods,* 9**,** 57-63.
UKROPEC, J., ANUNCIADO, R. P., RAVUSSIN, Y., HULVER, M. W. & KOZAK, L. P. 2006. UCP1-independent thermogenesis in white adipose tissue of cold-acclimated Ucp1-/- mice. *J Biol Chem,* 281**,** 31894-908.
VAN GAAL, L. F., RISSANEN, A. M., SCHEEN, A. J., ZIEGLER, O., ROSSNER, S. & GROUP, R. I.-E. S. 2005. Effects of the cannabinoid-1 receptor blocker rimonabant on weight reduction and cardiovascular risk factors in overweight patients: 1-year experience from the RIO-Europe study. *Lancet,* 365**,** 1389-97.
VARELA, L. & HORVATH, T. L. 2012. Leptin and insulin pathways in POMC and AgRP neurons that modulate energy balance and glucose homeostasis. *EMBO Rep,* 13**,** 1079-86.
VAZIRI, H., DESSAIN, S. K., NG EATON, E., IMAI, S. I., FRYE, R. A., PANDITA, T. K., GUARENTE, L. & WEINBERG, R. A. 2001. hSIR2(SIRT1) functions as an NAD-dependent p53 deacetylase. *Cell,* 107**,** 149-59.

VELASCO, G., GEELEN, M. J. & GUZMAN, M. 1997. Control of hepatic fatty acid oxidation by 5'-AMP-activated protein kinase involves a malonyl-CoA-dependent and a malonyl-CoA-independent mechanism. *Arch Biochem Biophys,* 337**,** 169-75.

VICKERS, S. P., JACKSON, H. C. & CHEETHAM, S. C. 2011. The utility of animal models to evaluate novel anti-obesity agents. *Br J Pharmacol,* 164**,** 1248-62.

VIOLLET, B., ANDREELLI, F., JORGENSEN, S. B., PERRIN, C., GELOEN, A., FLAMEZ, D., MU, J., LENZNER, C., BAUD, O., BENNOUN, M., GOMAS, E., NICOLAS, G., WOJTASZEWSKI, J. F., KAHN, A., CARLING, D., SCHUIT, F. C., BIRNBAUM, M. J., RICHTER, E. A., BURCELIN, R. & VAULONT, S. 2003. The AMP-activated protein kinase alpha2 catalytic subunit controls whole-body insulin sensitivity. *J Clin Invest,* 111**,** 91-8.

VIOLLET, B., HORMAN, S., LECLERC, J., LANTIER, L., FORETZ, M., BILLAUD, M., GIRI, S. & ANDREELLI, F. 2010. AMPK inhibition in health and disease. *Crit Rev Biochem Mol Biol,* 45**,** 276-95.

VIRTANEN, K. A., LIDELL, M. E., ORAVA, J., HEGLIND, M., WESTERGREN, R., NIEMI, T., TAITTONEN, M., LAINE, J., SAVISTO, N. J., ENERBACK, S. & NUUTILA, P. 2009. Functional brown adipose tissue in healthy adults. *N Engl J Med,* 360**,** 1518-25.

WAJCHENBERG, B. L. 2000. Subcutaneous and visceral adipose tissue: their relation to the metabolic syndrome. *Endocr Rev,* 21**,** 697-738.

WAJCHENBERG, B. L., GIANNELLA-NETO, D., DA SILVA, M. E. & SANTOS, R. F. 2002. Depot-specific hormonal characteristics of subcutaneous and visceral adipose tissue and their relation to the metabolic syndrome. *Horm Metab Res,* 34**,** 616-21.

WALLACE, D. P. 2011. Cyclic AMP-mediated cyst expansion. *Biochim Biophys Acta,* 1812**,** 1291-300.

WAN, Z., ROOT-MCCAIG, J., CASTELLANI, L., KEMP, B. E., STEINBERG, G. R. & WRIGHT, D. C. 2014. Evidence for the role of AMPK in regulating PGC-1 alpha expression and mitochondrial proteins in mouse epididymal adipose tissue. *Obesity (Silver Spring),* 22**,** 730-8.

WANG, Y. G. & YANG, T. L. 2015. Liraglutide reduces fatty degeneration in hepatic cells via the AMPK/SREBP1 pathway. *Exp Ther Med,* 10**,** 1777-1783.

WANG, Z., GERSTEIN, M. & SNYDER, M. 2009. RNA-Seq: a revolutionary tool for transcriptomics. *Nat Rev Genet,* 10**,** 57-63.

WEISBERG, S. P., MCCANN, D., DESAI, M., ROSENBAUM, M., LEIBEL, R. L. & FERRANTE, A. W., JR. 2003. Obesity is associated with macrophage accumulation in adipose tissue. *J Clin Invest,* 112**,** 1796-808.

WHITE, M. F. 2006. Regulating insulin signaling and beta-cell function through IRS proteins. *Can J Physiol Pharmacol,* 84**,** 725-37.

WILCOX, G. 2005. Insulin and insulin resistance. *Clin Biochem Rev,* 26**,** 19-39.

WILLOWS, R., NAVARATNAM, N., LIMA, A., READ, J. & CARLING, D. 2017a. Effect of different gamma-subunit isoforms on the regulation of AMPK. *Biochem J,* 474**,** 1741-1754.

WILLOWS, R., SANDERS, M. J., XIAO, B., PATEL, B. R., MARTIN, S. R., READ, J., WILSON, J. R., HUBBARD, J., GAMBLIN, S. J. & CARLING, D. 2017b. Phosphorylation of AMPK by upstream kinases is required for activity in mammalian cells. *Biochem J,* 474**,** 3059-3073.

WINDER, W. W., HOLMES, B. F., RUBINK, D. S., JENSEN, E. B., CHEN, M. & HOLLOSZY, J. O. 2000. Activation of AMP-activated protein kinase increases mitochondrial enzymes in skeletal muscle. *J Appl Physiol (1985),* 88**,** 2219-26.

WINGO, S. N., GALLARDO, T. D., AKBAY, E. A., LIANG, M. C., CONTRERAS, C. M., BOREN, T., SHIMAMURA, T., MILLER, D. S., SHARPLESS, N. E., BARDEESY, N., KWIATKOWSKI, D. J., SCHORGE, J. O., WONG, K. K. & CASTRILLON, D. H. 2009. Somatic LKB1 mutations promote cervical cancer progression. *PLoS One,* 4**,** e5137.

WOODS, A., CHEUNG, P. C., SMITH, F. C., DAVISON, M. D., SCOTT, J., BERI, R. K. & CARLING, D. 1996. Characterization of AMP-activated protein kinase beta and gamma subunits. Assembly of the heterotrimeric complex in vitro. *J Biol Chem,* 271**,** 10282-90.

WOODS, A., DICKERSON, K., HEATH, R., HONG, S. P., MOMCILOVIC, M., JOHNSTONE, S. R., CARLSON, M. & CARLING, D. 2005. Ca2+/calmodulin-dependent protein kinase kinase-beta acts upstream of AMP-activated protein kinase in mammalian cells. *Cell Metab,* 2**,** 21-33.

WOODS, A., JOHNSTONE, S. R., DICKERSON, K., LEIPER, F. C., FRYER, L. G., NEUMANN, D., SCHLATTNER, U., WALLIMANN, T., CARLSON, M. & CARLING, D. 2003. LKB1 is the upstream kinase in the AMP-activated protein kinase cascade. *Curr Biol,* 13**,** 2004-8.

WOODS, A., MUNDAY, M. R., SCOTT, J., YANG, X., CARLSON, M. & CARLING, D. 1994. Yeast SNF1 is functionally related to mammalian AMP-activated protein kinase and regulates acetyl-CoA carboxylase in vivo. *J Biol Chem,* 269**,** 19509-15.

WOODS, A., WILLIAMS, J. R., MUCKETT, P. J., MAYER, F. V., LILJEVALD, M., BOHLOOLY, Y. M. & CARLING, D. 2017. Liver-Specific Activation of AMPK Prevents Steatosis on a High-Fructose Diet. *Cell Rep,* 18**,** 3043-3051.

WU, J., BOSTROM, P., SPARKS, L. M., YE, L., CHOI, J. H., GIANG, A. H., KHANDEKAR, M., VIRTANEN, K. A., NUUTILA, P., SCHAART, G., HUANG, K., TU, H., VAN MARKEN LICHTENBELT, W. D., HOEKS, J., ENERBACK, S., SCHRAUWEN, P. & SPIEGELMAN, B. M. 2012. Beige adipocytes are a distinct type of thermogenic fat cell in mouse and human. *Cell,* 150**,** 366-76.

XIAO, B., SANDERS, M. J., CARMENA, D., BRIGHT, N. J., HAIRE, L. F., UNDERWOOD, E., PATEL, B. R., HEATH, R. B., WALKER, P. A., HALLEN, S., GIORDANETTO, F., MARTIN, S. R., CARLING, D. & GAMBLIN, S. J. 2013. Structural basis of AMPK regulation by small molecule activators. *Nat Commun,* 4**,** 3017.

XIAO, B., SANDERS, M. J., UNDERWOOD, E., HEATH, R., MAYER, F. V., CARMENA, D., JING, C., WALKER, P. A., ECCLESTON, J. F., HAIRE, L. F., SAIU, P., HOWELL, S. A., AASLAND, R., MARTIN, S. R., CARLING, D. & GAMBLIN, S. J. 2011. Structure of mammalian AMPK and its regulation by ADP. *Nature,* 472**,** 230-3.

XUE, Y., LIM, S., BRAKENHIELM, E. & CAO, Y. 2010. Adipose angiogenesis: quantitative methods to study microvessel growth, regression and remodeling in vivo. *Nat Protoc,* 5**,** 912-20.

YAMAUCHI, T., KAMON, J., ITO, Y., TSUCHIDA, A., YOKOMIZO, T., KITA, S., SUGIYAMA, T., MIYAGISHI, M., HARA, K., TSUNODA, M., MURAKAMI, K., OHTEKI, T., UCHIDA, S., TAKEKAWA, S., WAKI, H., TSUNO, N. H., SHIBATA, Y., TERAUCHI, Y., FROGUEL, P., TOBE, K., KOYASU, S., TAIRA, K., KITAMURA, T., SHIMIZU, T., NAGAI, R. & KADOWAKI, T. 2003. Cloning of adiponectin receptors that mediate antidiabetic metabolic effects. *Nature,* 423**,** 762-9.

YAN, M., AUDET-WALSH, E., MANTEGHI, S., DUFOUR, C. R., WALKER, B., BABA, M., ST-PIERRE, J., GIGUERE, V. & PAUSE, A. 2016. Chronic AMPK activation via loss of FLCN induces functional beige adipose tissue through PGC-1alpha/ERRalpha. *Genes Dev,* 30**,** 1034-46.

YANG, Q., LIANG, X., SUN, X., ZHANG, L., FU, X., ROGERS, C. J., BERIM, A., ZHANG, S., WANG, S., WANG, B., FORETZ, M., VIOLLET, B., GANG, D. R., RODGERS, B. D., ZHU, M. J. & DU, M. 2016a. AMPK/alpha-Ketoglutarate Axis Dynamically Mediates DNA Demethylation in the Prdm16 Promoter and Brown Adipogenesis. *Cell Metab,* 24**,** 542-554.

YANG, T., HUANG, Y. G., YE, W., HANSEN, P., SCHNERMANN, J. B. & BRIGGS, J. P. 2005. Influence of genetic background and gender on hypertension and renal failure in COX-2-deficient mice. *Am J Physiol Renal Physiol,* 288**,** F1125-32.

YANG, X., MUDGETT, J., BOU-ABOUT, G., CHAMPY, M. F., JACOBS, H., MONASSIER, L., PAVLOVIC, G., SORG, T., HERAULT, Y., PETIT-DEMOULIERE, B., LU, K., FENG, W., WANG, H., MA, L. J., ASKEW, R., ERION, M. D., KELLEY, D. E., MYERS, R. W., LI, C. & GUAN, H. P. 2016b. Physiological Expression of AMPKgamma2RG Mutation Causes Wolff-Parkinson-White Syndrome and Induces Kidney Injury in Mice. *J Biol Chem,* 291**,** 23428-23439.

YANG, Z., WANG, X., HE, Y., QI, L., YU, L., XUE, B. & SHI, H. 2012. The full capacity of AICAR to reduce obesity-induced inflammation and insulin resistance requires myeloid SIRT1. *PLoS One,* 7**,** e49935.

YAVARI, A., STOCKER, C. J., GHAFFARI, S., WARGENT, E. T., STEEPLES, V., CZIBIK, G., PINTER, K., BELLAHCENE, M., WOODS, A., MARTINEZ DE MORENTIN, P. B., CANSELL, C., LAM, B. Y., CHUSTER, A., PETKEVICIUS, K., NGUYEN-TU, M. S., MARTINEZ-SANCHEZ, A., PULLEN, T. J., OLIVER, P. L., STOCKENHUBER, A., NGUYEN, C., LAZDAM, M., O'DOWD, J. F., HARIKUMAR, P., TOTH, M., BEALL, C., KYRIAKOU, T., PARNIS, J., SARMA, D., KATRITSIS, G., WORTMANN, D. D., HARPER, A. R., BROWN, L. A., WILLOWS, R., GANDRA, S., PONCIO, V., DE OLIVEIRA FIGUEIREDO, M. J., QI, N. R., PEIRSON, S. N., MCCRIMMON, R. J., GEREBEN, B., TRETTER, L., FEKETE, C., REDWOOD, C., YEO, G. S., HEISLER, L. K., RUTTER, G. A., SMITH, M. A., WITHERS, D. J., CARLING, D., STERNICK, E. B., ARCH, J. R., CAWTHORNE, M. A., WATKINS, H. & ASHRAFIAN, H. 2016. Chronic Activation of gamma2 AMPK Induces Obesity and Reduces beta Cell Function. *Cell Metab,* 23**,** 821-36.

YE, R., WANG, Q. A., TAO, C., VISHVANATH, L., SHAO, M., MCDONALD, J. G., GUPTA, R. K. & SCHERER, P. E. 2015. Impact of tamoxifen on adipocyte lineage tracing: Inducer of adipogenesis and prolonged nuclear translocation of Cre recombinase. *Mol Metab,* 4**,** 771-8.

ZADRA, G., PHOTOPOULOS, C., TYEKUCHEVA, S., HEIDARI, P., WENG, Q. P., FEDELE, G., LIU, H., SCAGLIA, N., PRIOLO, C., SICINSKA, E., MAHMOOD, U., SIGNORETTI, S., BIRNBERG, N. & LODA, M. 2014. A novel direct activator of AMPK inhibits prostate cancer growth by blocking lipogenesis. *EMBO Mol Med,* 6**,** 519-38.

ZAMBO, V., SIMON-SZABO, L., SZELENYI, P., KERESZTURI, E., BANHEGYI, G. & CSALA, M. 2013. Lipotoxicity in the liver. *World J Hepatol,* 5**,** 550-7.

ZHANG, C. S., LI, M. & LIN, S. C. 2017. Methods to Study Lysosomal AMPK Activation. *Methods Enzymol,* 587**,** 465-480.

ZHANG, C. S. & LIN, S. C. 2016. AMPK Promotes Autophagy by Facilitating Mitochondrial Fission. *Cell Metab,* 23**,** 399-401.

ZHANG, Y., PROENCA, R., MAFFEI, M., BARONE, M., LEOPOLD, L. & FRIEDMAN, J. M. 1994. Positional cloning of the mouse obese gene and its human homologue. *Nature,* 372**,** 425-32.

ZIAUDDEEN, H., FAROOQI, I. S. & FLETCHER, P. C. 2012. Obesity and the brain: how convincing is the addiction model? *Nat Rev Neurosci,* 13**,** 279-86.

ZORDOKY, B. N., NAGENDRAN, J., PULINILKUNNIL, T., KIENESBERGER, P. C., MASSON, G., WALLER, T. J., KEMP, B. E., STEINBERG, G. R. & DYCK, J. R. 2014. AMPK-dependent inhibitory phosphorylation of ACC is not essential for maintaining myocardial fatty acid oxidation. *Circ Res,* 115**,** 518-24.

ZOU, L., SHEN, M., ARAD, M., HE, H., LOFGREN, B., INGWALL, J. S., SEIDMAN, C. E., SEIDMAN, J. G. & TIAN, R. 2005. N488I mutation of the gamma2-subunit results in bidirectional changes in AMP-activated protein kinase activity. *Circ Res,* 97**,** 323-8.

# 6 APPENDICES

## 6.1 RNA Sequencing Extended Data

***Table 6.1***

*List of genes significantly upregulated in WATsc of D316A-Tg HFD-fed mice relative to WT-Tg. Data are presented as Log2FC over WT-Tg with calculated fold change and an adjusted p value <0.05. N=6, 6*

| Gene Name | Symbol | Fold Change | padj | Gene ID (Ensembl) |
|---|---|---|---|---|
| **unspecified** | | 194.38 | 3.04E-10 | ENSMUSG00000087410 |
| **osteocrin** | Ostn | 126.34 | 1.09E-11 | ENSMUSG00000052276 |

| | | | | |
|---|---|---|---|---|
| **ankyrin repeat and SOCS box-containing 14** | Asb14 | 126.32 | 7.25E-10 | ENSMUSG00000021898 |
| **outer dense fiber of sperm tails 3-like 2** | Odf3l2 | 105.60 | 9.77E-08 | ENSMUSG00000035963 |
| **myosin light chain kinase family, member 4** | Mylk4 | 102.15 | 5.95E-11 | ENSMUSG00000044951 |
| **unspecified** | | 99.02 | 1.75E-10 | ENSMUSG00000087090 |
| **actinin alpha 3** | Actn3 | 95.07 | 8.47E-12 | ENSMUSG00000006457 |
| **myosin binding protein C, fast-type** | Mybpc2 | 92.13 | 2.86E-11 | ENSMUSG00000038670 |
| **phosphoglycerate mutase 2** | Pgam2 | 80.12 | 1.61E-10 | ENSMUSG00000020475 |
| **adenosine monophosphate deaminase 1** | Ampd1 | 78.45 | 1.61E-10 | ENSMUSG00000070385 |
| **myosin, heavy polypeptide 4, skeletal muscle** | Myh4 | 78.39 | 3.92E-09 | ENSMUSG00000057003 |
| **calcium-sensing receptor** | Casr | 77.70 | 3.82E-09 | ENSMUSG00000051980 |
| **ATPase, Ca++ transporting, cardiac muscle, fast twitch 1** | Atp2a1 | 77.61 | 7.25E-10 | ENSMUSG00000030730 |
| **creatine kinase, muscle** | Ckm | 76.76 | 2.25E-10 | ENSMUSG00000030399 |
| **kyphoscoliosis peptidase** | Ky | 75.61 | 4.19E-10 | ENSMUSG00000035606 |
| **ankyrin repeat and SOCS box-containing 11** | Asb11 | 68.73 | 6.82E-09 | ENSMUSG00000031382 |
| **tripartite motif-containing 63** | Trim63 | 64.56 | 2.07E-09 | ENSMUSG00000028834 |
| **myozenin 1** | Myoz1 | 62.74 | 3.05E-09 | ENSMUSG00000068697 |

| | | | | |
|---|---|---|---|---|
| **unspecified** | | 60.94 | 4.58E-08 | ENSMUSG00000010492 |
| **myomesin 2** | Myom2 | 60.47 | 5.05E-13 | ENSMUSG00000031461 |
| **tripartite motif-containing 54** | Trim54 | 59.69 | 1.92E-08 | ENSMUSG00000062077 |
| **troponin T3, skeletal, fast** | Tnnt3 | 54.89 | 1.62E-08 | ENSMUSG00000061723 |
| **obscurin, cytoskeletal calmodulin and titin-interacting RhoGEF** | Obscn | 54.29 | 5.27E-09 | ENSMUSG00000061462 |
| **titin** | Ttn | 53.13 | 5.89E-09 | ENSMUSG00000051747 |
| **myosin, light polypeptide kinase 2, skeletal muscle** | Mylk2 | 51.31 | 8.46E-09 | ENSMUSG00000027470 |
| **myopalladin** | Mypn | 51.18 | 3.04E-10 | ENSMUSG00000020067 |
| **unspecified** | | 50.10 | 4.89E-08 | ENSMUSG00000043795 |
| **troponin C2, fast** | Tnnc2 | 49.44 | 1.83E-08 | ENSMUSG00000017300 |
| **nebulin-related anchoring protein** | Nrap | 49.04 | 1.19E-09 | ENSMUSG00000049134 |
| **kelch-like 31** | Klhl31 | 48.42 | 2.39E-08 | ENSMUSG00000044938 |
| **muscle glycogen phosphorylase** | Pygm | 48.15 | 9.63E-11 | ENSMUSG00000032648 |
| **myosin light chain, phosphorylatable, fast skeletal muscle** | Mylpf | 45.98 | 3.30E-10 | ENSMUSG00000030672 |
| **troponin I, skeletal, fast 2** | Tnni2 | 45.32 | 3.26E-08 | ENSMUSG00000031097 |
| **serine protease inhibitor, Kazal type-like** | Spinkl | 44.84 | 4.28E-05 | ENSMUSG00000053729 |

| | | | | |
|---|---|---|---|---|
| **anoctamin 5** | Ano5 | 44.08 | 5.71E-08 | ENSMUSG00000055489 |
| **calcium channel, voltage-dependent, L type, alpha 1S subunit** | Cacna1s | 43.47 | 7.47E-09 | ENSMUSG00000026407 |
| **histidine rich calcium binding protein** | Hrc | 42.79 | 1.99E-07 | ENSMUSG00000038239 |
| **creatine kinase, mitochondrial 2** | Ckmt2 | 42.68 | 3.39E-07 | ENSMUSG00000021622 |
| **hedgehog acyltransferase-like** | Hhatl | 42.64 | 2.08E-07 | ENSMUSG00000032523 |
| **transmembrane protein 233** | Tmem233 | 42.16 | 5.52E-07 | ENSMUSG00000079278 |
| **calcium channel, voltage-dependent, gamma subunit 1** | Cacng1 | 39.31 | 2.53E-09 | ENSMUSG00000020722 |
| **parvalbumin** | Pvalb | 38.95 | 1.11E-07 | ENSMUSG00000005716 |
| **dual specificity phosphatase and pro isomerase domain containing 1** | Dupd1 | 38.79 | 3.25E-06 | ENSMUSG00000063821 |
| **ribosomal protein L3-like** | Rpl3l | 37.59 | 1.93E-07 | ENSMUSG00000002500 |
| **RIKEN cDNA 2310002L09 gene** | 2310002L09Rik | 37.43 | 2.08E-07 | ENSMUSG00000028396 |
| **dehydrogenase/reductase (SDR family) member 7C** | Dhrs7c | 36.70 | 8.80E-08 | ENSMUSG00000033044 |
| **calcium channel, voltage-dependent, gamma subunit 6** | Cacng6 | 36.49 | 9.30E-07 | ENSMUSG00000078815 |
| **eukaryotic translation elongation factor 1 alpha 2** | Eef1a2 | 36.34 | 1.85E-07 | ENSMUSG00000016349 |

| | | | | |
|---|---|---|---|---|
| **myotilin** | Myot | 34.66 | 1.03E-06 | ENSMUSG00000024471 |
| **tripartite motif-containing 55** | Trim55 | 32.77 | 8.08E-06 | ENSMUSG00000060913 |
| **unspecified** | | 32.73 | 9.45E-07 | ENSMUSG00000085888 |
| **actin-binding Rho activating protein** | Abra | 32.67 | 2.67E-06 | ENSMUSG00000042895 |
| **chloride channel, voltage-sensitive 1** | Clcn1 | 32.50 | 6.75E-08 | ENSMUSG00000029862 |
| **SH3-binding domain glutamic acid-rich protein** | Sh3bgr | 32.42 | 5.36E-08 | ENSMUSG00000040666 |
| **phospholipase C, delta 4** | Plcd4 | 32.39 | 6.06E-07 | ENSMUSG00000026173 |
| **immunoglobulin-like and fibronectin type III domain containing 1** | Igfn1 | 31.26 | 9.72E-09 | ENSMUSG00000051985 |
| **titin-cap** | Tcap | 30.80 | 6.38E-07 | ENSMUSG00000007877 |
| **ATPase type 13A5** | Atp13a5 | 30.59 | 8.97E-07 | ENSMUSG00000048939 |
| **protein phosphatase 1, regulatory subunit 27** | Ppp1r27 | 30.15 | 1.21E-06 | ENSMUSG00000025129 |
| **kelch-like 40** | Klhl40 | 29.70 | 1.35E-06 | ENSMUSG00000074001 |
| **RNA binding protein, fox-1 homolog (C. elegans) 1** | Rbfox1 | 29.63 | 1.60E-07 | ENSMUSG00000008658 |
| **collagen, type XXIV, alpha 1** | Col24a1 | 29.57 | 3.54E-10 | ENSMUSG00000028197 |
| **enolase 3, beta muscle** | Eno3 | 29.47 | 9.02E-12 | ENSMUSG00000060600 |
| **aquaporin 4** | Aqp4 | 28.54 | 1.25E-09 | ENSMUSG00000024411 |

| | | | | |
|---|---|---|---|---|
| **synaptophysin-like 2** | Sypl2 | 27.81 | 3.10E-07 | ENSMUSG00000027887 |
| **leucine rich repeat and Ig domain containing 3** | Lingo3 | 27.65 | 5.69E-06 | ENSMUSG00000051067 |
| **myoregulin** | Mrln | 26.96 | 7.82E-08 | ENSMUSG00000019933 |
| **unspecified** | | 26.15 | 3.03E-05 | ENSMUSG00000084169 |
| **apolipoprotein B mRNA editing enzyme, catalytic polypeptide 2** | Apobec2 | 25.98 | 1.12E-06 | ENSMUSG00000040694 |
| **potassium voltage-gated channel, subfamily F, member 1** | Kcnf1 | 25.93 | 4.50E-05 | ENSMUSG00000051726 |
| **heparan sulfate (glucosamine) 3-O-sulfotransferase 5** | Hs3st5 | 25.88 | 6.46E-06 | ENSMUSG00000044499 |
| **uncharacterized LOC102634333** | LOC102634333 | 25.79 | 3.67E-06 | ENSMUSG00000090066 |
| **unspecified** | | 25.71 | 4.08E-06 | ENSMUSG00000085348 |
| **potassium inwardly rectifying channel, subfamily J, member 11** | Kcnj11 | 25.68 | 7.35E-07 | ENSMUSG00000096146 |
| **sarcoglycan, alpha (dystrophin-associated glycoprotein)** | Sgca | 25.27 | 3.37E-06 | ENSMUSG00000001508 |
| **ryanodine receptor 1, skeletal muscle** | Ryr1 | 24.67 | 1.57E-06 | ENSMUSG00000030592 |
| **protein phosphatase 1, regulatory (inhibitor) subunit 14c** | Ppp1r14c | 24.17 | 5.85E-08 | ENSMUSG00000040653 |
| **actin, alpha 1, skeletal muscle** | Acta1 | 23.11 | 3.76E-06 | ENSMUSG00000031972 |

| | | | | |
|---|---|---|---|---|
| **kelch-like 41** | Klhl41 | 23.11 | 2.35E-07 | ENSMUSG00000075307 |
| **nicotinamide riboside kinase 2** | Nmrk2 | 22.59 | 0.0001887 | ENSMUSG00000004939 |
| **leucine rich repeat containing 38** | Lrrc38 | 22.45 | 1.59E-05 | ENSMUSG00000028584 |
| **single-minded homolog 2 (Drosophila)** | Sim2 | 22.07 | 0.0003379 | ENSMUSG00000062713 |
| **small muscle protein, X-linked** | Smpx | 22.06 | 7.50E-06 | ENSMUSG00000041476 |
| **myosin XVIIIb** | Myo18b | 22.04 | 7.66E-07 | ENSMUSG00000072720 |
| **potassium voltage-gated channel, subfamily G, member 4** | Kcng4 | 21.86 | 2.32E-06 | ENSMUSG00000045246 |
| **hemochromatosis type 2 (juvenile)** | Hfe2 | 21.76 | 6.47E-15 | ENSMUSG00000038403 |
| **potassium voltage-gated channel, shaker-related subfamily, member 7** | Kcna7 | 21.23 | 2.96E-05 | ENSMUSG00000038201 |
| **vestigial like family member 2** | Vgll2 | 20.72 | 0.0003713 | ENSMUSG00000049641 |
| **apolipoprotein L 7c** | Apol7c | 20.58 | 0.0002504 | ENSMUSG00000044309 |
| **potassium voltage gated channel, Shaw-related subfamily, member 1** | Kcnc1 | 20.54 | 2.06E-06 | ENSMUSG00000058975 |
| **ankyrin repeat and SOCS box-containing 2** | Asb2 | 20.25 | 1.72E-09 | ENSMUSG00000021200 |
| **ladybird homeobox homolog 1 (Drosophila)** | Lbx1 | 19.84 | 7.67E-06 | ENSMUSG00000025216 |
| **myogenic differentiation 1** | Myod1 | 19.77 | 0.000127 | ENSMUSG00000009471 |
| **unspecified** | | 19.55 | 0.0373837 | ENSMUSG00000096670 |

| | | | | |
|---|---|---|---|---|
| **unspecified** | | 19.41 | 0.0201285 | ENSMUSG00000076606 |
| **PPARGC1 and ESRR induced regulator, muscle 1** | Perm1 | 19.23 | 5.63E-06 | ENSMUSG00000078486 |
| **sodium channel, voltage-gated, type IV, alpha** | Scn4a | 19.19 | 1.21E-05 | ENSMUSG00000001027 |
| **WNK lysine deficient protein kinase 2** | Wnk2 | 19.06 | 4.29E-08 | ENSMUSG00000037989 |
| **triadin** | Trdn | 19.01 | 1.11E-05 | ENSMUSG00000019787 |
| **ankyrin repeat and SOCs box-containing 5** | Asb5 | 18.68 | 8.62E-07 | ENSMUSG00000031519 |
| **myogenic factor 6** | Myf6 | 18.25 | 7.02E-05 | ENSMUSG00000035923 |
| **nebulin** | Neb | 18.10 | 1.98E-09 | ENSMUSG00000026950 |
| **potassium inwardly-rectifying channel, subfamily J, member 12** | Kcnj12 | 17.79 | 3.69E-06 | ENSMUSG00000042529 |
| **opsin 1 (cone pigments), medium-wave-sensitive (color blindness, deutan)** | Opn1mw | 17.61 | 0.0002185 | ENSMUSG00000031394 |
| **prostaglandin D2 receptor 2** | Ptgdr2 | 17.54 | 0.0164513 | ENSMUSG00000034117 |
| **protein phosphatase 1, regulatory (inhibitor) subunit 3A** | Ppp1r3a | 17.52 | 1.13E-05 | ENSMUSG00000042717 |
| **tetraspanin 8** | Tspan8 | 17.38 | 3.30E-10 | ENSMUSG00000034127 |
| **dual specificity phosphatase 13** | Dusp13 | 17.22 | 5.43E-06 | ENSMUSG00000021768 |

| | | | | |
|---|---|---|---|---|
| **leucine rich repeat containing 2** | Lrrc2 | 17.21 | 2.80E-06 | ENSMUSG00000032495 |
| **leucine rich repeat containing 30** | Lrrc30 | 17.18 | 0.0004155 | ENSMUSG00000073375 |
| **acyl-CoA synthetase long-chain family member 6** | Acsl6 | 17.18 | 7.15E-08 | ENSMUSG00000020333 |
| **junctional sarcoplasmic reticulum protein 1** | Jsrp1 | 17.16 | 2.03E-05 | ENSMUSG00000020216 |
| **glutamate receptor, ionotropic, NMDA2C (epsilon 3)** | Grin2c | 17.16 | 8.41E-05 | ENSMUSG00000020734 |
| **unspecified** | | 16.78 | 0.0001543 | ENSMUSG00000086866 |
| **unspecified** | | 16.69 | 7.58E-05 | ENSMUSG00000081194 |
| **unspecified** | | 16.66 | 8.41E-06 | ENSMUSG00000085779 |
| **collagen, type IX, alpha 1** | Col9a1 | 16.60 | 0.0003023 | ENSMUSG00000026147 |
| **myozenin 3** | Myoz3 | 16.50 | 3.06E-06 | ENSMUSG00000049173 |
| **ectodysplasin-A receptor** | Edar | 16.42 | 9.61E-05 | ENSMUSG00000003227 |
| **single-pass membrane protein with coiled-coil domains 1** | Smco1 | 16.40 | 1.43E-05 | ENSMUSG00000046345 |
| **Usher syndrome 1C** | Ush1c | 16.31 | 0.0005041 | ENSMUSG00000030838 |
| **unspecified** | | 16.11 | 0.0469024 | ENSMUSG00000095633 |
| **tropomodulin 4** | Tmod4 | 16.09 | 1.36E-07 | ENSMUSG00000005628 |
| **DNA-damage-inducible transcript 4-like** | Ddit4l | 15.22 | 5.59E-09 | ENSMUSG00000046818 |

| | | | | |
|---|---|---|---|---|
| **ankyrin repeat and SOCS box-containing 18** | Asb18 | 15.05 | 0.0004229 | ENSMUSG00000067081 |
| **unspecified** | | 15.02 | 0.0013127 | ENSMUSG00000076613 |
| **calpain 3** | Capn3 | 14.76 | 4.90E-09 | ENSMUSG00000079110 |
| **solute carrier family 9 (sodium/hydrogen exchanger), member 2** | Slc9a2 | 14.73 | 8.92E-06 | ENSMUSG00000026062 |
| **myosin binding protein C, slow-type** | Mybpc1 | 14.51 | 0.0001293 | ENSMUSG00000020061 |
| **myoglobin** | Mb | 14.25 | 9.41E-05 | ENSMUSG00000018893 |
| **single-minded homolog 1 (Drosophila)** | Sim1 | 13.82 | 0.0005347 | ENSMUSG00000019913 |
| **transmembrane protein 38A** | Tmem38a | 13.62 | 1.30E-07 | ENSMUSG00000031791 |
| **methyltransferase like 21E** | Mettl21e | 13.30 | 0.0028831 | ENSMUSG00000046828 |
| **kelch-like 30** | Klhl30 | 13.29 | 1.47E-05 | ENSMUSG00000026308 |
| **methyltransferase like 11B** | Mettl11b | 13.08 | 0.0012756 | ENSMUSG00000040113 |
| **cardiomyopathy associated 5** | Cmya5 | 12.98 | 0.0001227 | ENSMUSG00000047419 |
| **ADP-ribosylhydrolase like 1** | Adprhl1 | 12.91 | 2.83E-05 | ENSMUSG00000031448 |
| **proline rich 29** | Prr29 | 12.90 | 0.0007141 | ENSMUSG00000009210 |
| **myeloid leukemia factor 1** | Mlf1 | 12.71 | 4.14E-06 | ENSMUSG00000048416 |
| **cadherin 15** | Cdh15 | 12.58 | 9.42E-05 | ENSMUSG00000031962 |

| | | | | |
|---|---|---|---|---|
| **myosin, heavy polypeptide 1, skeletal muscle, adult** | Myh1 | 12.52 | 0.0003122 | ENSMUSG00000056328 |
| **Ras-related GTP binding D** | Rragd | 12.40 | 3.06E-09 | ENSMUSG00000028278 |
| **unspecified** | | 12.24 | 0.006806 | ENSMUSG00000085014 |
| **cholinergic receptor, nicotinic, delta polypeptide** | Chrnd | 12.15 | 0.0032428 | ENSMUSG00000026251 |
| **family with sequence similarity 180, member A** | Fam180a | 12.03 | 6.85E-08 | ENSMUSG00000047420 |
| **RIKEN cDNA 3425401B19 gene** | 3425401B19Rik | 11.87 | 0.0004624 | ENSMUSG00000071540 |
| **bestrophin 3** | Best3 | 11.69 | 0.0006546 | ENSMUSG00000020169 |
| **receptor-interacting serine-threonine kinase 4** | Ripk4 | 11.52 | 1.87E-16 | ENSMUSG00000005251 |
| **unspecified** | | 11.47 | 0.0059058 | ENSMUSG00000095771 |
| **NIMA (never in mitosis gene a)-related expressed kinase 5** | Nek5 | 11.41 | 0.0013352 | ENSMUSG00000037738 |
| **SH3 domain containing ring finger 2** | Sh3rf2 | 11.31 | 0.0001757 | ENSMUSG00000057719 |
| **neural cell adhesion molecule 2** | Ncam2 | 11.28 | 8.26E-11 | ENSMUSG00000022762 |
| **potassium voltage gated channel, Shaw-related subfamily, member 4** | Kcnc4 | 11.26 | 4.94E-05 | ENSMUSG00000027895 |
| **PDZ and LIM domain 3** | Pdlim3 | 11.15 | 6.38E-05 | ENSMUSG00000031636 |
| **xin actin-binding repeat containing 2** | Xirp2 | 11.07 | 0.000422 | ENSMUSG00000027022 |

| | | | | |
|---|---|---|---|---|
| **integrin beta 6** | Itgb6 | 11.00 | 0.0003877 | ENSMUSG00000026971 |
| **ankyrin repeat and SOCS box-containing 15** | Asb15 | 10.93 | 0.0007884 | ENSMUSG00000029685 |
| **brain expressed X-linked 1** | Bex1 | 10.91 | 1.97E-06 | ENSMUSG00000050071 |
| **ST8 alpha-N-acetyl-neuraminide alpha-2,8-sialyltransferase 5** | St8sia5 | 10.76 | 5.44E-05 | ENSMUSG00000025425 |
| **family with sequence similarity 183, member B** | Fam183b | 10.76 | 0.0175854 | ENSMUSG00000049154 |
| **unspecified** | | 10.71 | 0.0422942 | ENSMUSG00000076583 |
| **dual specificity phosphatase 27 (putative)** | Dusp27 | 10.64 | 0.0001995 | ENSMUSG00000026564 |
| **caveolin 3** | Cav3 | 10.61 | 0.0001237 | ENSMUSG00000062694 |
| **unspecified** | | 10.61 | 0.0009515 | ENSMUSG00000085322 |
| **interleukin 22 receptor, alpha 2** | Il22ra2 | 10.44 | 0.0140036 | ENSMUSG00000039760 |
| **junctophilin 2** | Jph2 | 10.44 | 0.0001249 | ENSMUSG00000017817 |
| **RIKEN cDNA 4933415F23 gene** | 4933415F23Rik | 10.43 | 0.001044 | ENSMUSG00000073730 |
| **unspecified** | NA | 10.42 | 3.54E-08 | ENSMUSG00000001417 |
| **synaptopodin 2-like** | Synpo2l | 10.32 | 4.42E-05 | ENSMUSG00000039376 |
| **tropomyosin 2, beta** | Tpm2 | 10.28 | 3.06E-06 | ENSMUSG00000028464 |
| **predicted gene 572** | Gm572 | 10.26 | 0.000503 | ENSMUSG00000070577 |

| | | | | |
|---|---|---|---|---|
| **tripartite motif-containing 72** | Trim72 | 10.25 | 0.0001387 | ENSMUSG00000042828 |
| **sodium channel, type IV, beta** | Scn4b | 10.11 | 0.0002438 | ENSMUSG00000046480 |
| **unspecified** | | 10.03 | 0.0038749 | ENSMUSG00000053541 |
| **alpha-kinase 2** | Alpk2 | 10.00 | 0.0002359 | ENSMUSG00000032845 |
| **ATP/GTP binding protein-like 1** | Agbl1 | 9.94 | 0.002084 | ENSMUSG00000025754 |
| **xin actin-binding repeat containing 1** | Xirp1 | 9.93 | 0.0003069 | ENSMUSG00000079243 |
| **tumor protein D52-like 1** | Tpd52l1 | 9.92 | 1.10E-09 | ENSMUSG00000000296 |
| **unspecified** | | 9.83 | 0.0214499 | ENSMUSG00000076608 |
| **unspecified** | | 9.82 | 1.78E-06 | ENSMUSG00000091575 |
| **Yip1 domain family, member 7** | Yipf7 | 9.77 | 0.0005662 | ENSMUSG00000029158 |
| **unspecified** | | 9.74 | 0.004345 | ENSMUSG00000056366 |
| **orosomucoid 3** | Orm3 | 9.74 | 2.86E-08 | ENSMUSG00000028359 |
| **unspecified** | | 9.73 | 0.0465817 | ENSMUSG00000094694 |
| **predicted gene 9992** | Gm9992 | 9.66 | 3.44E-10 | ENSMUSG00000056133 |
| **ankyrin 1, erythroid** | Ank1 | 9.62 | 0.0004692 | ENSMUSG00000031543 |
| **cytochrome c oxidase subunit Vla polypeptide 2** | Cox6a2 | 9.54 | 0.0007356 | ENSMUSG00000030785 |
| **actinin alpha 2** | Actn2 | 9.44 | 0.0022843 | ENSMUSG00000052374 |

| | | | | |
|---|---|---|---|---|
| **solute carrier family 16 (monocarboxylic acid transporters), member 3** | Slc16a3 | 9.23 | 8.44E-07 | ENSMUSG00000025161 |
| **1-aminocyclopropane-1-carboxylate synthase (non-functional)-like** | Accsl | 9.03 | 2.89E-06 | ENSMUSG00000075023 |
| **RIKEN cDNA 1700040L02 gene** | 1700040L02Rik | 8.97 | 0.0018889 | ENSMUSG00000019945 |
| **RASD family, member 2** | Rasd2 | 8.96 | 0.0004712 | ENSMUSG00000034472 |
| **solute carrier family 15, member 5** | Slc15a5 | 8.94 | 1.75E-05 | ENSMUSG00000044378 |
| **glutamate decarboxylase-like 1** | Gadl1 | 8.91 | 0.0003498 | ENSMUSG00000056880 |
| **blood vessel epicardial substance** | Bves | 8.85 | 0.0008257 | ENSMUSG00000071317 |
| **CUB and zona pellucida-like domains 1** | Cuzd1 | 8.63 | 0.0038605 | ENSMUSG00000040205 |
| **leiomodin 2 (cardiac)** | Lmod2 | 8.61 | 0.0009192 | ENSMUSG00000029683 |
| **SH3 and cysteine rich domain 3** | Stac3 | 8.57 | 1.14E-05 | ENSMUSG00000040287 |
| **F-box protein 40** | Fbxo40 | 8.56 | 3.87E-06 | ENSMUSG00000047746 |
| **unspecified** | | 8.55 | 0.0048099 | ENSMUSG00000076612 |
| **leiomodin 3 (fetal)** | Lmod3 | 8.49 | 0.00017 | ENSMUSG00000044086 |
| **SET and MYND domain containing 1** | Smyd1 | 8.48 | 7.97E-10 | ENSMUSG00000055027 |
| **docking protein 7** | Dok7 | 8.48 | 9.69E-05 | ENSMUSG00000044716 |
| **phospholipase D family, member 5** | Pld5 | 8.39 | 0.0023445 | ENSMUSG00000055214 |

| | | | | |
|---|---|---|---|---|
| **ankyrin repeat and SOCS box-containing 10** | Asb10 | 8.35 | 0.0007988 | ENSMUSG00000038204 |
| **tubulin, alpha 8** | Tuba8 | 8.33 | 2.52E-05 | ENSMUSG00000030137 |
| **CD40 ligand** | Cd40lg | 8.30 | 0.0136704 | ENSMUSG00000031132 |
| **Ras association (RalGDS/AF-6) domain family member 6** | Rassf6 | 8.16 | 3.36E-11 | ENSMUSG00000029370 |
| **chemokine (C-C motif) receptor 9** | Ccr9 | 8.14 | 0.0122603 | ENSMUSG00000029530 |
| **Lrp2 binding protein** | Lrp2bp | 8.12 | 1.43E-05 | ENSMUSG00000031637 |
| **serine incorporator 2** | Serinc2 | 8.00 | 4.45E-05 | ENSMUSG00000023232 |
| **SEC14-like lipid binding 5** | Sec14l5 | 7.99 | 4.15E-05 | ENSMUSG00000091712 |
| **unspecified** | | 7.89 | 0.0093297 | ENSMUSG00000085965 |
| **family with sequence similarity 179, member A** | Fam179a | 7.88 | 0.0012312 | ENSMUSG00000045761 |
| **calsequestrin 1** | Casq1 | 7.88 | 0.0022072 | ENSMUSG00000007122 |
| **myosin, heavy polypeptide 7, cardiac muscle, beta** | Myh7 | 7.86 | 0.0158541 | ENSMUSG00000053093 |
| **phosphofructokinase, muscle** | Pfkm | 7.86 | 2.39E-08 | ENSMUSG00000033065 |
| **unspecified** | | 7.81 | 0.0114672 | ENSMUSG00000093861 |
| **phenylethanolamine-N-methyltransferase** | Pnmt | 7.74 | 0.0129821 | ENSMUSG00000038216 |
| **ATPase, (Na+)/K+ transporting, beta 4 polypeptide** | Atp1b4 | 7.72 | 0.0097926 | ENSMUSG00000016327 |

| | | | | |
|---|---|---|---|---|
| **unspecified** | | 7.63 | 0.0153499 | ENSMUSG00000096336 |
| **alpha-kinase 3** | Alpk3 | 7.63 | 0.0030741 | ENSMUSG00000038763 |
| **unspecified** | | 7.61 | 0.0012227 | ENSMUSG00000097336 |
| **myozenin 2** | Myoz2 | 7.52 | 0.0089768 | ENSMUSG00000028116 |
| **paired-like homeodomain transcription factor 2** | Pitx2 | 7.52 | 0.0041972 | ENSMUSG00000028023 |
| **protocadherin 15** | Pcdh15 | 7.43 | 0.033426 | ENSMUSG00000052613 |
| **snail family zinc finger 3** | Snai3 | 7.41 | 0.0008209 | ENSMUSG00000006587 |
| **C1q-like 3** | C1ql3 | 7.41 | 0.0052008 | ENSMUSG00000049630 |
| **acyl-CoA synthetase medium-chain family member 3** | Acsm3 | 7.37 | 1.95E-10 | ENSMUSG00000030935 |
| **LIM domain binding 3** | Ldb3 | 7.33 | 0.0015089 | ENSMUSG00000021798 |
| **urotensin 2 receptor** | Uts2r | 7.32 | 0.0081376 | ENSMUSG00000039321 |
| **inositol hexaphosphate kinase 3** | Ip6k3 | 7.32 | 0.0028381 | ENSMUSG00000024210 |
| **hypocretin (orexin) receptor 2** | Hcrtr2 | 7.31 | 0.0302003 | ENSMUSG00000032360 |
| **kelch-like 38** | Klhl38 | 7.30 | 0.0005386 | ENSMUSG00000022357 |
| **phospholipase A2, group IVF** | Pla2g4f | 7.21 | 0.0122651 | ENSMUSG00000046971 |
| **immunoglobulin joining chain** | Jchain | 7.17 | 0.0005178 | ENSMUSG00000067149 |

| | | | | |
|---|---|---|---|---|
| **myosin, light polypeptide 2, regulatory, cardiac, slow** | Myl2 | 7.14 | 0.0209014 | ENSMUSG00000013936 |
| **unspecified** | | 7.12 | 0.031465 | ENSMUSG00000094433 |
| **CD163 molecule-like 1** | Cd163l1 | 7.10 | 0.000522 | ENSMUSG00000025461 |
| **B and T lymphocyte associated** | Btla | 7.06 | 5.34E-05 | ENSMUSG00000052013 |
| **apolipoprotein L 7e** | Apol7e | 7.06 | 0.0006818 | ENSMUSG00000071716 |
| **unspecified** | | 7.04 | 0.0268362 | ENSMUSG00000089703 |
| **unspecified** | | 7.01 | 0.0114762 | ENSMUSG00000095438 |
| **multimerin 1** | Mmrn1 | 6.99 | 0.0006571 | ENSMUSG00000054641 |
| **neuralized E3 ubiquitin protein ligase 1A** | Neurl1a | 6.96 | 0.0002852 | ENSMUSG00000006435 |
| **desmin** | Des | 6.95 | 9.68E-05 | ENSMUSG00000026208 |
| **ATPase, Ca++ transporting, plasma membrane 3** | Atp2b3 | 6.93 | 0.0037722 | ENSMUSG00000031376 |
| **endogenous retroviral sequence 3** | Erv3 | 6.88 | 0.0129481 | ENSMUSG00000037482 |
| **chemokine (C-X-C motif) receptor 2** | Cxcr2 | 6.87 | 0.0131267 | ENSMUSG00000026180 |
| **RIKEN cDNA 4930415O20 gene** | 4930415O20Rik | 6.85 | 0.0091077 | ENSMUSG00000022993 |
| **solute carrier family 30 (zinc transporter), member 2** | Slc30a2 | 6.76 | 0.0007688 | ENSMUSG00000028836 |
| **GTP cyclohydrolase I feedback regulator** | Gchfr | 6.72 | 0.001478 | ENSMUSG00000046814 |

| | | | | |
|---|---|---|---|---|
| **phosphorylase kinase gamma 1** | Phkg1 | 6.69 | 0.0016533 | ENSMUSG00000025537 |
| **RAR-related orphan receptor gamma** | Rorc | 6.69 | 1.10E-17 | ENSMUSG00000028150 |
| **unspecified** | | 6.64 | 0.0312882 | ENSMUSG00000087505 |
| **interleukin 1 alpha** | Il1a | 6.63 | 0.0007553 | ENSMUSG00000027399 |
| **family with sequence similarity 132, member B** | Fam132b | 6.62 | 0.0034474 | ENSMUSG00000047443 |
| **5'-nucleotidase, cytosolic IA** | Nt5c1a | 6.62 | 0.0020841 | ENSMUSG00000054958 |
| **cation channel, sperm associated 4** | Catsper4 | 6.61 | 0.016221 | ENSMUSG00000048003 |
| **unspecified** | | 6.59 | 0.0300197 | ENSMUSG00000085651 |
| **heat shock protein 3** | Hspb3 | 6.59 | 0.0089756 | ENSMUSG00000051456 |
| **neurotrophin 5** | Ntf5 | 6.57 | 0.0086675 | ENSMUSG00000074121 |
| **tropomyosin 1, alpha** | Tpm1 | 6.56 | 2.03E-05 | ENSMUSG00000032366 |
| **fatty acid binding protein 3, muscle and heart** | Fabp3 | 6.54 | 0.0136779 | ENSMUSG00000028773 |
| **transcription elongation factor A (SII)-like 7** | Tceal7 | 6.53 | 0.0202367 | ENSMUSG00000079428 |
| **chemokine (C-C motif) ligand 21A (serine)** | Ccl21a | 6.49 | 0.025281 | ENSMUSG00000094686 |
| **diacylglycerol O-acyltransferase 2-like 6** | Dgat2l6 | 6.48 | 0.0189001 | ENSMUSG00000067597 |
| **myomesin 1** | Myom1 | 6.46 | 0.0009827 | ENSMUSG00000024049 |
| **methyltransferase like 21C** | Mettl21c | 6.45 | 5.46E-05 | ENSMUSG00000047343 |

| | | | | |
|---|---|---|---|---|
| **unspecified** | | 6.44 | 0.003 9283 | ENSMUSG00000057913 |
| **unspecified** | | 6.44 | 0.018 5919 | ENSMUSG00000049349 |
| **corticotropin releasing hormone receptor 2** | Crhr2 | 6.40 | 0.001 2363 | ENSMUSG00000003476 |
| **transmembrane protein 52** | Tmem52 | 6.25 | 0.000 5589 | ENSMUSG00000023153 |
| **RIKEN cDNA A430078G23 gene** | A430078G2 3Rik | 6.22 | 0.002 2052 | ENSMUSG00000074497 |
| **carbonic anhydrase 14** | Car14 | 6.20 | 5.74E -05 | ENSMUSG00000038526 |
| **unspecified** | | 6.17 | 0.030 3077 | ENSMUSG00000085710 |
| **unspecified** | | 6.13 | 9.69E -06 | ENSMUSG00000085180 |
| **myosin, heavy polypeptide 2, skeletal muscle, adult** | Myh2 | 6.11 | 0.018 8992 | ENSMUSG00000033196 |
| **transmembrane protein 108** | Tmem108 | 6.08 | 0.002 7327 | ENSMUSG00000042757 |
| **cadherin 4** | Cdh4 | 6.07 | 0.000 3509 | ENSMUSG00000000305 |
| **v-myc avian myelocytomatosis viral oncogene lung carcinoma derived** | Mycl | 6.07 | 2.12E -11 | ENSMUSG00000028654 |
| **histocompatibility 2, M region locus 2** | H2-M2 | 6.03 | 0.007 7268 | ENSMUSG00000016283 |
| **kelch-like 32** | Klhl32 | 6.01 | 0.013 9733 | ENSMUSG00000040387 |
| **unspecified** | | 5.99 | 0.028 6459 | ENSMUSG00000065399 |
| **predicted gene 590** | Gm590 | 5.99 | 0.035 3132 | ENSMUSG00000096393 |

| | | | | |
|---|---|---|---|---|
| **coiled-coil domain containing 146** | Ccdc146 | 5.98 | 0.017868 | ENSMUSG00000064280 |
| **unspecified** | | 5.95 | 0.026349 | ENSMUSG00000087404 |
| **ankyrin repeat domain 2 (stretch responsive muscle)** | Ankrd2 | 5.94 | 0.0024243 | ENSMUSG00000025172 |
| **myosin, light polypeptide 1** | Myl1 | 5.93 | 0.0116016 | ENSMUSG00000061816 |
| **UDP-GlcNAc:betaGal beta-1,3-N-acetylglucosaminyltransferase 5** | B3gnt5 | 5.92 | 0.0007734 | ENSMUSG00000022686 |
| **unspecified** | | 5.88 | 0.0063635 | ENSMUSG00000076749 |
| **transformation related protein 73** | Trp73 | 5.85 | 0.0195685 | ENSMUSG00000029026 |
| **thymocyte expressed, positive selection associated 1** | Tespa1 | 5.84 | 0.0056353 | ENSMUSG00000034833 |
| **unspecified** | | 5.82 | 5.44E-05 | ENSMUSG00000084819 |
| **unspecified** | NA | 5.81 | 0.0134307 | ENSMUSG00000089688 |
| **opioid receptor, delta 1** | Oprd1 | 5.76 | 0.0200098 | ENSMUSG00000050511 |
| **unspecified** | | 5.73 | 0.0046313 | ENSMUSG00000085887 |
| **ryanodine receptor 3** | Ryr3 | 5.71 | 0.0190339 | ENSMUSG00000057378 |
| **paired box 7** | Pax7 | 5.70 | 0.0328511 | ENSMUSG00000028736 |
| **carbohydrate (chondroitin 6/keratan) sulfotransferase 3** | Chst3 | 5.67 | 0.0003212 | ENSMUSG00000057337 |

| | | | | |
|---|---|---|---|---|
| **neuromedin B receptor** | Nmbr | 5.66 | 0.0244106 | ENSMUSG00000019865 |
| **erb-b2 receptor tyrosine kinase 4** | Erbb4 | 5.64 | 0.000472 | ENSMUSG00000062209 |
| **melanoregulin** | Mreg | 5.63 | 2.12E-09 | ENSMUSG00000039395 |
| **unspecified** | | 5.63 | 0.0058611 | ENSMUSG00000089781 |
| **tumor necrosis factor receptor superfamily, member 19** | Tnfrsf19 | 5.58 | 2.06E-06 | ENSMUSG00000060548 |
| **tumor necrosis factor (ligand) superfamily, member 8** | Tnfsf8 | 5.58 | 0.0022875 | ENSMUSG00000028362 |
| **nitric oxide synthase 1, neuronal** | Nos1 | 5.57 | 0.0006803 | ENSMUSG00000029361 |
| **hyperpolarization-activated, cyclic nucleotide-gated K+ 3** | Hcn3 | 5.57 | 0.0028787 | ENSMUSG00000028051 |
| **IKAROS family zinc finger 3** | Ikzf3 | 5.57 | 0.0009438 | ENSMUSG00000018168 |
| **unspecified** | | 5.56 | 0.0343525 | ENSMUSG00000089718 |
| **netrin 5** | Ntn5 | 5.55 | 0.011284 | ENSMUSG00000070564 |
| **fructosamine 3 kinase** | Fn3k | 5.50 | 1.08E-15 | ENSMUSG00000025175 |
| **CD96 antigen** | Cd96 | 5.50 | 0.016599 | ENSMUSG00000022657 |
| **unc-5 netrin receptor C** | Unc5c | 5.47 | 0.0059936 | ENSMUSG00000059921 |
| **unspecified** | | 5.46 | 0.0011068 | ENSMUSG00000097317 |
| **predicted gene 1045** | Gm1045 | 5.46 | 0.0422067 | ENSMUSG00000096035 |

| | | | | |
|---|---|---|---|---|
| **chemokine (C-X-C motif) ligand 13** | Cxcl13 | 5.44 | 0.0040918 | ENSMUSG00000023078 |
| **CD207 antigen** | Cd207 | 5.44 | 0.0099418 | ENSMUSG00000034783 |
| **cordon-bleu WH2 repeat** | Cobl | 5.44 | 1.15E-06 | ENSMUSG00000020173 |
| **insulin receptor-related receptor** | Insrr | 5.43 | 0.0257314 | ENSMUSG00000005640 |
| **interferon activated gene 208** | Ifi208 | 5.42 | 0.0012321 | ENSMUSG00000066677 |
| **unspecified** | NA | 5.41 | 0.0258321 | ENSMUSG00000095665 |
| **CD69 antigen** | Cd69 | 5.40 | 0.0079255 | ENSMUSG00000030156 |
| **deoxynucleotidyltransferase, terminal** | Dntt | 5.38 | 0.0027492 | ENSMUSG00000025014 |
| **cystatin F (leukocystatin)** | Cst7 | 5.34 | 0.0128532 | ENSMUSG00000068129 |
| **signaling mucin HKR1-like** | LOC102639543 | 5.34 | 0.0418002 | ENSMUSG00000037849 |
| **E74-like factor 3** | Elf3 | 5.34 | 0.0172078 | ENSMUSG00000003051 |
| **calcium channel, voltage-dependent, beta 1 subunit** | Cacnb1 | 5.31 | 5.77E-05 | ENSMUSG00000020882 |
| **interleukin 12a** | Il12a | 5.31 | 0.0095317 | ENSMUSG00000027776 |
| **cytochrome P450, family 2, subfamily e, polypeptide 1** | Cyp2e1 | 5.31 | 6.42E-06 | ENSMUSG00000025479 |
| **T-box 4** | Tbx4 | 5.27 | 0.0378572 | ENSMUSG00000000094 |
| **myosin, light polypeptide 3** | Myl3 | 5.26 | 0.0496735 | ENSMUSG00000059741 |

| | | | | |
|---|---|---|---|---|
| **dynein, axonemal, heavy chain 8** | Dnah8 | 5.25 | 0.0004731 | ENSMUSG00000033826 |
| **unspecified** | | 5.25 | 0.0407128 | ENSMUSG00000086582 |
| **unspecified** | | 5.22 | 0.0002852 | ENSMUSG00000087523 |
| **GRB2-related adaptor protein 2** | Grap2 | 5.20 | 0.0055502 | ENSMUSG00000042351 |
| **claudin 11** | Cldn11 | 5.16 | 0.0347291 | ENSMUSG00000037625 |
| **cytochrome P450, family 2, subfamily f, polypeptide 2** | Cyp2f2 | 5.16 | 2.82E-05 | ENSMUSG00000052974 |
| **unspecified** | | 5.15 | 0.0101542 | ENSMUSG00000084839 |
| **leucine-rich repeat-containing G protein-coupled receptor 6** | Lgr6 | 5.15 | 0.0212875 | ENSMUSG00000042793 |
| **RNA binding motif protein 20** | Rbm20 | 5.14 | 1.41E-06 | ENSMUSG00000043639 |
| **G protein-coupled receptor 174** | Gpr174 | 5.13 | 0.0051123 | ENSMUSG00000073008 |
| **CUB domain containing protein 1** | Cdcp1 | 5.12 | 0.0146727 | ENSMUSG00000035498 |
| **ADP-ribosyltransferase 5** | Art5 | 5.11 | 0.0123709 | ENSMUSG00000070424 |
| **cullin-associated and neddylation-dissociated 2 (putative)** | Cand2 | 5.10 | 0.0009073 | ENSMUSG00000030319 |
| **membrane-spanning 4-domains, subfamily A, member 1** | Ms4a1 | 5.09 | 0.0343519 | ENSMUSG00000024673 |
| **family with sequence similarity 169, member B** | Fam169b | 5.08 | 0.0026568 | ENSMUSG00000074071 |

| | | | | |
|---|---|---|---|---|
| **CD4 antigen** | Cd4 | 5.08 | 0.0059832 | ENSMUSG00000023274 |
| **copine family member IX** | Cpne9 | 5.07 | 0.000645 | ENSMUSG00000030270 |
| **shisa family member 7** | Shisa7 | 5.06 | 0.0422634 | ENSMUSG00000053550 |
| **unspecified** | | 5.04 | 0.0087484 | ENSMUSG00000085016 |
| **elastase, neutrophil expressed** | Elane | 5.04 | 0.0003313 | ENSMUSG00000020125 |
| **zinc finger protein 831** | Zfp831 | 5.01 | 0.0072282 | ENSMUSG00000050600 |
| **transcription factor 7, T cell specific** | Tcf7 | 5.01 | 0.0019965 | ENSMUSG00000000782 |
| **tigger transposable element derived 4** | Tigd4 | 5.00 | 0.0248972 | ENSMUSG00000047819 |
| **potassium channel tetramerisation domain containing 14** | Kctd14 | 4.99 | 5.37E-05 | ENSMUSG00000051727 |
| **glutamate decarboxylase 1** | Gad1 | 4.95 | 0.0379082 | ENSMUSG00000070880 |
| **unspecified** | | 4.93 | 0.0139861 | ENSMUSG00000085603 |
| **ST8 alpha-N-acetyl-neuraminide alpha-2,8-sialyltransferase 1** | St8sia1 | 4.93 | 0.0128566 | ENSMUSG00000030283 |
| **complement factor D (adipsin)** | Cfd | 4.92 | 0.0028755 | ENSMUSG00000061780 |
| **unspecified** | | 4.91 | 0.0039052 | ENSMUSG00000082706 |
| **chemokine (C-C motif) ligand 22** | Ccl22 | 4.91 | 0.0194736 | ENSMUSG00000031779 |
| **solute carrier organic anion transporter family, member 5A1** | Slco5a1 | 4.90 | 0.0042759 | ENSMUSG00000025938 |

| | | | | |
|---|---|---|---|---|
| **cholinergic receptor, nicotinic, alpha polypeptide 1 (muscle)** | Chrna1 | 4.87 | 0.003 5083 | ENSMUSG00000027107 |
| **ADAM-like, decysin 1** | Adamdec1 | 4.87 | 0.008 3746 | ENSMUSG00000022057 |
| **wingless-type MMTV integration site family, member 2B** | Wnt2b | 4.86 | 0.029 7635 | ENSMUSG00000027840 |
| **oligodendrocyte transcription factor 1** | Olig1 | 4.85 | 0.023 1375 | ENSMUSG00000046160 |
| **teneurin transmembrane protein 3** | Tenm3 | 4.83 | 1.72E -07 | ENSMUSG00000031561 |
| **leptin receptor** | Lepr | 4.82 | 1.89E -05 | ENSMUSG00000057722 |
| **melanoma associated antigen (mutated) 1-like 1** | Mum1l1 | 4.82 | 2.48E -08 | ENSMUSG00000042515 |
| **cochlin** | Coch | 4.82 | 0.021 1804 | ENSMUSG00000020953 |
| **unspecified** | | 4.82 | 0.024 4111 | ENSMUSG00000065460 |
| **calcium/calmodulin-dependent protein kinase II, beta** | Camk2b | 4.81 | 1.20E -05 | ENSMUSG00000057897 |
| **chordin-like 2** | Chrdl2 | 4.79 | 0.042 7989 | ENSMUSG00000030732 |
| **leucine-rich single-pass membrane protein 1** | Lsmem1 | 4.77 | 0.002 701 | ENSMUSG00000071342 |
| **leukocyte tyrosine kinase** | Ltk | 4.77 | 0.047 0175 | ENSMUSG00000027297 |
| **smoothelin-like 1** | Smtnl1 | 4.76 | 0.033 6836 | ENSMUSG00000027077 |
| **forkhead box P3** | Foxp3 | 4.75 | 0.020 0363 | ENSMUSG00000039521 |

| | | | | |
|---|---|---|---|---|
| **POU domain, class 2, associating factor 1** | Pou2af1 | 4.73 | 0.0373474 | ENSMUSG00000032053 |
| **unspecified** | | 4.69 | 0.0078327 | ENSMUSG00000087698 |
| **runt related transcription factor 3** | Runx3 | 4.68 | 0.0047288 | ENSMUSG00000070691 |
| **CAP, adenylate cyclase-associated protein, 2 (yeast)** | Cap2 | 4.68 | 0.0091285 | ENSMUSG00000021373 |
| **fat storage-inducing transmembrane protein 1** | Fitm1 | 4.68 | 0.000341 | ENSMUSG00000022215 |
| **cyclic nucleotide gated channel alpha 3** | Cnga3 | 4.65 | 0.0382346 | ENSMUSG00000026114 |
| **triggering receptor expressed on myeloid cells-like 2** | Treml2 | 4.64 | 0.0473737 | ENSMUSG00000071068 |
| **eva-1 homolog C (C. elegans)** | Eva1c | 4.64 | 6.49E-08 | ENSMUSG00000039903 |
| **family with sequence similarity 163, member B** | Fam163b | 4.63 | 0.00051 | ENSMUSG00000009216 |
| **unspecified** | | 4.61 | 0.0046647 | ENSMUSG00000090778 |
| **tubulin, alpha 4A** | Tuba4a | 4.61 | 1.61E-10 | ENSMUSG00000026202 |
| **von Willebrand factor A domain containing 7** | Vwa7 | 4.60 | 7.79E-05 | ENSMUSG00000007030 |
| **unspecified** | | 4.58 | 0.0290082 | ENSMUSG00000098099 |
| **ankyrin repeat and SOCS box-containing 16** | Asb16 | 4.58 | 0.0012519 | ENSMUSG00000034768 |
| **transcription elongation factor A (SII), 3** | Tcea3 | 4.58 | 1.21E-05 | ENSMUSG00000001604 |
| **unspecified** | | 4.52 | 0.0234279 | ENSMUSG00000090709 |

| | | | | |
|---|---|---|---|---|
| **spinster homolog 3** | Spns3 | 4.51 | 0.0006222 | ENSMUSG00000020798 |
| **cadherin-related family member 1** | Cdhr1 | 4.50 | 0.0454016 | ENSMUSG00000021803 |
| **interleukin 4 induced 1** | Il4i1 | 4.50 | 0.0001491 | ENSMUSG00000074141 |
| **guanylate-binding protein 8** | Gbp8 | 4.47 | 0.0003815 | ENSMUSG00000034438 |
| **interferon regulatory factor 4** | Irf4 | 4.44 | 2.78E-09 | ENSMUSG00000021356 |
| **unspecified** | | 4.44 | 0.002696 | ENSMUSG00000085653 |
| **amyloid beta (A4) precursor protein-binding, family A, member 2** | Apba2 | 4.44 | 0.0129892 | ENSMUSG00000030519 |
| **solute carrier family 2 (facilitated glucose transporter), member 3** | Slc2a3 | 4.43 | 9.84E-06 | ENSMUSG00000003153 |
| **CD22 antigen** | Cd22 | 4.43 | 0.0158365 | ENSMUSG00000030577 |
| **matrix metallopeptidase 25** | Mmp25 | 4.41 | 0.0014737 | ENSMUSG00000023903 |
| **unspecified** | | 4.41 | 0.0032591 | ENSMUSG00000051107 |
| **histocompatibility 2, blastocyst** | H2-Bl | 4.40 | 0.0405851 | ENSMUSG00000073406 |
| **cytotoxic T-lymphocyte-associated protein 4** | Ctla4 | 4.40 | 0.0063354 | ENSMUSG00000026011 |
| **ArfGAP with coiled-coil, ankyrin repeat and PH domains 1** | Acap1 | 4.39 | 0.0026984 | ENSMUSG00000001588 |
| **tryptophan hydroxylase 1** | Tph1 | 4.39 | 0.022779 | ENSMUSG00000040046 |

| | | | | |
|---|---|---|---|---|
| **sialic acid binding Ig-like lectin G** | Siglecg | 4.38 | 0.0379619 | ENSMUSG00000030468 |
| **unspecified** | | 4.36 | 0.0035544 | ENSMUSG00000048709 |
| **family with sequence similarity 167, member A** | Fam167a | 4.35 | 1.86E-05 | ENSMUSG00000035095 |
| **B cell leukemia/lymphoma 11B** | Bcl11b | 4.32 | 0.0229738 | ENSMUSG00000048251 |
| **unspecified** | | 4.32 | 2.16E-05 | ENSMUSG00000072852 |
| **microtubule-associated protein tau** | Mapt | 4.29 | 5.49E-09 | ENSMUSG00000018411 |
| **G protein-coupled receptor associated sorting protein 2** | Gprasp2 | 4.27 | 0.0022011 | ENSMUSG00000072966 |
| **actin, alpha, cardiac muscle 1** | Actc1 | 4.25 | 0.0431424 | ENSMUSG00000068614 |
| **immunoglobulin-like domain containing receptor 1** | Ildr1 | 4.25 | 0.0055856 | ENSMUSG00000022900 |
| **IL2 inducible T cell kinase** | Itk | 4.22 | 0.0165576 | ENSMUSG00000020395 |
| **cilia and flagella associated protein 70** | Cfap70 | 4.20 | 0.0248972 | ENSMUSG00000039543 |
| **myeloblastosis oncogene** | Myb | 4.19 | 0.0068394 | ENSMUSG00000019982 |
| **SH3/ankyrin domain gene 1** | Shank1 | 4.19 | 0.0004557 | ENSMUSG00000038738 |
| **contactin 1** | Cntn1 | 4.18 | 0.029937 | ENSMUSG00000055022 |
| **selectin, lymphocyte** | Sell | 4.16 | 0.0271297 | ENSMUSG00000026581 |
| **RAB26, member RAS oncogene family** | Rab26 | 4.16 | 0.0015288 | ENSMUSG00000079657 |

| | | | | |
|---|---|---|---|---|
| **chemokine (C-C motif) receptor 7** | Ccr7 | 4.15 | 0.0327596 | ENSMUSG00000037944 |
| **janus kinase and microtubule interacting protein 1** | Jakmip1 | 4.13 | 0.0312394 | ENSMUSG00000063646 |
| **cadherin, EGF LAG seven-pass G-type receptor 2** | Celsr2 | 4.13 | 1.77E-26 | ENSMUSG00000068740 |
| **serine/arginine-rich protein specific kinase 3** | Srpk3 | 4.13 | 0.0229753 | ENSMUSG00000002007 |
| **tripartite motif-containing 7** | Trim7 | 4.12 | 0.0004266 | ENSMUSG00000040350 |
| **interleukin 21 receptor** | Il21r | 4.10 | 0.0336846 | ENSMUSG00000030745 |
| **lymphocyte transmembrane adaptor 1** | Lax1 | 4.09 | 0.0052164 | ENSMUSG00000051998 |
| **SID1 transmembrane family, member 1** | Sidt1 | 4.09 | 0.0131861 | ENSMUSG00000022696 |
| **CD28 antigen** | Cd28 | 4.09 | 0.0009831 | ENSMUSG00000026012 |
| **forkhead box F1** | Foxf1 | 4.06 | 0.0133599 | ENSMUSG00000042812 |
| **solute carrier family 8 (sodium/calcium exchanger), member 2** | Slc8a2 | 4.04 | 0.0155491 | ENSMUSG00000030376 |
| **CD6 antigen** | Cd6 | 4.03 | 0.017132 | ENSMUSG00000024670 |
| **transcription elongation factor A (SII)-like 5** | Tceal5 | 4.02 | 0.0035904 | ENSMUSG00000054034 |
| **T-box 1** | Tbx1 | 4.02 | 0.0164582 | ENSMUSG00000009097 |
| **unspecified** | | 4.02 | 0.0182155 | ENSMUSG00000084969 |

| | | | | |
|---|---|---|---|---|
| **unspecified** | | 4.01 | 0.0488168 | ENSMUSG00000076609 |
| **unspecified** | | 4.00 | 0.0179259 | ENSMUSG00000076752 |
| **SH2 domain containing 2A** | Sh2d2a | 4.00 | 0.0131861 | ENSMUSG00000028071 |
| **solute carrier family 16 (monocarboxylic acid transporters), member 5** | Slc16a5 | 4.00 | 0.0497199 | ENSMUSG00000045775 |
| **IKAROS family zinc finger 4** | Ikzf4 | 4.00 | 0.0003704 | ENSMUSG00000002578 |
| **WAP, follistatin/kazal, immunoglobulin, kunitz and netrin domain containing 2** | Wfikkn2 | 3.99 | 0.0006425 | ENSMUSG00000044177 |
| **ribosomal protein S6 kinase polypeptide 6** | Rps6ka6 | 3.99 | 0.0117576 | ENSMUSG00000025665 |
| **unc-93 homolog A (C. elegans)** | Unc93a | 3.99 | 0.0484076 | ENSMUSG00000067049 |
| **aquaporin 3** | Aqp3 | 3.99 | 0.038111 | ENSMUSG00000028435 |
| **tetratricopeptide repeat domain 6** | Ttc6 | 3.98 | 0.0310442 | ENSMUSG00000046782 |
| **polycystin (PKD) family receptor for egg jelly** | Pkdrej | 3.98 | 0.0004624 | ENSMUSG00000052496 |
| **family with sequence similarity 65, member B** | Fam65b | 3.97 | 0.0023622 | ENSMUSG00000036006 |
| **unspecified** | | 3.97 | 0.0029526 | ENSMUSG00000066170 |
| **unspecified** | | 3.96 | 6.68E-05 | ENSMUSG00000084941 |
| **cholinergic receptor, nicotinic, epsilon polypeptide** | Chrne | 3.95 | 0.0154094 | ENSMUSG00000014609 |

| | | | | |
|---|---|---|---|---|
| **frizzled class receptor 9** | Fzd9 | 3.95 | 0.008 9768 | ENSMUSG00000049551 |
| **cholinergic receptor, nicotinic, alpha polypeptide 5** | Chrna5 | 3.94 | 0.007 1122 | ENSMUSG00000035594 |
| **CD3 antigen, gamma polypeptide** | Cd3g | 3.94 | 0.022 6754 | ENSMUSG00000002033 |
| **MORN repeat containing 4** | Morn4 | 3.94 | 0.000 2852 | ENSMUSG00000049670 |
| **cysteine and glycine-rich protein 3** | Csrp3 | 3.93 | 0.008 3083 | ENSMUSG00000030470 |
| **membrane-spanning 4-domains, subfamily A, member 4C** | Ms4a4c | 3.92 | 0.016 2219 | ENSMUSG00000024675 |
| **unspecified** | | 3.91 | 2.66E -05 | ENSMUSG00000085923 |
| **RAS protein activator like 3** | Rasal3 | 3.90 | 0.001 6561 | ENSMUSG00000052142 |
| **leucine rich repeat neuronal 4** | Lrrn4 | 3.89 | 0.004 7288 | ENSMUSG00000043110 |
| **unspecified** | | 3.87 | 0.018 1556 | ENSMUSG00000076757 |
| **unspecified** | | 3.86 | 1.95E -05 | ENSMUSG00000097613 |
| **A kinase (PRKA) anchor protein 6** | Akap6 | 3.85 | 0.009 0274 | ENSMUSG00000061603 |
| **mucosal vascular addressin cell adhesion molecule 1** | Madcam1 | 3.84 | 0.049 5645 | ENSMUSG00000020310 |
| **calcium/calmodulin-dependent protein kinase IV** | Camk4 | 3.84 | 0.030 0857 | ENSMUSG00000038128 |
| **WAP four-disulfide core domain 1** | Wfdc1 | 3.83 | 0.000 3757 | ENSMUSG00000023336 |

| | | | | |
|---|---|---|---|---|
| **unspecified** | | 3.82 | 0.042 5976 | ENSMUSG00000072591 |
| **DENN/MADD domain containing 2D** | Dennd2d | 3.81 | 1.15E -06 | ENSMUSG00000027901 |
| **cadherin, EGF LAG seven-pass G-type receptor 1** | Celsr1 | 3.81 | 0.000 7337 | ENSMUSG00000016028 |
| **inducible T cell co-stimulator** | Icos | 3.81 | 0.008 1381 | ENSMUSG00000026009 |
| **dual specificity phosphatase 2** | Dusp2 | 3.80 | 0.012 3697 | ENSMUSG00000027368 |
| **SAM domain, SH3 domain and nuclear localization signals, 1** | Samsn1 | 3.80 | 0.001 6945 | ENSMUSG00000022876 |
| **cysteine-rich protein 3** | Crip3 | 3.80 | 0.007 3901 | ENSMUSG00000023968 |
| **protein tyrosine phosphatase, non-receptor type 22 (lymphoid)** | Ptpn22 | 3.77 | 2.60E -05 | ENSMUSG00000027843 |
| **proteinase 3** | Prtn3 | 3.77 | 0.019 8021 | ENSMUSG00000057729 |
| **FCH domain only 1** | Fcho1 | 3.77 | 0.017 7268 | ENSMUSG00000070000 |
| **NLR family, apoptosis inhibitory protein 1** | Naip1 | 3.76 | 0.021 8696 | ENSMUSG00000021640 |
| **carbohydrate sulfotransferase 10** | Chst10 | 3.76 | 0.009 2127 | ENSMUSG00000026080 |
| **CD27 antigen** | Cd27 | 3.75 | 0.011 8735 | ENSMUSG00000030336 |
| **phospholipase A2, group IVE** | Pla2g4e | 3.74 | 0.041 6302 | ENSMUSG00000050211 |
| **acetylcholinesterase** | Ache | 3.74 | 4.05E -05 | ENSMUSG00000023328 |

| | | | | |
|---|---|---|---|---|
| **ankyrin repeat domain 23** | Ankrd23 | 3.74 | 0.0244036 | ENSMUSG00000067653 |
| **MSS51 mitochondrial translational activator** | Mss51 | 3.74 | 0.0004368 | ENSMUSG00000021815 |
| **MAS-related GPR, member H** | Mrgprh | 3.73 | 0.0347907 | ENSMUSG00000059408 |
| **synaptotagmin IX** | Syt9 | 3.73 | 0.0285167 | ENSMUSG00000062542 |
| **neurexophilin and PC-esterase domain family, member 3** | Nxpe3 | 3.73 | 0.0018641 | ENSMUSG00000075033 |
| **adenylate kinase 1** | Ak1 | 3.72 | 0.0271297 | ENSMUSG00000026817 |
| **unspecified** | | 3.72 | 0.0118753 | ENSMUSG00000085445 |
| **purinergic receptor P2Y, G-protein coupled 13** | P2ry13 | 3.71 | 0.0015762 | ENSMUSG00000036362 |
| **ets homologous factor** | Ehf | 3.69 | 0.0096119 | ENSMUSG00000012350 |
| **Ras-related GTP binding B** | Rragb | 3.68 | 0.00012 | ENSMUSG00000041658 |
| **exostoses (multiple)-like 1** | Extl1 | 3.68 | 0.0012519 | ENSMUSG00000028838 |
| **cadherin 22** | Cdh22 | 3.67 | 0.0488832 | ENSMUSG00000053166 |
| **aryl hydrocarbon receptor nuclear translocator 2** | Arnt2 | 3.66 | 0.0031265 | ENSMUSG00000015709 |
| **BEN domain containing 5** | Bend5 | 3.66 | 0.0078327 | ENSMUSG00000028545 |
| **src family associated phosphoprotein 1** | Skap1 | 3.66 | 0.0285877 | ENSMUSG00000057058 |
| **early growth response 3** | Egr3 | 3.65 | 0.0096044 | ENSMUSG00000033730 |

| | | | | |
|---|---|---|---|---|
| **RIKEN cDNA 1700029J07 gene** | 1700029J07Rik | 3.65 | 3.87E-06 | ENSMUSG00000071103 |
| **prospero homeobox 1** | Prox1 | 3.64 | 0.0006436 | ENSMUSG00000010175 |
| **potassium large conductance calcium-activated channel, subfamily M, beta member 4** | Kcnmb4 | 3.64 | 0.0305567 | ENSMUSG00000054934 |
| **uncharacterized LOC108167814** | LOC108167814 | 3.64 | 0.0354492 | ENSMUSG00000043126 |
| **regulator of G-protein signaling 11** | Rgs11 | 3.64 | 0.0005758 | ENSMUSG00000024186 |
| **family with sequence similarity 13, member A** | Fam13a | 3.63 | 1.60E-12 | ENSMUSG00000037709 |
| **unspecified** | | 3.62 | 0.0040448 | ENSMUSG00000056145 |
| **S100 calcium binding protein A9 (calgranulin B)** | S100a9 | 3.62 | 0.0424355 | ENSMUSG00000056071 |
| **unspecified** | | 3.62 | 0.0193706 | ENSMUSG00000040705 |
| **SLAM family member 6** | Slamf6 | 3.62 | 0.0382928 | ENSMUSG00000015314 |
| **receptor-associated protein of the synapse** | Rapsn | 3.61 | 0.0002339 | ENSMUSG00000002104 |
| **unspecified** | | 3.60 | 0.0198654 | ENSMUSG00000076928 |
| **unspecified** | | 3.60 | 0.0011068 | ENSMUSG00000072769 |
| **T cell immunoglobulin and mucin domain containing 4** | Timd4 | 3.60 | 0.0044583 | ENSMUSG00000055546 |

| | | | | |
|---|---|---|---|---|
| **solute carrier family 9 (sodium/hydrogen exchanger), member 7** | Slc9a7 | 3.59 | 9.84E-05 | ENSMUSG00000037341 |
| **synaptonemal complex central element protein 1** | Syce1 | 3.59 | 0.0098336 | ENSMUSG00000025480 |
| **chemokine (C-X-C motif) receptor 6** | Cxcr6 | 3.57 | 0.0074642 | ENSMUSG00000048521 |
| **membrane-spanning 4-domains, subfamily A, member 4B** | Ms4a4b | 3.56 | 0.0185872 | ENSMUSG00000056290 |
| **neuraminidase 2** | Neu2 | 3.55 | 0.0209995 | ENSMUSG00000079434 |
| **muscle-related coiled-coil protein** | Murc | 3.53 | 0.0489365 | ENSMUSG00000028348 |
| **unspecified** | | 3.52 | 0.0155442 | ENSMUSG00000095079 |
| **protein kinase C, theta** | Prkcq | 3.52 | 0.0022554 | ENSMUSG00000026778 |
| **Kv channel-interacting protein 2** | Kcnip2 | 3.52 | 0.0101491 | ENSMUSG00000025221 |
| **cytoplasmic FMR1 interacting protein 2** | Cyfip2 | 3.51 | 0.0070946 | ENSMUSG00000020340 |
| **signal transducer and activator of transcription 4** | Stat4 | 3.51 | 0.0123383 | ENSMUSG00000062939 |
| **C1q and tumor necrosis factor related protein 4** | C1qtnf4 | 3.51 | 0.0151779 | ENSMUSG00000040794 |
| **CUB and Sushi multiple domains 1** | Csmd1 | 3.51 | 0.0023816 | ENSMUSG00000060924 |
| **purinergic receptor P2Y, G-protein coupled 10** | P2ry10 | 3.50 | 0.0177246 | ENSMUSG00000050921 |
| **TRAF3 interacting protein 3** | Traf3ip3 | 3.50 | 0.0095448 | ENSMUSG00000037318 |
| **EGF-like-domain, multiple 6** | Egfl6 | 3.50 | 0.039599 | ENSMUSG00000000402 |

| | | | | |
|---|---|---|---|---|
| **Src-like-adaptor 2** | Sla2 | 3.50 | 0.0347511 | ENSMUSG00000027636 |
| **sialic acid binding Ig-like lectin H** | Siglech | 3.50 | 0.0020114 | ENSMUSG00000051504 |
| **crystallin, mu** | Crym | 3.49 | 0.0111275 | ENSMUSG00000030905 |
| **serine/threonine kinase 26** | Stk26 | 3.48 | 0.0020183 | ENSMUSG00000031112 |
| **zeta-chain (TCR) associated protein kinase** | Zap70 | 3.48 | 0.005918 | ENSMUSG00000026117 |
| **CD300 molecule like family member F** | Cd300lf | 3.47 | 0.0281959 | ENSMUSG00000047798 |
| **histocompatibility 2, O region beta locus** | H2-Ob | 3.47 | 0.0438296 | ENSMUSG00000041538 |
| **adenylosuccinate synthetase like 1** | Adssl1 | 3.46 | 0.0001497 | ENSMUSG00000011148 |
| **toll-like receptor 11** | Tlr11 | 3.46 | 0.0001362 | ENSMUSG00000051969 |
| **cell migration inducing protein, hyaluronan binding** | Cemip | 3.46 | 0.0376148 | ENSMUSG00000052353 |
| **schlafen 1** | Slfn1 | 3.45 | 0.0227954 | ENSMUSG00000078763 |
| **integrin alpha L** | Itgal | 3.45 | 0.0008181 | ENSMUSG00000030830 |
| **trans-acting transcription factor 6** | Sp6 | 3.44 | 0.0290082 | ENSMUSG00000038560 |
| **unspecified** | NA | 3.44 | 0.0069363 | ENSMUSG00000097758 |
| **shisa family member 3** | Shisa3 | 3.43 | 0.002191 | ENSMUSG00000050010 |
| **family with sequence similarity 134, member B** | Fam134b | 3.42 | 8.70E-06 | ENSMUSG00000022270 |

| | | | | |
|---|---|---|---|---|
| **RIKEN cDNA A530099J19 gene** | A530099J19Rik | 3.41 | 0.0095138 | ENSMUSG00000047462 |
| **capping protein regulator and myosin 1 linker 2** | Carmil2 | 3.41 | 0.0349179 | ENSMUSG00000050357 |
| **RIKEN cDNA C030006K11 gene** | C030006K11Rik | 3.41 | 0.012354 | ENSMUSG00000033707 |
| **interleukin 18 receptor 1** | Il18r1 | 3.40 | 0.0023164 | ENSMUSG00000026070 |
| **a disintegrin-like and metallopeptidase (reprolysin type) with thrombospondin type 1 motif, 20** | Adamts20 | 3.40 | 0.0096107 | ENSMUSG00000022449 |
| **interleukin 7 receptor** | Il7r | 3.39 | 0.001553 | ENSMUSG00000003882 |
| **CD24a antigen** | Cd24a | 3.37 | 0.0023102 | ENSMUSG00000047139 |
| **unspecified** | | 3.36 | 0.0418002 | ENSMUSG00000030638 |
| **complexin 1** | Cplx1 | 3.36 | 0.0240711 | ENSMUSG00000033615 |
| **FMS-like tyrosine kinase 3** | Flt3 | 3.36 | 0.0059871 | ENSMUSG00000042817 |
| **CAP-GLY domain containing linker protein family, member 4** | Clip4 | 3.35 | 0.0074851 | ENSMUSG00000024059 |
| **unspecified** | | 3.35 | 2.05E-10 | ENSMUSG00000086587 |
| **RIKEN cDNA D630039A03 gene** | D630039A03Rik | 3.34 | 0.0337204 | ENSMUSG00000052117 |
| **germinal center associated, signaling and motility** | Gcsam | 3.34 | 0.0056329 | ENSMUSG00000022659 |

| | | | | |
|---|---|---|---|---|
| **interaction protein for cytohesin exchange factors 1** | Ipcef1 | 3.34 | 0.0160526 | ENSMUSG00000064065 |
| **desmoglein 2** | Dsg2 | 3.33 | 0.0478769 | ENSMUSG00000044393 |
| **interferon activated gene 209** | Ifi209 | 3.33 | 0.0191572 | ENSMUSG00000043263 |
| **chemokine (C-C motif) ligand 5** | Ccl5 | 3.32 | 0.0472511 | ENSMUSG00000035042 |
| **adenylate cyclase 2** | Adcy2 | 3.32 | 0.0285399 | ENSMUSG00000021536 |
| **phosphoenolpyruvate carboxykinase 1, cytosolic** | Pck1 | 3.32 | 0.0006358 | ENSMUSG00000027513 |
| **RAS guanyl releasing protein 1** | Rasgrp1 | 3.32 | 0.0045588 | ENSMUSG00000027347 |
| **unspecified** | | 3.32 | 0.0211623 | ENSMUSG00000073538 |
| **TBC1 domain family, member 10c** | Tbc1d10c | 3.31 | 0.0119252 | ENSMUSG00000040247 |
| **sarcalumenin** | Srl | 3.30 | 0.0251617 | ENSMUSG00000022519 |
| **unspecified** | | 3.29 | 8.14E-06 | ENSMUSG00000085095 |
| **phosphoinositide-3-kinase interacting protein 1** | Pik3ip1 | 3.28 | 5.79E-05 | ENSMUSG00000034614 |
| **zinc finger and SCAN domain containing 30** | Zscan30 | 3.28 | 0.0093339 | ENSMUSG00000024274 |
| **unspecified** | | 3.28 | 0.0266242 | ENSMUSG00000084929 |
| **immunoglobulin superfamily, DCC subclass, member 3** | Igdcc3 | 3.27 | 0.0227399 | ENSMUSG00000032394 |

| | | | | |
|---|---|---|---|---|
| **sex comb on midleg-like 4 (Drosophila)** | Scml4 | 3.26 | 0.0196042 | ENSMUSG00000044770 |
| **a disintegrin and metallopeptidase domain 2** | Adam2 | 3.25 | 0.0396689 | ENSMUSG00000022039 |
| **unspecified** | | 3.24 | 0.0164941 | ENSMUSG00000097418 |
| **deoxyribonuclease 1-like 3** | Dnase1l3 | 3.24 | 0.0026995 | ENSMUSG00000025279 |
| **alanine and arginine rich domain containing protein** | Aard | 3.23 | 0.0020087 | ENSMUSG00000068522 |
| **G protein-coupled receptor 162** | Gpr162 | 3.23 | 0.0042012 | ENSMUSG00000038390 |
| **transient receptor potential cation channel, subfamily M, member 2** | Trpm2 | 3.23 | 0.0010026 | ENSMUSG00000009292 |
| **fatty acid amide hydrolase** | Faah | 3.22 | 0.0302397 | ENSMUSG00000034171 |
| **LanC lantibiotic synthetase component C-like 3 (bacterial)** | Lancl3 | 3.22 | 0.0052004 | ENSMUSG00000047344 |
| **solute carrier family 9, subfamily B (NHA2, cation proton antiporter 2), member 2** | Slc9b2 | 3.21 | 0.000643 | ENSMUSG00000037994 |
| **calcium/calmodulin-dependent protein kinase II alpha** | Camk2a | 3.21 | 0.0392437 | ENSMUSG00000024617 |
| **interferon lambda receptor 1** | Ifnlr1 | 3.20 | 0.0220032 | ENSMUSG00000062157 |
| **purinergic receptor P2X, ligand-gated ion channel, 3** | P2rx3 | 3.18 | 0.0005946 | ENSMUSG00000027071 |

| | | | | |
|---|---|---|---|---|
| **lysophosphatidic acid receptor 2** | Lpar2 | 3.17 | 0.0261193 | ENSMUSG00000031861 |
| **unspecified** | | 3.16 | 0.0005438 | ENSMUSG00000085962 |
| **Fc receptor, IgA, IgM, high affinity** | Fcamr | 3.15 | 0.0003123 | ENSMUSG00000026415 |
| **cytohesin 1 interacting protein** | Cytip | 3.15 | 0.0016672 | ENSMUSG00000026832 |
| **special AT-rich sequence binding protein 1** | Satb1 | 3.14 | 0.0014559 | ENSMUSG00000023927 |
| **major facilitator superfamily domain containing 4A** | Mfsd4a | 3.14 | 0.0089162 | ENSMUSG00000059149 |
| **growth factor independent 1** | Gfi1 | 3.14 | 0.0434361 | ENSMUSG00000029275 |
| **unspecified** | | 3.14 | 0.03995 | ENSMUSG00000097434 |
| **chloride channel accessory 3A1** | Clca3a1 | 3.13 | 0.002042 | ENSMUSG00000056025 |
| **unspecified** | | 3.13 | 0.0116756 | ENSMUSG00000078314 |
| **hypoxia inducible factor 3, alpha subunit** | Hif3a | 3.13 | 0.0373293 | ENSMUSG00000004328 |
| **thyroid hormone responsive** | Thrsp | 3.12 | 6.88E-08 | ENSMUSG00000035686 |
| **discs, large (Drosophila) homolog-associated protein 1** | Dlgap1 | 3.12 | 0.0090274 | ENSMUSG00000003279 |
| **BTB and CNC homology, basic leucine zipper transcription factor 2** | Bach2 | 3.11 | 0.0008558 | ENSMUSG00000040270 |
| **transmembrane protein 25** | Tmem25 | 3.11 | 1.89E-05 | ENSMUSG00000002032 |

| | | | | |
|---|---|---|---|---|
| **unspecified** | | 3.11 | 0.0203781 | ENSMUSG00000097993 |
| **unspecified** | | 3.10 | 0.0054057 | ENSMUSG00000041481 |
| **EF-hand domain (C-terminal) containing 2** | Efhc2 | 3.10 | 0.0154728 | ENSMUSG00000025038 |
| **regulator of G-protein signalling 9 binding protein** | Rgs9bp | 3.09 | 0.005162 | ENSMUSG00000056043 |
| **clusterin** | Clu | 3.09 | 0.0002652 | ENSMUSG00000022037 |
| **potassium inwardly-rectifying channel, subfamily J, member 10** | Kcnj10 | 3.08 | 0.0100899 | ENSMUSG00000044708 |
| **unspecified** | | 3.08 | 0.0018981 | ENSMUSG00000079457 |
| **ATP-binding cassette, sub-family G (WHITE), member 4** | Abcg4 | 3.07 | 0.0070914 | ENSMUSG00000032131 |
| **GTPase, IMAP family member 3** | Gimap3 | 3.07 | 0.0158003 | ENSMUSG00000039264 |
| **SH3-binding domain kinase family, member 2** | Sbk2 | 3.07 | 0.0120858 | ENSMUSG00000030433 |
| **ATP-binding cassette, sub-family C (CFTR/MRP), member 8** | Abcc8 | 3.07 | 0.0137634 | ENSMUSG00000040136 |
| **gamma-aminobutyric acid (GABA) C receptor, subunit rho 2** | Gabrr2 | 3.07 | 1.03E-06 | ENSMUSG00000023267 |
| **unspecified** | | 3.06 | 0.0441507 | ENSMUSG00000053263 |
| **nerve growth factor receptor (TNFR superfamily, member 16)** | Ngfr | 3.06 | 0.0058796 | ENSMUSG00000000120 |

| | | | | |
|---|---|---|---|---|
| **anti-Mullerian hormone type 2 receptor** | Amhr2 | 3.06 | 1.27E-07 | ENSMUSG00000023047 |
| **ubiquitin-conjugating enzyme E2Q family-like 1** | Ube2ql1 | 3.05 | 0.0444628 | ENSMUSG00000052981 |
| **unspecified** | | 3.04 | 0.0051123 | ENSMUSG00000085914 |
| **spermatogenesis associated 33** | Spata33 | 3.03 | 0.020691 | ENSMUSG00000048478 |
| **NIPA-like domain containing 1** | Nipal1 | 3.03 | 0.046659 | ENSMUSG00000067219 |
| **CD7 antigen** | Cd7 | 3.03 | 0.0389559 | ENSMUSG00000025163 |
| **ladinin** | Lad1 | 3.03 | 0.0211804 | ENSMUSG00000041782 |
| **chemokine (C-C motif) receptor 10** | Ccr10 | 3.03 | 0.033426 | ENSMUSG00000044052 |
| **ADP-ribosyltransferase 4** | Art4 | 3.02 | 0.0068214 | ENSMUSG00000030217 |
| **POU domain, class 2, transcription factor 2** | Pou2f2 | 3.02 | 0.0123133 | ENSMUSG00000008496 |
| **unspecified** | | 3.01 | 0.0087386 | ENSMUSG00000043773 |

***Table 6.2***

*List of genes significantly downregulated in WATsc of D316A-Tg HFD-fed mice relative to WT-Tg. Data are presented as Log2FC over WT-Tg with calculated fold change and an adjusted p value <0.05. N=6, 6*

| Gene Name | Symbol | Fold Change | padj | Gene |
|---|---|---|---|---|
| **keratin 15** | Krt15 | -45.63 | 0.00187779 8 | ENSMUSG00000054146 |

| | | | | |
|---|---|---|---|---|
| **discs, large (Drosophila) homolog-associated protein 2** | Dlgap2 | -38.30 | 3.50E-08 | ENSMUSG00000047495 |
| **keratin 5** | Krt5 | -34.05 | 0.009700148 | ENSMUSG00000061527 |
| **RIKEN cDNA 3110035E14 gene** | 3110035E14Rik | -25.35 | 0.0010558155 | ENSMUSG00000067879 |
| **keratin 14** | Krt14 | -24.77 | 0.01443804 6 | ENSMUSG00000045545 |
| **lectin, galactose binding, soluble 7** | Lgals7 | -18.49 | 0.009 23184 | ENSMUSG00000053522 |
| **unspecified** | | -18.25 | 0.000 10217 7 | ENSMUSG00000075027 |
| **5-hydroxytryptamine (serotonin) receptor 2B** | Htr2b | -10.53 | 0.000 18229 5 | ENSMUSG00000026228 |
| **RIKEN cDNA 9130409I23 gene** | 9130409I23Rik | -9.84 | 0.001 28814 5 | ENSMUSG00000038768 |
| **mannoside acetylglucosaminyltransferase 5, isoenzyme B** | Mgat5b | -9.25 | 0.002 26628 | ENSMUSG00000043857 |
| **UDP glucuronosyltransferase 2 family, polypeptide B37** | Ugt2b37 | -8.86 | 0.009690598 | ENSMUSG00000057425 |
| **solute carrier family 10 (sodium/bile acid cotransporter family), member 5** | Slc10a5 | -8.63 | 0.001658939 | ENSMUSG00000058921 |

| | | | | |
|---|---|---|---|---|
| **desmoplakin** | Dsp | -8.03 | 0.00050557 1 | ENSMUSG00000054889 |
| **lysozyme-like 4** | Lyzl4 | -7.94 | 0.00377847 | ENSMUSG00000032530 |
| **oxidized low density lipoprotein (lectin-like) receptor 1** | Olr1 | -7.64 | 0.00102067 2 | ENSMUSG00000030162 |
| **collagen, type X, alpha 1** | Col10a1 | -7.53 | 1.21E-06 | ENSMUSG00000039462 |
| **unspecified** | | -7.36 | 0.01129652 8 | ENSMUSG00000095134 |
| **fos-like antigen 1** | Fosl1 | -7.31 | 2.08E-06 | ENSMUSG00000024912 |
| **unspecified** | | -7.15 | 0.03953700 7 | ENSMUSG00000078685 |
| **integrin, alpha D** | Itgad | -7.03 | 0.01627982 6 | ENSMUSG00000070369 |
| **slit homolog 2 (Drosophila)** | Slit2 | -7.02 | 4.10E-07 | ENSMUSG00000031558 |
| **Fas apoptotic inhibitory molecule 2** | Faim2 | -6.93 | 0.02956527 9 | ENSMUSG00000023011 |
| **glutamate receptor, ionotropic, kainate 4** | Grik4 | -6.88 | 1.20E-05 | ENSMUSG00000032017 |
| **serine peptidase inhibitor, Kazal type 5** | Spink5 | -6.85 | 0.02354300 8 | ENSMUSG00000055561 |
| **neurocan** | Ncan | -6.39 | 6.96E-05 | ENSMUSG00000002341 |

| | | | | |
|---|---|---|---|---|
| **family with sequence similarity 25, member C** | Fam25c | -6.29 | 0.039452256 | ENSMUSG00000043681 |
| **neurexophilin 4** | Nxph4 | -6.28 | 0.021869607 | ENSMUSG00000040258 |
| **sprouty homolog 3 (Drosophila)** | Spry3 | -6.20 | 5.16E-05 | ENSMUSG00000061654 |
| **fibroblast growth factor 9** | Fgf9 | -6.15 | 2.35E-08 | ENSMUSG00000021974 |
| **arylacetamide deacetylase (esterase)** | Aadac | -6.14 | 0.003921205 | ENSMUSG00000027761 |
| **unspecified** | | -6.06 | 3.10E-09 | ENSMUSG00000090939 |
| **GIPC PDZ domain containing family, member 2** | Gipc2 | -6.05 | 1.38E-09 | ENSMUSG00000039131 |
| **high mobility group AT-hook 2** | Hmga2 | -6.04 | 0.007761282 | ENSMUSG00000056758 |
| **epiregulin** | Ereg | -5.99 | 0.025705884 | ENSMUSG00000029377 |
| **unspecified** | | -5.99 | 0.019568456 | ENSMUSG00000065778 |
| **loricrin** | Lor | -5.95 | 0.049193888 | ENSMUSG00000043165 |
| **cytochrome P450, family 21, subfamily a, polypeptide 1** | Cyp21a1 | -5.90 | 0.03205992 | ENSMUSG00000024365 |

| | | | | |
|---|---|---|---|---|
| **unspecified** | | -5.88 | 0.000185941 | ENSMUSG00000072844 |
| **TOX high mobility group box family member 3** | Tox3 | -5.86 | 0.002451633 | ENSMUSG00000043668 |
| **unspecified** | | -5.83 | 0.030263271 | ENSMUSG00000095532 |
| **myosin, heavy chain 15** | Myh15 | -5.65 | 0.009431981 | ENSMUSG00000092009 |
| **GRB2 associated regulator of MAPK1 subtype 2** | Garem2 | -5.60 | 0.026738043 | ENSMUSG00000044576 |
| **S100 calcium binding protein A14** | S100a14 | -5.59 | 0.016765039 | ENSMUSG00000042306 |
| **transmembrane protein 200A** | Tmem200a | -5.58 | 0.001120009 | ENSMUSG00000049420 |
| **angiopoietin-like 8** | Angptl8 | -5.55 | 3.67E-17 | ENSMUSG00000047822 |
| **major urinary protein 9** | Mup9 | -5.50 | 0.035313166 | ENSMUSG00000078686 |
| **fatty acid binding protein 2, intestinal** | Fabp2 | -5.49 | 0.003956795 | ENSMUSG00000023057 |
| **elongation of very long chain fatty acids (FEN1/Elo2, SUR4/Elo3, yeast)-like 4** | Elovl4 | -5.38 | 0.001269033 | ENSMUSG00000032262 |

| | | | | |
|---|---|---|---|---|
| **claudin 23** | Cldn23 | -5.38 | 0.009610663 | ENSMUSG00000055976 |
| **glutathione S-transferase, mu 3** | Gstm3 | -5.37 | 0.005185094 | ENSMUSG00000004038 |
| **platelet-derived growth factor receptor-like** | Pdgfrl | -5.30 | 3.87E-06 | ENSMUSG00000031595 |
| **kinesin family member 26B** | Kif26b | -5.27 | 0.000648237 | ENSMUSG00000026494 |
| **adhesion G protein-coupled receptor V1** | Adgrv1 | -5.27 | 1.14E-05 | ENSMUSG00000069170 |
| **von Willebrand factor A domain containing 5B1** | Vwa5b1 | -5.24 | 0.003513265 | ENSMUSG00000028753 |
| **unspecified** | | -5.21 | 0.020458021 | ENSMUSG00000084983 |
| **fibulin 7** | Fbln7 | -5.12 | 1.19E-09 | ENSMUSG00000027386 |
| **interleukin 20 receptor beta** | Il20rb | -5.01 | 4.09E-14 | ENSMUSG00000044244 |
| **PERP, TP53 apoptosis effector** | Perp | -4.87 | 2.55E-05 | ENSMUSG00000019851 |
| **unspecified** | NA | -4.87 | 7.72E-06 | ENSMUSG00000086869 |
| **WW, C2 and coiled-coil domain containing 1** | Wwc1 | -4.78 | 2.50E-07 | ENSMUSG00000018849 |
| **UDP glucuronosyltransferase 2 family, polypeptide B5** | Ugt2b5 | -4.74 | 0.009544413 | ENSMUSG00000054630 |
| **acyl-coenzyme A amino acid N-acyltransferase 1** | Acnat1 | -4.73 | 0.040206973 | ENSMUSG00000070985 |

| | | | | |
|---|---|---|---|---|
| **transmembrane protein 132B** | Tmem132b | -4.66 | 0.011437304 | ENSMUSG00000070498 |
| **BTB (POZ) domain containing 17** | Btbd17 | -4.64 | 0.025589461 | ENSMUSG00000000202 |
| **major urinary protein 18** | Mup18 | -4.60 | 0.027504787 | ENSMUSG00000078674 |
| **APOBEC1 complementation factor** | A1cf | -4.52 | 0.033540249 | ENSMUSG00000052595 |
| **histidine ammonia lyase** | Hal | -4.51 | 0.029010111 | ENSMUSG00000020017 |
| **ubiquitin D** | Ubd | -4.45 | 0.011542304 | ENSMUSG00000035186 |
| **membrane frizzled-related protein** | Mfrp | -4.44 | 0.029369068 | ENSMUSG00000034739 |
| **calcium channel, voltage-dependent, gamma subunit 5** | Cacng5 | -4.42 | 0.00027986 8 | ENSMUSG00000040373 |
| **solute carrier family 4 (anion exchanger), member 1** | Slc4a1 | -4.41 | 0.043186538 | ENSMUSG00000006574 |
| **transient receptor potential cation channel, subfamily C, member 4** | Trpc4 | -4.36 | 0.036338887 | ENSMUSG00000027748 |
| **matrix metallopeptidase 3** | Mmp3 | -4.35 | 0.000990905 | ENSMUSG00000043613 |
| **lipocalin 2** | Lcn2 | -4.33 | 0.0011282 | ENSMUSG00000026822 |

| | | | | |
|---|---|---|---|---|
| **hydroxysteroid (17-beta) dehydrogenase 6** | Hsd17b6 | -4.32 | 0.04661225 3 | ENSMUSG00000025396 |
| **G protein-coupled receptor 39** | Gpr39 | -4.29 | 0.00095686 5 | ENSMUSG00000026343 |
| **deiodinase, iodothyronine, type I** | Dio1 | -4.28 | 0.02084371 2 | ENSMUSG00000034785 |
| **complement component 9** | C9 | -4.25 | 0.01980211 1 | ENSMUSG00000022149 |
| **carboxylesterase 1G** | Ces1g | -4.19 | 0.01367044 3 | ENSMUSG00000057074 |
| **sal-like 1 (Drosophila)** | Sall1 | -4.19 | 0.00513191 2 | ENSMUSG00000031665 |
| **small leucine-rich protein 1** | Smlr1 | -4.17 | 0.03466743 4 | ENSMUSG00000096546 |
| **unspecified** | | -4.16 | 0.02638938 2 | ENSMUSG00000093622 |
| **carbonic anhydrase 6** | Car6 | -4.08 | 0.02997410 2 | ENSMUSG00000028972 |
| **chitinase-like 1** | Chil1 | -4.06 | 0.04893653 3 | ENSMUSG00000064246 |
| **serine (or cysteine) peptidase inhibitor, clade A (alpha-1 antiproteinase, antitrypsin), member 11** | Serpina11 | -4.06 | 0.03761673 7 | ENSMUSG00000063232 |

| | | | | |
|---|---|---|---|---|
| **epithelial mitogen** | Epgn | -4.03 | 0.00027986 8 | ENSMUSG00000035020 |
| **hyaluronan and proteoglycan link protein 4** | Hapln4 | -4.02 | 3.87E-05 | ENSMUSG00000007594 |
| **potassium voltage gated channel, Shaw-related subfamily, member 2** | Kcnc2 | -3.95 | 4.15E-07 | ENSMUSG00000035681 |
| **UDP glucuronosyltransferase 1 family, polypeptide A5** | Ugt1a5 | -3.94 | 0.03858581 5 | ENSMUSG00000089943 |
| **serum amyloid A 1** | Saa1 | -3.91 | 0.03801305 3 | ENSMUSG00000074115 |
| **tryptophan 2,3-dioxygenase** | Tdo2 | -3.89 | 0.03769338 9 | ENSMUSG00000028011 |
| **hemopexin** | Hpx | -3.87 | 0.00615973 7 | ENSMUSG00000030895 |
| **UDP glucuronosyltransferase 2 family, polypeptide A3** | Ugt2a3 | -3.86 | 0.04833057 7 | ENSMUSG00000035780 |
| **RAS, dexamethasone-induced 1** | Rasd1 | -3.86 | 5.73E-07 | ENSMUSG00000049892 |
| **iodotyrosine deiodinase** | Iyd | -3.81 | 0.01861830 8 | ENSMUSG00000019762 |
| **serum amyloid A 4** | Saa4 | -3.79 | 0.02997410 2 | ENSMUSG00000040017 |
| **zinc finger protein 750** | Zfp750 | -3.76 | 0.04998498 5 | ENSMUSG00000039238 |

| | | | | |
|---|---|---|---|---|
| **UDP glucuronosyltransferase 2 family, polypeptide B35** | Ugt2b35 | -3.74 | 0.017507496 | ENSMUSG00000035811 |
| **spondin 2, extracellular matrix protein** | Spon2 | -3.71 | 1.67E-06 | ENSMUSG00000037379 |
| **aldo-keto reductase family 1, member C6** | Akr1c6 | -3.70 | 0.036505945 | ENSMUSG00000021210 |
| **lumican** | Lum | -3.69 | 2.12E-09 | ENSMUSG00000036446 |
| **Ly6/Plaur domain containing 1** | Lypd1 | -3.67 | 0.001150413 | ENSMUSG00000026344 |
| **butyrobetaine (gamma), 2-oxoglutarate dioxygenase 1 (gamma-butyrobetaine hydroxylase)** | Bbox1 | -3.66 | 0.00513757 | ENSMUSG00000041660 |
| **mannose-binding lectin (protein C) 2** | Mbl2 | -3.64 | 0.03704101 | ENSMUSG00000024863 |
| **S100 calcium binding protein A3** | S100a3 | -3.64 | 0.044122661 | ENSMUSG00000001021 |
| **hydroxysteroid (17-beta) dehydrogenase 13** | Hsd17b13 | -3.63 | 0.020135553 | ENSMUSG00000034528 |
| **V-set and immunoglobulin domain containing 4** | Vsig4 | -3.62 | 0.00027986 8 | ENSMUSG00000044206 |
| **hydroxysteroid 11-beta dehydrogenase 2** | Hsd11b2 | -3.59 | 0.002697573 | ENSMUSG00000031891 |

| | | | | |
|---|---|---|---|---|
| **chemokine (C-X-C motif) ligand 2** | Cxcl2 | -3.57 | 0.02440359 8 | ENSMUSG00000058427 |
| **calmodulin-like 3** | Calml3 | -3.56 | 0.00615041 4 | ENSMUSG00000063130 |
| **cytochrome P450, family 17, subfamily a, polypeptide 1** | Cyp17a1 | -3.55 | 0.02396678 7 | ENSMUSG00000003555 |
| **sodium channel, voltage-gated, type VIII, alpha** | Scn8a | -3.54 | 0.00462598 5 | ENSMUSG00000023033 |
| **refilin A** | Rflna | -3.53 | 0.01111442 | ENSMUSG00000037962 |
| **complement component 3a receptor 1** | C3ar1 | -3.52 | 0.00062060 1 | ENSMUSG00000040552 |
| **hephaestin-like 1** | Hephl1 | -3.50 | 0.00503772 5 | ENSMUSG00000031936 |
| **carboxylesterase 3A** | Ces3a | -3.50 | 0.04979706 8 | ENSMUSG00000069922 |
| **galanin receptor 1** | Galr1 | -3.50 | 0.00772676 5 | ENSMUSG00000024553 |
| **apolipoprotein M** | Apom | -3.49 | 0.01035531 2 | ENSMUSG00000024391 |
| **retrotransposon gag domain containing 1** | Rgag1 | -3.48 | 0.00047311 6 | ENSMUSG00000085584 |
| **oncoprotein induced transcript 3** | Oit3 | -3.47 | 0.00076089 6 | ENSMUSG00000009654 |

| | | | | |
|---|---|---|---|---|
| **collectin sub-family member 10** | Colec10 | -3.44 | 0.017991283 | ENSMUSG00000038591 |
| **clarin 1** | Clrn1 | -3.44 | 0.024198843 | ENSMUSG00000043850 |
| **C-reactive protein, pentraxin-related** | Crp | -3.44 | 0.013593351 | ENSMUSG00000037942 |
| **solute carrier family 22 (organic cation transporter), member 1** | Slc22a1 | -3.44 | 0.036505945 | ENSMUSG00000023829 |
| **cytochrome P450, family 2, subfamily c, polypeptide 68** | Cyp2c68 | -3.42 | 0.049848887 | ENSMUSG00000074882 |
| **hyaluronic acid binding protein 2** | Habp2 | -3.40 | 0.000190257 | ENSMUSG00000025075 |
| **coagulation factor XII (Hageman factor)** | F12 | -3.40 | 0.040186086 | ENSMUSG00000021492 |
| **unspecified** | | -3.39 | 0.002521755 | ENSMUSG00000085058 |
| **neuronal cell adhesion molecule** | Nrcam | -3.38 | 0.000733731 | ENSMUSG00000020598 |
| **FAT atypical cadherin 3** | Fat3 | -3.37 | 0.001847775 | ENSMUSG00000074505 |
| **unspecified** | | -3.33 | 0.02980968 | ENSMUSG00000087593 |
| **fructose bisphosphatase 1** | Fbp1 | -3.32 | 0.029033144 | ENSMUSG00000069805 |

| | | | | |
|---|---|---|---|---|
| **unspecified** | | -3.32 | 0.03697302 6 | ENSMUSG00000089855 |
| **olfactory receptor 733** | Olfr733 | -3.31 | 0.02167874 | ENSMUSG00000090874 |
| **Fras1 related extracellular matrix protein 1** | Frem1 | -3.30 | 0.00065823 4 | ENSMUSG00000059049 |
| **histone cluster 1, H2ad** | Hist1h2ad | -3.29 | 0.03130497 5 | ENSMUSG00000071478 |
| **shisa family member 6** | Shisa6 | -3.28 | 0.00062223 9 | ENSMUSG00000053930 |
| **unspecified** | | -3.26 | 0.03040594 1 | ENSMUSG00000092545 |
| **aquaporin 8** | Aqp8 | -3.25 | 0.02182817 9 | ENSMUSG00000030762 |
| **folate receptor 2 (fetal)** | Folr2 | -3.25 | 5.04E-05 | ENSMUSG00000032725 |
| **coagulation factor IX** | F9 | -3.24 | 0.02634899 7 | ENSMUSG00000031138 |
| **betaine-homocysteine methyltransferase 2** | Bhmt2 | -3.24 | 0.03665342 | ENSMUSG00000042118 |
| **vasoactive intestinal peptide receptor 2** | Vipr2 | -3.23 | 0.01566243 1 | ENSMUSG00000011171 |
| **mannose-binding lectin (protein A) 1** | Mbl1 | -3.21 | 0.04222303 1 | ENSMUSG00000037780 |

| | | | | |
|---|---|---|---|---|
| **actin filament associated protein 1-like 2** | Afap1l2 | -3.21 | 7.66E-07 | ENSMUSG00000025083 |
| **aminoadipate aminotransferase** | Aadat | -3.21 | 0.031044178 | ENSMUSG00000057228 |
| **unspecified** | | -3.21 | 0.035092626 | ENSMUSG00000071204 |
| **DNA (cytosine-5-)-methyltransferase 3-like** | Dnmt3l | -3.19 | 0.002275419 | ENSMUSG00000000730 |
| **chemokine (C-X-C motif) ligand 1** | Cxcl1 | -3.19 | 2.28E-05 | ENSMUSG00000029380 |
| **tissue inhibitor of metalloproteinase 1** | Timp1 | -3.18 | 0.009906544 | ENSMUSG00000001131 |
| **potassium large conductance calcium-activated channel, subfamily M, beta member 1** | Kcnmb1 | -3.18 | 0.02731409 | ENSMUSG00000020155 |
| **a disintegrin-like and metallopeptidase (reprolysin type) with thrombospondin type 1 motif, 4** | Adamts4 | -3.17 | 0.00075122 | ENSMUSG00000006403 |
| **triggering receptor expressed on myeloid cells-like 1** | Treml1 | -3.16 | 0.03462681 | ENSMUSG00000023993 |
| **ubiquitin specific peptidase 43** | Usp43 | -3.16 | 1.83E-05 | ENSMUSG00000020905 |
| **unspecified** | | -3.15 | 0.00197700 3 | ENSMUSG00000096841 |

| | | | | |
|---|---|---|---|---|
| **aquaporin 9** | Aqp9 | -3.15 | 0.00172244 6 | ENSMUSG00000032204 |
| **triggering receptor expressed on myeloid cells 2** | Trem2 | -3.12 | 0.04830727 | ENSMUSG00000023992 |
| **apolipoprotein C-II** | Apoc2 | -3.11 | 0.00053860 2 | ENSMUSG00000002992 |
| **unspecified** | | -3.10 | 0.01957013 3 | ENSMUSG00000085913 |
| **ring finger protein 128** | Rnf128 | -3.10 | 0.00010798 7 | ENSMUSG00000031438 |
| **C-type lectin domain family 12, member a** | Clec12a | -3.09 | 0.00046918 9 | ENSMUSG00000053063 |
| **interleukin 13 receptor, alpha 2** | Il13ra2 | -3.08 | 0.00197723 6 | ENSMUSG00000031289 |
| **cytochrome P450, family 3, subfamily a, polypeptide 13** | Cyp3a13 | -3.08 | 0.03123492 4 | ENSMUSG00000029727 |
| **unspecified** | | -3.08 | 0.03233979 | ENSMUSG00000047728 |
| **tetraspanin 11** | Tspan11 | -3.07 | 4.52E-06 | ENSMUSG00000030351 |
| **aurora kinase A and ninein interacting protein** | Aunip | -3.07 | 0.03192120 2 | ENSMUSG00000078521 |
| **apolipoprotein N** | Apon | -3.07 | 0.03070016 7 | ENSMUSG00000051716 |

| | | | | |
|---|---|---|---|---|
| **wingless-type MMTV integration site family, member 16** | Wnt16 | -3.06 | 0.04893653 | ENSMUSG00000029671 |
| **carbohydrate (chondroitin 4) sulfotransferase 13** | Chst13 | -3.06 | 0.00015445 2 | ENSMUSG00000056643 |
| **collagen, type XII, alpha 1** | Col12a1 | -3.05 | 4.05E-05 | ENSMUSG00000032332 |
| **tumor necrosis factor receptor superfamily, member 12a** | Tnfrsf12a | -3.04 | 2.05E-06 | ENSMUSG00000023905 |
| **CD300 molecule like family member B** | Cd300lb | -3.02 | 0.00540350 2 | ENSMUSG00000063193 |
| **lactase-like** | Lctl | -3.02 | 0.02033136 7 | ENSMUSG00000032401 |
| **apelin receptor** | Aplnr | -3.02 | 0.00109181 5 | ENSMUSG00000044338 |
| **asialoglycoprotein receptor 1** | Asgr1 | -3.02 | 0.04345378 6 | ENSMUSG00000020884 |
| **hexokinase 3** | Hk3 | -3.00 | 0.00190545 9 | ENSMUSG00000025877 |
| **periostin, osteoblast specific factor** | Postn | -2.98 | 2.42E-05 | ENSMUSG00000027750 |
| **Fc receptor, IgG, high affinity I** | Fcgr1 | -2.97 | 0.00274919 3 | ENSMUSG00000015947 |
| **patched domain containing 1** | Ptchd1 | -2.96 | 0.01584947 5 | ENSMUSG00000041552 |

| | | | | |
|---|---|---|---|---|
| **chemokine (C-C motif) ligand 7** | Ccl7 | -2.96 | 0.041128603 | ENSMUSG00000035373 |
| **hydroxysteroid (17-beta) dehydrogenase 2** | Hsd17b2 | -2.95 | 0.02573143 | ENSMUSG00000031844 |
| **snail family zinc finger 1** | Snai1 | -2.95 | 3.11E-06 | ENSMUSG00000042821 |
| **melan-A** | Mlana | -2.94 | 0.039373372 | ENSMUSG00000024806 |
| **cyclin-dependent kinase 15** | Cdk15 | -2.94 | 0.00396967 4 | ENSMUSG00000026023 |
| **MICAL-like 2** | Micall2 | -2.93 | 4.05E-05 | ENSMUSG00000036718 |
| **DnaJ heat shock protein family (Hsp40) member B13** | Dnajb13 | -2.92 | 0.00330077 1 | ENSMUSG00000030708 |
| **coxsackie virus and adenovirus receptor** | Cxadr | -2.91 | 4.12E-10 | ENSMUSG00000022865 |
| **chemokine (C-C motif) receptor 5** | Ccr5 | -2.91 | 5.24E-05 | ENSMUSG00000079227 |
| **adhesion G protein-coupled receptor E1** | Adgre1 | -2.91 | 0.00042882 9 | ENSMUSG00000004730 |
| **macrophage scavenger receptor 1** | Msr1 | -2.86 | 8.96E-05 | ENSMUSG00000025044 |
| **serine (or cysteine) peptidase inhibitor, clade D, member 1** | Serpind1 | -2.86 | 0.02254586 3 | ENSMUSG00000022766 |
| **collagen, type IV, alpha 5** | Col4a5 | -2.84 | 5.09E-08 | ENSMUSG00000031274 |
| **urate (5-hydroxyiso-) hydrolase** | Urah | -2.84 | 0.03726108 1 | ENSMUSG00000025481 |

| | | | | |
|---|---|---|---|---|
| **dipeptidase 2** | Dpep2 | -2.83 | 0.00546193 6 | ENSMUSG00000053687 |
| **ryanodine receptor 2, cardiac** | Ryr2 | -2.83 | 1.14E-06 | ENSMUSG00000021313 |

## 6.2 Extended Metabolic Data

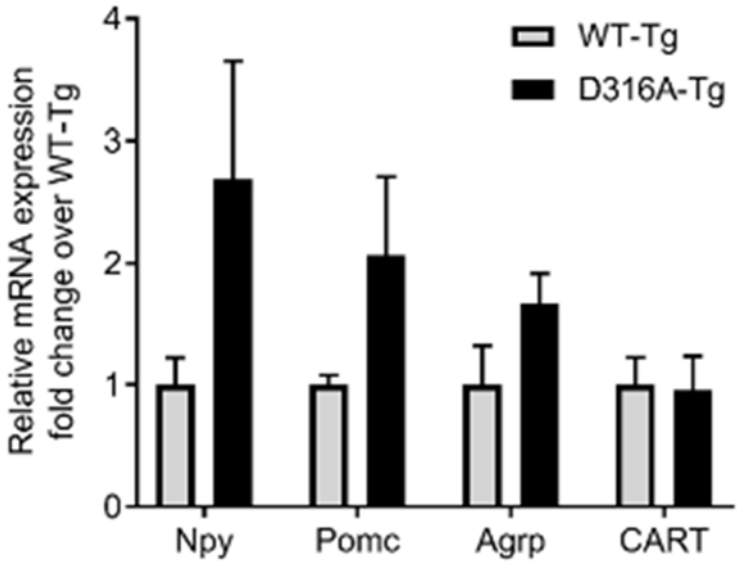



***Figure 6.1 Neuropeptide expression in chow-fed mice***

*Relative mRNA expression of Npy, Pomc, Agrp and CART neuropeptides in the hypothalamus of chow-fed WT-Tg and D316A-Tg mice. Expression is presented as fold change over WT-Tg, qPCR performed by Dr. Luis Martins N=6, 6. Data are presented as mean ±SEM.*

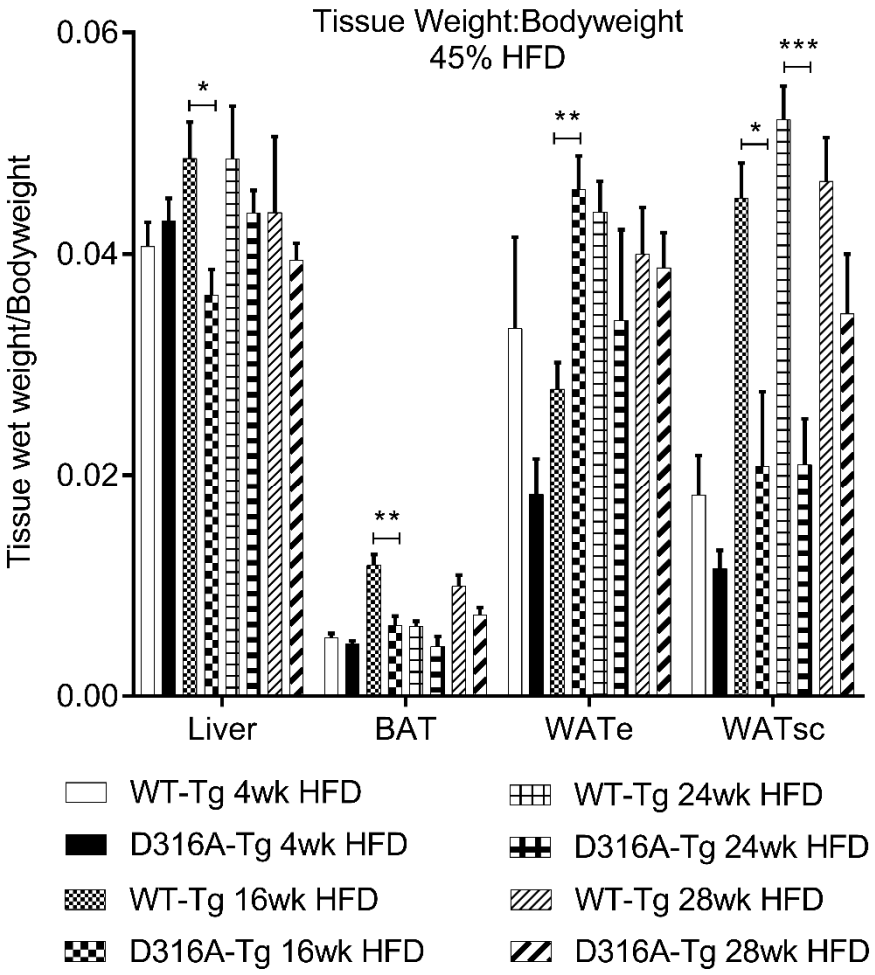



***Figure 6.2 Normalised tissue wet weight***

*Tissue weights from 4-week, 16-week and 28-week HFD-fed mice at harvest. 2-way ANOVA with Bonferroni multiple comparisons test was used to determine statistical significance. N=7, 7 (4-week HFD, 12-weeks old). N=8, 6 (16-week HFD, 24-weeks old). N=9, 8 (28-week HFD, 36-weeks old) Data are presented as mean ±SEM. *P<0.05, **P<0.01, ***P<0.001.*

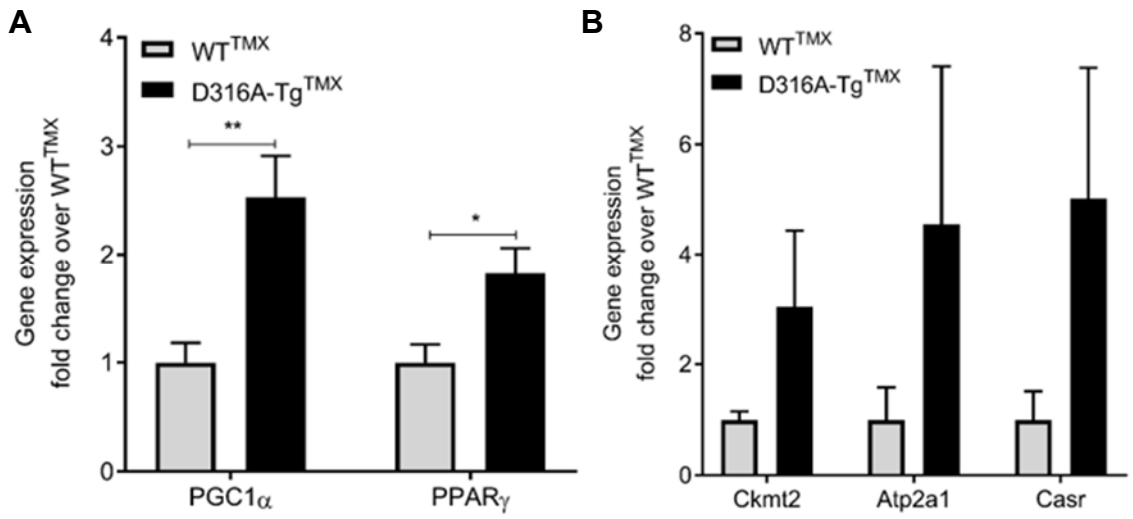



***Figure 6.3 BAT/muscle gene expression in D316A-Tg$^{TMX}$ WATsc***

***A)*** *Expression of key brown adipocyte genes in WATsc from 14-week HFD-fed WT$^{TMX}$ and D316A-Tg$^{TMX}$ mice. Data are presented as mean ±SEM. N=6, 6, *P<0.05, **P<0.01.*

***B)*** *Expression of key muscle genes in WATsc from 14-week HFD-fed WT$^{TMX}$ and D316A-Tg$^{TMX}$ mice. N=6, 6, Data are presented with permission as mean ±SEM.*

*qPCR kindly performed by Dr. Luis Martins.*

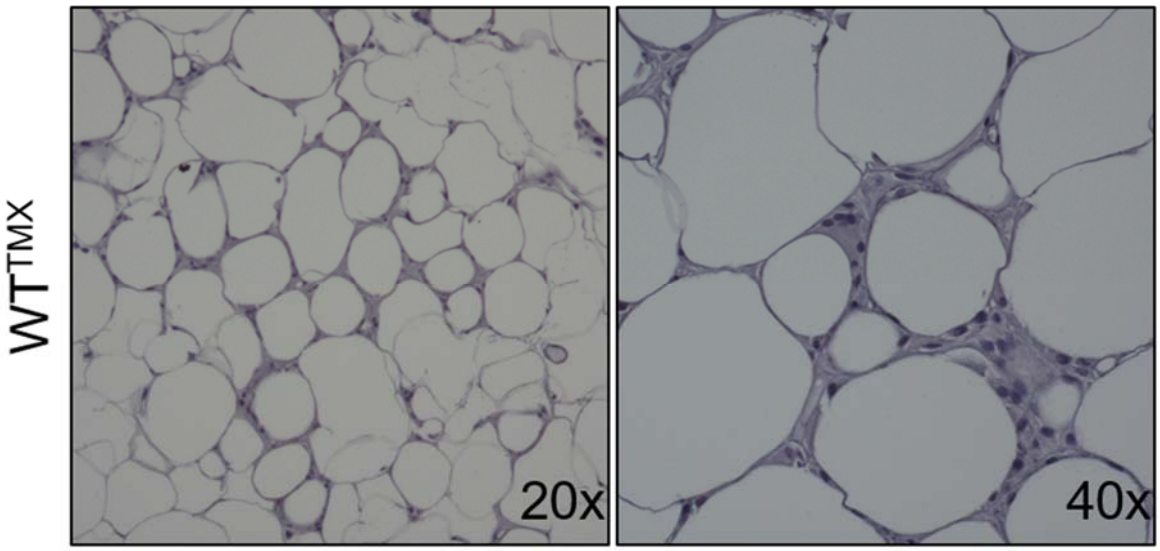



***Figure 6.4 Lipolysis in tamoxifen-treated gonadal WAT***

*Representative histological evidence for tamoxifen-induced lipolysis in gonadal white adipose tissue from HFD-fed WT-Tg mice, 10-weeks post-induction, n=1, 1.*

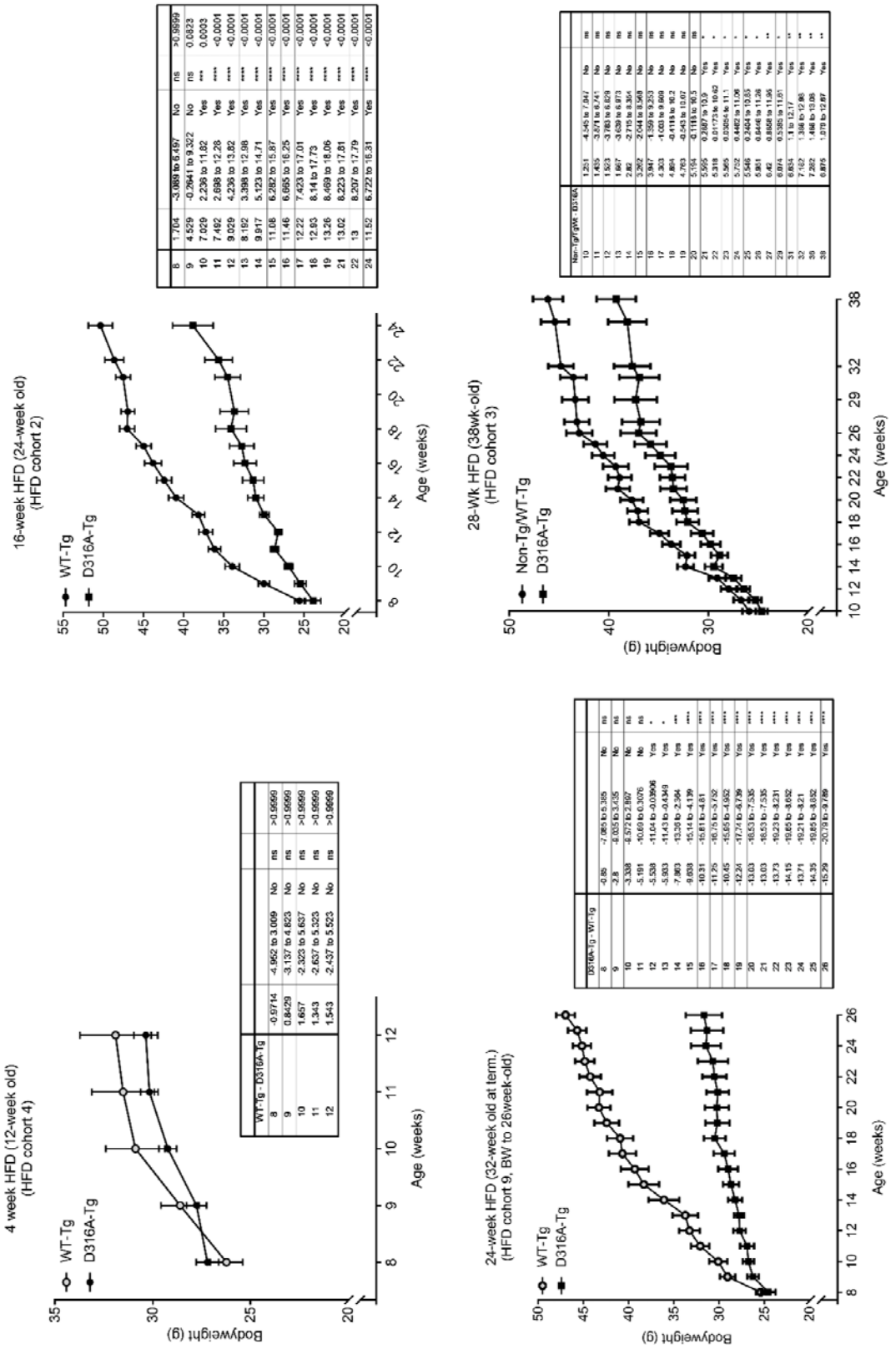



***Figure 6.5 Individual cohort bodyweight curves (HFD)***

*Bodyweight measurements of 4, 16, 24 and 28-week HFD-fed (12-, 24-, 32- and 38-week old) male mice. High-fat diet was administered from 8-weeks of age, excluding 28-week cohort, started at 10 weeks of age. Data are presented as mean ± SEM. *P<0.05, **P<0.01, ***P<0.001, ****P<0.0001.*